



# Chemical bonding on surfaces probed by X-ray emission spectroscopy and density functional theory

Anders Nilsson<sup>a,b,\*</sup>, Lars Gunnar Moody Pettersson<sup>b</sup>

<sup>a</sup>Stanford Synchrotron Radiation Laboratory, P.O. Box 20450, Stanford, CA 94309, USA

<sup>b</sup>FYSIKUM, AlbaNova University Center, Stockholm University, S-10691 Stockholm, Sweden

Accepted in final form 19 June 2004

2 September 2004

## Abstract

X-ray emission spectroscopy applied to surface adsorbates is an experimental technique that provides an atom-specific projection of the electronic structure. In combination with theoretical density functional spectrum simulations, it becomes an extremely powerful tool to analyze in detail the surface chemical bond. The present review discusses both the experimental and computational techniques related to the spectroscopy and summarizes all applications to surface adsorbates published up to May 2004. The surface chemical bond is discussed in depth for a number of example systems taken from the five categories of bonding types: (i) atomic radical, (ii) diatomics with unsaturated  $\pi$  systems (Blyholder model), (iii) unsaturated hydrocarbons (Dewar–Chatt–Duncanson model), (iv) lone pair interactions, and (v) saturated hydrocarbons (physisorption).

© 2004 Elsevier B.V. All rights reserved.

**Keywords:** Chemical bonding; X-ray emission spectroscopy; Density functional theory; Blyholder model; Chemisorption; CO; N<sub>2</sub>; NH<sub>3</sub>; Formate; Acetate; Glycine; Ethylene; Benzene; Water; Octane

## Contents

1. Introduction	51
2. The spectroscopic process	55
2.1. Resonant inelastic X-ray scattering and X-ray emission	57
2.2. Atom-specific probing	59

\* Corresponding author. Tel.: +1 650 926233; fax: +1 650 9264100.

E-mail address: [nilsson@slac.stanford.edu](mailto:nilsson@slac.stanford.edu) (A. Nilsson).

2.3.	X-ray emission and photoemission	60
2.4.	Orientalional symmetry probing	65
2.5.	Selective excitations	66
2.5.1.	Non-diagram transitions	67
2.5.2.	X-ray absorption resonances	68
2.5.3.	Symmetry selection rules	70
3.	Methodology	71
3.1.	Experimental	71
3.1.1.	Beamline and experimental endstation	72
3.1.2.	Soft X-ray emission spectrometer	74
3.1.3.	Future instrumental development	75
3.2.	Computational	77
3.2.1.	Dynamic core hole effects	80
3.2.2.	The final state rule	81
3.2.3.	Intensity Scale	84
3.2.4.	Cluster models	85
4.	Adsorbate systems	86
4.1.	Radical atomic adsorption	87
4.1.1.	Electronic structure of N on Cu(1 0 0)	88
4.1.2.	Chemical bonding of C, N and O on Ni and Cu	92
4.2.	Diatomic molecules	95
4.2.1.	N <sub>2</sub> adsorbed on Ni(1 0 0)	96
4.2.2.	CO adsorbed on Ni(1 0 0)	105
4.2.3.	CO adsorbed on Cu(1 0 0) and other metals	110
4.2.4.	Adsorption site dependent electronic structure of CO	113
4.2.5.	Co-adsorption of CO and K on Ni(1 0 0)	115
4.2.6.	Metal carbonyls and CO coordination to the heme group	118
4.3.	Unsaturated hydrocarbons	120
4.3.1.	Symmetry selection rules for ethylene and benzene adsorption on Cu(1 1 0)	121
4.3.2.	Chemical bonding of benzene on Cu(1 1 0) and Ni(1 0 0) surfaces	128
4.4.	Lone pair interactions	130
4.4.1.	Water on Pt(1 1 1)	130
4.4.2.	Adsorption of formate and acetate on Cu(1 1 0)	133
4.4.3.	Adsorption of ammonia on Cu(1 1 0)	138
4.4.4.	More complex molecules and interactions: glycine and hydrogen bonding	140
4.5.	Saturated hydrocarbons	149
4.5.1.	<i>n</i> -Octane adsorbed on Cu(1 1 0)	150
4.5.2.	Difference between octane on Ni and Cu surfaces	154
4.6.	Summary of adsorbate–metal bonding	156
5.	Future outlook	160
	Acknowledgements	161
	References	162

## 1. Introduction

Most of the important chemical reactions in nature and technology take place at surfaces and interfaces [1]. In order to understand many of these reactions, it is essential to establish a fundamental knowledge of how atoms and molecules interact with surfaces. When a molecule is adsorbed, new electronic states are formed due to the bonding to the surface. The nature of the surface chemical bond will determine the properties and reactivity of the adsorbed molecule. It is essential to have tools that allow studies of the electronic structure of adsorbates in a molecular orbital (MO) picture. In the present review, we will demonstrate how we can use X-ray emission spectroscopy (XES) together with density functional theory (DFT) calculations to obtain an understanding of the local electronic structure and chemical bonding of adsorbates on metal surfaces.

In the early 20th century, prior to the introduction of photoelectron spectroscopy (XPS), XES was the method of choice in its provision of an atom-specific tool for studying the electronic structure in matter [2]. It was mainly used for solids utilizing hard X-ray transitions between valence and core electron levels where the core hole was generated through electron beam excitation. The chemically important C, N and O edges in the soft X-ray regime were not accessible with reasonable resolution until the development of high-resolution grazing incidence grating spectrometers [3]. In the last decade, the spectroscopy has undergone a rapid development through the appearance of intense third-generation synchrotron radiation sources which have made selective excitation possible [4]. These sources opened the field for investigations of a number of different systems and phenomena, ranging from free molecules to magnetic materials. XES is inherently bulk sensitive since it is based on both incoming and outgoing X-rays. However, using grazing incidence of the incoming radiation, the method can be made more surface sensitive [5].

A large number of surface sensitive spectroscopic techniques are available for the study of the electronic structure of adsorbed molecules on surfaces [6]. However, it is often important to enhance the local information around the adsorbed entity. XES provides a method to locally study the electronic properties centered around one atomic site. This is particularly important when investigating complex systems such as molecular adsorbates with many different atomic sites. Fig. 1 shows a  $N_2$  molecule

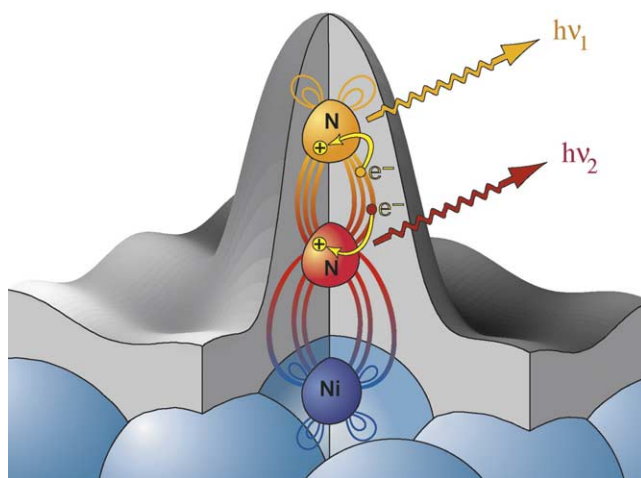


Fig. 1. Schematic picture illustrating the local probe character in XES for  $N_2$  adsorbed on a Ni surface. From the total charge density (gray envelope), valence electrons with p angular momentum (contour lines) decay into the N 1s core hole.

adsorbed on a Ni surface in a perpendicular geometry. The gray zone represents the charge density of the valence electrons extending outside the metal surface and we have made a cut around the adsorbate to see more deeply into the molecule. Inside, we can see one particular molecular orbital overlapping both the nitrogen and Ni atoms and the core electrons that are localized to one atom. Since the inner and outer nitrogen atoms are non-equivalent, the core levels of the two atoms are shifted relative to each other [7]. We can create a core hole on either one of the nitrogen atoms through selective excitation using highly energy-resolved synchrotron radiation. The core holes can decay through transitions between core and valence levels with the emission of X-rays. Since the core electrons are localized to one atom, we can in an atom-specific way study the valence electrons [8]. Furthermore, angle-resolved measurements allow a separation of valence levels of different symmetries. We thus have a tool to look into the nature of the surface chemical bond by disentangling the valence contributions from the different atoms.

The most common way to measure the occupied electronic structure is with valence band photoemission, also denoted ultraviolet photoelectron spectroscopy (UPS), where the overall electronic structure is probed through ionization of the valence electrons [9]. Since the method is based on detection of electrons the technique is inherently surface sensitive and a significant fraction of the spectral contribution can be associated with the adsorbate. Fig. 2 shows a comparison of UPS [10] and XE [8,11] spectra for N<sub>2</sub> adsorbed on Ni(1 0 0) (for a detailed discussion see Section 4.2.1). We can observe adsorbate-induced features in the region of 7–12 eV binding energy in both spectroscopies. However, in the important regime around 0–5 eV, where the metal valence d electrons reside, the UPS spectrum only shows strong substrate emission whereas the XE spectra reveal adsorbate-derived states. In addition, the XES provides a projection on the two different nitrogen atoms and a separation of  $\pi$  and  $\sigma$  states. However, there are special cases where the whole adsorbate electronic structure can be fully determined with UPS [12]. Using angular-resolved photoemission or UPS, the  $k$ -dispersion and symmetry of the electronic states and thereby the band structure can be measured [13]. If XES measures the local aspects of the electronic structure, UPS determines the more collective aspects. In this regard, the two techniques become complementary to each other.

Let us discuss XES in the context of the other different core-level spectroscopies. Fig. 3 shows schematic pictures of the core electrons and the electronic structure in a metal in terms of occupied and unoccupied valence states divided by a Fermi level. The different techniques can be separated into two classes: creation and decay of core holes. We can create a core hole through the absorption of incoming light. The core electron can be excited to a bound state or to the continuum where it will become a free particle. If the latter is the case, we can measure the outgoing kinetic energy of the photoelectron and determine the binding energy of the core level. The technique that makes such use of the ionization process is denoted photoelectron spectroscopy [14–18]. We can also measure the ionization process via the number of absorbed photons versus energy corresponding to an excitation into the ionization continuum [19]. In this case, we measure the total photoionization cross-section above a core-level threshold as function of energy. If the excitation energy is not high enough to reach the ionization continuum, we can populate bound states above the Fermi level. The method is generally denoted X-ray absorption spectroscopy (XAS). It is also divided into two regimes: near-edge X-ray absorption fine structure (NEXAFS) for bound states and low-energy resonances in the continuum, and extended X-ray absorption fine structure (EXAFS) when the outgoing electron is well above the ionization continuum. In the NEXAFS regime, the spectroscopy provides information about the empty electronic states above the Fermi level [20].

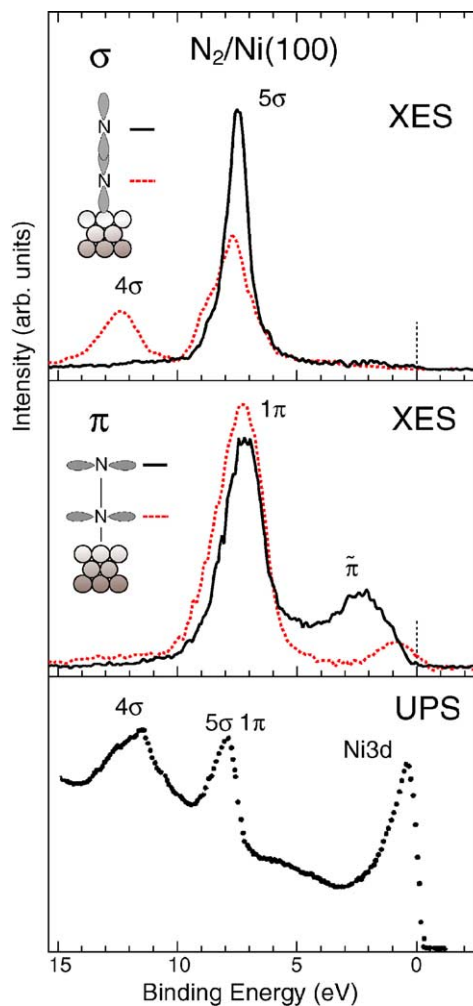


Fig. 2. Comparison between atom-specific and symmetry-resolved XE spectra [8] with an UPS spectrum measured at a photon energy of 35 eV [10] of  $N_2$  adsorbed on  $Ni(100)$ .

The core hole can decay through two different mechanisms involving non-radiative and radiative processes. The first process will lead to electron emission denoted Auger decay and the second to emission of X-rays (XES), the topic of this review. In Auger decay, an electron from one of the outer shells fills the core hole and a second electron, which is emitted from the system, takes up the excess energy. In the radiative XES process, the core hole is filled with an outer shell electron and the excess energy is emitted in the form of a photon. For all core levels, both types of processes contribute to the decay. The added rates of these decay channels determines the lifetime of the core hole state and thereby the intrinsic width of the core electron line. In order to obtain information about the bonding electrons, we are primarily interested in decay processes involving the valence states. The analysis of the emitted electrons or photons is the basis for Auger electron spectroscopy (AES) [21–23] or X-ray emission spectroscopy [4,24]. The final states of the two decay processes are rather different, AES leads to a two-

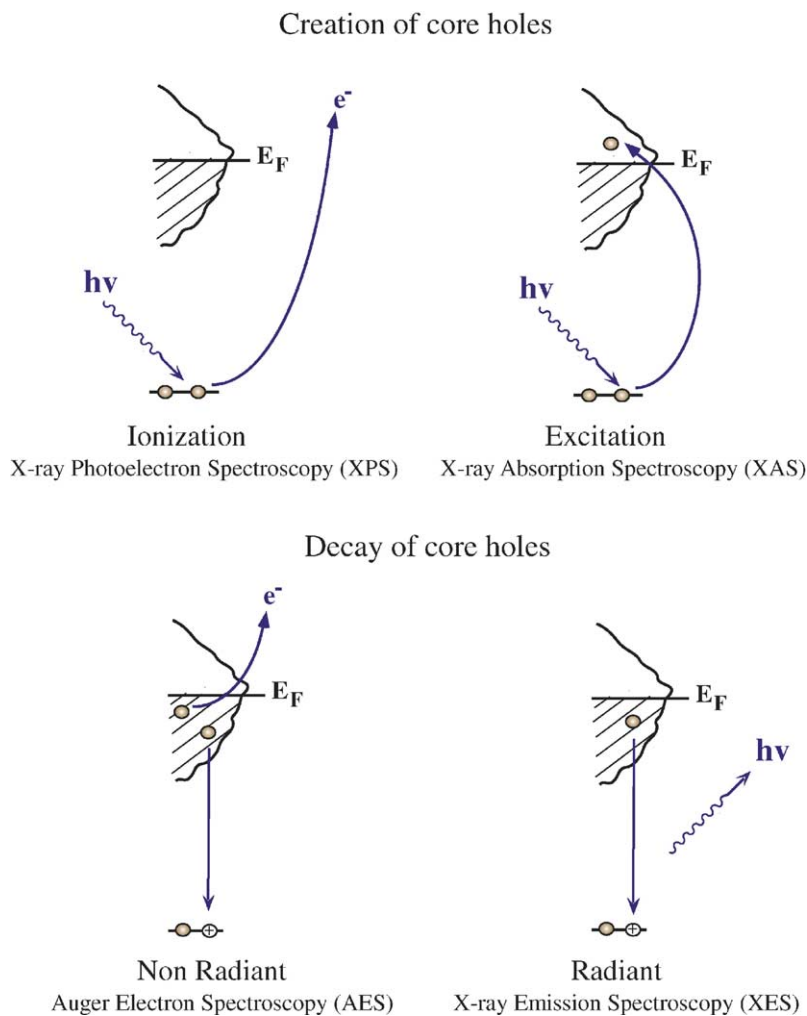


Fig. 3. A schematic illustration of core-level ionization, excitation and decay processes.

hole state whereas XES to a one-hole state. If we are interested in a simple one-electron picture, XES provides a direct tool for looking at the local valence electronic structure. The final states in AES often lead to strong interaction between the two holes and a simple interpretation in a one-electron picture is not possible. However, it does provide a way for investigating correlation effects between charged particles. So far, we have only considered a core-ionized initial state prior to the decay. An initial state with the core electron instead excited into a bound state can modify the decay process. The two steps, creation and decay, can lead to coupling and the whole process can be considered a one-step event [24–26].

There is a close connection between XES and NEXAFS. The former gives information on the occupied orbitals while the latter relates to the character and symmetry of the unoccupied levels. Both are governed by the dipole selection rule and the localized character of the core orbitals allows a simple atom-specific projection of the electronic structure; the major difference is in the final states.

In NEXAFS, the empty electronic states are probed in the presence of the core hole which can lead to major deviations from a simple ground state picture. In contrast, the XES final state contains no core hole and is similar to the valence hole state in UPS [27].

One additional important aspect is the connection between experiment and theory. Computational chemistry has undergone a tremendous development over the past few years and has developed into a powerful interpretative tool. One of the most important developments is within the field of density functional theory, which introduces a description of the dynamical, instantaneous correlation between electrons at the same computational cost as in the simpler Hartree–Fock self-consistent field (HF-SCF) approach. Here, the exchange interaction as well as the effects of dynamical, instantaneous correlation in the electron motion, are parameterized through functionals of the density and the gradient of the density. The accuracy of this approach is critically dependent on the class of functional that is used. The early local density approximation (LDA) only includes the density in the functional and this is not sufficient for a description of the energetics involved in bond formation, which naturally involves strong variations in the density. With the development of gradient-corrected functionals ( $F(\rho, \nabla\rho)$ ) as well as hybrid functionals (including contributions from Hartree–Fock exchange) sufficient accuracy for chemical applications has been achieved. DFT is thus now the preferred tool also for chemical applications.

The interplay between experiment and theory will be a recurrent theme in the present review. Due to the dipole selection rules in the X-ray emission process, only specific angular momentum contributions will be experimentally observable. For instance, in decays into a 1s core level, only 2p atomic contributions can contribute to the rate. The theoretical model can then be calibrated against the experiment and information on the remaining orbital contributions to the bonding, as well as a deeper analysis of the energetics, etc. can be obtained from theory. As will be evident in the following, the experimental spectra will often contain mixtures of contributions from different orbital symmetries. In order to obtain pure spectra, subtractions of spectra must be performed. The theory, on the other hand, naturally generates pure symmetry-resolved spectra which, after summation of the individual contributions, can be compared to the raw experimental data. This provides important independent controls of the validity of the analysis. Furthermore, in order to relate the intensities obtained from different elements in a multi-centered molecule to the 2p population on each center, we need to scale the independently normalized experimental cross-section using computed cross-sections for the atom with a known number of 2p electrons.

## 2. The spectroscopic process

In the following section, we will discuss some of the fundamental aspects of XES that are important for the applications to adsorbates on metal surfaces. There are a few essential steps involving different approximations that lead to a simple interpretation of the spectra in terms of an atom-specific and orbital symmetry-selective view of the electronic structure. The reader that can accept the simple one-electron picture and is more interested in the applications to chemical bonding on surfaces may go directly to Section 4.

Usually, we distinguish between non-resonant and resonant X-ray emission spectroscopy as illustrated in Fig. 4. The former corresponds to the case when the excitation energy well exceeds the core ionization threshold and the XES spectral profile is practically independent of the excitation energy. We can consider the process as a simple one-electron projection of the valence electronic structure in a one-step

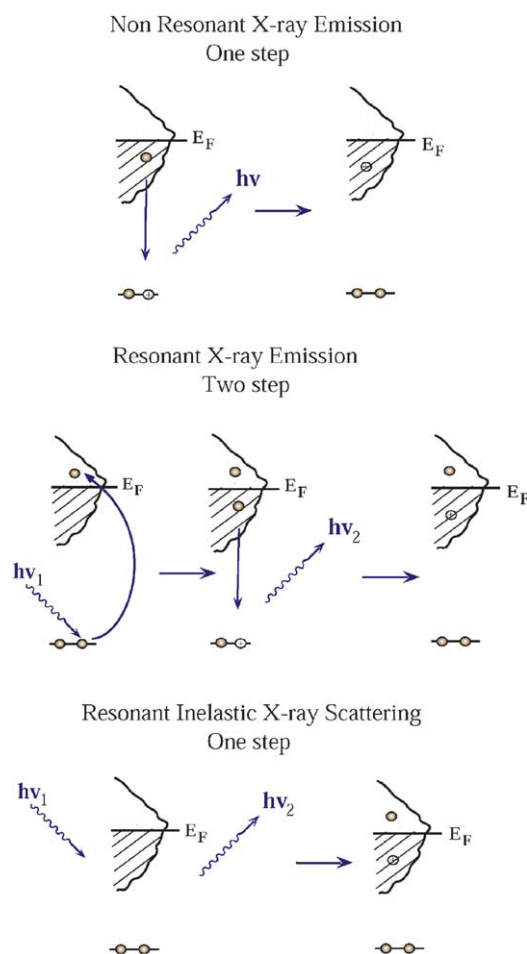


Fig. 4. A schematic illustration of non-resonant XES, resonant XES and resonant inelastic X-ray scattering processes in one-step and two-step descriptions.

manner, shown in the top part of Fig. 4. In the case of resonant XES, we have prepared a core-excited state that subsequently decays with the emission of a photon, in a two-step manner (middle part of Fig. 4). Here, we could expect that the spectral shape could vary depending on the nature of the core-excited state. In this model, we treat the excitation and decay steps independently of each other. A more general case of the latter process is when we regard both excitation and decay in a one-step manner as a non-separable inelastic X-ray scattering event [24,26] (see bottom part of Fig. 4). The incident photon is scattered and loses part of its energy creating an electron-hole pair in the solid. The cross-section for such an event in the soft X-ray regime is extremely small and is usually only observed above a core-level threshold. It is therefore usually denoted resonant inelastic X-ray scattering (RIXS). We will discuss under which circumstances we can regard the process in a one- or two-step model. The first step provides a means for selectively obtaining specific core holes on inequivalent atoms of the same element from chemically shifted XAS resonances. However, for systems with high symmetry the coupled two-step process provides an additional symmetry selection rule where the intensities of different transitions depend on the

specific core-excited state. The final state of the XES process is similar to UPS and we will show how the energy scales can be related to each other. In the two-step picture, the intermediate state contains a core hole. An important question is whether the transition intensities are affected by the core hole. It will be empirically shown that in most cases modifications due to the intermediate core hole state can be neglected. Another essential issue is if the presence of the excited electron can modify the spectrum. For all chemisorbed systems, the strong coupling to the substrate allows for an extremely fast delocalization of the excited state prior to the decay of the core hole state. We can therefore in most cases disregard the presence of the excited electron.

### 2.1. Resonant inelastic X-ray scattering and X-ray emission

If we want to derive a one-electron picture of the occupied electronic states, we should consider the X-ray emission process where one valence electron fills the inner hole vacancy and an X-ray photon is emitted. This would correspond to non-resonant XES. The question is why we want to make resonant excitations that make the picture much more complex. There are three main reasons: (i) to avoid non-diagram transitions, (ii) selective excitation of chemically shifted atoms of the same element, and (iii) symmetry-selective excitation of specific core hole states. This will be discussed in more detail in Section 2.5. It is necessary to use excitation energies close to threshold to create core hole states without any additional satellites. We can also excite into specific X-ray absorption resonances that are attributed to atoms in different chemical surroundings in a complex molecular adsorbate. In the case of N<sub>2</sub> on Ni, it is necessary to selectively excite the two inequivalent nitrogen atoms in the core excitation process using the chemical shift in the  $\pi$  resonance. For molecular systems with a high degree of symmetry, the more complex RIXS process can be used in a favorable way to gain more information (see Section 2.5.3). In the first two cases, we like to regard the X-ray emission process as a non-resonant decay process and only use the selective excitation to prepare a well-defined core hole state on a specific atom. Let us see which approximations from the general RIXS formalism that we need to apply to achieve this goal and what the limitations are.

From the perturbational treatment of resonant inelastic X-ray scattering, the modified Kramers–Heisenberg scattering formula of the spectral distribution is found [24,28]:

$$I_{\text{RIXS}}(\omega', \omega) \propto \sum_F \left| \sum_M \frac{\langle F | \vec{D} \cdot \vec{E}' | M \rangle \langle M | \vec{D} \cdot \vec{E} | G \rangle}{\hbar\omega - (E_M - E_F) + i\Gamma_M/2} \right|^2 \delta(\hbar\omega - \hbar\omega' + E_G - E_F) \quad (1)$$

Here,  $|F\rangle$ ,  $|M\rangle$  and  $|G\rangle$  are the total wave functions with energies  $E_F$ ,  $E_M$  and  $E_G$  of the final, intermediate and ground states, respectively. In the resonant case, the intermediate states are core excitations where  $\Gamma_M$  is the lifetime broadening of the intermediate core-excited state. The energies of the incoming and outgoing photons are given by  $\hbar\omega$  and  $\hbar\omega'$  with electric field vectors  $\vec{E}$  and  $\vec{E}'$ , respectively.  $\vec{D}$  represents the dipole operator. The scattering process is often viewed as two subsequent steps (see Fig. 4): first X-ray absorption from the ground state  $|G\rangle$  to the intermediate states  $|M\rangle$  and subsequent X-ray emission from  $|M\rangle$  to all final states  $|F\rangle$ . The possible scattering paths involving different intermediate states lead to channel interference if their energetic separation is comparable to the lifetime-broadening  $\Gamma_M$  of the different core hole intermediate states [24]. In general, the total nuclear and electronic symmetry of the scatterer has to be considered, since the nuclear and electronic motions are coupled. In the RIXS process, the initial and final states belong to the same irreducible representation.

A special case of RIXS is the situation where only a single core hole intermediate state  $|M\rangle$  is reached. Then, the spectral distribution is given by the spontaneous radiative decay of valence electrons into the core hole state, described by Fermi's golden rule:

$$I_{\text{XE}}(\omega') \propto \sum_F (E_M - E_F)^3 |\langle F | \vec{D} \cdot \vec{E}' | M \rangle|^2 \delta(E_M - E_F - \hbar\omega') \quad (2)$$

We refer to this situation as resonantly excited X-ray emission (see Fig. 4). However, if RIXS is approximated by XE, channel interference is effectively neglected. To predict when RIXS can be approximated with XE, we have to understand how different types of core hole intermediate states can be produced. They can be due to closely spaced virtual orbitals, closely spaced core orbitals, i.e. symmetry-adapted core hole wave functions, or to vibrationally excited states. In most adsorbate systems, we can consider the core-excited state to correspond to a single intermediate state and the interference effects will not be important. However, for systems with a high degree of symmetry, interference effects could become important and this will be discussed in connection with the symmetry selection rules in Section 2.5.3. Vibrational effects will usually only have a rather small influence in chemisorbed molecules and will be discussed in Section 2.3. In the following, we will only consider the simple XES process where the excitation and decay processes can be treated separately. There is still a difference between non-resonant and resonant XES in terms of the final state. In the resonant case, there is an additional excited electron since the final state in the scattering process corresponds to an electron-hole pair similar to an optically excited state. The question is if there is an influence of this additional spectator electron on the X-ray emission decay process.

The valence electronic structure of chemisorbed molecules on metal surfaces has in many aspects metallic character with a characteristic screening response towards core ionization and excitation [25,29–31]. In these systems, independent of excitation energy, the same fully screened core-excited intermediate state is reached locally, since the excited electron will couple to the continuum of the delocalized metal states during the core hole lifetime. This fully screened and relaxed core hole state is therefore equivalent to a single intermediate state in the RIXS process, which allows using the simple case of X-ray emission (Eq. (2)). In metallic systems, we can assume that the presence of the excited electron has a negligible influence on the X-ray emission process and the spectra can be interpreted in a two-step picture with a fully relaxed initial core hole state corresponding to non-resonant XES [32]. In a simple picture, we can think in terms of an ultrafast charge transfer of the excited electron from the adsorbate into the substrate prior to the decay. The electron is no longer present at the time of the core hole decay and can be neglected. In the case of weakly adsorbed species, this charge transfer process can be much slower with the possibility of both final states in decay spectra where the excited electron is either present on the adsorbate or transferred into the substrate [25,31,33]. All adsorbed species covered by the current review correspond to the case of rather strong coupling to the substrate and we do not need to regard such a complication.

In adsorbate systems with equivalent atomic centers, intermediate core-excited states of different symmetries may be reached [34,35]. In cases where the different excited states are well separated in energy in comparison with the core hole lifetime, we can view the process as preparation of core hole states of different symmetries and the subsequent emission follows the dipole selection rule in a two-step picture (see Section 2.5.3). One example of this is ethylene adsorbed on Cu(1 1 0) [34,35]. However, when the energy separation is small, channel interference may occur and we have to treat the process in a one-step RIXS picture using the Kramers–Heisenberg scattering formula. This has been seen in adsorbed benzene, leading to a more complex interpretation [34,36]. All other cases with distinguishable atomic

centers may be treated without any consideration of core hole symmetry using a simple two-step picture. In the following, we will only consider the simple XES process according to Eq. (2).

## 2.2. Atom-specific probing

The most essential aspect of XES applied to adsorbates is that it provides an atom-specific probing of the electronic structure around a specific site. This comes from the unique property to probe the valence electrons close to the core electron shell where the matrix element in the transition becomes atomic like, which forms the basis for the “one-center approximation”. Let us illustrate in a simple manner this principle for the CO molecule. First, we need to consider the transition matrix element from Eq. (2):

$$I \propto |\langle F | \vec{D} \cdot \vec{E}' | M \rangle|^2 \quad (3)$$

Both the intermediate and final state wave functions contain all electrons in the whole system. We may attempt to approximate the matrix element over the determinantal wave functions  $|F\rangle$  and  $|M\rangle$ , representing the final and intermediate states, in such a way that we separate the one-electron core  $\phi_c$  and valence  $\phi_v$  orbitals that are directly involved in the decay process from the rest of the system,  $\psi_f$  and  $\psi_m$ . We distinguish the one-electron part from the many-body part of the matrix element in the following way:

$$I \propto |\langle \phi_v | \vec{D} \cdot \vec{E}' | \phi_c \rangle \langle \psi_f | \psi_m \rangle|^2 \quad (4)$$

The term  $\langle \psi_f | \psi_m \rangle$  is the codeterminant of orbital overlaps obtained by eliminating the orbitals  $\phi_v$  and  $\phi_c$  from the full determinant. In the case that the remaining orbitals are only slightly perturbed by the transition then the codeterminant will be approximately unity and the cross-section can be approximated by the single term shown in Eq. (4). If we assume that this is the case we can furthermore neglect the many-body overlap term and the matrix element is reduced to an overlap between the core and valence orbitals times the dipole operator. Fig. 5 shows the 1s and 2p wave functions for the C and O atoms, that are the quantities involved in the determination of the transition moments in Eq. (4). The atoms are positioned relative to each other at 1.15 Å corresponding to the bonding distance in CO. We observe the strong overlap of the O 2p and C 2p wave functions that will lead to the formation of molecular orbitals. The energy positions of the resulting molecular orbitals will depend on the nature of this overlap. If we inspect where in the atoms the 1s levels overlap with the valence orbitals, we see that it takes place deep inside the atom in the region of the core electrons. This region will make the largest contribution to the matrix element in Eq. (4). There are no significant interatomic contributions between the O 1s and C 2p or C 1s and O 2p orbitals. The contribution to the one-electron matrix element comes only from the particular center on which the core electron is located; the magnitude of off-center 2p orbital contributions is determined through the gradient in the amplitude over the core region and this is extremely small. We note that the transition moment is related to the atomic part of the molecular orbitals whereas the energy of the transition will be more connected to the extended part of the molecular orbital where overlap between different atomic centers takes place. The intensity of the X-ray emission transition is directly related to the partial population of atomic 2p character in the different molecular orbitals. We can apply a simple atomic picture of the dipole selection rule where the change in angular momentum of the X-ray transition is given by:

$$\Delta l = \pm 1 \quad (5)$$

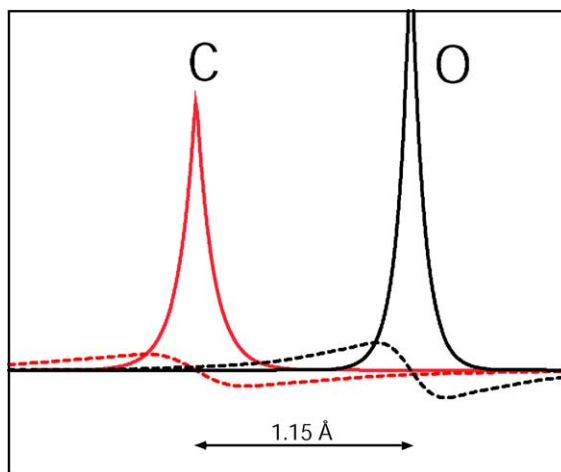


Fig. 5. Orbital amplitudes along the bond axis of the atomic (dashed lines) C 2p, O 2p, and (full lines) C 1s and O 1s wave functions with C and O atoms at the interatomic distance, 1.15 Å, of the CO molecule. Note that the amplitudes are normalized to give the correct atomic orbital normalization over volume.

From s core hole decay, we probe occupied p orbitals and for a p core hole, we observe decays involving s and d electrons. The former is very useful if we want to observe the valence electronic structure in low-Z elements such as C, N, O and F, whereas the latter is more important for systems where the valence d electrons determine their unique properties such as in correlated materials and magnetic systems [4]. In the present review, we will only discuss 1s core levels of C, N and O that are of primary interest for molecular adsorbates.

Based on this simple approximation, we can create a spectrum of the CO molecule from a knowledge of the molecular orbital structure, shown in Fig. 6. The three outermost molecular orbitals are shown in the left column in a simple atomic 2p basis set. The relative energies of the three MOs are shown with respect to the C 1s and O 1s levels. In the first step, we generate a core hole and in the second step a valence electron fills the core hole with subsequent emission of an X-ray photon. The relative energy separation of the emission lines reflects the difference in binding energies of the MOs as obtained with ultraviolet photoelectron spectroscopy. The new aspect that XES provides compared with UPS is the difference in intensities through core hole decay involving the C 1s or O 1s levels that corresponds to how the orbitals are distributed on the two different centers. In Fig. 7, we see both in the experimental and theoretical spectra [37] how the intensity difference reflects the atomic 2p population in the different MOs. The difference in lineshape of the  $1\pi$  orbital in the C 1s and O 1s emission spectra is due to differences in vibrational excitations in the decay process [37]. In a way, the method provides an experimental version of the linear combination of atomic orbitals (LCAO) concept in molecular orbital theory.

### 2.3. X-ray emission and photoemission

In order to make use of XES, we need to put the XE spectrum on a valence electron binding energy scale. Since the most direct way to measure the energy position of a valence orbital is by UPS or often denoted photoemission [16], it is essential that the two methods can be compared.

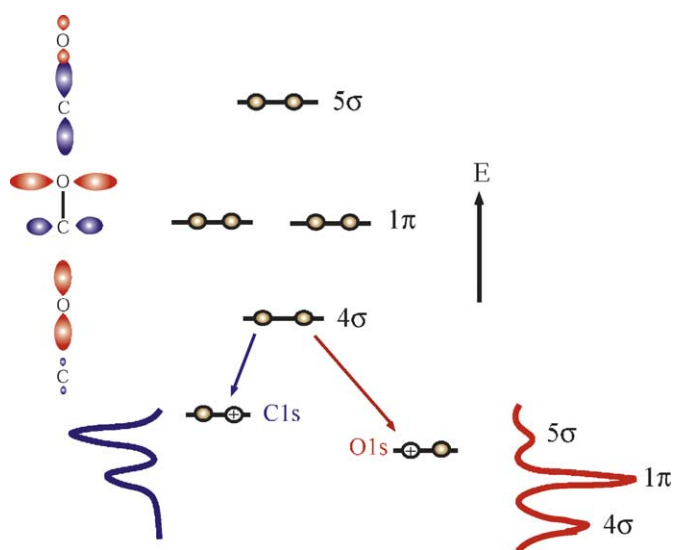


Fig. 6. Schematic picture illustrating the atom-specific probing of the orbital structure in CO using XES. The left column shows the spatial distribution of the molecular orbitals in terms of a simple 2p basis set. The right column shows the relative energy position of the orbitals with respect to the core-levels. The bottom part of the figure illustrates the decay process of one valence electron into the core hole with the emission of X-rays that makes up the spectra. The left part shows a C 1s emission process and the right part the O 1s.

In Fig. 8, we schematically show how we can generate a similar valence hole state through two different channels, UPS and XES. The vertical axis of the diagram gives the total energy scale. On the right-hand side of the figure, there is a density of states versus energy distribution for a typical metallic solid with an indicated Fermi level position. The left-hand side indicates the total energy of the ground

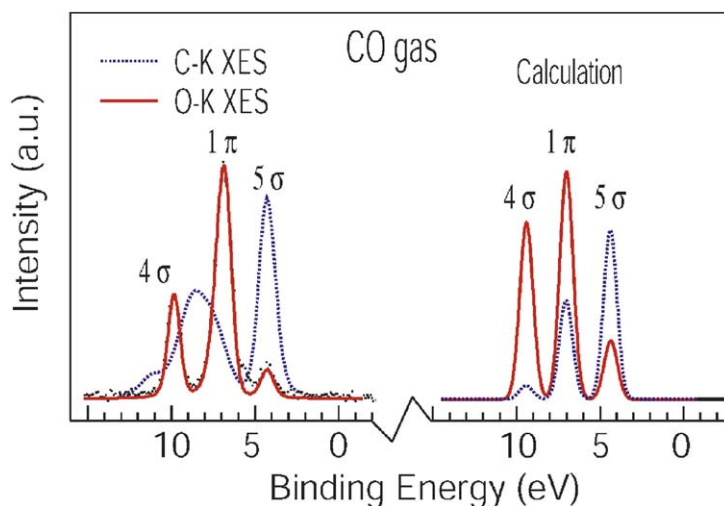


Fig. 7. Experimental [37] and theoretical C and O K emission spectra of CO in the gas phase. The C 1s and O 1s binding energies have been subtracted from the emission energies in order to align the two spectra on the same energy scale.

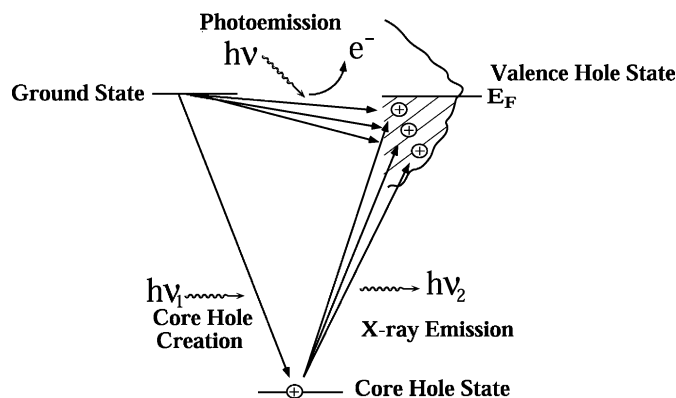


Fig. 8. Schematic picture showing the energy relationship between UPS and XES.

state, which is the starting point for both processes. Electron binding energies are defined in terms of the difference in total energy between the hole and ground states. In valence band photoemission or UPS, a photon is absorbed and the energy is given to eject an electron giving a final state with a valence hole. For solids, the valence hole state binding energy is usually determined with respect to the Fermi level. This corresponds to the difference in the ionization energy between a specific valence electron state and an electron at the Fermi level. The lower part of the figure shows the XES process in a two-step picture. The first step corresponds to the creation of the intermediate core hole state where we define the binding energy in the same manner as for the valence hole state, i.e. with respect to the Fermi level. The second step is the decay of the core hole state with a valence electron resulting in the emission of an X-ray photon. The energy of the photon is given by the difference in total energy between the core and valence hole states. The emission energy for an electron that decays from the Fermi level will correspond to the binding energy of the core hole state [20,38]. In a metallic system where the total number of valence electrons is extremely large, there is no difference in energy between removing or adding an electron at the Fermi level. We therefore regard the core-level binding energy as a core to Fermi level excitation–deexcitation energy. In this way, we use the core-level binding energy position to identify the Fermi level in our XE spectra. By subtracting the core binding energy ( $E_b^c$ ) from the emission energy scale ( $E_{em}$ ), we obtain the spectra on a valence hole binding energy scale ( $E_b^v$ ), which can be directly compared with photoemission or UPS:

$$E_b^v = E_{em} - E_b^c \quad (6)$$

The similarity of the final states of the two processes is demonstrated in Fig. 9 with UPS and XE spectra for atomic N adsorbed on Cu(1 0 0) [39]. The figure shows UPS spectra both for a clean and N covered Cu(1 0 0) surface. The dominating structure around 2–5 eV is due to the Cu d band and the flat distribution close to the Fermi level is the Cu sp band. Upon adsorption, there are some new weak features seen around 1 and 5 eV binding energy. The same structures are clearly seen in the XE spectrum, which has been put on a binding energy scale by subtracting the core-level binding energy from the emission energies. We clearly see the difference in the adsorbate sensitivity. In XES, we project the electronic states onto the adsorbate atom whereas in photoemission the joint electronic structure of the whole system is probed.

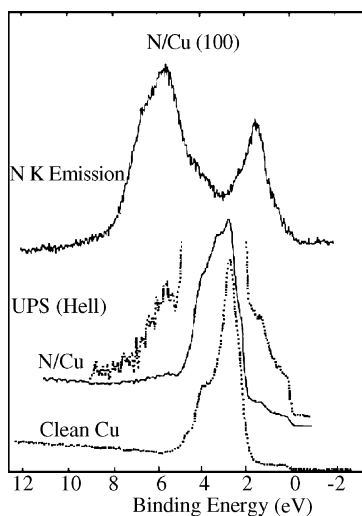


Fig. 9. Comparison between XES and UPS spectra for N adsorbed on Ni(1 0 0).

Contrary to photoemission, the initial state in the XES process contains a core hole. An important question is if the core hole could have some influence on the XE spectrum. Based on the experimental results from XES on simple metals, von Barth and Grossmann formulated what has become known as the *final state rule* [40]. In principle, this rule states that the spectral distribution is governed by the final-state electronic configuration (without a core hole) times a dynamic factor giving a singular behavior near the Fermi level. Recent cluster calculations of the XES process for CO on Cu, however, show the best agreement using ground state frozen orbitals [32]. There are no strong enhancements observed experimentally close to the Fermi level. In the following discussion, we regard the XES process to reflect the ground state electronic structure without any direct core hole effects. Further discussion on this topic will be presented in Section 3.2.2, describing how spectra are computed based on ab initio calculations.

In some cases, the spectral features show a deviation in the energy position in a comparison between XES on different sites and photoemission or UPS. First of all, there could be large error bars in the calibration of the absolute emission energy scale. However, using third-generation synchrotron sources the calibration procedure has become routine with a high level of accuracy (see Section 3.1.2). There are a number of effects that could generate different final states in the two spectroscopies [32]. In the present review, we attribute this to three different cases: two-dimensional band structure formation, atomic cross-section variations and vibrational excitations.

Let us start by discussing band structure effects and momentum space. XES resolves atomic contributions to the valence electronic structure, but in a metallic system it integrates over valence hole final states spanning the whole momentum space. Angle-resolved photoemission or UPS on the other hand separates valence hole final states of different momenta [9,13], but integrates over all atomic contributions. Therefore, differences are expected between the momentum-averaged XES binding energies and the photoemission binding energies, which select a certain momentum interval unless the photoemission data has been measured integrating over momentum space, i.e. the first Brillouin zone. The band related to the 6 eV feature in Fig. 9 has a band dispersion of 2 eV, which will be discussed in

**Section 4.1.1.** We can anticipate that the structure in the photoemission spectrum is related to a specific point in the momentum space which can cause a deviation from the XE spectrum. We can also envisage that band dispersion could provide different atomic orbital contributions at specific momenta. If the band dispersion is large, it can give rise to shifts between XE spectra measured on different atomic sites. The assumption is that the relative atomic 2p contributions vary within the broadened valence levels for the different atomic centers, e.g. the carbon and oxygen atomic contributions in adsorbed CO can have different relative weights at the bottom and top of the valence band. As XES is a local, atom-specific probe of the local atomic 2p contributions, different parts within the broadened valence level will be projected out and XE spectra measured on the carbon and oxygen atomic centers may have different emphasis, resulting in binding energy shifts.

There is another related effect that is important in the comparison related to Fig. 9. In XES, we only measure the N 2p contribution whereas in photoemission all atomic contributions are valid. However, in the latter case, there are differences in the atomic cross-sections. In a simple atomic basis, the bands in the N on Cu(1 0 0) system will have contributions from both the Cu and N atoms. The specific atomic character will be different at different momenta. Since the cross-section of Cu d states is extremely high, we will mainly project out the d contribution in the photoemission spectrum. It is essential to consider differences in atomic contributions to the photoemission cross-section when broad density of states features are compared between the two spectroscopies. Molecular hybridization can also give rise to shifts. In UPS, the photoionization cross-section is higher for the atomic 2s than for the 2p contributions [41], whereas XES probes selectively final states of atomic 2p character.

The last consideration that can lead to deviations in binding energy positions is vibrational excitations due to different potential energy curves in the ground, core-excited and final states. This has to be formally treated using the Franck–Condon principle where the nuclear coordinates are frozen during ionization, excitation and decay processes. Furthermore, under special circumstances, not discussed here, vibrational interference can occur where a full RIXS treatment is necessary [24]. The difference in the  $1\pi$  position and line shape between C 1s and O 1s excited CO gas phase spectra shown in Fig. 7 is attributed to vibrational effects. It can be explained as due to an extremely large difference in potential energy curves of the core-ionized states in the free CO molecule [42]. Ionization of the carbon atom leads to bond length shortening whereas an elongation occurs for oxygen ionization. The removal of a  $1\pi$  electron in the final state leads to bond length elongation since a bonding orbital becomes less populated. The largest difference between the potential energy curves of the intermediate core-ionized states and the final state are therefore in the C K emission process creating a large vibrational envelope in Fig. 7. However, similar effects on the  $1\pi$  level in adsorbed CO have not been observed [32,43]. Due to metallic screening of the core hole state in adsorbed CO through the population of an additional electron in the  $2\pi^*$  orbital, the difference in the potential energy curves between the two core hole states becomes much smaller [30,44]. Both give rise to a bond length elongation resulting in a similar geometry compared to the final state providing a smaller difference in population of vibrational states in the decay process. Although the  $1\pi^{-1}$  final state in free CO represents an extreme case, similar phenomena could exist for adsorbed molecules. Also large differences in vibrational excitations can occur between direct photoemission and XES since in the former the ground state potential energy curve comes into consideration as the initial state instead of different intermediate states. This leads to deviations in the binding energy position of spectral features corresponding to similar electronic states but obtained through either direct ionization or decay processes on different atomic sites.

## 2.4. Orientational symmetry probing

Another important property of XES for oriented adsorbed molecules is the orbital symmetry sensitivity. Through angular-resolved measurements, we can separate the different  $2p_x$ ,  $2p_y$  and  $2p_z$  contributions to the molecular orbitals. One of the main utilizations of the XAS or NEXAFS methods for studies of adsorbed molecules has been to derive molecular orientations from angular-resolved measurements [19]. The incoming synchrotron light is polarized and the  $E$ -vector can be oriented in different directions with respect to the surface. The spectral intensity shows an angular dependence of the  $E$ -vector due to the directional character of the empty orbitals. If the symmetry of the orbitals involved in the specific spectral transitions is known the angular dependence can be used to determine the orientation of the molecular axis of the adsorbates with respect to the surface. Since the XE process involves the same dipole operator and localized core orbitals, we will have a similar angular dependence in XES of adsorbed molecules. We can envisage that we can now instead use the angular dependence to derive the symmetry of different spectral features if the molecular orientation is known.

In Fig. 10, we illustrate in a simple way the angular dependence of the dipole selection rule. In the previous section we have shown, based on the one-center approximation, that the spectral intensity of an orbital is given by the population of atomic  $2p$  valence character on the atom that contains the  $1s$  hole. Based on the same argument, we only need to consider the orientation of the atomic  $2p$  valence orbitals at the atomic center where the X-ray decay takes place. Since the initial  $1s$  hole state is spherically symmetric and the final  $2p$  hole state has a specific direction, it can be shown [19] that the emitted light will have the  $E$ -vector oriented parallel with the amplitude of the  $2p$  orbital. For a diatomic molecule such as CO, there are orbitals of two different symmetries,  $\sigma$  and  $\pi$ , where the atomic  $2p$  orbitals in the  $\sigma$  symmetry are oriented along the molecular axis while the  $p\pi$  orbitals are perpendicular to this axis. This means that we will have the emitted light  $E$ -vector, respectively, parallel and perpendicular to the molecular axis for decay from  $\sigma$  and  $\pi$  orbitals.

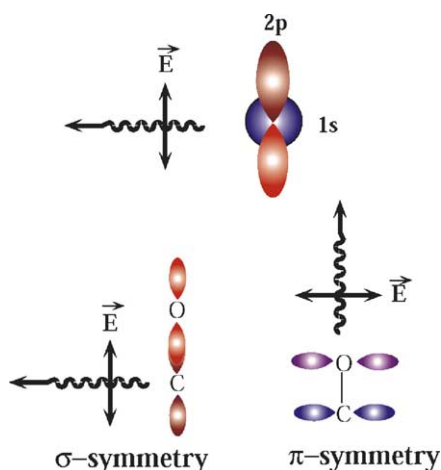


Fig. 10. Schematic picture illustrating the  $E$ -vector orientation of the emitted light with respect to the amplitude of the atomic  $2p$  orbital according to the dipole selection rule. Through angular dependent measurements, molecular orbitals of different symmetries can be probed.

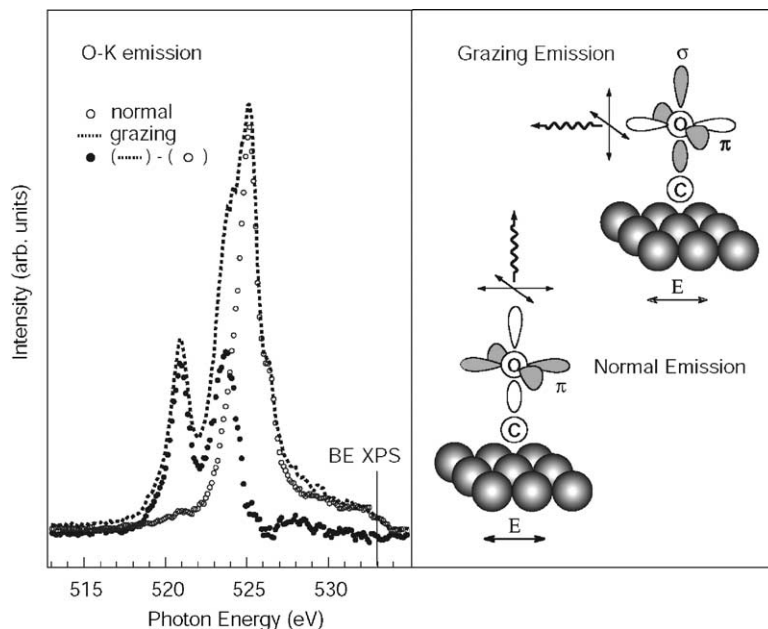


Fig. 11. States of  $\pi$  and  $\sigma$  symmetry separated by switching the direction of observation between grazing and normal emission. This is shown for the O K spectra of CO on Cu(1 0 0).

For an oriented adsorbed molecule, we could envisage to use the polarization of the emitted light to separate contributions from orbitals of different symmetries. However, since we at the present time cannot experimentally analyze the polarization of the emitted X-rays, symmetry information only comes from the fact that the  $E$ -vector is always perpendicular to the direction of the emitted X-rays [34,45]. Thus, emission detected in a direction normal to the surface is due only to transitions involving valence states parallel with the surface plane, i.e.  $2p_{xy}$ , whereas detection at grazing angles gives spectral intensity related to both in-plane  $2p_{xy}$  and out-of-plane states  $2p_z$ . This can be seen in Fig. 11 for CO on Cu(1 0 0), adsorbed in a perpendicular orientation, where O K XES spectra are measured at two different emission angles [32]. Normal emission shows spectra of pure  $\pi$  symmetry while the grazing emission spectra contain a mixture of  $\pi$  and  $\sigma$  symmetry. Assuming a superposition of  $\pi$  and  $\sigma$  states in the XE spectra, a simple subtraction of the scaled normal emission spectrum from the grazing emission spectrum reveals the states of pure  $\sigma$  symmetry (see Fig. 11).

### 2.5. Selective excitations

In the following, we will go through in detail the three different aspects that are important for selective excitations. Without these aspects, there would be no need for monochromatized synchrotron radiation as source for generating XE spectra. The first experiments on XES applied to adsorbates were conducted using white light from a bending magnet source as an excitation source [5,39,46]. With white light, much higher intensities can be achieved compared to monochromatized radiation and it would also be possible to use high-current electron sources. However, it was early on realized that at high excitation energies the interpretation of XE spectra becomes severely complicated by the existence of non-diagram transitions. Furthermore, for molecules with several atomic centers of the same element, core-level shifts can be used

to separate out the different atomic contributions while molecules with a high degree of symmetry can allow for additional selection rules; this, however, requires tuning the excitation energy to reach the required core-excited state. It is therefore necessary to use selective excitations close to the core-level threshold as a source for XES experiments in order to simplify the interpretation as well as maximize the information obtained.

### 2.5.1. Non-diagram transitions

If we create a core hole through an ionization process with high excess energy there is a large probability of creating multi-electron excitations in the core hole state. These are normally seen as shake-up and shake-off satellites in XPS spectra. The presence of additional initial states for the decay process gives rise to X-ray satellites [47], denoted non-diagram lines, and these can have a substantial overlap in energy with the main lines. This will make the assignment of the “one-electron states” difficult. Using excitation energies close to threshold, there is not enough energy to create these satellites and only one well-defined core hole state is generated.

Fig. 12 demonstrates the appearance of non-diagram transitions in the O K emission spectra of CO on Ni(1 0 0) [48]. At resonance, the core electron is excited into the  $2\pi^*$  level at 533.5 eV and a typical XE spectrum from a single intermediate state is observed. The interpretation of the spectrum will be discussed in Section 4.2.2. When the excitation energy is increased other spectral features grow on the high-energy side of the main peak. These are attributed to non-diagram transitions that have been observed for many molecular systems and usually appear at higher emission energies [47]. The intensity of the non-diagram spectral features continues to increase up to the highest measured excitation energy of 100 eV above threshold. The high-energy excited O1s XPS satellite spectrum of CO on Ni shows the appearance of rather intense shake-up and shake-off intensities [49]. There is a shake-off continuum that extends to extremely high energies, well above 100 eV. The satellite intensity will continue to increase with excitation energy until the whole shake-off continuum can be fully developed energetically.

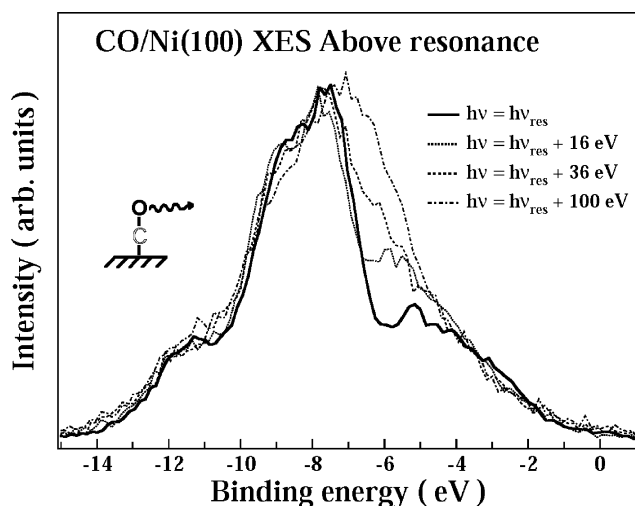


Fig. 12. O K-edge grazing emission spectra of CO on Ni(1 0 0) recorded at different excitation energies.

### 2.5.2. X-ray absorption resonances

The book by Stöhr [19] gives a full and comprehensive description of the applications of X-ray absorption spectroscopy (or also denoted NEXAFS) to adsorbates. However, there are a few aspects of particular relevance for XES applications to adsorbates that were not covered by the book. If we want to use XAS for studying the empty electronic states in terms of chemical bonding it is important to consider the final state rule. The influence of the core hole will modify the empty orbital structure in terms of symmetry and energy shifts. Core-level shifts can also be observed in XA spectra and can be used to selectively generate core holes on different atoms of the same element for XES studies.

The final state rule states that the spectral features reflect the eigenstates of the final state Hamiltonian [40]. In the case of XAS, a core hole is present in the final state. The influence of the core hole may be very different for different systems. One way to estimate the static influence of the core hole, i.e. the shift in position and change of the shape of the spectrum, is to use the  $Z + 1$  approximation, which implies that the core-excited atom is replaced by the atom with nuclear charge increased by one ( $Z + 1$ ) corresponding to the reduced screening due to the removal of a  $1s$  electron. In XES, as described in Section 2.3, the core hole is filled by a valence electron leading to a similar final state as in valence band photoemission.

The electronic structure of the interaction of CO with metal surfaces will be discussed in Section 4.2.2. There is a hybridization between the orbitals in the metal and on the molecule leading to mixed states. The  $2\pi^*$  is the first unoccupied orbital of the system and will have both molecular and Ni  $3d$  contributions. We can probe this orbital in a number of different ways: either through a local core excitation on the C or Ni sites using XAS or the total projected unoccupied states using inverse photoemission (IP). Fig. 13 compares the C  $1s$  and Ni  $2p$  XA spectra [20,50] with IP spectra [51]. When plotting the XA spectra, the corresponding core-level photoemission binding energies have been subtracted to provide an energy scale relative the Fermi level. In the IP spectrum of CO on Ni, the empty  $2\pi^*$ - $3d$  hybrid states can be observed at around 3.5 eV above the Fermi level. When probing these states through core excitations on the C or Ni sites, we observe energy differences. In the C  $1s$  XA spectrum, the  $2\pi^*$  resonance appears at 1.5 eV above the Fermi level, a shift of 2 eV in comparison with the IP spectrum. This can be understood from the final state rule. We can estimate the effect of the final state using the  $Z + 1$  approximation. At the bottom of Fig. 13, the NO on Ni IP spectrum is shown and as can be seen the  $2\pi^*$  state appears at 1.5 eV above the Fermi level. This nicely correlates with the position in the C  $1s$  XA spectrum and validates the  $Z + 1$  approximation. Next, we turn to the Ni  $2p$  XA spectrum which also probes the  $2\pi^*$ - $3d$  hybrid states but now on the Ni site. The spectrum has been obtained using one monolayer of Ni on Cu as a model substrate [50]. When CO is chemisorbed a new CO-induced ( $2\pi^*$ -derived) feature appears in the Ni  $2p$  XA spectrum at an energy of 3 eV above the core-ionization threshold. In this case, the perturbation due to the core hole is not as large. Using the  $Z + 1$  approximation, the change in the  $2\pi^*$  position when CO is instead adsorbed on Cu is small. This is shown in the IP spectrum of CO on Cu [52] at the top of Fig. 13.

The XA spectrum of the  $2\pi^*$  resonance of  $N_2$  adsorbed on Ni(1 0 0) [53] is shown in Fig. 14. The spectrum consists of a main peak at a photon energy of 401.0 eV with a shoulder at 400.4 eV. This can be compared with the core-level binding energies of the two atoms at 399.4 and 400.7 eV [7]. We can see that the XA threshold for the two main structures corresponds to the core-level binding energies. Using the resonant Auger decay process to decompose the XA spectrum [53], the individual XA spectra for each nitrogen atom could be obtained and are shown in Fig. 14. The position of the  $2\pi^*$  resonance was estimated to 400.6 and 401.0 eV for the outer and the inner N atoms, respectively. The splitting of 0.4 eV between the two resonances is much smaller compared to the 1.3 eV splitting in the core-level binding

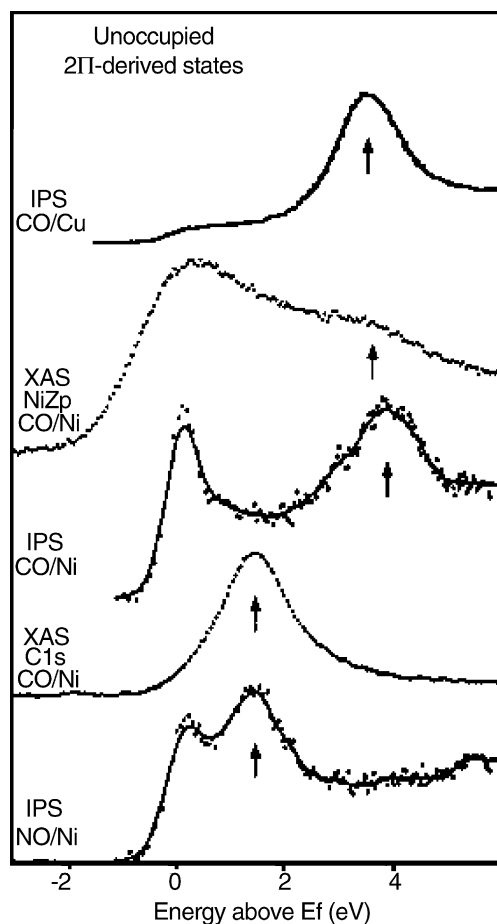


Fig. 13. C 1s and Ni 2p XA spectra of CO adsorbed on Ni and inverse photoemission spectra of CO on Ni and Cu and NO on Ni. The arrows indicate the energy position of the CO  $2\pi^*$  orbital.

energy positions. Furthermore, the widths of the two resonances are rather different, 1.6 eV for the outer atom and 0.9 eV for the inner atom. The fact that the XA positions are separated by less than the XPS peaks is a result of the differences in the final state density of states of the two atoms. We can use the  $Z+1$  approximation to again describe the influence of the core hole corresponding to NO for core-excited  $N_2$ . Excitation on the outer atom leads to NO with nitrogen down, which is the normal chemisorption geometry for adsorbed NO. For this NO geometry, we generate a rather strong surface bond resulting in a large hybridization of the  $2\pi^*$  with the metal electrons with a broad resonance. It is interesting to note that the same final state can be reached from core-excitation of the carbon atom in adsorbed CO, as described earlier. The width of the  $C\ 1s^{-1}\ 2\pi^*$  resonance is 1.7 eV, closely resembling what is obtained for the outer nitrogen in  $N_2$ . Furthermore, the peak position is at 1.5 eV above the core-level binding energy compared with 1.2 eV for the outer nitrogen. Part of the difference in the latter comparison comes from vibrational effects. In the case of the XA spectrum from the inner nitrogen, it corresponds to NO adsorbed with oxygen down leading to an extremely weak binding to the substrate. The resonance maximum is located 0.4 eV above the core-level binding energy position. Both shape and width are

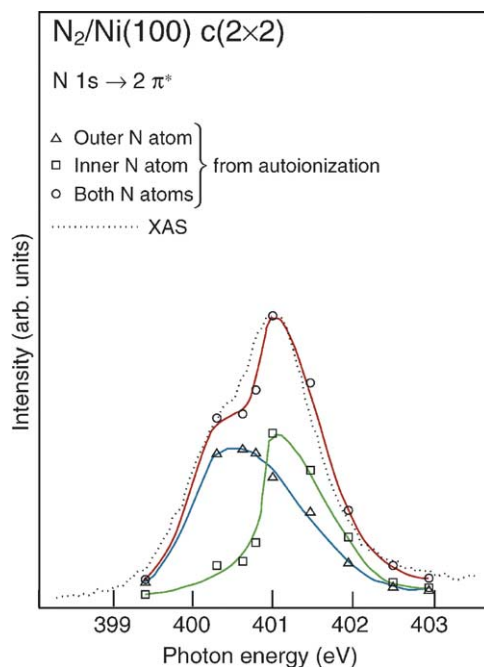


Fig. 14. Separation of the N 1s XAS  $2\pi^*$  resonance for the  $c(2 \times 2)$   $N_2/Ni(100)$  into individual XAS spectra from inner and outer atoms.

similar to the vibrational envelope of the corresponding excitation of the free molecule implying that the hybridization broadening is rather small in the inner nitrogen  $2\pi^*$  XAS spectrum.

From detailed knowledge of the different XAS resonances and how they are associated with different atoms in a complex adsorbate, we can use selective excitation to obtain an atom-specific probing of the electronic structure using XES. Similar arguments have been used as shown in  $N_2$  on Ni to selectively excite CO molecules chemisorbed in different adsorption sites [54,55] or to distinguish between the  $CH_3$  and the COO groups in acetate [56] or the  $CH_2$  and the COO groups in glycine [57].

### 2.5.3. Symmetry selection rules

For molecules with elements of symmetry, the RIXS process will obey specific symmetry selection rules [24,34,58,59]. From the form of the matrix elements leading to the cross-section in Eq. (1), it is evident that, for a non-vanishing contribution, the integrand giving the amplitude for absorption into the intermediate state as well as that giving the amplitude for emission from this state, leading to the final state, both have to contain the totally symmetric irreducible representation. Since these two steps are intimately coupled via the intermediate state  $|M\rangle$  this results in selection rules for the overall scattering process determining which final states can be reached as well as the polarization of the outgoing photon as function of the polarization and energy of the incoming photon. For gas phase, or otherwise disordered samples, the dependence on the initial polarization entails an averaging over all orientations of the molecules [24,34,58,59]. For the ordered adsorbate overlayer studies that form the scope of the present review, the bonding to the substrate fixes the molecules in space as well as breaks at least part of the symmetry of the gas phase molecule. In the present context, we will limit the discussion to a few specific

cases of relevance to the adsorbate systems discussed in the present review: molecules with inversion symmetry leading to a parity selection rule (ethylene and benzene) and systems with (near)  $C_{2v}$  symmetry and two (near-degenerate) core levels (formate, acetate, glycinate).

Beginning with the case of inversion symmetry, we consider first the gas phase ethylene molecule. The two C 1s atomic levels will form near-degenerate *gerade* and *ungerade* inversion symmetry molecular orbitals. Due to the dipole transition character, excitation into the  $\pi^*$  LUMO ( $1\pi_g$ ) can only occur from the  $1\sigma_u$  *ungerade* core level creating a vacancy in that orbital. Again, since the emission is also guided by the dipole selection rules we can now only observe decay from the *gerade* valence levels. Excitation into the  $\pi^*$  level thus selects only this subset of the valence levels for the emission. In order to observe the occupied *ungerade* valence orbitals, the excitation energy must be increased to correspond to that of the first *ungerade* unoccupied state. Thus, the scattering process connects initial and final states of *the same parity* and large variations in the XE spectrum are obtained as the excitation energy is scanned hitting various unoccupied states [24,59,60].

For surface adsorbed ethylene and benzene, the strict parity selection rule no longer applies. The impact on the spectrum however, depends on the strength of the interaction with the substrate. Note that, from a group theory viewpoint, the symmetry is formally broken just from the presence of the surface even if there is no interaction. However, no, or only negligible, symmetry-breaking matrix elements are generated in such a case [36]. We can thus use this fact to estimate the strength of the interaction with the substrate through the induced orbital mixings in the cases of ethylene and benzene [35,61].

The formate anion,  $\text{HCOO}^-$ , has  $C_{2v}$  symmetry and two symmetry-related oxygens in the carboxylic group giving rise to core levels of  $a_1$  and  $b_2$  symmetry. Using the character tables for  $C_{2v}$  symmetry, we find the following possible transitions from these two levels for the different polarizations:  $x$  ( $a_1 \rightarrow b_1$  and  $b_2 \rightarrow a_2$ ),  $y$  ( $a_1 \rightarrow b_2$  and  $b_2 \rightarrow a_1$ ) and  $z$  ( $a_1 \rightarrow a_1$  and  $b_2 \rightarrow b_2$ ). Neither  $a_1 \rightarrow a_2$  nor  $b_2 \rightarrow b_1$  are thus dipole allowed. Resonant excitation into the  $b_1$  (“ $\pi^*$ ”) orbital thus leads to an intermediate state which only involves the  $a_1$  core level. Since there is no allowed transition that connects  $a_1$  with  $a_2$  the result is that the valence  $a_2$  symmetry orbitals should be absent in the resulting XE spectrum. However, in the treatment above we have neglected, e.g. vibronic coupling which may break the symmetry sufficiently to make these transitions partly allowed. We will return to this subject in Sections 4.4.1 and 4.4.3 dealing with the carboxylic acids and glycine, respectively.

### 3. Methodology

In this section, we will describe in detail the different methods used to derive the atom-specific projected electronic structure using XES applied to molecules on surfaces. It has both experimental and computational components which are essential in order to obtain a coherent understanding.

#### 3.1. Experimental

XES applied to monolayers on surfaces is experimentally very demanding, and it is only recently that the field has begun to be exploited, much due to the appearance of third-generation synchrotron radiation sources. The main difficulty is the low count rate, due to three cooperative factors: (i) with only one sample layer, the target density for the exciting beam is very low, (ii) most of the core holes that are created in the layer will decay by non-radiative processes, and (iii) only a small fraction (about  $10^{-8}$ ) of

the emitted photons is actually detected. This is mainly due to the inherently small acceptance angle of high-resolution grating instruments. Therefore, experiments of this kind require a highly efficient excitation source. Furthermore, it was discussed in Section 2.5 that it is essential to use selective excitation, which makes monochromatic synchrotron radiation the best choice. In order to have a reasonable count rate, a photon flux in the order of  $10^{13}$ – $10^{14}$  photons per second is required on the sample within a  $100\ \mu\text{m} \times 200\ \mu\text{m}$  spot.

### 3.1.1. Beamline and experimental endstation

The experiments in the present contribution have been carried out at the Advanced Light Source (ALS), using beamline 8.0. Fig. 15 illustrates the overall experimental system optimized for surface studies in ultra high vacuum (UHV), where all core-level spectroscopies can be applied to the same surface preparation [31]. We need to measure the corresponding core-level binding energy positions with XPS to calibrate our energy scale, discussed in Section 3.2. For many systems, it is essential to measure the XA spectra in order to analyze the different resonances that can be used for selective excitation. Often we need these additional techniques to also characterize the different sample preparations. It is therefore essential for XES studies of molecular adsorbates to allow XPS and XAS measurements in the same experimental set up.

Beamline 8.0 at the ALS consists of an undulator with 98 5-cm periods and a spherical grating monochromator with three interchangeable gratings. The total beamline covers an energy range between 100 to 1000 eV with a maximum energy resolution  $E/\Delta E$  of 5000–10,000. A photon flux of  $10^{13}$ – $10^{14}$  photons/s can be achieved with a medium energy resolution of 1000, important for XES experiments. In order to match the size of the incoming beam with the size of the entrance slit of the

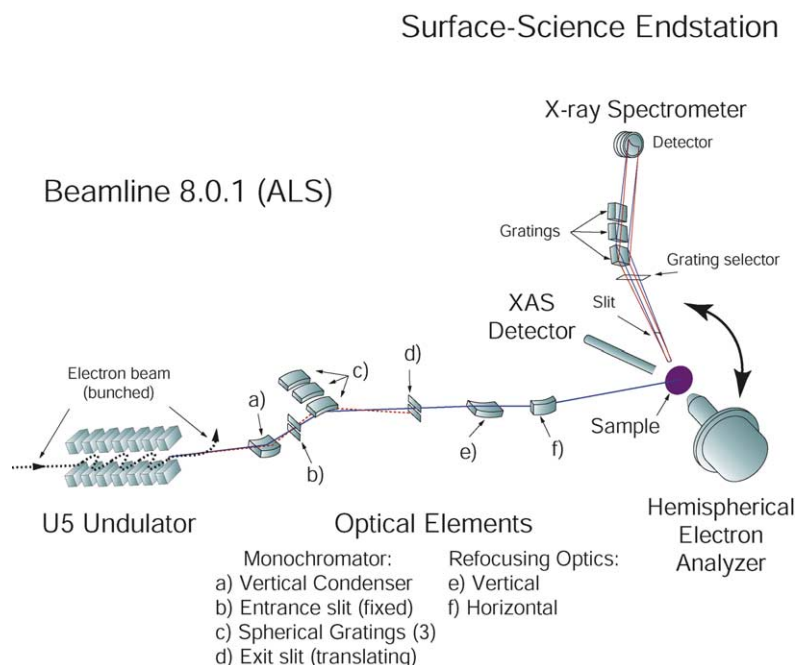


Fig. 15. Schematic overview of beamline 8.0 at the ALS and the surface science endstation.

spectrometers, the photon beam was focused down to  $100\ \mu\text{m} \times 100\ \mu\text{m}$  using a pair of spherical mirrors.

One of the unique characteristics of synchrotron radiation is the polarization of the light and in beamline 8.0 the radiation on axis is nearly 100% linear polarized. Since many adsorbates are well oriented on the surface we want to make use of the polarization by allowing the light incident on the sample to have the  $E$ -vector at different angles with respect to the surface plane. For one particular  $E$ -vector orientation, we want to be able to measure the emitted photons in any angle relative to the surface. Since the  $E$ -vector orientation is fixed from the insertion device, we have to rotate both the sample and the spectrometers. In order to reach high-symmetry orientations such as normal emission with the  $E$ -vector either in-plane or out-of-plane, we need to have grazing incidence of the light onto the surface. By rotating both the sample and the spectrometers around the axis of the incoming light, all orientations can be reached. However, for pure high-symmetry orientations, the angle of incidence of the light should be close to zero. In the described set up, we used an incidence angle of  $3\text{--}5^\circ$ . The grazing incidence also increases the sensitivity to the adsorbate layer with respect to the substrate. Soft X-rays have a penetration depth of the order of  $1000\ \text{\AA}$  and by using grazing incidence the radiation is adsorbed more in the surface region where the adsorbate is located.

Fig. 16A shows a projection of the analysis chamber of the experimental endstation along the incident beam direction containing an SES 200 Scienta electron spectrometer [62], X-ray spectrometer (see Section 3.1.2) and a partial yield electron detector [19]. Fig. 16B shows a side view of the endstation

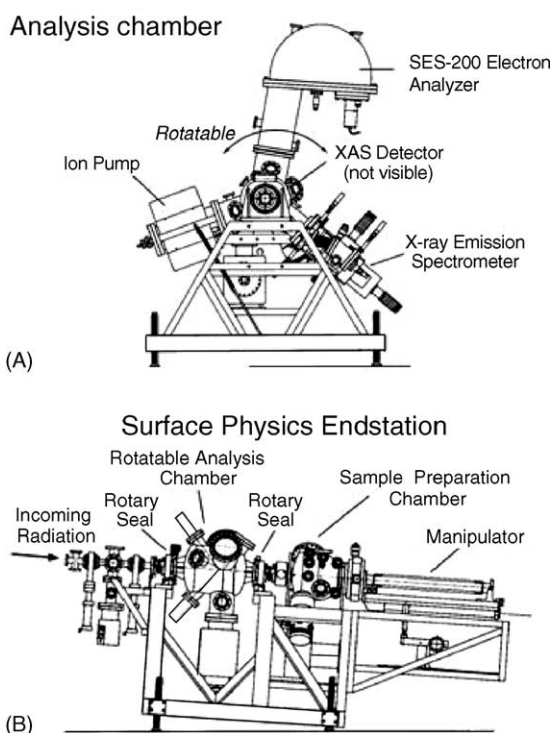


Fig. 16. Front view (A) and side view (B) graphs of the surface science endstation displaying the rotatable analyzer chamber with spectrometers and the sample preparation chamber.

where also the sample preparation chamber and manipulator can be seen. The analyzer vacuum chamber is made rotatable around the axis of the incoming beam using differentially pumped rotatable seals. In order to allow rotation of the chamber without too much stress on the vacuum chamber, the electron and X-ray spectrometers are supported via wires to a crane located above the instrument. The wires are connected to a spring block that has a counter weight force matching the weight of each spectrometer. The wires are attached at the center of mass on the spectrometers and can glide on the crane during rotation. This means that the spectrometers exert no force on the vacuum chamber and the rotation can be made very easily. The angle of the chamber can be set within  $1^\circ$ . There is a preparation chamber behind the analysis chamber separated by a valve (see Fig. 16B). A motorized long travel manipulator allows for motion of the sample between the two chambers. The preparation chamber contains equipment for sample preparation and characterization with an ion-sputter gun, gas inlet system, evaporators, mass spectrometer and low-energy electron diffraction (LEED) system. The substrates are single crystals that are mounted on a sample holder where temperatures between 30 and 1500 K can be achieved through cooling with liquid He or N<sub>2</sub> and heating performed radiatively or by electron bombardment. The base pressure in both chambers varied between  $5 \times 10^{-11}$  and  $1 \times 10^{-10}$  Torr.

For many adsorbates, the high intensity beam from a third-generation synchrotron source is destructive. In the present review, all adsorbate systems except for the atomic C, N and O were measured while continuously scanning the sample during data acquisition. The time scale for destruction has to be investigated for each individual system before any reliable data can be measured. To give an example of the variation in scan rate that is necessary in order to obtain spectra without any trace of beam damage, we used 400 mm/h for benzene on Cu and 40 mm/h for benzene on Ni. Usually, many samples needed to be prepared and a large number of individual spectra measured until a summed spectrum with reasonable statistics could be obtained.

### 3.1.2. *Soft X-ray emission spectrometer*

All soft X-ray spectrometers currently being used in the energy region of the C, N and O K-edges are based on a grazing incidence grating design [63]. The instrument used in all studies presented in the current review on adsorbates has been developed in the group of Joseph Nordgren in Uppsala, Sweden [3]. Fig. 17 shows schematically the optical outline of the instrument. It is based on three interchangeable gratings, all mounted together with the entrance slit on a precision slab in a Rowland circle arrangement. The three gratings together cover an energy range between 70 and 800 eV in first order. The gratings are spherical with 5, 5 and 3 m radius, and have groove densities of 1200, 400, and 300 lines/mm, respectively. The slit is positioned along the direction of the incoming X-rays on the Rowland circles of all three gratings with grazing incidence angles of 1.9, 2.6 and  $5.4^\circ$ , respectively. The entrance slit consists of two fixed edges separated by 0.6 mm. The projected slit size can then be varied continuously by rotation of the slit assembly around the slit center. In this way, the slit size, and ultimately the energy resolution, can be varied from 100  $\mu\text{m}$  down to a completely closed slit. Selection of grating in use is done by means of two shutters forming an aperture, which defines the illumination of the selected grating. In this way, no parts of crucial nature for the alignment of the instrument need to be moved.

The diffracted photons are detected using a two-dimensional detector which is movable in the normal plane of the gratings and slit. It can be rotated on an axis through the detector center allowing for the detector to be placed tangential to the Rowland circle. The detector consists of multichannel plates coated with CsI for enhanced efficiency and resistive readout of the detected position [63]. The area of the two-dimensional detector is 40 mm  $\times$  40 mm providing 100  $\mu\text{m}$  resolution. A negative potential electrode at

## Soft x-ray spectrometer

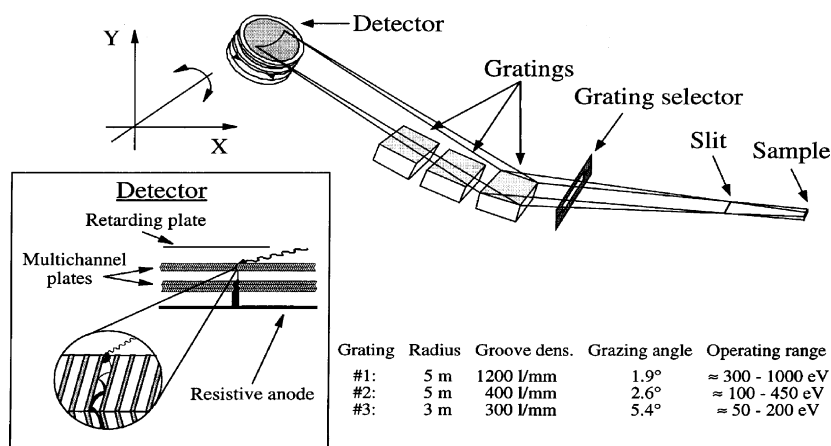


Fig. 17. An overview of the grazing incidence soft X-ray spectrometer.

the input of the detector reduces the intensity loss due to escaping secondary electrons. This is particularly important when multichannel plates are used at grazing incidence detection since then the interstitial surfaces rather than the channels will provide the effective photoemissive surface. It is estimated that the overall efficiency of the detector is up to about 20% [63].

There is a trade off between resolution and intensity in spectroscopy. Since XES is an extremely demanding experiment it is essential to be as efficient as possible. In the experiments relevant to the present review, the spectra were recorded using a resolution of 0.5–0.6 eV. This matches the width of most spectral features observed for adsorbate systems. In order to obtain this resolution, slit sizes of around 15–20  $\mu\text{m}$  were used. The C K emission spectra were measured using a 400 lines/mm grating and the N and O K emission spectra with a 1200 lines/mm grating.

It is essential to have a reliable method for energy calibration of the spectra. In Fig. 18, the carbon K-edge XES spectrum of CO adsorbed on Cu(1 0 0) measured normal to the surface is shown. The spectrum contains both inelastically and elastically scattered light. The spectral features at 287.7 eV constitute the elastic contribution, corresponding to the chosen excitation energy of the C 1s to  $2\pi^*$  transition. This is used for the absolute energy calibration. The relative energy scale of the spectrum is calibrated by measuring elastically scattered light from the sample at two different photon energies. In the next step, we need to subtract the elastic peak from the inelastic contributions. In order to do this, we model the peak of the elastically scattered light, approximating the monochromator function.

### 3.1.3. Future instrumental development

To perform XES measurements on monolayers is still an experimentally rather demanding technique due to both low sensitivity and beam damage effects from the incident radiation. Since the method is based on photon in–photon out probes there is inherently the potential to perform experiments under non-vacuum conditions. Recently, XES measurements have been performed on liquid water using SiN windows to separate the sample compartment from the beamline and the spectrometer [64]. There is the potential to apply this methodology to surface and interface studies under more realistic conditions at intermediate gas pressures and in the presence of liquid water. This would open up new research areas

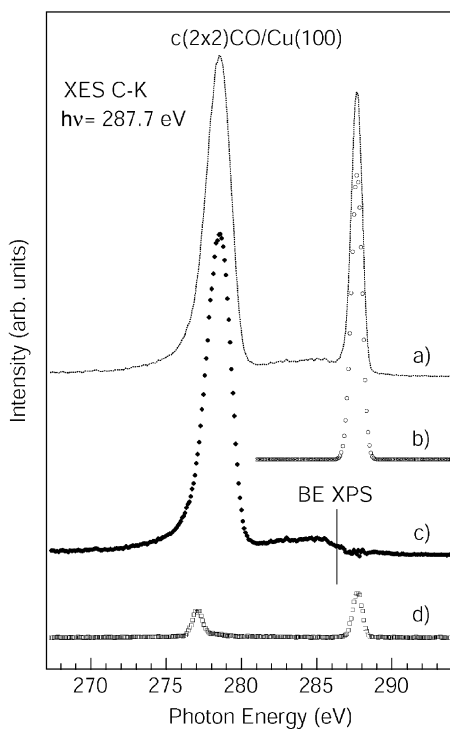


Fig. 18. Resonantly excited carbon K-edge XE spectrum of CO adsorbed on Cu(1 0 0). (a) The spectrum consists of elastically scattered light, conserving the photon energy and inelastically scattered light. The elastic peak (b) is subtracted and the spectrum is energy calibrated with elastically scattered light at two photon energies (d). In the final spectrum (c), the Fermi level is clearly visible, coinciding with the XPS binding energy position.

directly connected to heterogeneous catalysis, electrochemistry, molecular environmental science and biological surface science. Many adsorbate species of importance for surface chemistry and catalysis are active at defect sites. Furthermore, species formed under reaction conditions are expected to be present in rather small concentrations. If we want to be able to take the next step in the development of this technique, it is essential to make the measurements much more simple and the detection scheme more efficient. We cannot gain more by increasing the incoming photon flux since that would mostly increase the degree of beam damage.

One complication is the necessity to rotate the analyzer chamber around the incoming light direction to perform angular-resolved measurements. However, with the development of new elliptical undulator sources it is now possible to rotate the polarization vector of the incoming light, keeping the spectrometer fixed in space. This provides a unique opportunity to construct a more compact endstation that can provide new capabilities. There exist presently only two beamlines, 5.0 at SSRL and 11.0 at ALS, that utilize such elliptical undulators where future XES experiments on surfaces and interfaces will be performed.

Improvement of spectrometer efficiency is extremely essential to increase the detection sensitivity. The limiting factor of the set up described in Section 3.1.2 is the low acceptance angle of the instrument. This can be improved in two ways. In order to fill the full solid angle of acceptance, the source size needs to be as small as the entrance slit of the spectrometer. We can thereby remove the entrance slit of the

spectrometer and allow the incoming light spot to be the source. In order to achieve this, we need to make refocusing optics that can make the spot size in order of 10–20  $\mu\text{m}$ . In order to keep the resolution and flux of the incoming beam with the optimum monochromator exit slit setting, it will be necessary to obtain a factor of 3–10 in demagnification of the incident light. This would increase the recorded intensity in the spectra by a factor of 3–10. The other important development is to increase the solid acceptance angle of the spectrometer. This can be achieved by allowing a larger grating or by increasing the incidence angle. Spherical gratings based on Rowland geometry have the limitation that spherical aberration limits the resolution if the illumination of the grating along the dispersive direction is too large. There are two possibilities to compensate for the aberrations either through the line density or the shape of the grating substrate. It has recently been demonstrated that a varied line spacing (VLS) grating instrument provides a larger acceptance angle compared to instruments based on a Rowland circle concept [65]. When the line density can vary across the grating surface in the dispersive direction, any type of focus condition can be achieved allowing for the use of normal incidence CCD detectors with high efficiency. Another new design is to use an elliptical substrate for the grating in a Rowland circle type of instrument where small adjustment of the shape allows a much longer grating to be used [66]. There are also attempts to build instruments based on a plane grating design where the grating size can be increased to a large extent [63]. In this case also, collimating and focusing optics need to be included which will increase the number of reflections. The latter design will allow for a substantial improvement in resolution with a relatively high efficiency. With all these improvements in spectrometers, we can anticipate that new applications of XES to more complex systems will be possible in the near future.

### 3.2. Computational

In the following section, we will discuss the different ways to compute XE spectra based on either the Hartree–Fock or DFT methods. We will describe how we from a computational viewpoint can regard the XE spectrum as a projection of the electronic structure in an atom-specific way without any consideration of core hole effects. This will be the basis for the simple interpretation of XE spectra as discussed in the previous section.

However, before entering the discussion of the various theoretical approaches we would like to make a comment on the choice of substrates for the experiments, Cu and Ni, since this was decisive for the success of the project in terms of the combination of experiment with theory. This combination was immediately recognized as a prerequisite for the detailed analysis that was the goal of the project. The transition metals, with their open d shells and accompanying spin-coupling, near-degeneracy and dynamical correlation problems, represent a challenge to theoretical treatments. Since the techniques to compute spectra were recently developed, a good calibration system would be beneficial where a direct comparison of spectra could be made without the computational difficulties of the open-shell d metals and where a large number of spectrum calculations could easily be performed. Cu, with its basically  $d^{10}$  closed-shell configuration, represents an ideal choice for this purpose and, for comparison with a more reactive metal, the studies were also performed on Ni and Pt. The experimental data for adsorption on Cu were essential for the development of the theoretical treatment and also gave confidence in the reliability of the treatment of the other substrates.

Returning to the discussion of the theoretical approaches, we can view the hierarchy of quantum chemical methods as divided into two classes: wave function-based techniques and functionals of the density and its derivatives. In the former, one works with a simple Hamiltonian which describes the

interactions and uses wave functions of increasing complexity to improve the calculation. With this approach, it is in principle possible to come arbitrarily close to the correct solution, but at the expense of interpretability of the wave function. The latter statement becomes obvious when one considers expansions, such as  $\Psi = C_0\Phi_0 + \sum_{\mu} C_{\mu}\Phi_{\mu}$ , where  $\Phi_0$  is the Hartree–Fock determinant built from the molecular orbitals and the correction term has  $\mu$  in the range  $10^2$ – $10^9$ ; each  $\Phi_{\mu}$  is a combination of determinants built up of different molecular orbitals. In DFT, on the other hand, the complexity is built into the energy expression, rather than in the wave function, and the wave function corresponds in structure to the single-determinant Hartree–Fock. Thus, we can still interpret our results in terms of a simple molecular orbital picture.

We have earlier implemented theoretical treatments of both XES [67] and XAS [68] within a direct Hartree–Fock self-consistent field approach and have applied these techniques to the calculation of theoretical absorption and emission spectra for a large number of free molecules, polymers and surface adsorbates (for a review, we refer to [69]). For strongly chemisorbed systems, where the interaction with the d band gives a large contribution to the chemisorption energy, it is necessary to account for the dynamical correlation in the calculations. It is desirable to maintain the simple molecular orbital interpretation from the Hartree–Fock description while still introducing the effects of correlation in the electron distribution; density functional theory then becomes a natural choice. As one example of the importance of including these effects and the improvements that can be obtained, we show in Fig. 19 the computed X-ray emission and absorption spectra for atomic nitrogen adsorbed in a four-fold hollow (FFH) site of the Cu(1 0 0) surface [70]. The theoretical spectra were computed at the Hartree–Fock and DFT levels and are compared with experiment. The calculations were done for large Cu<sub>61</sub> cluster models of the Cu(1 0 0) substrate and it is immediately clear that the Hartree–Fock calculations fail to reproduce the electronic structure with formation of bonding and anti-bonding states with the 3d orbitals of Cu. This is due to both the placement of the 3d levels, which is wrong by several eV in the HF approximation, and to the strong exchange-coupling and dynamical correlation within the compact 3d<sup>10</sup> configuration; DFT, however, reproduces the electronic structure quite well.

DFT has emerged as a computational approach of comparable accuracy to the traditional correlated quantum chemical methods, but with a computational cost comparable to that of Hartree–Fock. Although the Hohenberg–Kohn theorem was derived for the ground state [71], and as such sometimes has been considered to restrict DFT to the ground state only, it is easy to see that the DFT method has a wider validity. The proof of the uniqueness of the energy functional relies on an application of the variational principle and as such can be derived also for any well-defined state that is bounded from below, i.e. the lowest excited triplet state, the lowest state with a specific occupation for cases where molecular symmetry is applied or the lowest state in a restricted variational space. Considering X-ray absorption, we can variationally determine the lowest core-excited state using the constraint that the core level in question should contain only one electron. The connection between the Kohn–Sham (KS) orbitals and the density, i.e.  $\rho(\mathbf{r}) = \sum |\phi_i(\mathbf{r})|^2$ , corresponds to the probability density from a single-determinantal wave function as in Hartree–Fock theory. Having determined the orbital corresponding to the lowest excitation, we can now remove it from the variational space. This is easily achieved by giving it zero occupation and disallowing any mixings with the remaining orbitals by eliminating all off-diagonal matrix elements connecting it with other orbitals in the Kohn–Sham matrix in MO basis. Now the variational principle applied to the remaining orbital space, with the constraint on the core occupation, will produce the best approximation to the second excited state. This procedure may be continued and leads to a set of orthogonal singly-excited states [72].

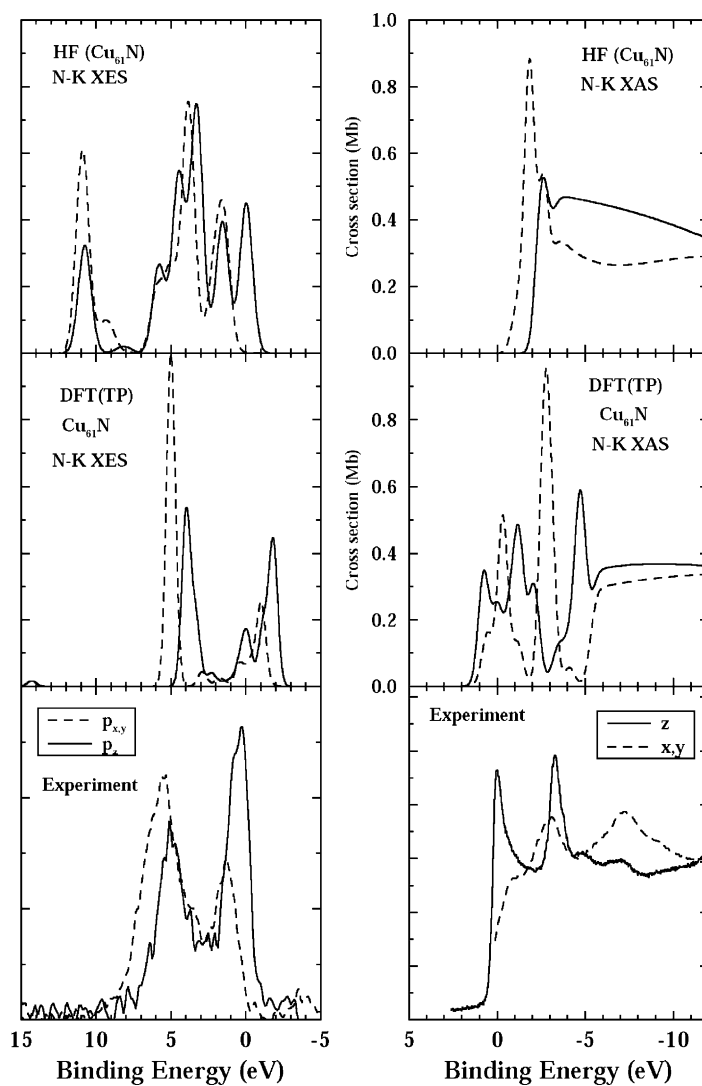


Fig. 19. Comparison of the emission/absorption spectra for  $\text{Cu}_{61}\text{N}$  obtained by the HF static exchange (STEX) and DFT transition-potential approaches with the XES experiment of  $\text{N/Cu}(1\ 0\ 0)$ .

As a first approximation to the excited states, we may thus take unoccupied orbitals of the Kohn–Sham equations to replace occupied orbitals in the determinantal wave function representation of the density. The ionization and excitation energies may then be evaluated as differences of total energies of final and initial states ( $\Delta\text{KS} - \text{SCF}$ ), or approximated as an orbital energy difference in a transition state calculation [73,74] in which half an electron is removed from the initial orbital and put into the final orbital for transition energies, or half an electron is removed only from the initial orbital for ionization energies. The latter procedure takes into account relaxation effects to second order upon ionization or excitation. The  $\Delta\text{KS} - \text{SCF}$  approach includes all relaxation effects from the core hole and interaction of the excited electron with the molecular ion core, but is restricted by the requirement to variationally obtain each excited state. In the transition-potential approach, on the other hand, it is possible to

approximately obtain all states from one calculation by taking as the potential for the unoccupied levels the density corresponding to the molecule with a half-occupied core hole; half an electron is thus removed from the molecule. This defines the orbital energies sufficiently well to allow them to be used to estimate the excitation energies. An overall shift of the entire spectrum can then be made based on the  $\Delta$ KS computed fully relaxed core ionization potential and adding relativistic effects. Finally, differential relaxation effects in prominent low-lying excited states can be included through the excited state procedure outlined above. This summarizes the implementation of XAS within the StoBe-deMon code [75] and we will now turn to a discussion of the approximations underlying the calculation of XE spectra within our DFT implementation.

As described in Section 2.1, the XE spectral distributions should be calculated according to Fermi's golden rule as spontaneous dipole transitions between all possible valence hole final states,  $\psi_v$ , and the core hole state,  $\psi_{CH}$ . In this picture, each state must be fully optimized in the appropriate valence and core hole potentials, respectively. However, this scheme leads to difficulties with non-orthogonal and interacting final states unless all valence hole states are obtained from the same operator or with specific orthogonality constraints. To simplify the calculations, we thus replace both the initial and different final state potentials with a single potential. Thus, the Kohn–Sham orbitals of the ground state are used to represent both the initial core hole state and the final valence hole states and the transition is treated as an explicit one-electron transition. The evaluation of the dipole transition moments then simply requires the computation of one-electron states  $\varphi_i$  which is performed using the DFT formalism.

The calculation of the XES transition moments from ground state orbitals has given good agreement with experiment [11,32,43,67,76–80]. The use of transition potentials or relaxed core hole states has been shown to not necessarily improve the description [81]. This is somewhat surprising as these ground state calculations represent the most simple one-electron picture of a passive core hole into which the ground state valence electrons decay. Along these lines, XES is often interpreted in a simple one-electron picture as the radiative decay of valence electrons into a core vacancy which has been created previously in X-ray absorption (XA). The presence of a core hole in the intermediate state can intuitively be expected to affect the spectrum since the energetically very large relaxation effects associated with the core-levels upon ionization are well established. To discuss core hole effects, we will compare with XES transition elements calculated using Hartree–Fock between the fully relaxed core hole wave function and the ground state wave function [67]. To compare experimental and calculated XE spectra, we relate the highest occupied one-electron Kohn–Sham orbital to the experimental Fermi edge and apply a Gaussian broadening of typically 0.5 eV FWHM to the calculated discrete spectra. We will now turn to a detailed discussion of the underlying approximations.

### 3.2.1. *Dynamic core hole effects*

The interpretation of XES spectral features is a long-standing issue originating from the application of this spectroscopy to determine the bulk electronic structure of metals. In the interpretation of XES intensities, core hole creation and annihilation play important roles. In particular, the dynamic response due to the creation of the core hole must be considered, as this can lead to substantial effects on the spectroscopic observables. The term “dynamic effects” has been coined to summarize the equilibration response of valence electrons to the sudden core hole creation or annihilation. For homogeneous systems, model calculations on a non-interacting electron gas have been performed [40,82–85]. In this treatment, two extreme cases are computationally accessible: The first case is the short-time limit where the duration of the interaction between the core hole and the electron gas is infinitely short. In this case, the effects of

the presence of the core hole are negligible and the final-state electronic configuration determines all spectral features which are then calculated as the one-particle transition elements obtained from orbitals calculated in the final state potential of the X-ray process. The other scenario is the long-time limit. Here, the core hole is also annihilated suddenly, but has been present before as a static state. Spectroscopically, the latter case is characterized by the occurrence of the Mahan–Nozieres–de Dominicis (MND) X-ray edge divergence or threshold singularity [83,86,87]. As a matter of fact, the spectral distributions obtained for the long-time limit and the short-time limit are related directly since the spectral distribution obtained in the long-time limit is the spectral distribution of the short-time limit modified by multiplicative exponential threshold singularities, varying for each angular momentum.

### 3.2.2. *The final state rule*

The treatment of dynamic core hole effects as outlined above has led to the formulation of the “dynamic” final state rule and the “static” final state rule for the relative XES intensities by von Barth and Grossmann in 1979 [84]. According to the dynamic final state rule, the energetic positions and relative intensities in the XE spectra of simple metals are given by the one-particle transition elements calculated from orbitals in the final state potential of the X-ray process and multiplicative singularity functions at the Fermi level for each angular momentum, which take care of the dynamic core hole effects [40,84,85,88]. As an extension to the dynamic final state rule, von Barth and Grossmann found that the XE spectra generated by their dynamic calculations in many cases can be mimicked rather well by the static one-particle transition elements only, calculated from orbitals in the final state potential of the X-ray process.

Within this thinking, the final state rule has been extended to narrow-band metals and varying core hole strength [88]. The influence of dynamic core hole effects can be categorized depending on the occupation of the valence band. The singularity behavior increases with decreasing occupancy. This means that for nearly empty bands the dynamic effects become large. In the case of highly occupied bands, dynamic effects are negligible and the spectral distribution is given by the one-electron description [88].

As these rules are based on model calculations for a homogeneous and non-interacting electron gas, their applicability depends on how well an interacting electron system is approximated by this model. The valence electronic structure of simple sp metals is well approximated by a non-interacting electron gas. Therefore, the final state rule is directly applicable to the XES spectroscopic results on these systems. For adsorbates on transition metals, a description of the valence electronic structure based on an independent electron model is questionable; here, the adsorbate atoms and the localized d states in transition and noble metals are expected to cause large deviations.

With this in mind, we will discuss the XES relative intensities for CO/Cu [32]. Our interpretation is based on the relative intensities and energy positions within the XES spectral distribution at each atomic center. In the top panel of Fig. 20, computed C K XES of  $\pi$  symmetry is shown calculated at the Hartree–Fock level as the dipole-transition between the relaxed core hole wave function  $\psi_{\text{CH}}$  and the ground state wave function  $\psi_{\text{GS}}$  [67]. In this calculation, a significant enhancement of states close to the Fermi level is observed in contradiction to the experimental spectrum that is shown for direct comparison in the lower panel of Fig. 20. We furthermore note that the neglect of correlation in Hartree–Fock leads to significant deviations in energy. All valence hole final states are described using the ground state molecular orbitals in the calculation. This is correct for independent electron models and a good approximation for simple metals and consequently represents the calculation in the long-time limit or the dynamic final state rule with a threshold singularity as discussed earlier. However, for interacting electrons valence hole

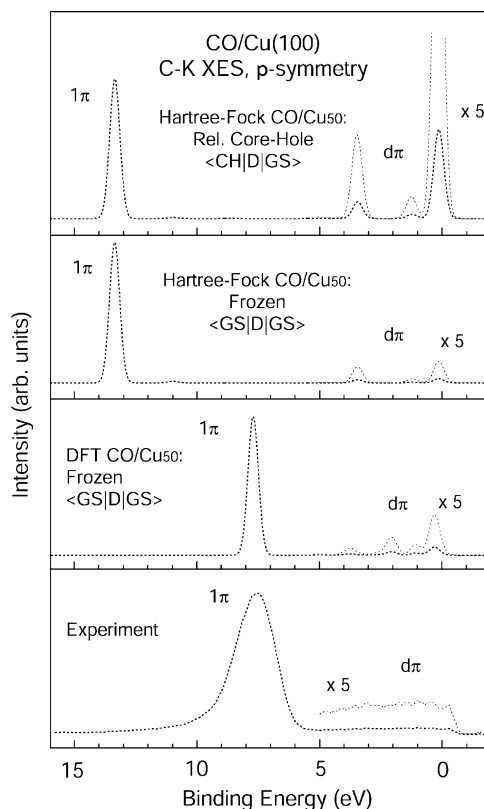


Fig. 20. Experimental and computed C 1s X-ray emission  $\pi$  symmetry spectra for CO/Cu(1 0 0). From top to bottom: Hartree–Fock relaxed core hole and ground state final wave function, Hartree–Fock ground state (frozen orbitals), DFT ground state (frozen orbitals) and experiment (bottom). The same CO/Cu<sub>50</sub> cluster model was used in all calculations.

relaxation and screening may be sizable and may cause orbital changes similar to those due to the relaxed core hole; using the ground state orbitals to describe the final (valence hole) state in combination with the fully relaxed core hole may then be a poor and unbalanced approximation. Therefore, it can be anticipated that the neglect of valence hole relaxation could be the reason for the obvious discrepancy between experiment and the Hartree–Fock calculation with a relaxed core hole only. However, it also brings up the question whether the conceptual framework of intermediate core hole states is appropriate.

In CO/Cu, the valence electronic structure to a large extent involves the Cu 3d states, which have large electron correlation effects. One main difference between an independent electron gas and a correlated electron system is the response to a valence vacancy. The valence hole relaxation in CO/Cu should vary significantly and increase with the energy of the valence vacancy. If we consider the energy difference between the ground state and the real valence hole final state, the valence hole relaxation can be seen as a correction to the ground state calculation. As a model for chemisorbates, the energetics associated with final state relaxation has been calculated for Cr(CO)<sub>6</sub> [89] and may be characterized as follows: metal 3d level very large 6–7 eV, adsorbate valence levels large 3–4 eV and metal conduction levels small, 0.2–1 eV. This trend is intuitively clear, as the relaxation due to a vacancy in an outer-valence state (most extreme, the HOMO) is much less than for an inner-valence vacancy.

For the discussion of valence-relaxation effects, we consider three different approaches to compute the C K XES of  $\pi$  symmetry in comparison with experiment. All the spectra are summarized in Fig. 20. To allow an easy comparison of the relative intensities within each spectrum we have normalized the respective  $1\pi$  to equal height. The top panel shows the Hartree–Fock calculation with non-orthogonal transition moments calculated between the fully relaxed core hole wave function  $\psi_{\text{CH}}$  and the ground state wave function  $\psi_{\text{GS}}$  with a vacancy in the appropriate (frozen) valence level. In the two middle panels, we show the results from using frozen ground state orbitals within both the Hartree–Fock and the DFT techniques. Here, both the initial and final state wave functions have been calculated using the ground state potential; in this case, core hole relaxation and valence hole relaxation are both neglected. The lower panel, finally, shows the experimental spectrum.

It is directly seen that the calculations which give best agreement with the experimental relative intensities are obtained in the frozen orbital approach [32]. Here, we do not observe the significant enhancement of states close to the Fermi level which dominates the calculated spectrum between  $\psi_{\text{CH}}$  and  $\psi_{\text{GS}}$  when the relaxed core hole is included (top panel). In the frozen orbital approach, both the core hole effects and the valence hole relaxation are neglected, nevertheless the agreement with experiment is very good. This suggests that either the dynamic core hole effects are balanced by a variation in final state relaxation, which is not included when only the intermediate core hole state is fully relaxed while the valence hole relaxation is neglected, or that the excitation–deexcitation process is a true one-step process where relaxation effects are minimal.

Let us now investigate the notion of balance between dynamic core hole effects and varying valence hole relaxation by considering the general structure of the XES transition elements within Fermi’s golden rule. The matrix elements between respective initial and final state wave functions  $|F\rangle$  and  $|M\rangle$  are conveniently split into the one-electron dipole transition between the active  $1s$  core orbital  $\varphi_{1s}$  and each valence orbital  $\varphi_v$ . The orbital overlaps of all other orbitals, which are not involved in the one-particle transition, result in the codeterminant factor “Codet” for each  $\varphi_v$ :

$$\langle F|\mathbf{D}|M\rangle \approx \langle \varphi_v|\mathbf{D}|1s\rangle \text{Codet}$$

If both the initial and final states are calculated in the same potential, Codet is equal to one for all valence hole final states and the relative intensities are given by the one-electron transition elements only. This is the case in the frozen orbital calculations.

The difference between the frozen orbital calculation and the transitions calculated between a fully relaxed  $\psi_{\text{CH}}$  and  $\psi_{\text{GS}}$  is a modification of all one-electron transition elements due to the core orbital contraction and the response of the valence orbitals to the created core vacancy in the relaxed core hole wave function  $\psi_{\text{CH}}$ . More important, a strong variation of the Codet towards threshold strongly emphasizes transitions from threshold valence levels over lower-lying valence levels, thus forming a threshold singularity.

Let us now consider the hypothetical case of calculating the XES transition between all possible relaxed valence hole final states  $\psi_v$  and the relaxed core hole state  $\psi_{\text{CH}}$ . Here, we have not only core hole effects, but also valence hole relaxation. The valence hole relaxation will modify the energetic positions of all valence states but we now consider only the relative intensities. If we assume small changes of the one-electron transition elements in comparison to when only the core hole relaxation is included, the difference between these two calculations must be determined by Codet. Consequently, Codet should vary little for the hypothetical full calculation with relaxed valence and core holes; this is in contrast to when only core relaxation is included where Codet varies strongly towards the Fermi level. The reason

behind this should be that towards threshold Codet is large due to the X-ray edge divergence, but towards deeper valence holes, where the influence of the threshold singularity decreases, the increasing valence hole relaxation keeps the magnitude of Codet comparable at a compensating rate.

Consequently, the experimental spectra and the hypothetical exact calculation of the matrix elements between the relaxed core hole wave function  $\psi_{\text{CH}}$  and the different relaxed valence hole wave functions  $\psi_{\text{v}}$  are approximated very well by calculations with the initial and final states calculated in the same potential, i.e. the ground state. In this case, Codet is constant for different valence hole final states.

Another possibility is to use a transition-potential approach (DFT-TP) where the initial and final states are calculated in the same core hole potential. In the DFT-TP calculation, the initial core-ionized state is represented accurately, but all valence orbitals in the final state are evaluated in the presence of the core hole. As in the frozen orbital approach, Codet is also constant and equal to one. However, in contrast to the ground state calculation the 4–5 $\sigma$  intensity ratio of 2.77 in the DFT-TP calculation deviates significantly from the 0.9 obtained both experimentally and with the frozen orbital ground state calculation [32]. As in both the ground state picture and the relaxed core hole picture (DFT-TP), Codet is unity the difference in the 4–5 $\sigma$  ratio must be directly related to the final state wave function. Therefore, the good agreement between the one-electron ground state calculation and experiment shows that the experimental XES intensities are a good representation of the ground state valence electronic structure.

In summary, for a balanced treatment of dynamic core hole effects and valence hole relaxation either the full calculation of core and valence hole relaxation should be performed—if computationally possible—or not be included at all. In this case, the initial and final states must be calculated in the ground state potential.

Our interpretation so far of the XES relative intensities has been centered on a cancellation of dynamic core hole effects and valence hole relaxation. This cancellation, as presented, is rather coincidental and therefore conceptually unsatisfying. Especially, as the one-electron ground state model works surprisingly well for a large range of systems; from metals via insulators to free molecules. Experimentally, the core hole intermediate state is not an observable. We only know that RIXS leads to a valence excitation of an electronic system with an enhanced cross-section at core-level thresholds. The formulation of the core hole intermediate state is, strictly speaking, the construction of the second-order perturbation treatment of the photon–electron interaction. In a true one-step description of the valence-excitation in the X-ray scattering process, the agreement with the ground state model which neglects both core hole relaxation and valence hole relaxation would be less puzzling as no core hole intermediate state would be formed.

### 3.2.3. Intensity Scale

The XE spectra have the quality of an experimental decomposition of the molecular orbitals into contributions from the different atoms in the molecule, i.e. an experimental *population analysis*. This very important aspect comes from the extremely localized character of the intermediate core hole and the fact that only valence orbitals, which have amplitude within the spatial extent of the core orbital (or rather the core orbital scaled with  $r$ , corresponding to the dipole operator), can contribute to the XE spectrum. This ensures a projection onto that specific site. Due to the dipole character of the transition, we will only obtain the valence 2p character in case of a 1s core level. The remaining contributions to the bonding can, however, be obtained from theoretical calculations once the theoretical model has been calibrated against the 2p contribution.

In order to use the XE spectra to assign a distribution of electrons within the molecule, we must calibrate the spectra for the different atoms relative to each other and furthermore, for each element,

establish a correlation between spectral intensity and 2p population. Experimentally, the emission count-rate depends both on the proportion of molecules that are excited (i.e. the XA spectrum), the branching rate for Auger versus radiative decay for that element and that energy as well as the transition probability for decay from a given valence orbital into the core hole. From a practical viewpoint, each experimental spectrum is separately normalized and we must think of a way to relate the spectra to each other. How can this be done?

For a case, where the total number of 2p electrons is well known, such as, e.g. an atom in a specific atomic state, we can determine a scaling factor corresponding to the total 2p electron count according to:

$$A \sum_{i=1}^{n_v} |\langle 1s | \vec{D} \cdot \vec{E}' | \phi_i \rangle|^2 = N_v$$

What this amounts to is a summation of the squares of the transition dipole moments for the atom over all  $n_v$  valence orbitals and determining the factor  $A$  such that the sum scaled by this factor becomes equal to the number,  $N_v$ , of 2p electrons on the atom. Applicability of this simple normalization to molecular systems is based on the assumption that the 2p orbital shape does not vary strongly with the atomic state; tests on different excited states of the atoms treated so far show that normalization factors determined for different excited states of the atom vary by less than 5%, which then becomes an estimate of the accuracy in the deduced populations. For the atoms discussed in the present review, the so determined scaling factors were: 148.2, 198.0, and 249.5 for carbon, nitrogen and oxygen, respectively.

In the cases where this normalization was used theoretically, the spectra were generated by simply convoluting the (square of the) transition dipoles with Gaussian functions and scaling the overall spectrum with the factor  $A$ . Hence, the difference in energy dependence of XES intensities between the atom and the molecule was not included, which can have a small effect on the scaling. This scaling was also used experimentally to relate the intensities between contributions from different atoms in a molecule. Here, the overall spectra were area normalized and then scaled according to the determined factors. Applying this procedure gives a near-quantitative experimental estimate of the amount of local atomic 2p contribution to each of the molecular orbitals, i.e. an experimental population analysis in the spirit of the LCAO picture.

### 3.2.4. Cluster models

In order to describe the chemisorption systems, we employ a series of cluster models of the metal surface with adsorbate. As examples, we have in the case of N/Cu(1 0 0) [70] used clusters  $\text{Cu}_5$ ,  $\text{Cu}_{25}$  and  $\text{Cu}_{61}$ , to study convergence of the computed spectra with cluster size (Fig. 21). Here, only the central five Cu atoms were described with all electrons and the remaining were described using a one-electron (Cu 4sp) effective core potential (ECP) description [90]. For the emission, which measures the character of the occupied states, the main features are reproduced already with the small  $\text{Cu}_5$  cluster, while for absorption the computed spectrum changes strongly also when going from  $\text{Cu}_{25}$  to  $\text{Cu}_{61}$ . Since absorption spectra depend on the unoccupied states, that for copper have mainly diffuse and delocalized 4sp character, the absorption spectra tend to require larger cluster models than what is necessary to treat the emission spectra. When treating resonantly excited XES, it is therefore necessary to extend the models of the surface electronic structure, compared to a treatment where the intermediate X-ray excited state is not included. For example, the study of RIXS of ethylene on Cu(1 1 0) required extending the cluster size up to  $\text{Cu}_{86}$  in order to obtain a reliable description of the relative weights of the different intermediate states

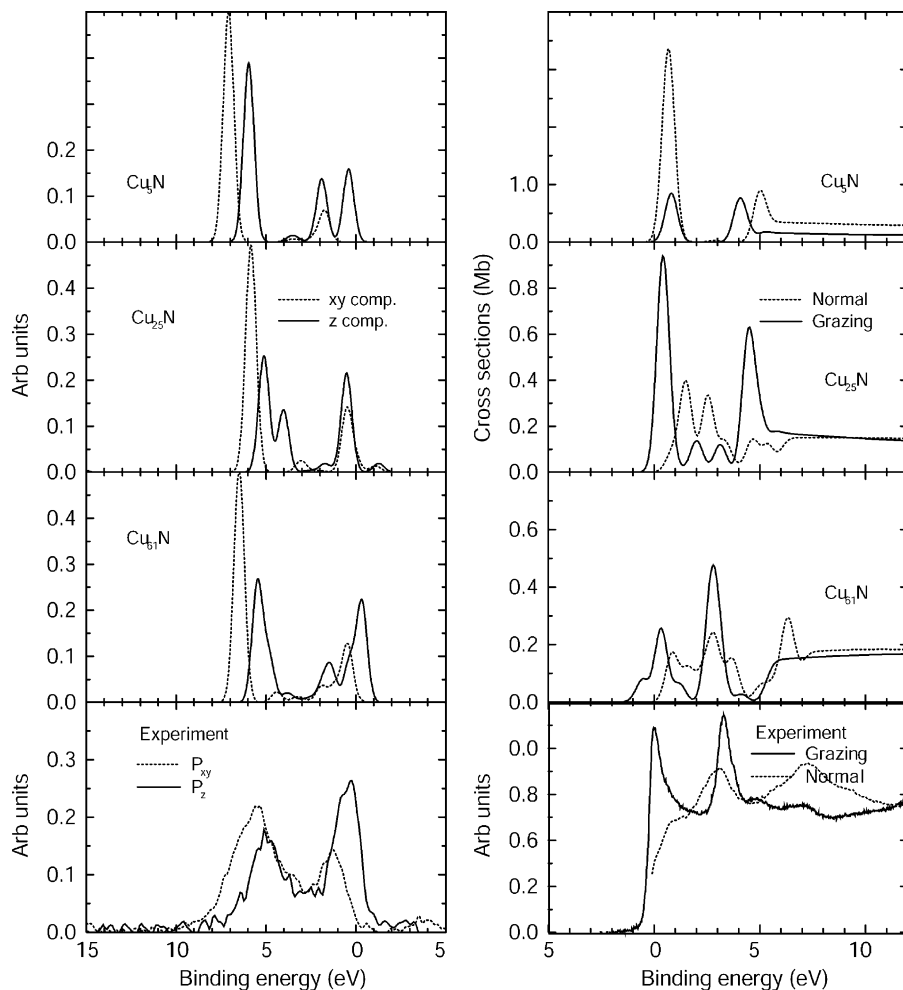


Fig. 21. N 1s emission (left panels) and absorption (right panels) spectra computed for different cluster sizes (Cu<sub>5</sub>, Cu<sub>25</sub> and Cu<sub>61</sub>) compared with experiment (bottom).

[61]. Similar considerations apply to the cluster models of Ni metal that will be discussed in the present review.

#### 4. Adsorbate systems

Here, we will discuss a number of different chemisorption systems that have been studied using XES experiments and DFT calculations. The systems are presented with a goal to obtain an overview of different interactions of adsorbates on surfaces. We have classified the interactions into five different groups with decreasing adsorption strength: (1) radical chemisorption with a broken electron pair that is directly accessible for bond formation, (2) interactions with unsaturated  $\pi$  electrons in diatomic molecules, (3) interactions with unsaturated  $\pi$  electrons in hydrocarbons, (4) lone pair interactions,

Table 1  
Adsorbed molecules studied experimentally with XES

Adsorbate	Substrate	References	Figures
Atomic C	Ni(1 0 0)	[215]	Fig. 28
Atomic N	Ni(1 0 0)	[39,215]	Figs. 9, 26 and 28
	Cu(1 0 0)	[39,99]	Figs. 19, 21, 22, 26 and 28
Atomic O	Ni(1 0 0)	[5,46,215]	Fig. 28
	Cu(1 0 0)	[5,46,99,215]	Fig. 28
Nitrogen (N <sub>2</sub> )	Ni(1 0 0)	[8,11]	Figs. 2 and 30
Carbon monoxide (CO)	Ni(1 0 0)	[43,45,55]	Figs. 12, 39, 43 and 45
	Cu(1 0 0)	[32,43,45]	Figs. 11, 18, 20 and 43
	Ru(0 0 1)	[216]	
Nitrogen monoxide (NO)	K/Ni(1 0 0)	[162]	Fig. 48
	Ru(0 0 1)	[77]	
Ethylene (C <sub>2</sub> H <sub>4</sub> )	Cu(1 1 0)	[34,35,166]	Fig. 55
	Ni(1 1 0)	[166]	
	Si(0 0 1)	[205]	
Acetylene (C <sub>2</sub> H <sub>2</sub> )	Cu(1 1 0)	[217]	
Benzene (C <sub>6</sub> H <sub>6</sub> )	Ni(1 0 0)	[8,36]	Fig. 60
	Cu(1 1 0)	[34–36]	Figs. 58 and 59
	Si(0 0 1)	[205]	
<i>n</i> -Octane (C <sub>8</sub> H <sub>18</sub> )	Cu(1 1 0)	[189,190]	Fig. 78
Water (H <sub>2</sub> O)	Pt(1 1 1)	[172]	Fig. 62
Formate (HCO <sub>2</sub> )	Cu(1 1 0)	[56,57]	Figs. 65 and 67
Acetate (H <sub>3</sub> C–CO <sub>2</sub> )	Cu(1 1 0)	[56,57]	Fig. 67
Ammonia (NH <sub>3</sub> )	Cu(1 1 0)	[57,76]	Fig. 69
Glycine (NH <sub>2</sub> –CH <sub>2</sub> –COOH)	Cu(1 1 0)	[57,79,80]	Figs. 71, 72, 73 and 76
PTCDA <sup>a</sup>	Ag(1 1 1)	[218]	

<sup>a</sup> 3,4,9,10-Perylene-tetracarboxylicacid-dianhydride (PTCDA).

and (5) saturated hydrocarbons which represent molecular systems without  $\pi$  or lone pair orbitals. At the end of the section, there is a summary where all the fundamental aspects of the adsorbate bonding situations in the different systems are compared with each other providing a general overview. In order for the reader to find the appropriate references, we have collected all adsorbate systems so far studied with XES in Table 1. In the cases that the spectra are displayed in the present review, there is also a reference to the related figure.

#### 4.1. Radical atomic adsorption

Over the years, atomic adsorbates on Ni and Cu surfaces have served as prototype systems for strong chemisorption. These systems represent bonding to surfaces where the adsorbate atoms have unpaired electrons available for covalent interaction with unsaturated electronic states on the metal surface. We denote this bonding mechanism as radical adsorption where the open-shell electrons on the adsorbate atom can form electron pairs with the metal atoms at the surface. We will start to describe the electronic structure of atomic N adsorbed on Cu(1 0 0) in great detail. This will lead to a general concept of chemical bond formation for adsorbed C, N and O on Ni(1 0 0) and Cu(1 0 0) surfaces. We anticipate that this bonding mechanism can be expected to be general for many atomic adsorbates on transition and noble metal surfaces.

#### 4.1.1. Electronic structure of N on Cu(1 0 0)

The atomic N on Cu(1 0 0) system is an ideal case to understand the electronic structure of radical adsorption for a number of different reasons. Since the 3d band in Cu is located a few eV below the Fermi level (see Fig. 9), a significant fraction of the N 2p–Cu 3d states will be occupied and can be directly observed in XES. Furthermore, the structure of N on Cu is nearly planar to the first Cu layer making the geometry relatively simple. The much more studied atomic O on Cu(1 0 0) shows a complexity with several phases due to surface reconstructions [91–94].

There is only a single phase of N adsorbed on Cu(1 0 0) showing a  $c(2 \times 2)$  low-energy electron diffraction pattern [95]. A surface extended X-ray absorption fine structure (SEXAFS) study [96] proposed that the N atoms are located in four-fold hollow sites at a vertical height of 0.4 Å above the topmost Cu layer and thus being nearly coplanar with the surface. The bond length between the N and its nearest neighbor was determined to be 1.85 and 2.29 Å to the next nearest neighbor. Recently, this simple model has been questioned based on scanning tunneling microscopy (STM) [97] and photoelectron diffraction (PhD) [98] studies where there are indications for a reconstruction of the substrate. The surface appears to undergo a large amplitude symmetry lowering rumpling of the outermost Cu layer, with alternate up and down displacements of these atoms relative to the surface plane. These rumpings do not reduce the point group symmetry of the surface structure. We assume for simplicity that these rumpings can be neglected in the discussion of the electronic structure where we only consider a nearly coplanar nitrogen atom in FFH site.

Fig. 22 shows XE spectra of N adsorbed on Cu(1 0 0) in the  $c(2 \times 2)$  structure symmetry-resolved in  $2p_{xy}$  and  $2p_z$  components [99]. The spectra have been generated by selective excitation at 400 eV photon energy, corresponding to 3.3 eV above the N 1s core-level binding energy position. The spectra were

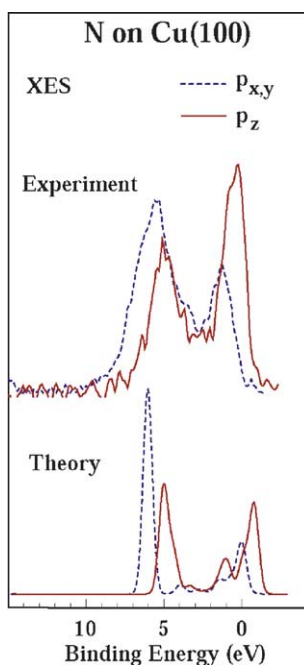


Fig. 22. Experimental and theoretical symmetry-resolved XA and XE spectra of N adsorbed on Cu(1 0 0).

obtained by assuming that half of the intensity at grazing emission comes from the  $2p_{xy}$  and the other half from the  $2p_z$  component, see Section 2.4. With this assumption  $2p_z$  is obtained by subtracting 50% of the normal emission spectra from the grazing spectra, both normalized to the same area. The spectra show two strong main components separated by 4–5 eV. The  $2p_{xy}$  spectrum is also shown in Fig. 9 where a comparison between XES and UPS was made. We can directly note that the two components are located below and above the d band in Cu. These can be attributed to bonding and antibonding states with respect to the Cu d orbitals. It is interesting to observe that the  $2p_z$  spectra are shifted towards lower energy in comparison with the  $2p_{xy}$  spectrum. In the lower part of Fig. 22 we show the theoretical spectra obtained by DFT calculations on a  $\text{Cu}_{61}\text{N}$  cluster to simulate the XES spectroscopic process [78]. There is in general a good agreement between experiment and theory. The theoretical spectra are much narrower in comparison with the experiment which partly can be related to the fact that only a single N atom is treated in the calculation. The partial N  $2p_{xy}$  and N  $2p_z$  densities of states obtained by band structure calculation of the  $c(2 \times 2)$  overlayer show a much broader distribution as discussed further in [99]. We can also see in the experimental spectra substantial intensity between the two features corresponding to energies where the Cu d band is located.

Let us go through the full electronic structure of the  $c(2 \times 2)$  overlayer based on the band structure description [99] and later return to a simple chemical bonding picture. We will first characterize the different types of interactions between the adsorbate atom and the metal atoms in the unit cell and derive how these interactions differ at high-symmetry points in the surface Brillouin zone (SBZ). We can then make a correlation between a calculated band structure of the surface and the spectral features in terms of different interactions.

Fig. 23 shows the atomic N 2p orbitals surrounded by atomic Cu 3d orbitals in an ideal, FFH adsorbate geometry where the N atom is located at the same vertical height as the first-layer Cu atoms. The upper part of the figure shows the in-plane N  $2p_{xy}$  atomic orbitals while the lower part shows the out-of-plane N  $2p_z$  orbital. We have chosen to plot only the N  $2p_x$  and  $2p_z$  orbitals as well as selected Cu 3d orbitals that have non-zero overlap with the N 2p orbitals. The simplified adsorbate geometry has  $C_{4v}$  symmetry and therefore the N  $2p_y$  and Cu  $3d_{xz}$  orbitals are obtained by a  $90^\circ$  rotation about the  $z$ -axis. The N  $2p_x$  orbital forms both  $\sigma$  and  $\pi$  bonds with the Cu 3d orbitals. The  $\sigma$  bonds result from the overlap with the first-layer Cu  $3d_x^2 - d_y^2$  and  $4s$  orbitals, while the  $\pi$  bonds arise from the overlap with the Cu  $3d_{xy}$  orbitals in the first layer and the  $3d_{xz}$  orbital on the second-layer Cu atom located directly below the adsorbate. For this idealized geometry, the remaining nearest-neighbor Cu orbitals have zero overlap with the N  $2p_x$  orbital. The lower portion of Fig. 23 shows that the N  $2p_z$  orbital forms  $\pi$  bonds with the first-layer Cu  $3d_{yz}$  and  $3d_{xz}$  orbitals. The N  $2p_z$   $\sigma$  bonds result from the overlap with the second-layer Cu  $3d_z^2$  and  $4s$  orbitals. The actual adsorbate geometry involves a displacement of the N atom outwards away from the first Cu layer by 0.4 Å. This displacement makes possible contributions from additional Cu orbitals other than those shown for the idealized geometry in Fig. 23 and also introduces some mixing of the N  $2p_{xy}$  and N  $2p_z$  orbitals in the  $\sigma$  and  $\pi$  bonds described earlier. However, as we will see below, the primary contributions to the adsorbate-induced states are similar to those of the simpler idealized geometry.

Fig. 24 shows the SBZ of the  $c(2 \times 2)$  overlayer on Cu(1 0 0). The high-symmetry points in the SBZ are denoted  $\bar{\Gamma}$ ,  $\bar{X}$ , and  $\bar{M}$ . Since there are one N and two Cu atoms per unit cell there should exist two bands for each N 2p atomic orbital. Thus, there are six predominantly surface-derived bands arising from the bonding and antibonding combinations of the N  $2p_x$ ,  $2p_y$  and  $2p_z$  orbitals with the underlying Cu 3d and  $4s$  orbitals. Each of these six bands contains both  $\sigma$  and  $\pi$  contributions at different points in the SBZ, as shown in Fig. 24. A straightforward tight-binding analysis of the model problem [100] can directly

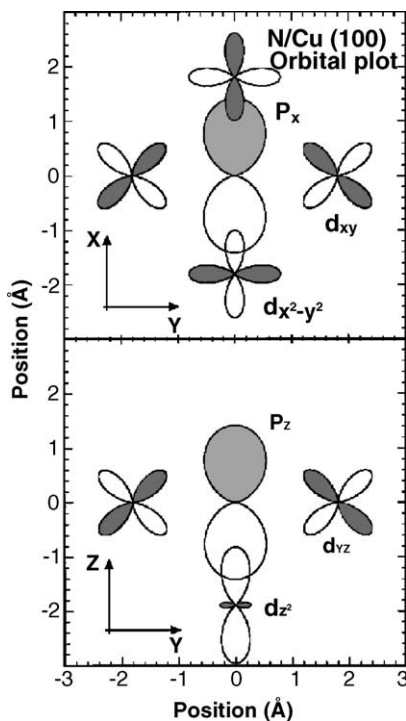


Fig. 23. Schematic N 2p and Cu 3d orbital plots. The top figure shows the surface from above and the N sitting in a hollow adsorption site surrounded by four Cu atoms. The bottom picture shows a side view with a Cu atom from the second layer located directly below the N atom.

indicate the bonding nature of the N-derived surface states at the different symmetry points. This is shown in Fig. 24 for the N  $2p_x$  and N  $2p_y$  orbitals in the  $xy$ -plane (parallel to the surface) in terms of bonding (or antibonding) interactions. There is a degeneracy for the N  $2p_x$  and N  $2p_y$  bands at the  $\bar{\Gamma}$  and  $\bar{M}$  points and therefore only the N  $2p_x$  orbital is shown. At the  $\bar{\Gamma}$  point, the phases of the wave functions of the two Cu  $3d_x^2-d_y^2$  orbitals and the two Cu  $3d_{xy}$  orbitals have to be the same leading to both an in-phase and out of phase overlap with the N  $2p_x$  orbital. This leads to  $\sigma$  and  $\pi$  non-bonding interactions. At the  $\bar{M}$  point, the phase of the Cu orbitals in both directions has to be different which gives  $\sigma$  and  $\pi$  bonding interactions. We therefore expect that the bonding bands will disperse to higher binding energies from the zone center to the edges and the antibonding bands to lower energies. At the  $\bar{X}$  point, the interactions are generally a mixture of non-bonding as well as bonding or antibonding. The  $\sigma$  interactions between N  $2p_x$  and the first layer Cu  $3d_x^2-d_y^2$ ,  $3d_z^2$ , and  $4s$  are bonding or antibonding while the  $\pi$  interaction with the first layer Cu  $3d_{xy}$  is non-bonding. The reverse is true for N  $2p_y$ , with the  $\sigma$  interactions being non-bonding and the  $\pi$  interactions bonding or antibonding. Similar arguments can be made for the N  $2p_z$  orbital, not shown. The  $\pi$  interaction of N  $2p_z$  with the first layer Cu  $3d_{yz}$  is bonding or antibonding while the  $\pi$  interaction with  $3d_{xz}$  is non-bonding. In all cases, the interactions of the N orbitals with those of the second layer Cu are independent of  $k$ .

We plot the calculated energy bands [99] for the  $c(2 \times 2)$  N/Cu(1 0 0) surface in Fig. 25. We identify some surface states and resonances [9]. For example, there is a flat N-derived surface band 7.5 eV below the Fermi level along  $\bar{X}$ – $\bar{M}$  in Fig. 25. A number of surface resonances are also visible, such as the

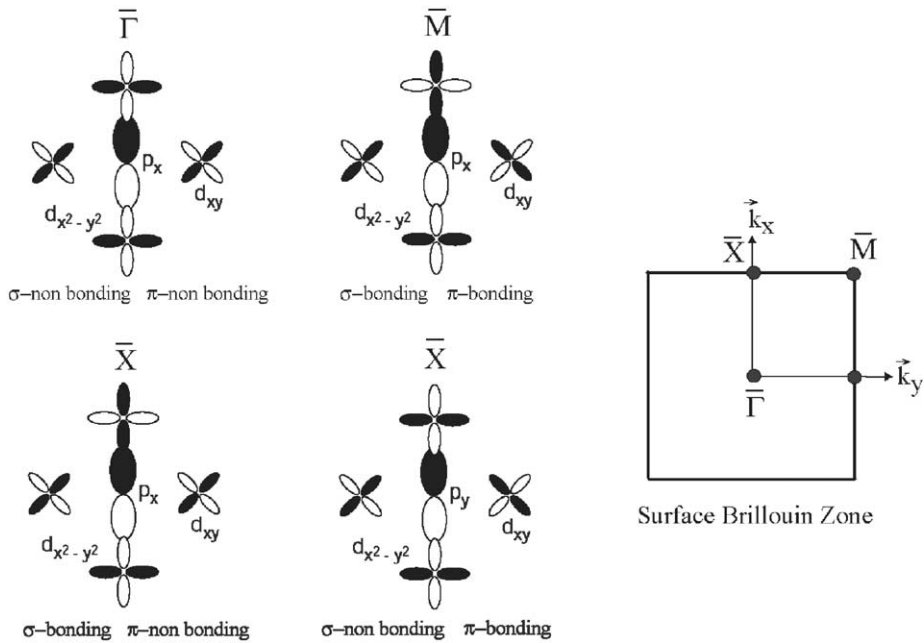


Fig. 24. Schematic N  $2p_x$ , N  $2p_y$  and Cu 3d orbital plots at the different high symmetry points in the surface Brillouin zone. Note that the degeneracy is lifted at the  $\bar{X}$  point where both N  $2p_x$  and N  $2p_y$  orbitals are shown.

continuation of the  $-7.5$  eV surface band near the  $\bar{X}$  point which disperses upwards to  $-5$  eV at the  $\bar{\Gamma}$  point in Fig. 25. The region with the highest density of bands corresponds to the Cu 3d states. Adsorbate-induced bands are clearly visible around the  $\bar{M}$  point of the surface Brillouin zone, in part because there are gaps in the projected bulk bands around this point. However, it is more difficult to

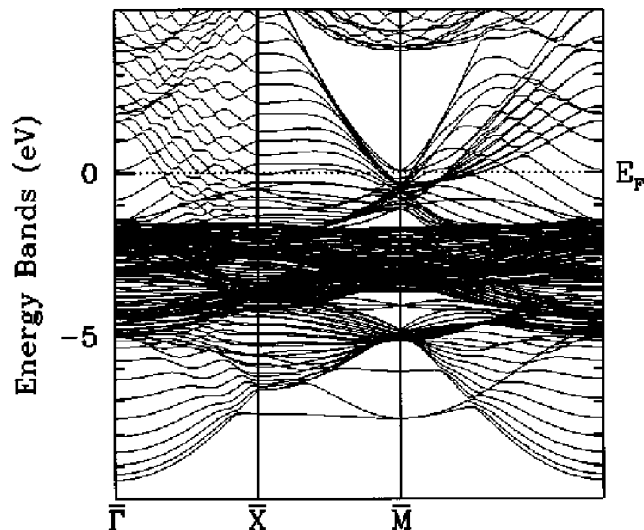


Fig. 25. The first-principles energy bands calculated for the  $c(2 \times 2)$  N/Cu(1 0 0) surface.

distinguish the surface-derived bands when they overlap with the large density of Cu states forming surface resonances.

From an inspection of the experimental spectra in Fig. 22, we observe that the width of the bonding spectral features (7–5 eV) is much larger for the N  $2p_{xy}$  component compared to the N  $2p_z$  component. This can be understood based on the bandstructure [99]. The two bands with energies of –7.5 and –5.5 eV at the  $\bar{M}$  point can be affiliated with the N  $2p_{xy}$  and N  $2p_z$  components, respectively. The lower energy of the N  $2p_z$  indicates a weaker interaction with the substrate since it forms predominantly  $\pi$  bonds with the first Cu layer and the  $\sigma$  bonds to the second layer are weaker due to the larger N–Cu bond length. Both bands disperse to lower energies towards the  $\bar{\Gamma}$  point due to increasing non-bonding interactions. At the  $\bar{\Gamma}$  point, both surface resonances are non-bonding with respect to the interactions in the first layer and we therefore expect small N  $2p$  contributions and mainly Cu 3d character. The width of the two bonding spectral features in Fig. 22 is directly related to the difference in band dispersion for the two bands. We note that the N  $2p_{xy}$  component is split into a surface state at 7.5 eV and a surface resonance 5.5 eV at the  $\bar{X}$  point. This is due to the non-degeneracy of the N  $2p_x$  and N  $2p_y$  related bands and reflects the difference in energetics depending on whether the  $\sigma$  or  $\pi$  interaction is bonding or non-bonding. The band at 7.5 eV is related to the N  $2p_x$  components since the  $\sigma$  interaction provides much larger overlap and stronger bonding compared to the  $\pi$  interaction. If the N  $2p_x$  band would be flat between the  $\bar{M}$ – $\bar{X}$  points we would expect to see a sharp peak in the XE spectrum at 7.5 eV. Since this is not what we observe, the band must disperse more towards lower energies providing a smaller splitting between the N  $2p_x$  and N  $2p_y$  related bands at the  $\bar{X}$  point. We assign the N  $2p_{xy}$  spectral feature at 4 eV primarily to a surface resonance at the  $\bar{X}$  point. This resonance is a continuation of the surface state in the gap around 4 eV at the  $\bar{M}$  point and has a large contribution from the Cu orbitals which is consistent with the presence of a surface state for the clean Cu(1 0 0) surface in the same  $\bar{M}$  point gap but at a slightly lower energy [99]. Similar arguments can also be made for the antibonding bands although they are more difficult to identify in Fig. 25 since there is a large contribution of substrate bands in the same energy region.

These results confirm the general picture obtained in previous work of bonding states below and antibonding states above the bulk Cu d band. The states with the largest bonding character occur at the  $\bar{M}$  point and have a large N  $2p$  contribution while the non-bonding states are predominantly Cu 3d. The implication of the occupancy of both the bonding and antibonding bands will be discussed in Section 4.1.2.

#### 4.1.2. Chemical bonding of C, N and O on Ni and Cu

In Section 4.1.1, we have discussed the occupied electronic structure of N adsorbed on Cu. Let us now also consider the unoccupied states and the difference between the adsorption on Cu and Ni. We will relate the difference in the electronic structure to the difference in chemical reactivity between transition and noble metals.

Let us compare atomic N adsorbed on the Ni(1 0 0) and Cu(1 0 0) surfaces [101]. The adsorbed atoms are located in four-fold hollow sites on both Ni(1 0 0) and Cu(1 0 0) with a coverage of half a monolayer. N on Cu(1 0 0) forms a  $2 \times 2$  non-reconstructed overlayer, discussed earlier, while N on Ni(1 0 0) reconstructs the surface through a rotation of the Ni atoms around the adsorption site to allow for a penetration of the N atom into the first layer thus forming a primitive  $2 \times 2$  structure with  $p4g$  symmetry [102,103]. Fig. 26 shows the XE spectra on a common binding energy scale [99,101]. In order to follow the unoccupied part we also show the corresponding X-ray absorption spectra [99,104]. Spectra related to

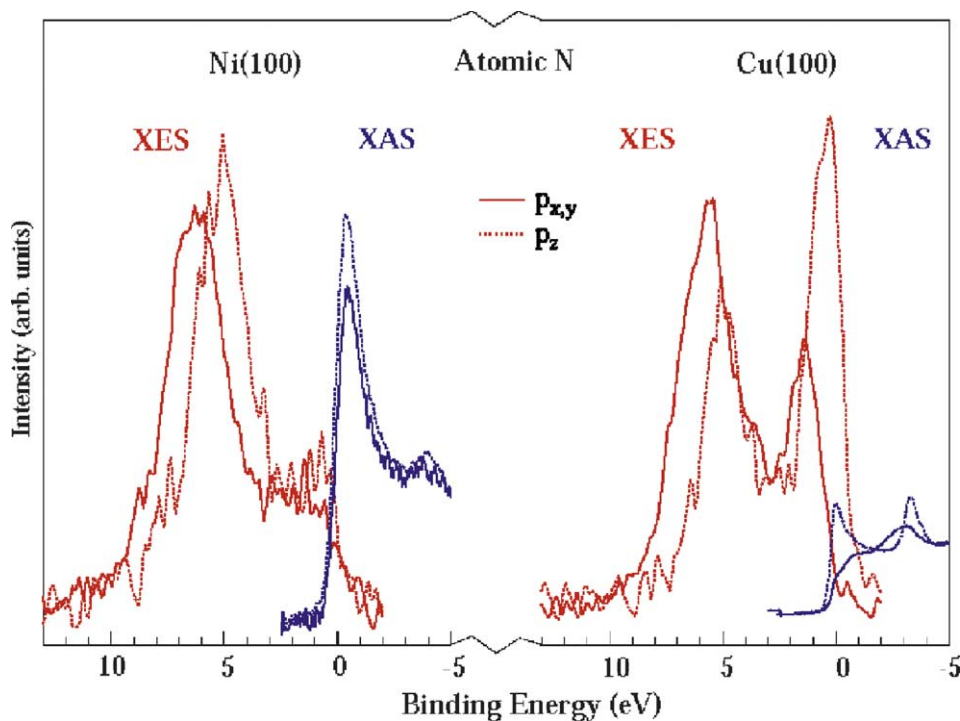


Fig. 26. Comparison of the XE and XA spectra of atomic N adsorbed on Ni(1 0 0) and Cu(1 0 0) with separated p components. The intensity scaling between the XE and XA spectra is arbitrary.

adsorbate (in-plane)  $p_{xy}$  states are drawn with solid lines while spectra due to (out-of-plane)  $p_z$  states are plotted with dotted lines. The position of the Fermi level in the spectra is indicated by dotted vertical lines. The XA spectra are shown to the right of the vertical line, all normalized to the same step height well above the Fermi level. The scaling between the emission and absorption spectra is arbitrary.

In the XE spectra of N adsorbed on Cu, both the  $p_{xy}$  and  $p_z$  components exhibit two strong peaks, representing the bonding and antibonding states, discussed in Section 4.1.1. In the XA spectra, on the other hand, no strong peaks are observed. For N adsorbed on Ni, we only observe one strong peak at high binding energy in the XE spectra, due to occupied bonding states. The antibonding states can now be seen in the XA spectra directly above the Fermi level. The results clearly show how the antibonding states are shifted from below to above the Fermi level going from Cu to Ni.

Fig. 27 shows, in a schematic way, the interactions between the 3d band and the atomic 2p level. There are also metal 4sp states that are important for the electronic structure, which we have neglected in this simplified picture. The 2p–3d interaction leads to the formation of bonding and antibonding states. The bonding states will be located below the metal d band and the antibonding states above the d band. The population of the antibonding states will have a large influence on the total adsorption energetics. If the antibonding states are occupied the net bonding effect will cancel, resulting in Pauli repulsion. In Ni metal, the Fermi level is located at the top of the d band whereas in Cu it is located 2 eV above the d band. This implies that the antibonding states are occupied for the adsorption on Cu and unoccupied in the case of Ni. For adsorption on Cu, the only net bonding effect would come from the remaining 4sp interaction. This has been discussed in terms of the concept of noble metals [105].

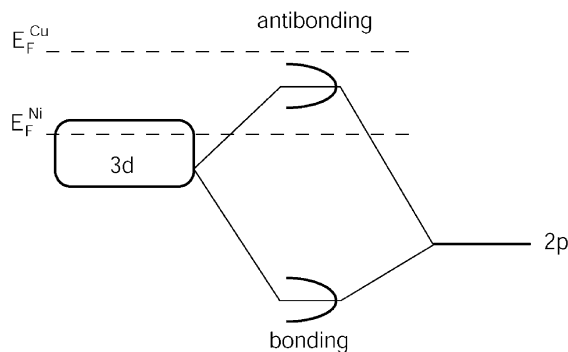


Fig. 27. Schematic illustration of the orbitals arising from the interaction of the 2p level in an adsorbate and the 3d band in a metal. The different positions of the Fermi levels in Ni and Cu metal are indicated.

In the spectra, we observe some differences with respect to the different 2p components. The  $p_z$  states are observed closer to the Fermi level than the  $p_{xy}$  states. If we look at the N on Cu XE  $p_z$  spectrum, we can see that the antibonding states are located right at the Fermi level whereas the corresponding peak in the  $p_{xy}$  spectrum is located 1 eV below the Fermi level. The XA spectra reveal a small peak just above the Fermi level for the  $p_z$  component, but only a broad continuum for the  $p_{xy}$  component. This implies that the  $p_z$  antibonding states have a small part which extends above the Fermi level and therefore gives an important net bonding contribution. The  $p_z$  component on an atom in a four-fold hollow site is directed towards a Cu atom in the second layer, giving a significant overlap, see discussion in Section 4.1.1. The bonding to the second layer could therefore be of significance for the adsorption energetics. This might be one of the reasons why the atomic nitrogen has a tendency to slightly open the metal lattice around the hollow site to allow the adsorbate atom to sink deeper into the substrate.

The question is if this simple chemical bonding picture is general for other atomic adsorbates including both C and O atoms. Fig. 28 shows XA and XE spectra for C on Ni(1 0 0) and O on both Ni(1 0 0) and Cu(1 0 0) in comparison with the previously discussed atomic N adsorption system. Adsorption of C on Ni(1 0 0) leads to a nearly identical adsorption site as for N on Ni(1 0 0) and a similar substrate reconstruction [106,107]. There exists for O on Cu(1 0 0) a low coverage non-reconstructed phase with a FFH site [91] which we have used in order to allow a simple comparison with the other adsorbate systems. In all cases, we see a very similar trend where the interaction gives rise to bonding and antibonding states, where the latter are occupied for the adsorption on Cu and unoccupied for Ni. It is interesting to note the difference in intensity ratio between the bonding and antibonding states for N and O on Cu. The atomic 2p orbital in Fig. 27 is lower in energy for O compared to N. This results in a more polarized bond and as seen in Fig. 28 the bonding states contain more adsorbate character than the antibonding states. Since the oxygen atom has one electron more compared to nitrogen we expect that the two unpaired electrons will be in the O  $2p_{xy}$  states for a completely planar geometry. This would lead to the O  $2p_z$  atomic orbital being fully occupied implying Pauli repulsion with respect to interactions with the second layer below the O atoms. Therefore, the O atomic adsorbate is located 0.5 and 0.8 Å above the first surface layer on Cu [108] and Ni [109], respectively. The different adsorbate geometry will imply that the O  $2p_{xy}$  and O  $2p_z$  components form new hybrids that will bond to the surface atoms in the FFH

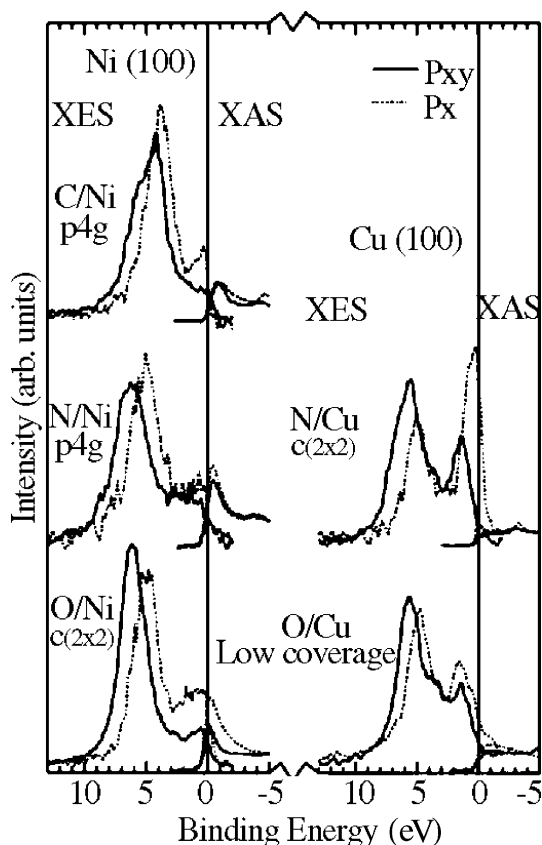


Fig. 28. A comparison of the XE and XA spectra of C, N, O/Ni(1 0 0) and N, O/Cu(1 0 0) with  $p_{xy}$  (solid lines) and  $p_z$  (dotted lines) separated. The intensity scaling between the XES and XAS is arbitrary.

site. We expect similar bonding configurations as discussed above also for second-row elements such as Si, P and S. Both F and Cl should become more extreme in ionic character where nearly all adsorbate character will be in the bonding state.

#### 4.2. Diatomic molecules

CO and N<sub>2</sub> adsorbed on the late transition metals have become prototype systems regarding the general understanding of molecular adsorption. There has been a large controversy over the years as to how to describe the electronic structure and bonding in these systems. The adsorption energy is only 5–10% of the molecular dissociation energy. This has led to the plausible assumption of a weak molecule surface interaction where the chemisorption process causes only a small modification of the molecular orbital structure of the free molecule. Therefore, most models have treated the molecule as a unit and only considered the interaction of the HOMO and LUMO orbitals with the metal [110–117]. Fig. 29 shows a description of the assumed bonding mechanism where a dative bond between the 5σ and metal states of σ symmetry is formed, leading to charge donation into the metal which is compensated by a back-donation into the molecular 2π\*. In this frontier orbital picture, a synergism between the π and σ bonds is

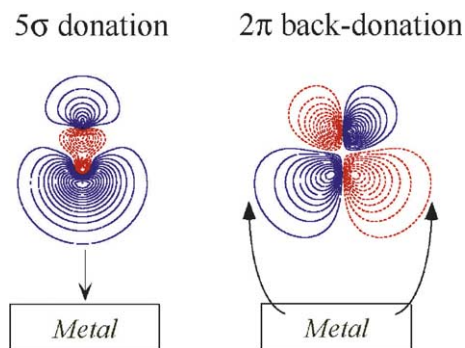


Fig. 29. Schematic picture of the frontier orbital description of CO metal bonding via 5σ donation and 2p back-donation interactions with metal electron states.

achieved, where the internal molecular bond is weakened due to the increased population of the antibonding  $2\pi^*$  in the back-donation. This simplistic model has been challenged repeatedly: substantial mixing especially between the  $\sigma$  orbitals has been proposed [118–120] and the concept of a repulsive  $\sigma$  interaction has been discussed [121–123]. We will in this section show how XES can provide atom-specific information to test if the assumptions leading to the simple picture are reasonable. What is the nature of the new electronic states formed upon adsorption and are there any changes in the remaining molecular orbitals? It will be shown below that the simple frontier orbital model is not a correct description: the  $\sigma$  donation instead leads to repulsive interaction and the description of the  $\pi^*$  back-donation needs to be modified to involve the complete set of  $\pi$  orbitals. We will demonstrate how we can build a new picture of the surface chemical bond for CO and  $N_2$  adsorbed on Ni(1 0 0) and how this can be applied to understand adsorption in different sites and co-adsorption between CO and alkali metals. Furthermore, this model is more generally applicable to many inorganic systems involving CO coordination chemistry.

#### 4.2.1. $N_2$ adsorbed on Ni(1 0 0)

The upright adsorption geometry of the  $N_2$  molecule on Ni(1 0 0) in the on-top site leads to two chemically inequivalent N atoms. If a separation between the two atoms can be made this system provides an ideal case to study how the electronic states redistribute in a homonuclear molecule upon adsorption. Furthermore, the adsorption energy is very small, around 0.4 eV [124], and we might expect that the influence of the adsorption process on the electronic structure should be minor. When chemisorbed on Ni(1 0 0) the molecular axis of  $N_2$  has been found to be perpendicular to the surface [7,125] with a Ni–N bond distance of 1.81 Å [126,127]. We showed in Section 2.5.2, that the XA spectrum for  $N_2$  on Ni(1 0 0) exhibits two 1s to  $2\pi^*$  resonances at 400.6 and 401.0 eV, corresponding to the outer and inner N atoms, respectively [53]. Hence, by using different excitation energies, site-specific XE spectra can be recorded.

The resulting XE spectra for the outer and inner N atoms are shown in the left part of Fig. 30 [8,11]. The spectra are plotted on a common binding energy scale relative to the Fermi level, obtained by subtracting the N 1s core-level photoemission binding energies of the two atoms from the emission energies. The figure is divided in an upper part, displaying states of  $\sigma$  symmetry (obtained by subtracting from the grazing emission spectra the normal emission spectra scaled by 0.5) and a lower part, displaying

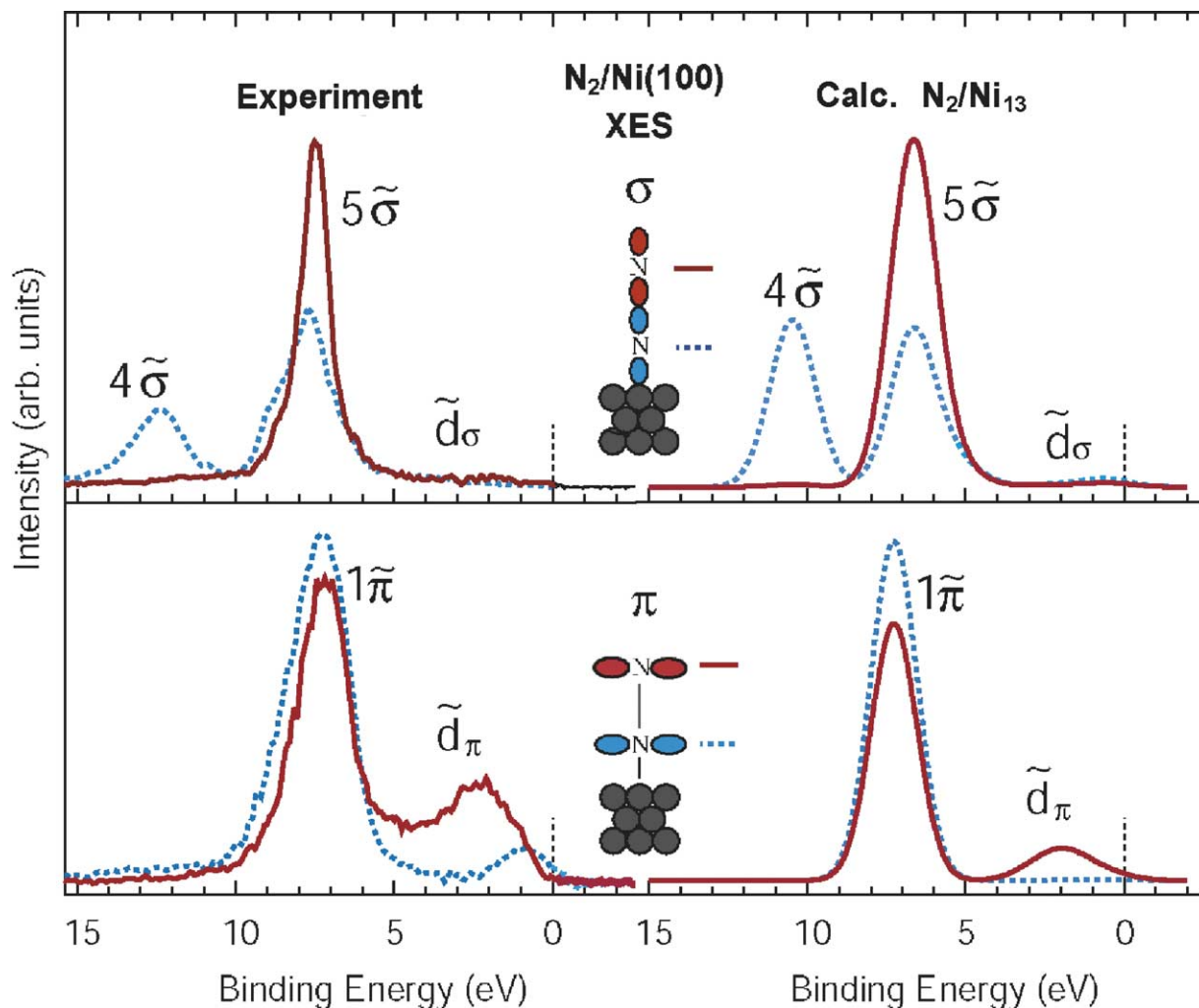


Fig. 30. Experimental and theoretical atomically resolved XE spectra for  $N_2$  adsorbed on Ni(1 0 0). The upper panel displays states of  $\sigma$  symmetry and the lower panel states of  $\pi$  symmetry.

states of  $\pi$  symmetry (the normal emission spectra). From the symmetry and binding energies of the spectral features, it is straightforward to assign all features above 5 eV binding energy in analogy with UPS measurements [10,128] (see Fig. 2). In order to facilitate the comparison with the much studied CO molecule we shall use  $C_{\infty v}$  symmetry notation for the molecular orbitals.

The novel information contained in Fig. 30 is the large difference in the states located on the inner and outer N atoms and the clearly resolved structures within 5 eV binding energy, i.e. in the Ni d band region. All spectral peaks, representing the 2p atom-projected molecular orbitals, exhibit different intensities or shapes for the inner and outer N atoms. Interesting findings are the localization of the  $4\sigma$  state to the inner N atom, with no visible spectral intensity from the outer N atom, and the larger  $5\sigma$  localization to the outer N atom. There is also a small polarization of the  $1\pi$  orbital towards the inner nitrogen atom. Near the Fermi level we find the molecular states that are important for the surface chemical bond. These states

arise from interaction of molecular  $\pi$  states, as discussed further, with the Ni d states. There is a state located on the outer N atom centered at about 2.5 eV binding energy denoted  $d\pi$ . In some sense, we can label this state as a lone pair orbital on the outer atom. Closer to the Fermi level there is also intensity on the inner nitrogen atom.

Density functional theory calculations simulating the radiative decay process using a  $\text{Ni}_{13}$  cluster have been performed in order to provide further understanding of the XE spectra, shown in the right part of Fig. 30 [101]. The polarization of the  $\sigma$  system is well reproduced by the calculations. By inspecting the calculated wave functions, we find that the 2s contribution (which is not probed in the experiment) also polarizes in the same way as the 2p contribution, but not to the same extent. Furthermore, the polarization of the  $1\pi$  orbital as well as the appearance of the  $d\pi$  state is also clearly seen in the calculations. An important question is how the  $\pi$  system can be bonding when the new substrate-induced orbital essentially is a lone pair orbital on the outer nitrogen atom.

Let us now interpret the adsorbate electronic structure by considering the orbital contour plots which have been obtained from the same calculation that led to good agreement with the experimental XE spectra. In Fig. 31, orbital plots for gas phase and adsorbed  $\text{N}_2$  for molecular orbitals of  $\pi$  symmetry are shown. In the lower panel, the gas phase  $1\pi$  and the adsorbate  $1\tilde{\pi}$  orbital are shown. As seen in the XE spectra, the  $1\pi$  polarizes upon adsorption towards the inner nitrogen atom. It also mixes with the  $d\pi$  of the interacting Ni atom. The amplitude of the  $1\tilde{\pi}$  orbital has the same phase between the Ni and two nitrogen atoms, constituting a bonding orbital between all three centers. In the middle panel of Fig. 31, orbital plots of the lone pair  $d\pi$  states are shown. The orbital is mainly of Ni 3d character with a nodal plane centered at the inner nitrogen atom. It clearly shows the outer nitrogen lone pair of this state as seen experimentally. In the top panel of Fig. 31, we show the  $2\pi^*$  and  $2\tilde{\pi}^*$  orbitals which are unoccupied and therefore cannot be observed with XES. It is to this orbital that the N 1s electron is excited when preparing the core hole state for the XES process as discussed in Section 2.5.2. It has two nodal planes between the two nitrogen atoms and the metal atom and can be denoted antibonding.

The orbital structure does not resemble a simple back-bonding picture according to Fig. 29. In order to create the new adsorbate orbitals, we need to involve the whole original  $\pi$  system of the free molecule, i.e. both the  $1\pi$  and  $2\pi^*$  orbitals. This is described as a three-orbital allylic interaction involving the formation of a totally bonding ( $1\tilde{\pi}$ ), a non-bonding ( $d\pi$ ) and a totally antibonding orbital ( $2\pi$ ) as illustrated in Fig. 32 [11,129,130]. The allylic configuration can be readily derived by first- and second-order perturbation theory [131,132]. First order corresponds to charge transfer between the  $\text{N}_2$  unit and the metal atom and second order to polarization within the  $\text{N}_2$  unit. If we only consider the Ni atom that is directly involved in the bonding, the  $\pi$  system will involve three atoms and three  $\pi$  orbitals will thus be generated. The lowest orbital will always be bonding between all three centers and the highest orbital will be antibonding. The intermediate orbital should be antibonding between the end-atoms, which for a symmetrical molecule results in no contribution on the center atom and this orbital can be denoted non-bonding. The bonding orbital is similar to the free molecule  $1\pi$  orbital, but slightly polarized on the inner nitrogen atom with a small but significant contribution from the Ni 3d orbital. Since the  $1\pi$  population is smaller compared with the free molecule we have weakened the N–N bond and instead formed a covalent Ni–N interaction. The intermediate orbital is essentially non-bonding with a main contribution from the metal.

We need to address how the  $1\pi$  and  $2\pi^*$  orbitals of the free molecules are perturbed to build up the allylic configuration. We illustrate this in Fig. 33 where a mixing of  $\text{N}_2$   $1\pi$  and  $2\pi^*$  orbitals can be viewed

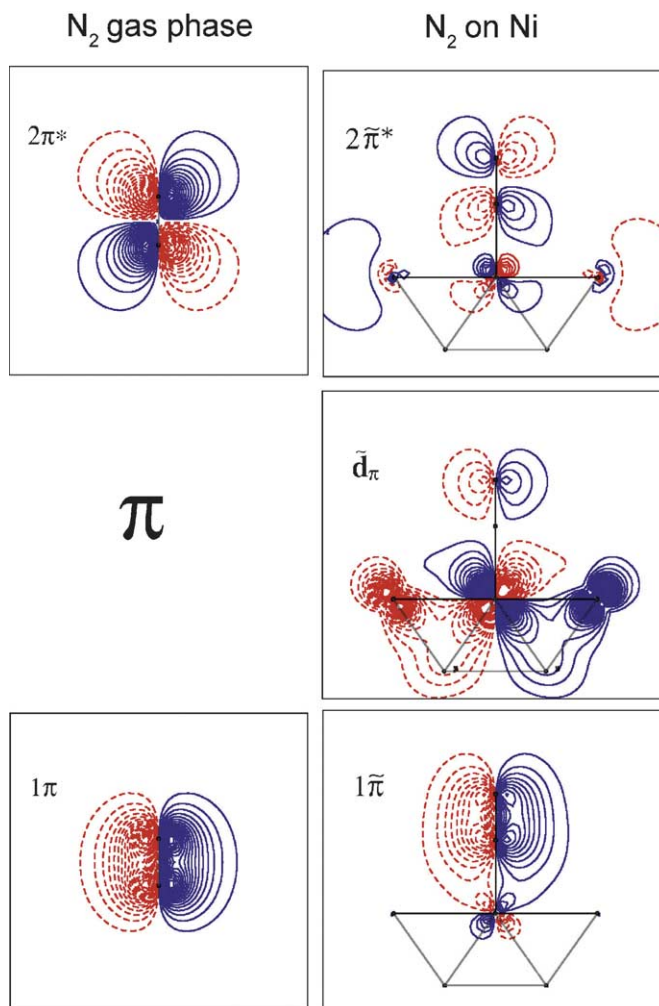


Fig. 31. Contour plots of  $\pi$  orbitals for  $\text{N}_2$  in the gas phase and adsorbed on Ni(1 0 0). Solid (blue) and dashed (red) lines indicate different phases of the wave function.

as a partial breaking of the internal  $\pi$  bond preparing the molecule for bonding to the metal. As an extreme case let us consider first the complete breaking of the internal  $\text{N}_2$   $\pi$  bond by mixing the  $1\pi$  and the  $2\pi^*$  orbitals until the original atomic orbitals at each atomic center are obtained. A positive combination of the  $1\pi$  and  $2\pi^*$  leads to an atomic orbital on the inner nitrogen atom and a negative combination to an atomic orbital on the outer nitrogen atom. In chemical terms, the breaking of the internal  $\text{N}_2$   $\pi$  bond into atomic radicals, the original atomic orbitals, allows to make additional bonds at the expense of the internal  $\text{N}_2$  bond. However, the initial bond breaking increases the total energy of the system and the energy gain through new bonds must compensate the first step for bonding to occur. Due to this energetic balance the internal  $\pi$  bond is not broken completely for the molecule, but only polarized in order to increase the bonding interaction between the  $\text{N}_2$   $\pi$  system and the metal  $d\pi$  states. The  $1\pi$  orbital is polarized towards the inner nitrogen atom, thereby making this atom more available for bonding

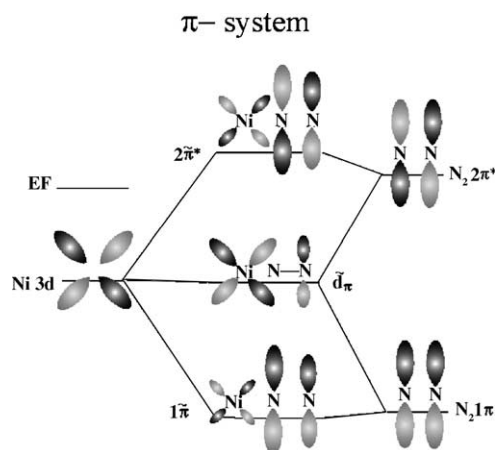


Fig. 32. Schematic illustration of the  $\pi$  orbital interactions in the  $N_2/Ni$  adsorption system in terms of the atomic N 2p and Ni 3d orbitals.

to the Ni atom and simultaneously the internal  $N_2$  bond is weakened; the outer nitrogen part of the broken  $\pi$  electron pair then forms the lone pair  $d_\pi$  orbital.

So far, we have reduced the chemisorbate electronic structure to the treatment of a triatomic model. For the real surface, the orbitals illustrated in Fig. 32 will undergo changes due to the interaction with the localized d band and the free-electron-like 4sp band, which form extended states in the metal. In Ni metal the d band dominates between 4 eV and the Fermi level. The  $d_\pi$  has largely metal character whereas both the  $1\tilde{\pi}$  and  $2\tilde{\pi}^*$  are localized on the  $N_2$  molecule and largely preserve their molecular character. We therefore concentrate on the  $d_\pi$  state as here the influence from the broad metal band is the largest. In

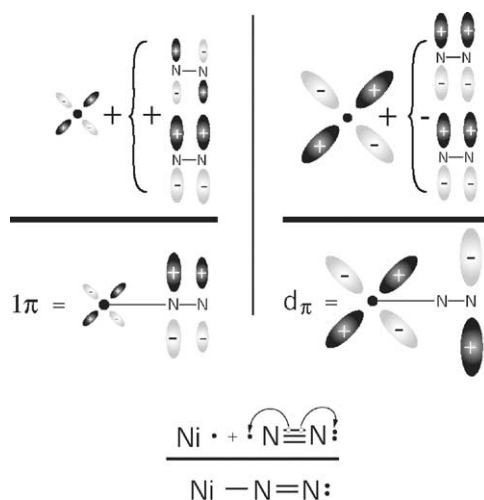


Fig. 33. The composition of the adsorbate orbitals of  $\pi$  symmetry in a perturbational treatment for  $N_2$  adsorbed on Ni. Polarization is achieved through intergroup and intragroup mixing. In terms of a valence bonding model, this can be seen as the partial breaking of the  $N_2$   $\pi$  bond, forming carbon and oxygen radicals.

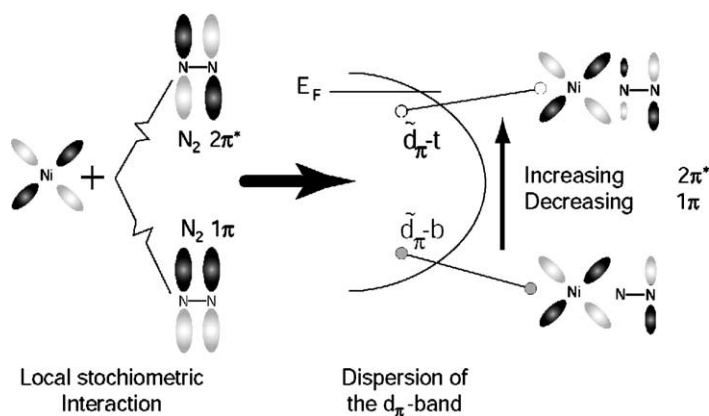


Fig. 34. The modification of the non-bonding  $d\pi$  orbital into a band due to the band character of the metal d states.  $\tilde{d}_{\pi-b}$  and  $\tilde{d}_{\pi-t}$  refer to d orbitals at the bottom and top of the d band, respectively.

Fig. 34, the variation of the  $d\pi$  state across the Ni d band is shown schematically. The  $d\pi$  state always has a nodal plane parallel to the surface. At the bottom of the band, this nodal plane coincides with the inner nitrogen atom forming the lone pair state. Going towards the top of the band this nodal plane is located more between the inner and outer nitrogen atoms. In the perturbative description, the mixing of the  $1\pi$  orbitals into the metal  $d\pi$  will change according to the variation of the relative orbital energies across the d band. Towards the top of the band the relative  $2\pi^*$  contribution increases and the  $1\pi$  contribution decreases; this affects the location of the nodal plane in the molecule. We can clearly see the signature of this effect in the inner nitrogen spectrum shown in Fig. 30 where additional intensity on the inner nitrogen atom close to the Fermi level is seen. We have more contribution of  $2\pi^*$  character at these energies. Similar effects will also be seen for all the CO adsorption systems that will later be described.

Let us now turn to the  $\sigma$  system. The important adsorbate orbitals of  $\sigma$  symmetry are depicted in Fig. 35. From the orbital plots, we observe the same polarization as the experimental and theoretical XE spectra indicate  $4\tilde{\sigma}$  to the inner atom and  $5\tilde{\sigma}$  to the outer nitrogen atom. The experimental XE spectra do not indicate any intensity in the  $4\tilde{\sigma}$  orbital on the outer nitrogen atom, however, from inspection of the orbital plot we can attribute the component on the outer nitrogen to N 2s character. It is interesting to note that the charge redistribution of the  $5\sigma$  orbital into the adsorbate  $5\tilde{\sigma}$  orbital goes in opposite direction compared with a  $\sigma$  donation picture. We also show a  $d\tilde{\sigma}$  orbital which mainly consists of metal character and can be seen in the XE spectra between the  $5\tilde{\sigma}$  state and the Fermi level.

The  $\sigma$  system can be summarized in a molecular orbital diagram, similar to the allylic configuration of the  $\pi$  system, shown in Fig. 36. However, for symmetry reasons more atomic orbitals are involved (N 2s, N 2p and Ni bands), making the situation more complicated. We can in a way picture some of the highest orbitals as the  $4\tilde{\sigma}$  and  $5\tilde{\sigma}$  with mainly adsorbate character and the  $d\tilde{\sigma}$  orbitals with mainly metal character, where we use, e.g. the  $4\tilde{\sigma}$  to indicate the  $4\sigma$ -derived orbital resulting from the interaction with the metal. The  $4\tilde{\sigma}$  and  $5\tilde{\sigma}$  are bonding orbitals with respect to the metal and will undergo a downwards shift in energy in comparison with the free molecule while the essentially metal  $d\tilde{\sigma}$  is an antibonding orbital which will therefore shift upwards in energy. In this orbital diagram all orbitals, both bonding and antibonding, are occupied which will lead to Pauli repulsion. The  $N_2$   $6\sigma^*$  orbital has been seen in XA spectra of  $N_2$  around 20 eV above the  $2\pi$  resonance [133] and to mix with this orbital is very costly. This is an essential difference as compared to the  $\pi$  system where the orbital mixing involves a low-lying

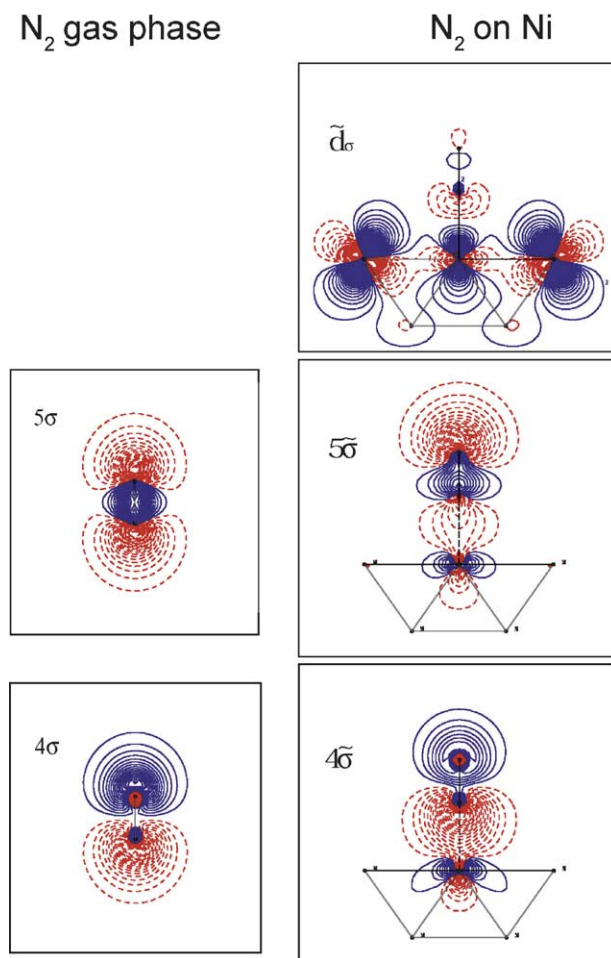


Fig. 35. Contour plots of  $\sigma$  orbitals for  $N_2$  in the gas phase and adsorbed on Ni(1 0 0). Solid (blue) and dashed (red) lines indicate different phases of the wave function.

unoccupied orbital. In order to minimize the Pauli repulsion the system will depopulate some of the  $d\tilde{\sigma}$  orbitals through a polarization of the 4sp density from the central Ni atom out towards the surrounding metal centers. However, the energy gain is not enough to overcome the Pauli repulsion including the costs for  $6\sigma^*$  orbital mixing and metal polarization. The resulting picture is a repulsive  $\sigma$  system. This interpretation is supported by calculations where the energetic gain of  $\sigma$  and  $\pi$  interactions can be separated based on a constrained space orbital variation (CSOV) theoretical method [11,43,121,122]. At a longer molecule–metal bond distance the Pauli repulsion could become smaller and the  $\sigma$  system net bonding. However, the energy gain through  $\pi$  bonding is large enough to overcome the  $\sigma$  repulsion at the equilibrium bond distance. It is interesting to note that this experimentally based picture is rather different compared with the considered  $5\sigma$  donation bonding scheme.

We can observe the signature of attractive  $\pi$  interaction and repulsive  $\sigma$  interaction from charge density difference plots. Let us first identify some fundamental aspects of covalent bonding. Fig. 37 shows a molecular orbital diagram for the  $H_2$  and  $He_2$  molecules. In the former only the bonding  $1s_g$  state

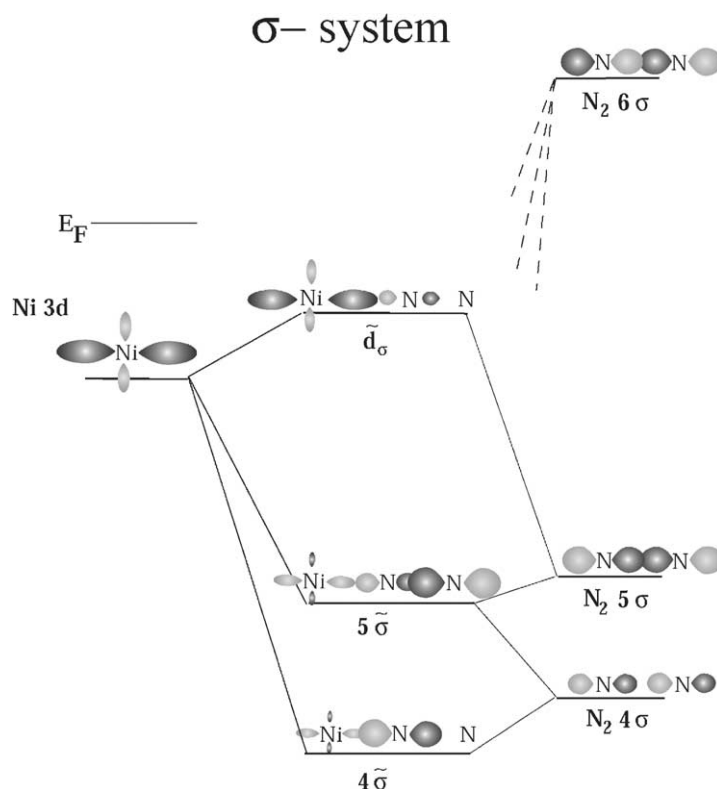


Fig. 36. Schematic illustration of the  $\sigma$  orbital interactions in the  $N_2/Ni$  adsorption system in terms of the atomic N 2p and Ni 3d orbitals.

is populated whereas in the latter molecule the antibonding  $1s_g$  orbital is also occupied. The charge density difference plots are composed of a frozen charge density of the two atoms at the correct bonding geometry minus the fully relaxed molecular system. Such a plot illustrates how charge has redistributed upon chemical bonding. We directly see a large difference between the two molecular systems [134]. In the case of  $H_2$ , there is charge building up between the two atoms forming an electron pair in the covalent bond. In  $He_2$ , there is instead a depletion of charge between the two connecting atoms due to repulsive interaction. Since both bonding and antibonding orbitals are occupied the resulting Pauli repulsion leads to a polarization of the charge away from the connection points in the charge distribution. The same thing can be seen for  $N_2$  coordinating to Ni, shown in Fig. 38. We observe loss of charge on all three atoms along the Ni–N–N axis corresponding to  $\sigma$  interaction whereas charge has been gained perpendicular to this axis. The latter is due to  $\pi$  bonding. There seems to be charge building up between the inner nitrogen and Ni atom that could mistakenly be interpreted as  $\sigma$  bonding, however, this is attributed to the  $\pi$  bond, see discussion about CO in the next section. Furthermore, if the  $\sigma$  donation picture were valid we would expect to see a decrease of charge on the inner nitrogen atom along the bonding axis and an increase in charge on the Ni atom corresponding to the  $d\sigma$  orbital. Since both lose charge we have a situation similar to the  $He_2$  case. There is a polarization of charge away from the coordinated Ni atom into the surrounding metal and a d–d rehybridization on the Ni atom to increase the  $d\pi$  character [11]. The latter could be

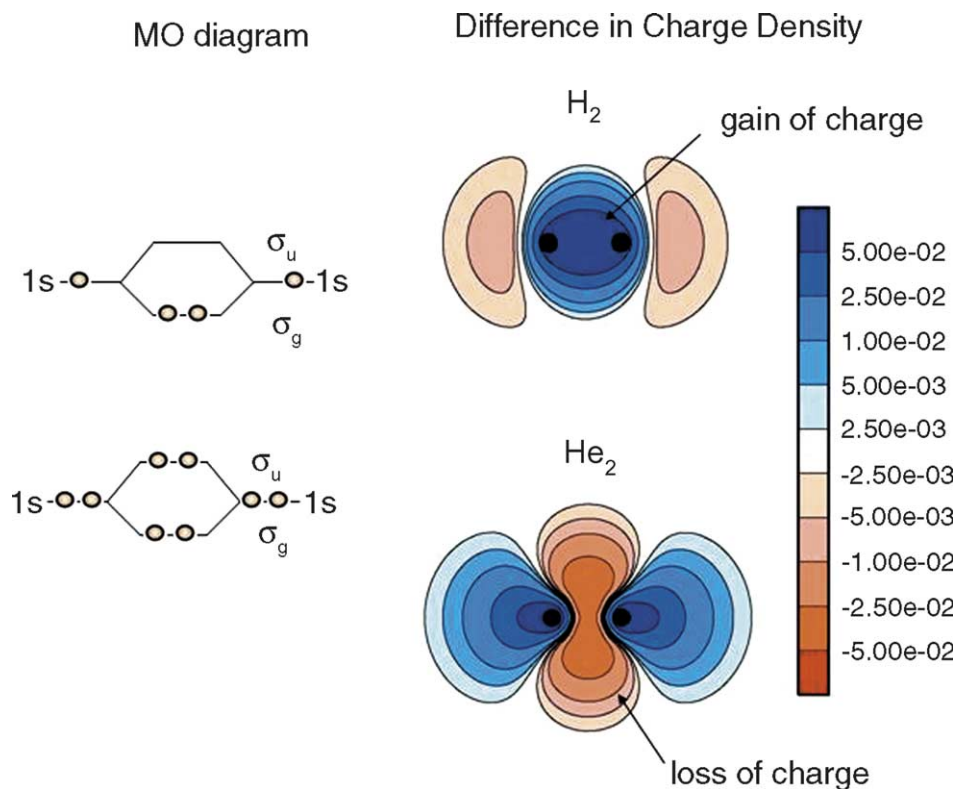


Fig. 37. Molecular orbital scheme and differences in charge density for  $H_2$  and  $He_2$  molecules.

argued to be essential for the  $\pi$  bonding and therefore there is a strong synergism. However, from a careful analysis of the energy gain of different orbital interactions there is no large difference in the strength of the  $\pi$  interaction if the  $\sigma$  interaction is taken into account or not. We can note that the increase in charge density on both nitrogen atoms implies that more  $2\pi^*$  character has become occupied

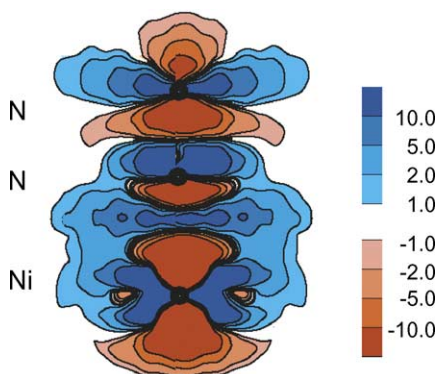


Fig. 38. Charge density difference plot of  $N_2$  adsorbed on Ni(1 0 0). Regions of electron loss are indicated with dashed outer line (red) and increase with full line. We have chosen a plane containing the interacting metal atom with one  $N_2$  molecule in the same plane.

compared to loss of  $1\pi$  character into the empty orbital space. Let us return to this issue in the discussion about CO adsorption on Ni.

From these results, we can derive a model of the surface chemical bond that is different from the traditional picture in that it involves all molecular orbitals and where the resulting binding energy is obtained from a balance between repulsion in the  $\sigma$  system and bonding based on the  $\pi$  orbitals. Instead of bonding through  $\sigma$  donation the main effect from the  $\sigma$  system is thus a repulsive interaction. The balance between attractive  $\pi$  interaction and repulsive  $\sigma$  interaction explains why the adsorption energy is weak even though the adsorbate electronic structure is the result of a complete rehybridization. Likewise, the attractive adsorbate-metal interaction in the  $\pi$  channel leads to a weakening of the internal molecular bond, which is countered by a strengthening of the internal molecular bond through the repulsive molecule–metal interaction in the  $\sigma$  channel [11].

#### 4.2.2. CO adsorbed on Ni(1 0 0)

As a next step, we compare the  $N_2$  system to the much more studied isoelectronic CO molecule adsorbed on Ni(1 0 0). Like  $N_2$ , CO adsorbs geometrically equivalent in the  $c(2 \times 2)$  overlayer structure on Ni(1 0 0), occupying on-top sites with the carbon end down [125,135] with a C–Ni distance of 1.73 Å [127,136]. However, in this case the adsorption energy of 1.2 eV [137] is much higher in comparison to that of  $N_2$ . It is therefore very interesting to see how the difference in electronegativity of the carbon and oxygen atoms influences the surface chemical bond in comparison to the isoelectronic  $N_2$ . The experimental and calculated XE spectra [43] for CO adsorbed on Ni(1 0 0) are summarized in Fig. 39. The core hole states have been prepared by excitation into the  $2\pi^*$  resonance. In Fig. 39, states of  $\sigma$  symmetry are displayed in the top panel and those of  $\pi$  symmetry at the bottom. The experimental carbon and oxygen spectra were scaled to each other using the calculated oscillator

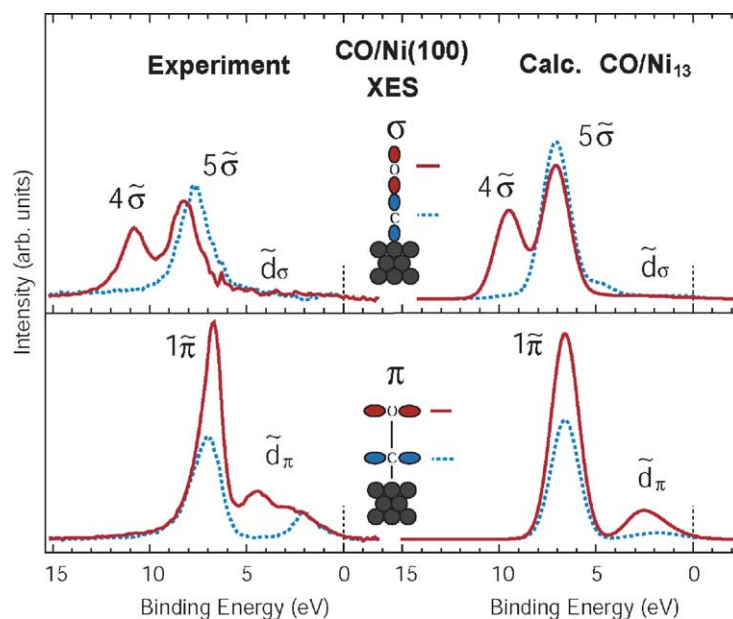


Fig. 39. Experimental and theoretical atomically resolved XE spectra for CO adsorbed on Ni(1 0 0). The upper panel displays states of  $\sigma$  symmetry and the lower panel states of  $\pi$  symmetry.

strengths for the dipole transition between the occupied  $\pi$  states and a  $1s$  core hole on the carbon respectively oxygen atoms; good agreement between experiment and calculation is found. The carbon and oxygen XE spectra share a common binding energy scale as they are related via their respective O  $1s$  and C  $1s$  XPS core-level binding energies [20,32] (see Section 2.3).

As for  $N_2$ , we treat the  $\sigma$  and  $\pi$  systems separately. The total electronic structure is then the sum of both interactions. Let us begin with the  $\pi$  system. We observe the dominant  $1\tilde{\pi}$  state in both the carbon and oxygen XES spectra. Towards lower binding energy, new states are observed, which differ in the oxygen and carbon spectra. We denote these spectral features as the  $d\pi$  band, similar to  $N_2$ . At the bottom of the  $d\pi$  band (higher binding energy), intensity is only observed in the oxygen spectrum. This state is a characteristic oxygen lone pair state of  $\pi$  symmetry at 4.5 eV binding energy. At the top of the band, close to the Fermi level, intensity is present in both the carbon and oxygen XES data, as described in connection to Fig. 34. Plots of  $\pi$  symmetry orbitals are shown in the right panel of Fig. 40 [43]. Putting the CO  $\pi$  electronic structure into the perspective of the isoelectronic  $N_2$ , we find that in principle these systems behave equivalently. This follows from the overall similarity of the XE spectra for the two adsorbates and their similar orbital character. Both systems can be described in terms of an allylic molecular orbital diagram as shown in Fig. 32. For both molecules, the  $1\pi$  forms a bonding combination to the metal  $d$  states, maximizing overlap through internal polarization. In the orbital plots in Fig. 40, we see that the  $1\tilde{\pi}$

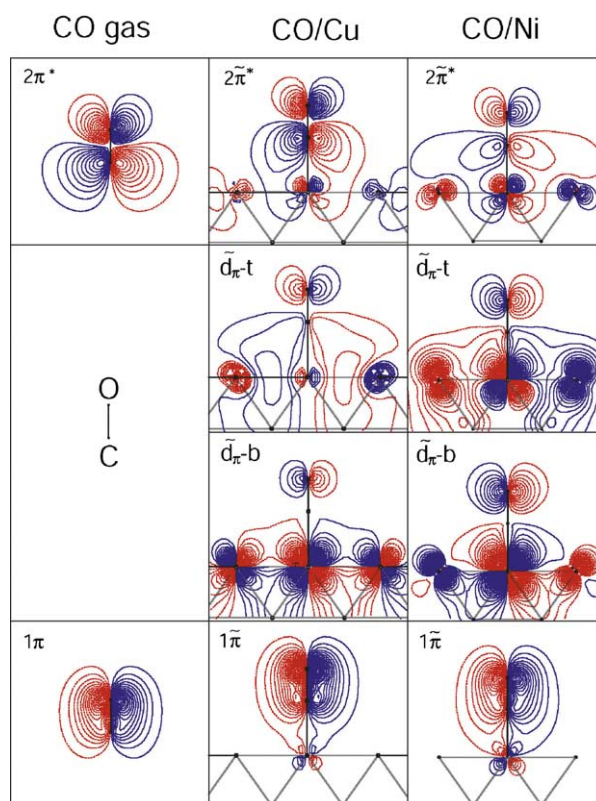


Fig. 40. Contour plots of  $\pi$  orbitals for CO in the gas phase and adsorbed on  $Ni_{13}$  and  $Cu_{26}$  clusters. Solid and dashed lines indicate different phases of the wave function.

orbital is more polarized towards carbon in comparison with the free molecule. At the same time, a characteristic lone pair state on the outer atom is formed with large Ni d character. Due to the width of the Ni d band, these states are rather broad and towards the Fermi-level contributions on both atoms can be seen in analogy with Fig. 34. We show in the orbital plots in Fig. 40 both the states at the top ( $d\pi$ -t) and bottom ( $d\pi$ -b) of the Ni d band. From an inspection of the orbitals, we note that there are small contributions from the carbon atom in the  $d\pi$  orbital close to the Fermi level. There is one significant difference compared to  $N_2$  in terms of the orbital character. In the adsorbate the  $2\tilde{\pi}^*$  level is mainly polarized towards the oxygen atom whereas it is the reverse for the free molecule. This means that the orbital rotation in the  $\pi$  orbital space has a large effect on the  $2\tilde{\pi}^*$  and significant  $1\pi$  character must thus have moved into the empty orbital space. In the case of adsorbed  $N_2$ , the  $2\tilde{\pi}^*$  level has equal contributions from both atoms indicating that there is only a minor rotation of the orbital space to make the  $1\pi$  level partially unoccupied.

In accordance with UPS [114,138], we identify the modified  $5\tilde{\sigma}$  and  $4\tilde{\sigma}$  states. In addition to these features, we find weak intensity tailing off to the Fermi-level. Similar to the  $N_2$  case a dramatic redistribution of the  $\sigma$  molecular orbitals takes place upon adsorption. This is also seen in the orbital contour plots shown in Fig. 41 [43]. The  $5\tilde{\sigma}$  orbital polarizes towards the (outer) oxygen atom and the  $4\tilde{\sigma}$  towards the (inner) carbon atom (mainly C 2s character) similar to adsorbed  $N_2$ . The relative strength of the  $4\tilde{\sigma}$  and  $5\tilde{\sigma}$  states in the oxygen XE spectrum is a measure of the degree of polarization upon adsorption. In the free CO molecule the intensity of the  $4\sigma$  is five times larger than the  $5\sigma$  (see Fig. 7). On Ni, this ratio changes dramatically and the  $4\tilde{\sigma}$  is even weaker than the  $5\tilde{\sigma}$ . This is the same trend as found for  $N_2$ . Upon adsorption the relative energy positions of the  $4\tilde{\sigma}$  and  $5\tilde{\sigma}$  orbitals also deviate from the free molecule. In the adsorbate this difference is 2.5 eV in comparison to 5.5 eV for the free molecule. It is interesting to compare this to the  $N_2$  on Ni(1 0 0) system, where the opposite trend, with an increased

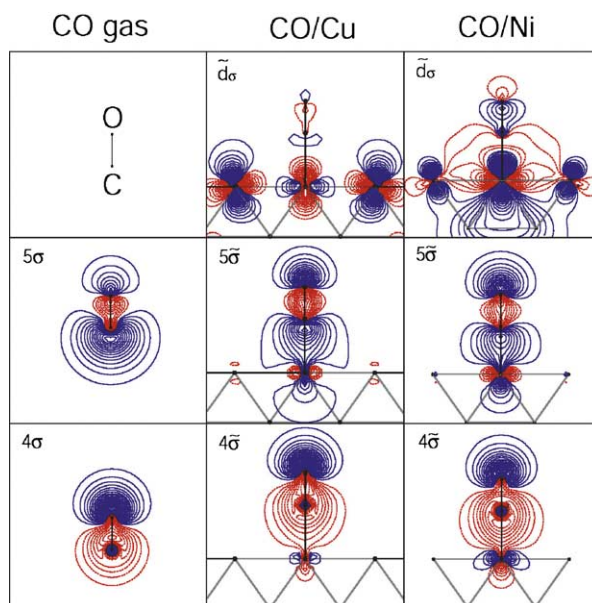


Fig. 41. Contour plots of  $\sigma$  orbitals for CO in the gas phase and adsorbed on  $Ni_{13}$  and  $Cu_{26}$  clusters. Solid and dashed lines indicate different phases of the wave function.  $\tilde{d}_{\pi}$ -b and  $\tilde{d}_{\pi}$ -t refer to d orbitals at the bottom and top of the d band, respectively.

energy splitting between the two  $\sigma$  orbitals, is observed; the  $4\tilde{\sigma}$  orbital undergoes a larger shift to higher binding energy than the  $5\tilde{\sigma}$  orbital [11]. The different behavior found for the two isoelectronic molecules can be directly related to the difference in orbital character of the  $5\tilde{\sigma}$  and  $4\tilde{\sigma}$  orbitals [43]. The  $5\sigma$  is an antibonding orbital in the free CO molecule as evidenced, e.g. by the bond contraction found upon ionization from the  $5\sigma$  level [139]. It is due to the large C 2s contribution that becomes antibonding with respect to the O 2p contribution. Upon adsorption, the polarization away from the carbon atom towards oxygen results in the orbital changing character to bonding leading to higher binding energy. The opposite occurs for the  $4\tilde{\sigma}$  orbital which is bonding for the free molecule and becomes antibonding in the adsorbate leading to a decrease in binding energy; the orbital splitting therefore becomes much smaller [43]. The  $5\sigma$  orbital in  $N_2$  is bonding and loses bonding character upon polarization since the atoms no longer give the same contribution to the orbital character leading to a shift closer to the Fermi level; the opposite is true for the antibonding  $4\sigma$  orbital. These arguments show that the internal redistribution is essential for understanding the energetic positions of the orbitals. However, the bonding character towards the metal will also shift the orbital down in energy. It is interesting to note that the shift in the  $5\sigma$  orbital to higher energies in comparison with the  $4\sigma$  orbital in the past has been interpreted as a sign of attractive  $5\sigma$  donation [110,117]. Instead the  $\sigma$  system shows a strong internal redistribution in order to minimize the adsorbate–metal repulsive interaction affecting the binding energy of the orbitals [43].

Fig. 42 shows the difference in charge density of CO adsorbed on Ni compared to CO in gas phase. The results are rather similar to what has been observed previously [117,136,140] which was interpreted in

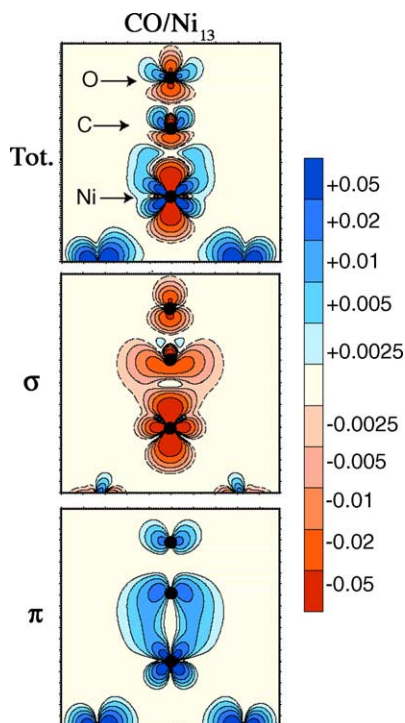


Fig. 42. Charge density difference plots of CO adsorbed on a  $Ni_{13}$  cluster. Regions of electron loss are indicated with dashed outer line (red) and increase (blue) with full line. We have chosen a plane containing the interacting metal atom with one CO molecule in the same plane.

terms of the simple frontier orbital picture in Fig. 29. The top of Fig. 42 shows the total difference in the charge density and it is very similar to N<sub>2</sub> on Ni shown in Fig. 38. There seems to be a gain of charge of  $\pi$  symmetry resembling back-bonding into the  $2\pi^*$  orbital. If we look at the  $\sigma$  interaction on the axis between the O–C–Ni centers in the charge difference plot we observe similar changes as in the case for N<sub>2</sub> on Ni. There is a loss of charge on all atomic centers and there seems to be some small gain in charge between the C and Ni atoms. It has been discussed in terms of an electron pair creation due to a suggested  $\sigma$  donation [136]. However, in the theoretical calculations it is possible to individually relax the  $\sigma$  and  $\pi$  systems, the result of which is shown in the other two pictures in Fig. 42. We observe that the entire  $\sigma$  system loses charge and the entire  $\pi$  system gains charge. The antibonding  $d\tilde{\sigma}$  orbital is depopulated as much as possible to minimize the repulsion. Since it involves both Ni 3d and Ni 4s orbitals it will also lead to a weakening in the substrate Ni–Ni bonds. The  $\pi$  interaction looks like a bonding combination between the CO  $2\pi^*$  and Ni 3d orbitals. However, investigation of the relationship between charge transfer to and polarization within the adsorbed CO unit in forming the allylic configuration reveals that the  $2\pi^*$  becomes populated by 22% while the  $1\pi$  is depopulated by 12%. The net effect is the observed 10% increase of the CO  $\pi$  population. This result highlights the importance of orbital mixing within the  $\pi$  system upon adsorption and supports the allylic configuration picture as shown in Fig. 32. In this context, it is also interesting to note that the calculated energetic separation between the  $1\pi$  and  $2\pi^*$  orbitals is comparable for CO (9.60 eV) and N<sub>2</sub> (9.55 eV). Consequently, the internal polarization results from orbital mixing of similar magnitude for the two adsorbates on the metal surface. This is seen in the relative intensities in the XE spectra from the new lone pair states of  $\pi$  symmetry and the gain in charge of  $\pi$  character in the charge difference plots, which are all rather similar. However, breaking up the internal  $\pi$  bond in homonuclear N<sub>2</sub> takes significantly more energy compared to heteronuclear CO, which could explain the large difference in adsorption energy between the two systems.

Let us address one fundamental concept that is essential to a complete understanding of CO adsorption on metal surfaces. CO adsorbs on nearly all systems with the carbon end down. This has in the past been attributed to the fact that the frontier orbitals  $5\sigma$  and  $2\pi^*$  are located on the carbon atom. However, the preference for adsorption through carbon can easily be understood based on the allylic configuration. Since the O 2p is much lower in energy compared to C 2p it is energetically much more favorable to form the lone pair state on the oxygen. Such reasoning also explains why there is O lone pair character in the non-bonding orbitals of CO<sub>2</sub> and H<sub>2</sub>CO.

In summary, the electronic structure of N<sub>2</sub> and CO adsorbed on Ni is characterized by a complete rehybridization of the adsorbate valence states in the presence of the metal surface. In the  $\pi$  system, a characteristic allylic orbital structure is found both for N<sub>2</sub> and for CO, slightly modified due to the varying electronegativity of the involved atoms. The experimentally observed  $\pi$  electronic structure is at odds with the usual frontier orbital model where only the frontier orbitals of the adsorbate molecule are modified. Often the simple picture in Fig. 29 has been denoted the Blyholder model, but this has no real connection to his original paper [141]. In that study, there is no discussion of the  $\sigma$  interaction while the  $\pi$  system is described in a three-orbital model similar to the allylic configuration. Our result confirms that it is important to consider changes in the complete molecular orbital framework. In the electronic structure of local  $\sigma$  symmetry, a full rehybridization of the participating molecular orbitals is observed. Energetically, the  $\pi$  and  $\sigma$  systems behave in opposite ways. The  $\pi$  interaction is stabilizing the adsorbate–substrate complex, whereas the  $\sigma$  interaction is destabilizing [43] in agreement with previous work by Bagus and coworkers [121,122]. The attractive  $\pi$  interaction is balanced by the repulsive  $\sigma$  interaction. This balance explains why the total adsorption energy and the molecule–metal bond is weak

even though the adsorbate electronic structure is the result of a complete rehybridization. Likewise, the attractive adsorbate metal interaction in the  $\pi$  channel leads to a weakening of the internal molecular bond, which is countered by a strengthening of the internal molecular bond through the repulsive CO–metal interaction in the  $\sigma$  channel. A thorough discussion of these mechanisms is given in references [43,55].

#### 4.2.3. CO adsorbed on Cu(1 0 0) and other metals

The adsorption of CO has been studied on a large number of different metals. It is important to understand the trends in chemical bonding and electronic structure and how they depend on the properties of the metal. It has been established that a linear relationship between the adsorption energy and the energetic position of the metal d band exists [116,142]. The adsorption energy increases for CO adsorption on transition metals going to the left in the periodic table. This trend has been interpreted in the past in terms of the energy position of the CO  $2\pi^*$  level and metal d band center in a bonding picture corresponding to Fig. 29 [116]. In the following section, we will discuss this trend based on our current understanding of the ingredients for the CO chemisorption bond formation in terms of the allylic  $\pi$  interaction and repulsive  $\sigma$  interaction. We will make a comparison between CO adsorbed on Ni and Cu where the former corresponds to an open d shell configuration ( $d^{8.4}$ ) and the latter to a situation where the d shell is more or less completely filled ( $d^{9.6}$ ). The center of the d band in Cu is lower by 2 eV in comparison with Ni and the question is how this is reflected in the electronic structure of the adsorbate.

CO forms a  $c(2 \times 2)$  overlayer also on Cu(1 0 0) with an on-top geometry similar to Ni(1 0 0) [135,143]. The adsorption energy is lower by 0.5 eV [144] in comparison with Ni(1 0 0) which is also manifested as a longer Cu–CO bond of 1.9 Å [145]. The experimental XE spectra of CO adsorbed on Ni and Cu [43] are shown in comparison with gas phase CO [37] on a common energy scale in Fig. 43. The XE spectra representing states of  $\pi$  symmetry are displayed on the left-hand side and those of  $\sigma$  symmetry on the right-hand side. The energy scale of the spectra is aligned according to the core ionization potentials in CO (see discussion in Section 2.3). Figs. 40 and 41 show contour plots of the dominant molecular orbitals as previously discussed for CO on Ni in the preceding section.

If we look at the  $\pi$  symmetry spectra in Fig. 43, we observe that there is quite a dramatic difference in the  $d\pi$  states for CO on Cu compared to Ni. First of all, there is much lower intensity in this spectral region corresponding to smaller adsorbate character of CO on Cu and a broad distribution extending from the  $1\tilde{\pi}$  and all the way to the Fermi level. There is larger intensity in the oxygen spectrum compared to that of carbon illustrating that the allylic configuration is still a reasonable description. From the orbital plots we see that the 3d involvement in the  $1\tilde{\pi}$  state is much smaller in Cu compared to Ni and that the lone pair orbital contains more  $d\pi$  metal orbital character. Also the  $2\tilde{\pi}^*$  orbital resembles more the original gas phase  $2\pi^*$  level indicating less rotation involving the  $1\pi$  orbital. Furthermore, there is also an energy shift towards the Fermi level of the  $1\tilde{\pi}$  state in adsorbed CO compared to the  $1\pi$  orbital in gas phase CO. Since there is small mixing of  $2\pi^*$  character in the  $1\tilde{\pi}$  state, as shown in Fig. 33, there is a destabilization of the orbital; the effect is larger in Ni than for Cu. All this evidence points clearly to a much smaller  $\pi$  interaction with the surface for CO on Cu. The allylic configuration is still applicable, but with much less orbital mixing: the resulting orbitals retain more of the pure CO, respectively, metal d orbital character. It is interesting to note that the orbital plots indicate that the nature of states in the  $d\pi$  state close to the Fermi level for adsorption on Cu is rather different from that on Ni. The wave function on the metal shows a clear 4p character on Cu due to the fact that the Cu d band lies at much higher binding energy and the metal states close to the Fermi level correspond to the Cu 4sp band. In this sense,

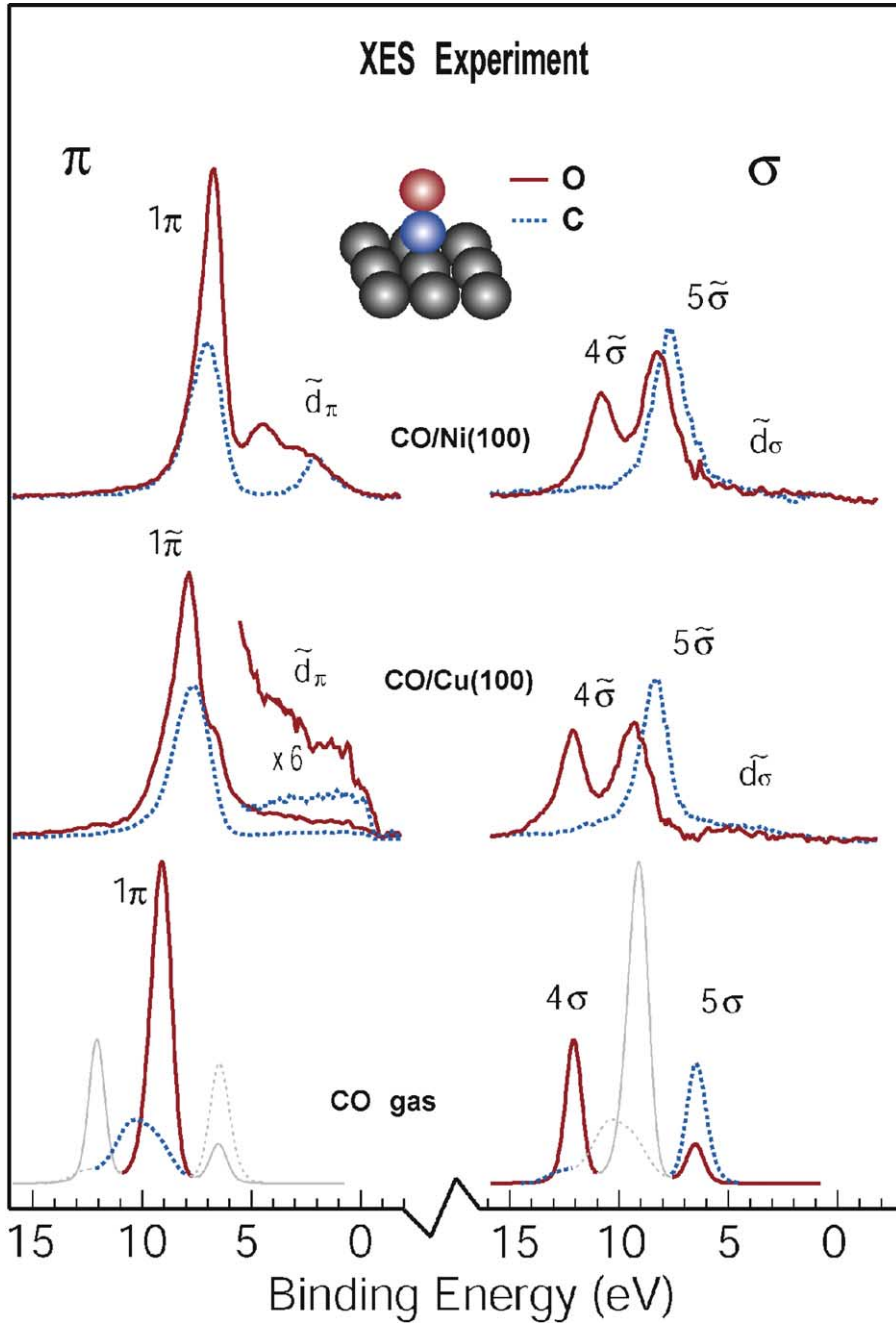


Fig. 43. Experimental XE spectra for CO gas and adsorbed on Ni(1 0 0) and Cu(1 0 0).

the width of the metal states in the  $d\pi$  band is much larger in Cu than Ni since it contains both Cu 3d and 4sp states giving rise to the broad distribution in the spectra.

In the spectra of  $\sigma$  symmetry and in the orbital plots we see a large similarity between CO on Ni and Cu. The polarization of the  $5\sigma$  orbital is slightly smaller on Cu than on Ni which is also seen in the orbital plots. There is a smaller contribution of Cu 3d in the  $5\sigma$  and  $4\sigma$  orbitals in comparison with Ni. Since the d band is further down in Cu we expect that the  $d\sigma$  orbital will be more occupied for CO on Cu leading to increased  $\sigma$  repulsion. Since both the  $\pi$  interaction is much less for CO on Cu and the  $\sigma$  repulsion larger it leads to lower adsorption energy and longer metal–carbon bond length. The longer bond will result in smaller overlap between the CO and metal orbitals as is also seen in the orbital contour plots.

Fig. 44 shows the difference in charge density for CO on Cu at two different molecule–metal distances, 1.75 and 1.95 Å [146]. These two distances correspond to the adsorbate bond-lengths in CO on Ni and Cu, respectively. First of all, we note that the interaction is rather similar at both distances, only with stronger changes for the short bond distance. It means that no new channel in bond interactions opens at the CO on Ni distance. We note essentially a rather similar change in the electron density as for CO on Ni with one exception. There is no increase in d population of  $\pi$  symmetry on the Cu atom as seen in the case of Ni. This can be understood based on that Cu has a full d band and cannot accept any additional charge.

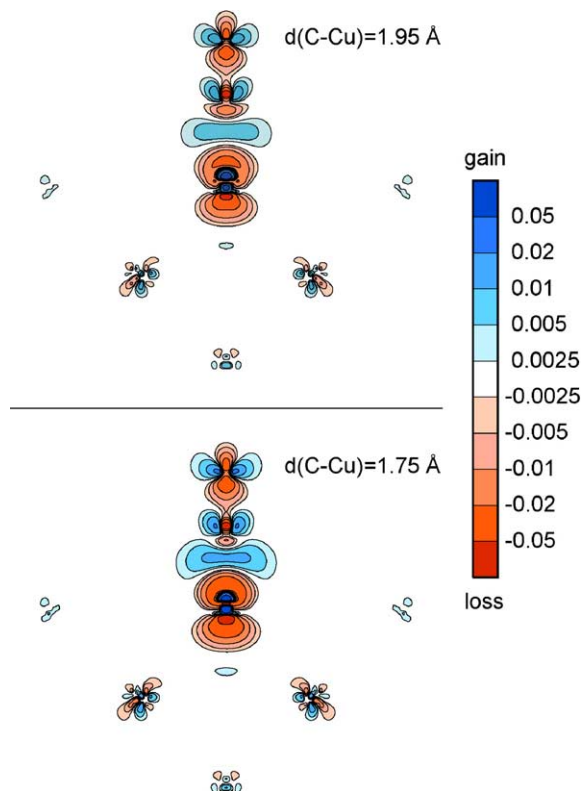


Fig. 44. Charge density difference plot of CO adsorbed on a Cu<sub>26</sub> cluster for two different CO–Cu distances, 2.95 and 2.75 Å. Regions of electron loss are indicated with dashed outer line (red) and increase (blue) with full line. We have chosen a plane containing the interacting metal atom with one CO molecule in the same plane.

The gain in charge between the C and Cu atoms is related to the  $\pi$  interaction and not the  $\sigma$  donation which is repulsive (see discussion in the previous section).

Let us now address the relationship between the energetic position of the center of the d band in different transition and noble metals and the CO adsorption bond strength [116,142]. From the allylic model of the  $\pi$  electronic structure, it is expected that variation of the d band position changes the relative weights of the CO  $1\pi$ ,  $2\pi^*$  and metal d and p orbitals in the adsorbate  $1\tilde{\pi}$ ,  $2\tilde{\pi}^*$  and  $d\pi$  hybrid orbitals. The energetically most favorable situation is where the d band is centered between the CO  $1\pi$  and  $2\pi^*$  levels since this would allow for the most favorable mixing of all three orbitals. However, it is important to consider that there is twice as much  $2\pi^*$  character in the occupied orbitals than there is  $1\pi$  character in the unoccupied orbitals for CO on Ni. This indicates that the d center should be shifted more towards the  $2\pi^*$  level for maximum  $\pi$  interaction. As the CO gas phase  $1\pi$  and  $2\pi^*$  orbitals are fixed in energy separation, the adsorption energetics for different metals can be parameterized according to the energy distance between the 3d band and the  $2\pi^*$  level only, simultaneously determining the energetic distance between the 3d band and the  $1\pi$ . The  $\sigma$  repulsion will also depend on the d band center. When the d band becomes less filled the  $d\tilde{\sigma}$  orbital will reside more above the Fermi level, resulting in a smaller Pauli repulsion. It could be that at the beginning of the transition metal series the  $\sigma$  interaction becomes attractive. In this sense, both the  $\pi$  and  $\sigma$  interactions contribute to the adsorption energy in such a manner that the CO bond strength increases when the d band center shifts towards the Fermi level.

#### 4.2.4. Adsorption site dependent electronic structure of CO

The interplay between the electronic and geometric structures of adsorbates is of fundamental importance for the understanding of many surface phenomena. Molecular CO is known for its ability to populate different adsorption sites, depending on the metal, substrate structure, coverage, temperature and influence from co-adsorbate species. These often coexisting phases indicate only small energetic differences for different sites, which has been interpreted as indicative of rather similar bonding. The nature of CO bonding in different sites has been studied using the CO–H co-adsorption system on Ni, where CO can be populated in on-top, bridge and hollow sites [138,147]. Selective excitations at chemically shifted  $\pi$  resonances [54] have been used to separately probe the adsorbate in a specific site for mixed overlayers [55,148].

Fig. 45 shows C and O K emission spectra of CO in different sites together with spectral calculations [55]. On the left side, spectra of  $\pi$  symmetry are displayed and on the right side spectra of  $\sigma$  symmetry. All spectral features with a binding energy above 5 eV can be readily assigned in accordance to previous photoemission measurements [138]. The theoretical spectra show good agreement with experiment. From these calculations, orbital contour plots of the most interesting valence orbitals in CO gas and adsorbed on a  $\text{Ni}_{13}$  cluster in on-top and hollow sites were also generated. The plots are shown in Figs. 46 and 47 for  $\pi$  and  $\sigma$  symmetry, respectively.

We note similar qualitative changes in the electronic structure upon adsorption for CO in bridge and hollow sites as observed in the previous case of the on-top site. The  $5\sigma$  orbital polarizes towards the (outer) oxygen atom and the  $4\sigma$  towards the (inner) carbon atom (mainly C 2s character). The relative strength of the  $4\sigma$  and  $5\sigma$  states in the oxygen XE spectra is a measure of the degree of polarization upon adsorption. In the free CO molecule, the intensity of the  $4\sigma$  in the oxygen spectrum is five times larger than that of the  $5\sigma$ . On Ni, this ratio changes dramatically and the  $4\tilde{\sigma}$  is even weaker than the  $5\tilde{\sigma}$  orbital. The degree of polarization increases with increasing Ni coordination. In the  $\pi$  system, we observe the

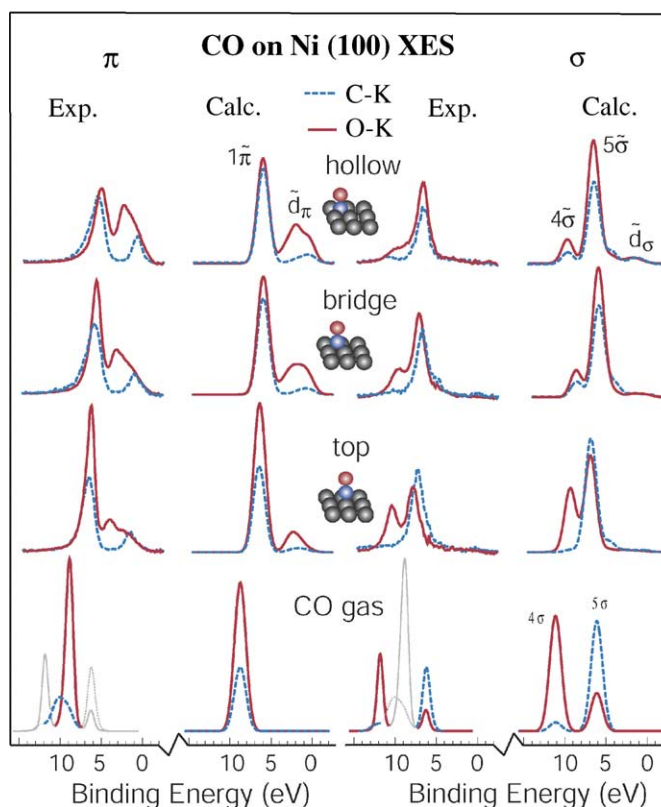


Fig. 45. Experimental and theoretical XE spectra for CO gas and adsorbed on Ni(100) in on-top, bridge and hollow sites.

dominant  $1\tilde{\pi}$  state in both the carbon and oxygen XE spectra. Towards lower binding energy the  $d\tilde{\pi}$  band state can be observed with a dominant oxygen lone pair character. Both the amount of  $1\tilde{\pi}$  polarization and adsorbate character in the lone pair state increases with increasing Ni coordination. We observe that the  $1\tilde{\pi}$  orbital for CO in the hollow site has the same contribution on both atoms which is rather different compared with the free molecule. We can also see a dramatic polarization of the  $2\tilde{\pi}^*$  towards the oxygen atom for CO in the hollow site indicating a major mixing with the  $1\pi$  orbital.

Both the  $\pi$  bonding and the  $\sigma$  repulsion increase with increasing Ni coordination such that the resulting adsorption energy is rather similar for on-top and bridge sites and slightly less favorable for hollow sites. The gain in  $\pi$  bonding with increased Ni coordination is thus lost due to the increased  $\sigma$  repulsion. The energetics of the two symmetry channels partly compensates each other. However, the interaction is very different between the sites causing a dramatic change in the electronic structure which increases with increasing Ni coordination. Based on these findings we can understand the change in vibrational frequencies and the different reactivity of CO in the different adsorption sites [55]. In adsorption systems where the  $\pi$  interaction is weaker, such as CO on Cu and  $N_2$  on Ni the  $\sigma$  repulsion will dominate at higher coordination, leading to population of only on-top sites. We anticipate that for NO with one additional electron the  $\pi$  interaction will increase while the  $\sigma$  interaction remains quite similar to that of CO leading to a larger probability for adsorption in sites with higher coordination.

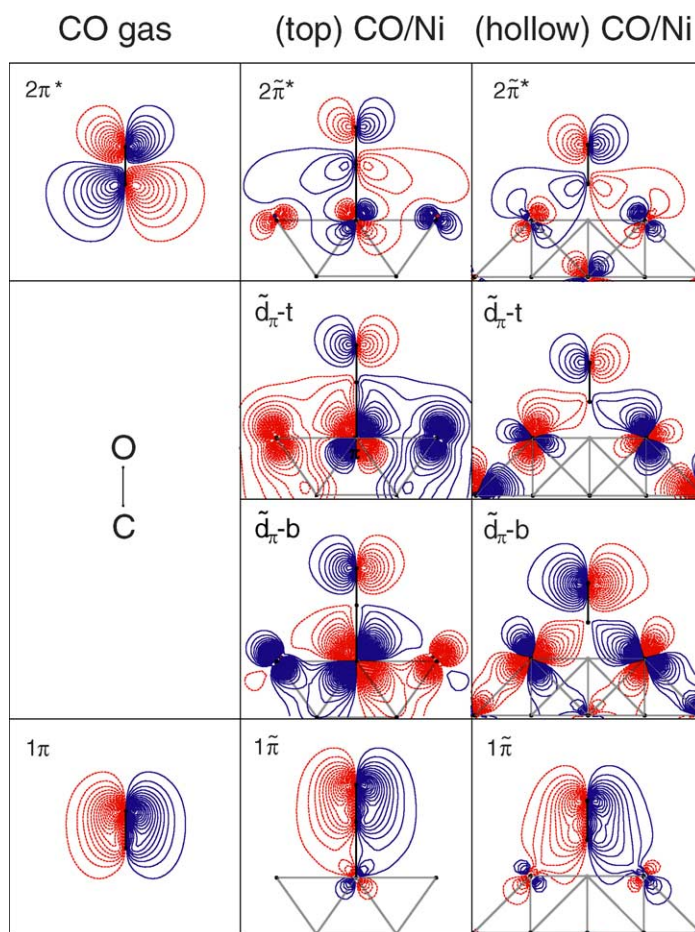


Fig. 46. Contour plots of  $\pi$  orbitals for CO in the gas phase and adsorbed on Ni(1 0 0) on on-top and hollow sites. Solid and dashed lines indicate different phases of the wave function.  $\tilde{d}_{\pi-b}$  and  $\tilde{d}_{\pi-t}$  refer to d orbitals at the bottom and top of the d band, respectively.

#### 4.2.5. Co-adsorption of CO and K on Ni(1 0 0)

The promotor action of alkali metals in heterogeneous catalysis has been an intriguing issue for a long time for which the co-adsorption of CO and K on single crystal surfaces has become the prototype system [149,150]. There are three important changes in the chemisorption properties of CO on metal surfaces due to the presence of K: the heat of adsorption of CO increases, the internal C–O bond is weakened and the adsorption site shifts to maximum substrate coordination. The extra stabilization of the co-adsorbate overlayer has been related to the formation of an essentially ionic  $K^+-CO^-$  lattice [149,151,152]. The extra charge on the CO molecule has been attributed to an increased population of the CO  $2\pi^*$  [51,153,154] which furthermore weakens the intramolecular C–O bond.

In the saturated co-adsorbed phase of CO and K on Ni(1 0 0) a  $c(2 \times 2)$  overlayer is formed. The XPS spectra show C 1s and O 1s binding energies similar to CO adsorbed in the hollow site [138]. This finding is in general agreement with other observations that CO tends to occupy high coordination (hollow) adsorption sites on alkali-promoted transition metal surfaces; among the studied substrates are

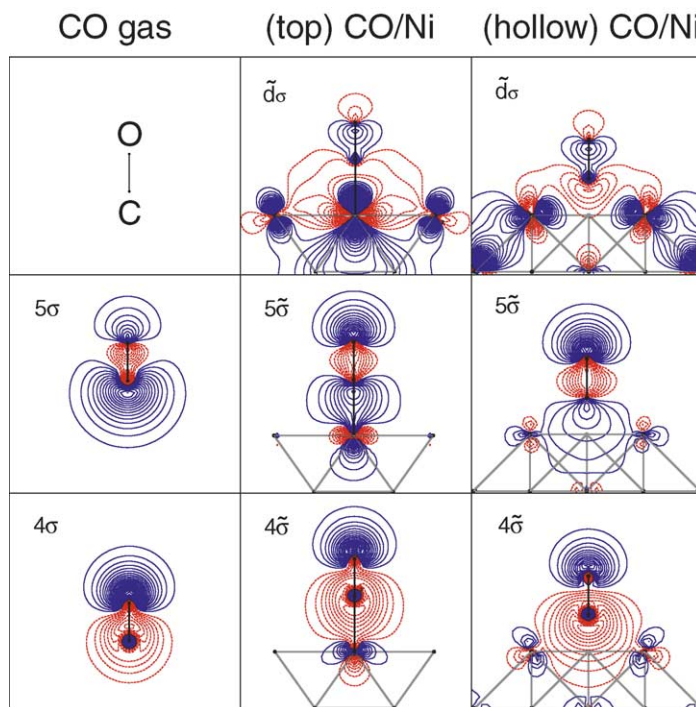


Fig. 47. Contour plots of  $\sigma$  orbitals for CO in the gas phase and adsorbed on Ni(1 0 0) in on-top and hollow sites. Solid and dashed lines indicate different phases of the wave function.

Ru(0 0 0 1) [155,156], Pt(1 1 1) [157,158], Ni(1 1 1) [159], and Rh(1 1 1) [160]. This indicates that the balance between  $\pi$  bonding and  $\sigma$  repulsion changes when K is present. Note that this interplay is also related to the intramolecular CO bond, i.e. an increased repulsive  $\sigma$  interaction between the adsorbate and the substrate gives rise to a somewhat strengthened CO bond [43]. Recently, DFT calculations have shown that the K atom lies 0.14 Å above the level of the neighboring O atoms in CO co-adsorbed with K on Co(1 0 1 1) [161]. The lack of direct bonding between K and the metal surface indicates a strong interaction between the CO and K atoms in the first layer, covalent or ionic. It was observed recently that the K 2p XA spectrum for CO and K co-adsorbed on Ni(1 0 0) exhibits crystal-field splitting demonstrating a large degree of ionic interaction between CO and K [152].

The spectra for the CO/K/Ni(1 0 0) system are presented in the bottom panel of Fig. 48 [162]. In the upper part of Fig. 48, we also show XE spectra of CO on Ni(1 0 0) in hollow sites on hydrogen precovered Ni(1 0 0), discussed in the previous section. Starting with the  $1\tilde{\pi}$  system a strong interaction is observed, similar to hollow site CO. A closer inspection of the  $d\pi$  distribution for the two hollow adsorption systems indicates a somewhat stronger  $\pi$  interaction for the alkali system. By applying a curve-fitting procedure to the oxygen spectra, a similar ratio between the integrated  $d\pi$  and the  $1\pi$  features is obtained. The main spectral difference is instead found in the carbon spectrum at the upper part of the  $d\pi$  band, which is significantly more intense for the alkali-modified system. As evident from Fig. 34, larger  $2\pi^*$  character in the  $d\pi$  states gives rise to electronic states with an increased amplitude on the carbon atom, as compared to the oxygen atom. This can be viewed as an upward shift of the Fermi level with respect to the  $d\pi$  band seen in Fig. 34 and increased population of  $2\pi^*$  character. The  $1\tilde{\pi}$  state shifts to higher binding

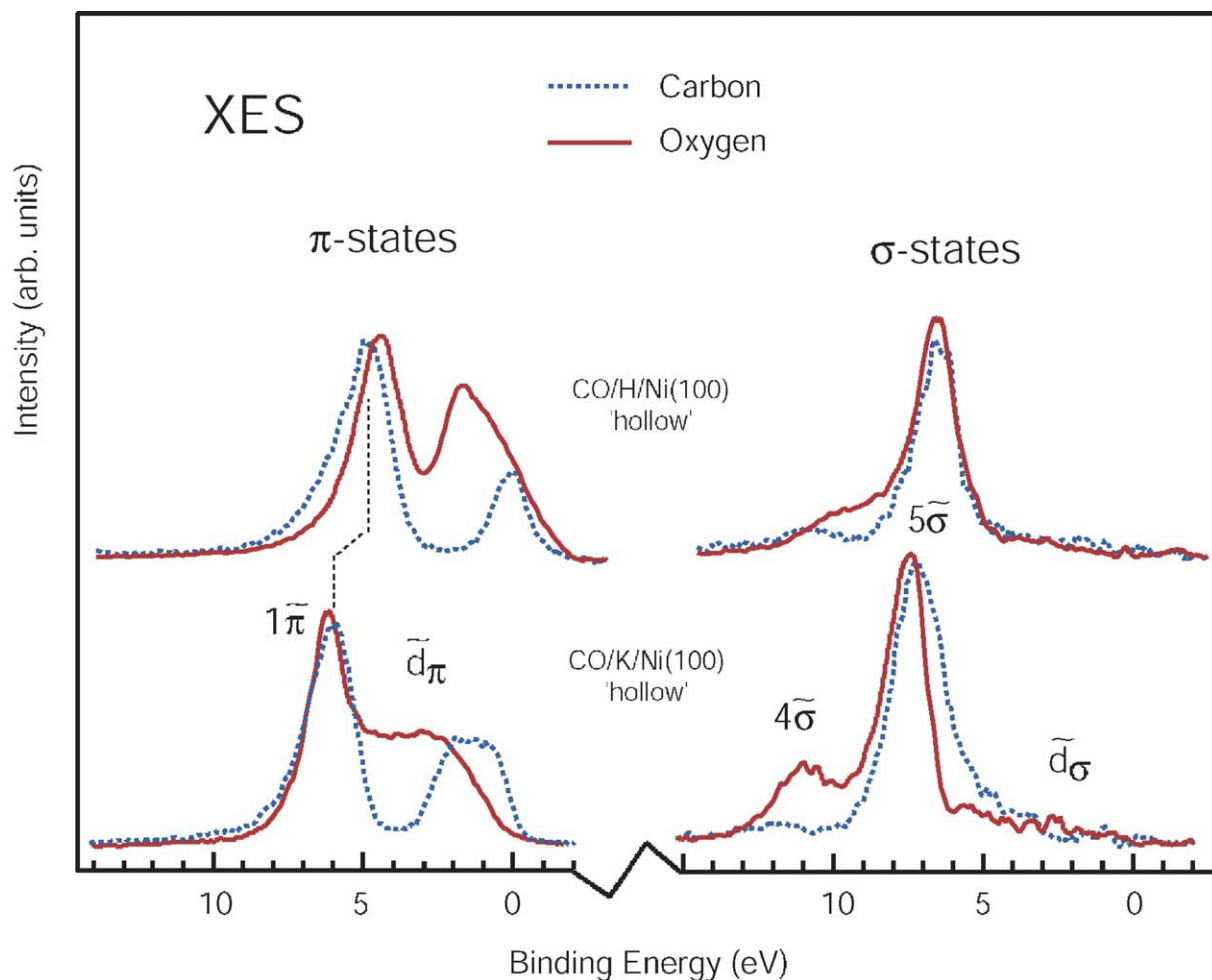


Fig. 48. Experimental XE spectra for CO adsorbed on Ni(1 0 0) in hollow sites co-adsorbed with hydrogen and potassium.

energy by 1 eV, compared with hollow site CO on the hydrogen co-adsorbed system, supporting the energy shift of the Fermi level. This clearly fits into the picture of a negatively charged CO through increased  $2\pi$  population.

Turning to the  $\sigma$  system, the amount of  $\sigma$  polarization for the alkali system appears smaller than for the other hollow phase; in the oxygen spectrum a more distinct  $4\tilde{\sigma}$  feature is found. The degree of internal polarization is somewhere in between the case of CO adsorption in bridge site on Ni(1 0 0), and in hollow sites on hydrogen modified Ni(1 0 0) (see Fig. 45). Thus, in terms of the bonding properties, these findings indicate that the presence of alkali decreases the repulsive interaction of the  $\sigma$  system, leading to a shorter adsorbate distance, in agreement with previous work on Ni(1 1 1) [159].

The driving force for the reduced  $\sigma$  repulsion upon co-adsorption of alkali can be understood by considering the interplay between the electrostatic properties of the CO–alkali overlayer and the local covalent interaction. For the  $c(2 \times 2)$ CO/K/Ni(1 0 0) system, the formation of an essentially ionic  $K^+CO^-$  lattice has been established [151,152,163], seen also in the downward shift of the  $\pi$  system. This

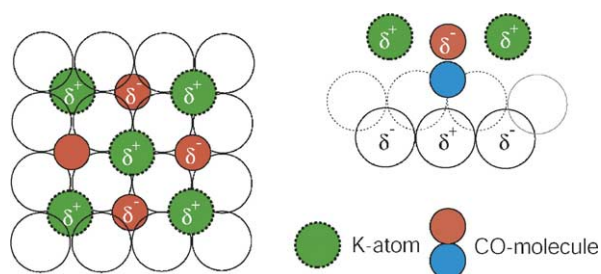


Fig. 49. Top (left) and side (right) view of the image charge lattice formed for the  $c(2 \times 2)$  CO/K/Ni(1 0 0) system.

gives rise to an image charge plane in the substrate of opposite sign (see Fig. 49). Locally, the Ni atom directly coordinated to the CO unit is depleted of charge whereas the CO unit carries additional charge. The charge depletion in the metal can be related to a decreased metal 4sp density. This means that the local  $\sigma$  repulsion between the CO  $\sigma$  system and the metal states is reduced, altering the energetic balance of  $\pi$  attraction and  $\sigma$  repulsion such that adsorption in higher coordinated sites becomes favored. Consequently, the CO metal distance decreases leading to an increased spatial overlap between the respective states and to a stronger, attractive  $\pi$  interaction.

The co-adsorption of alkali induces fairly large shifts of the intramolecular CO stretch frequency, indicative of an increased C–O distance [6,149,153]. It is thus appropriate to correlate our present findings to the character of the intramolecular C–O bond. In this context, we must consider two different possible contributions. The change from on-top adsorption to higher-coordinated adsorption site lowers the CO stretch frequency by about 50 meV [147]. In addition, based on investigation of CO on Ni(1 1 1), where CO does not change adsorption sites upon alkali co-adsorption, a reduction of 30–50 meV has been reported depending on the CO coverage [164]. As manifest above for the two hollow phases, the  $\pi$  interaction is stronger for the alkali-modified system. This strengthens the Ni–C bond at the expense of a weaker internal carbon–oxygen bond. However, the reduced  $\sigma$  repulsion observed upon alkali co-adsorption also results in a smaller contribution to the  $\sigma$  bond strength from the  $5\sigma$  polarization. That is, since the  $5\sigma$  orbital is slightly anti-bonding [139], the substrate-induced polarization in the  $\sigma$  system reduces the anti-bonding character and increases the C–O bond strength; a less repulsive adsorbate–substrate  $\sigma$  interaction thus gives rise to a decreased C–O  $\sigma$  bond stabilization. We thus conclude that co-adsorption of alkali atoms shifts the balance between the attractive  $\pi$  interactions and the repulsive  $\sigma$  interactions, which induces a significant elongation (weakening) of the intramolecular bond.

#### 4.2.6. Metal carbonyls and CO coordination to the heme group

We have in the previous sections discussed in detail the electronic structure and bonding mechanism in adsorbed CO on metal surfaces based on the information obtained from XES and DFT. It is now essential to raise the question whether this bonding mechanism is applicable to CO in general in inorganic chemistry and to metal carbonyls and CO coordination to the heme group in particular. We address this issue in the context of spectrum calculations.

Fig. 50 shows XE spectra for CO in a number of different bonding configurations, on Ni<sub>13</sub>, Ni(CO)<sub>4</sub>, Fe(CO)<sub>5</sub>, Cr(CO)<sub>6</sub> and coordinated to the heme group [165]. If we inspect the spectra of  $\pi$  symmetry, we observe changes similar to those for adsorbed CO. The  $1\tilde{\pi}$  orbital is slightly more polarized to the carbon atom compared with the  $1\pi$  orbital in free CO and the appearance of the  $d\pi$  lone pair orbital on the oxygen atom is confirmed. The latter has a larger amount of carbon character on Cr(CO)<sub>6</sub> compared to the

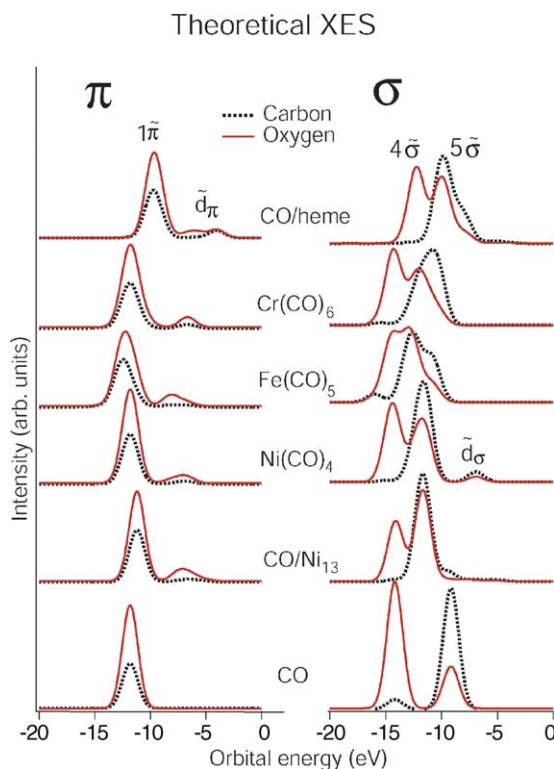


Fig. 50. Theoretical XE spectra for CO in the gas phase adsorbed on Ni<sub>13</sub> in on top site, in different metal carbonyls and coordinated to the heme group.

other carbonyls. These observations indicate that also in these cases the  $\pi$  system can be described in terms of an allylic configuration as shown in Fig. 51 for Fe(CO)<sub>5</sub>. In this case, the C<sub>3v</sub> symmetry orbitals are delocalized over the carbonyl complex. We can clearly identify the  $1\tilde{\pi}$ ,  $d\tilde{\pi}$  and  $2\tilde{\pi}^*$  orbitals. The increase of carbon character in Cr(CO)<sub>6</sub> in the  $d\tilde{\pi}$  orbital in comparison to Ni(CO)<sub>4</sub> is related to the higher energy of the d states in Cr compared to Ni involving more  $2\tilde{\pi}^*$  in the lone pair orbital (see discussion in connection to Fig. 34). It is interesting to note that the  $d\tilde{\pi}$  band in CO coordinated to the heme group is rather similar to that of CO adsorbed on metals. The width is much larger compared to the carbonyls and the carbon character is higher at the upper part of the band. The band formation comes from the interaction of the Fe 3d with the surrounding porphyrin skeleton and the histidine residue [165].

In the spectra from the  $\sigma$  orbitals in Fig. 50, we see that the  $4\tilde{\sigma}$  and  $5\tilde{\sigma}$  states seem to be split into several components. We attribute this to the fact that there is no clear separation of  $4\sigma$  and  $5\sigma$  orbitals but instead a number of orbitals form based on the overall symmetry of the whole molecule. The relative intensity of the carbon and oxygen contributions is different in the different orbitals. We can make a connection to adsorbed CO where the  $\sigma$  bands could have different contributions of carbon and oxygen character at different points in the Brillouin zone (see Section 2.3). If we compare CO adsorbed on Ni to Ni(CO)<sub>4</sub> there is quite a difference in how the  $\sigma$  orbitals have changed as compared to the free molecule. The smaller redistribution of the  $\sigma$  orbitals in Ni(CO)<sub>4</sub> is related to the fact that four CO molecules interact with a single Ni atom whereas for CO adsorbed on Ni there is only one molecule per metal atom

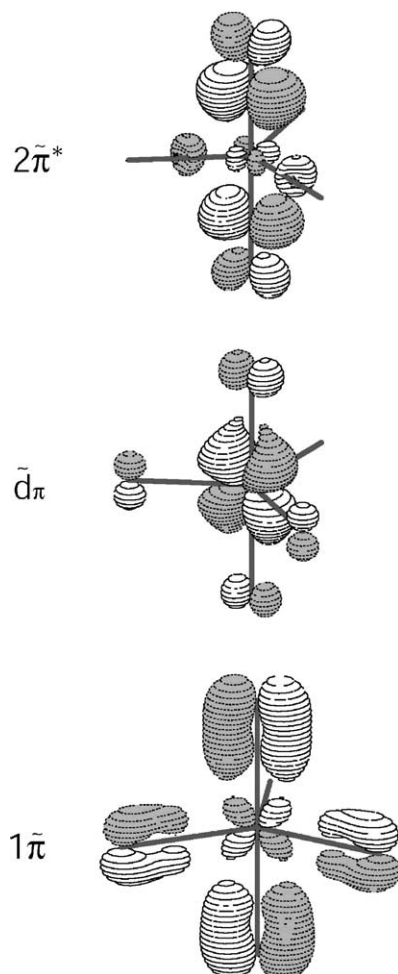


Fig. 51. The  $\pi$  allylic molecular orbital configuration in  $\text{Fe}(\text{CO})_5$ .

causing a stronger  $\sigma$  interaction. Overall, we conclude that the bonding mechanism previously discussed for adsorbed CO also holds for CO coordinated to inorganic compounds.

#### 4.3. Unsaturated hydrocarbons

In the previous sections, we have described how we can obtain atom-specific and polarization-selective electronic structure information from XE spectra of diatomic molecules. However, for specific systems more information can be extracted. For molecular adsorbate systems with equivalent atoms we can generate core holes of different symmetries, providing an additional symmetry-specific selection of the final states. This has been extremely useful in order to distinguish the character of new adsorbate states in simple unsaturated hydrocarbons such as ethylene and benzene [34,35,166]. The description of bonding in these systems was originally developed by Dewar, Chatt and Duncanson (DCD model) based on a frontier orbital concept [167,168]. The interaction has been viewed in terms of a donation of charge

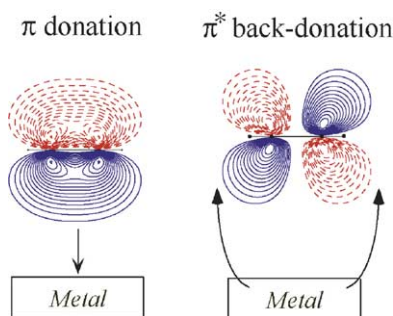


Fig. 52. Schematic picture of the frontier orbital description of ethylene metal bonding via  $\pi$  donation and  $\pi^*$  back-donation interactions with metal electron states.

from the highest occupied  $\pi$  orbital into the metal and a subsequent back-donation from filled metal states into the lowest unoccupied  $\pi^*$  orbital (see Fig. 52). If we can experimentally identify and quantify the involvement of the different  $\pi$  orbitals involved in the interaction with the surface, we can test this model. In the following section, we will describe how we can use the symmetry selection rules in the case of chemisorbed molecules when the molecules have equivalent atoms. The DCD model will be shown to describe the chemical bonding of ethylene on Cu and Ni surfaces very well. Furthermore, the differences in bonding of benzene to Cu and Ni will be discussed.

#### 4.3.1. Symmetry selection rules for ethylene and benzene adsorption on Cu(1 1 0)

As described in Section 2.5.3, it has been shown that XE spectra of free molecules with high symmetry show a strong variation with the excitation energy [60]. The selective excitation of a core-excited intermediate state of a particular symmetry, yields emission spectra reflecting this property. For molecules with an inversion symmetry this has been denoted the parity selection rule, which can provide distinction of states of either *gerade* or *ungerade* symmetry [24,59,60]. In the following, we will apply this to analyze the DCD model for two cases: ethylene and benzene adsorbing on copper and nickel. We will use the symmetry selection in RIXS to identify orbitals involved in the surface chemical bond and use computed XE oscillator strengths to convert the spectral intensities to atomic 2p populations. We will begin by describing the properties of the chemisorbed molecules.

Both ethylene and benzene are molecules with inversion symmetry and should thus follow the parity selection rule. Upon adsorption on the Cu(1 1 0) surface, the symmetry is reduced to  $C_{2v}$  due to the coordination to the metal. The carbon atoms are still equivalent, or nearly so in the case of benzene, but the electronic states are not labeled according to *gerade* or *ungerade* symmetry. However, since the symmetry-breaking interaction with the substrate is not too strong we will still denote the molecular orbitals using the gas phase symmetry labels in order to relate more easily to the electronic structure of the free molecule.

The Cu(1 1 0) surface has two-fold symmetry with Cu rows in the first atomic layer. We can thus project the electronic structure in three different directions if there is an alignment of the molecule on the surface. Fig. 53 shows XA spectra for ethylene adsorbed on Cu(1 1 0) where the  $E$ -vector has been oriented in the three high symmetry directions: out-of-plane ( $[110]$ ), in-plane parallel with the surface Cu atomic rows ( $[1\bar{1}0]$ ) and in-plane perpendicular to the Cu rows ( $[001]$ ) [166]. We identify the strong  $\pi^*$  resonance at 284.8 eV only in the out-of-plane spectrum directly showing that the molecule is lying with

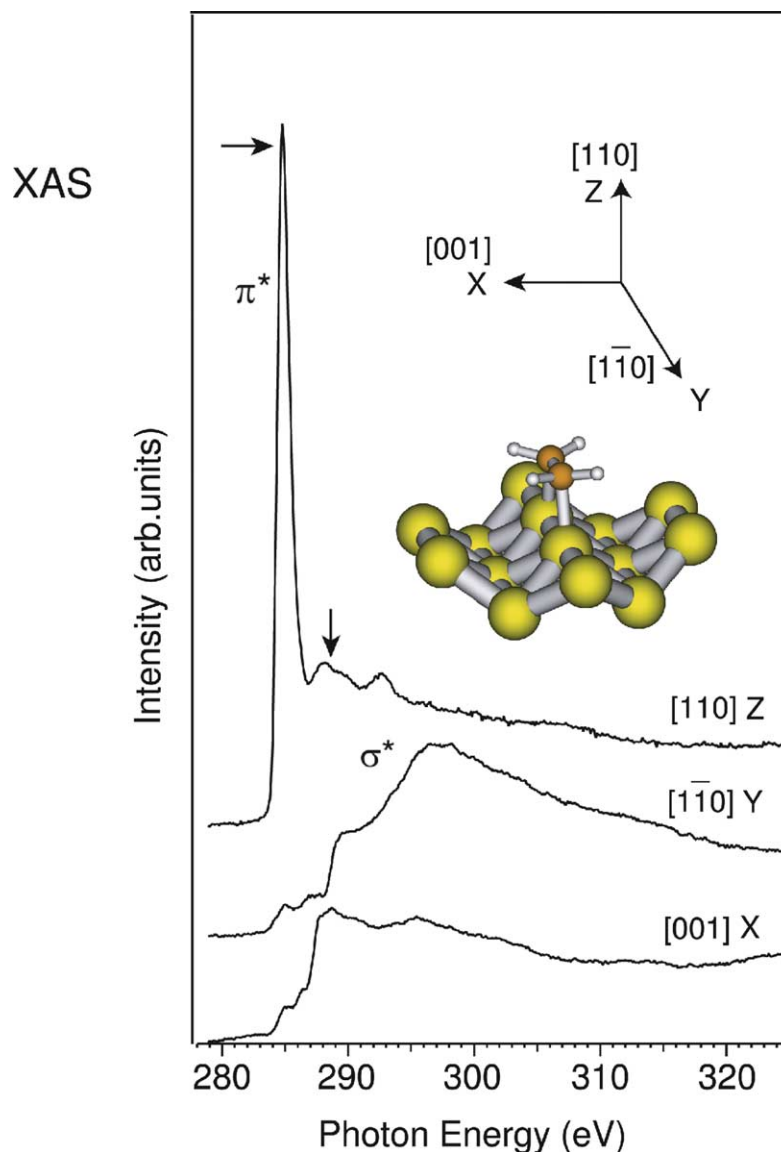
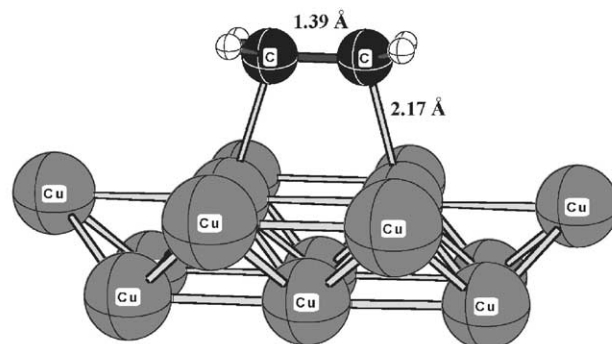
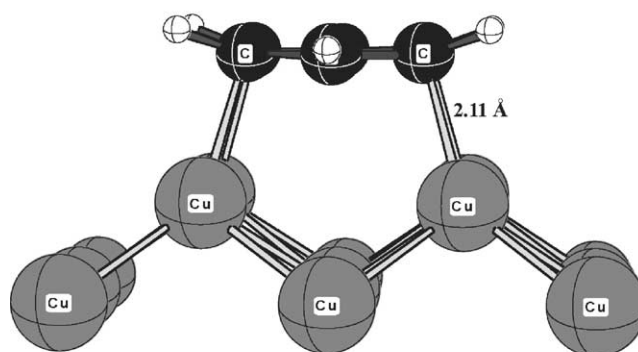


Fig. 53. Angular-resolved XA spectra for ethylene on Cu(1 1 0). The excitation energies used to generate XE spectra are indicated through the arrows.

the molecular plane parallel with the surface. The C–C  $\sigma^*$  resonance is seen as a broad feature at 297 eV in the [1  $\bar{1}$  0] spectrum demonstrating an alignment of the C–C axis parallel with the Cu rows on the (1 1 0) surface. Together with theoretical calculations it has been shown that the ethylene molecule is adsorbed lying down with the molecular axis parallel with the rows in a bridge site coordinating to two Cu atoms (see Fig. 54). This adsorption geometry implies that the ethylene molecule is bound in the so-called di- $\sigma$  configuration. For an azimuthally oriented adsorbate, the dipole selection rules governing XES discriminate different emission directions. By recording XE spectra in three different directions

Chemisorbed ethylene on Cu(110); di- $\sigma$  site

Chemisorbed benzene on Cu(110)

Fig. 54. Optimized structures for di- $\sigma$ -bound ethylene and  $\pi$ -bound benzene on Cu(1 1 0).

(normal emission, and grazing emission along the  $[0\ 0\ 1]$  and  $[1\ \bar{1}\ 0]$  directions), we can project the valence electronic structure on the corresponding atomic  $2p_x$ ,  $2p_y$ , and  $2p_z$  orbitals [56].

For ethylene on Cu(1 1 0) XE spectra were measured following excitation with two different photon energies [34,35]. Fig. 55 shows the XE spectra after subtractions, to obtain the pure p components. The polarization of the exciting radiation was perpendicular to the substrate surface. Hence only transitions into states derived from the  $\pi$  and  $\pi^*$  orbitals of the free molecule could be generated. The lower energy was chosen to coincide with the first XA resonance (*resonant excitation*) of ethylene and the second energy (*off-resonant excitation*) yields an excitation in the Rydberg region; the excitations used are indicated by arrows in Fig. 53.

What can be learned from the symmetry-decomposed XE spectra in Fig. 55? Beginning with the upper panel of Fig. 55, we have the X-component of the XE spectra of chemisorbed ethylene, which corresponds to the direction perpendicular to the atomic rows of the Cu(1 1 0) surface, i.e. along the  $[0\ 0\ 1]$  direction. Hence, only the C-H  $\sigma$  orbitals ( $b_{2g}$  and  $b_{3u}$ ) contribute. The middle panel contains the Y-component, which coincides with the C-C axis. In this spectrum, we observe decay channels involving the C-C molecular  $\sigma$  orbitals ( $3a_g$  and  $2b_{1u}$ ). The lower panel in the figure contains the Z-component. Here, the  $\pi$  and  $\pi^*$  orbitals, mainly responsible for the bonding between the ethylene molecule and the surface are shown. Comparing all three sets of spectra, a simple and unambiguous assignment of all the

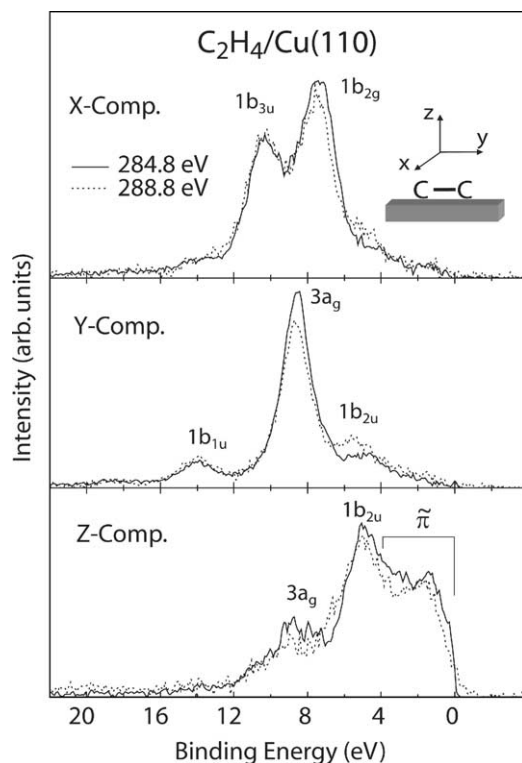


Fig. 55. Angular-resolved XE spectra of ethylene on Cu(1 1 0) using two different excitation energies.

emission lines is possible. The  $\sigma$  states are quite similar to those of the free molecule. In the  $\pi$  channels, on the other hand, a new maximum ( $\tilde{\pi}$ ) at 2 eV is observed, which extends up to the Fermi edge and which has no correspondent in the spectrum of free ethylene. Obviously, this feature is the signature of the surface chemical bond.

For the free ethylene molecule resonant excitation into the  $\pi^*$  resonance imposes strict symmetry selection rules on the subsequent X-ray fluorescence. Since the  $\pi^*(1b_{3g})$  orbital is of *gerade* parity, the core hole can only be created in the *ungerade*  $1b_{1u}(\sigma_u)$  level. The parity selection rule then only allows valence orbitals with *gerade* parity to participate in the radiative decay [58,61]. The XE spectra of chemisorbed ethylene, on the other hand, show a less pronounced dependence on the excitation energy since the hybridization of molecular  $\pi$  and  $\pi^*$  orbitals with metallic band states leads to a coexistence of both symmetries at any given excitation energy.

There is a weak excitation energy dependence on the relative intensities of the two orbitals in each of the *X*- and *Y*-component spectra as seen in Fig. 55. The  $1b_{2g}$  and  $3a_g$  orbitals are enhanced indicating that we generate more core holes of *ungerade* symmetry than *gerade* symmetry when we excite to the first resonance close to the Fermi level. This indicates that we have more contributions of  $\pi^*(1b_{2g})$  than  $\pi(1b_{3u})$  character on the adsorbate in the states right above the Fermi level. For the free molecule resonant excitation into the  $\pi^*$  resonance imposes strict parity selection rules on the subsequent XES [58,61]. If we now look in the *Z*-component spectra we do not see any significant change in the intensity between the two  $\pi$  states for the different excitation energies. We can conclude from the experiment that both the empty states close to the Fermi level and the occupied states should have both  $\pi^*(1b_{2g})$  and

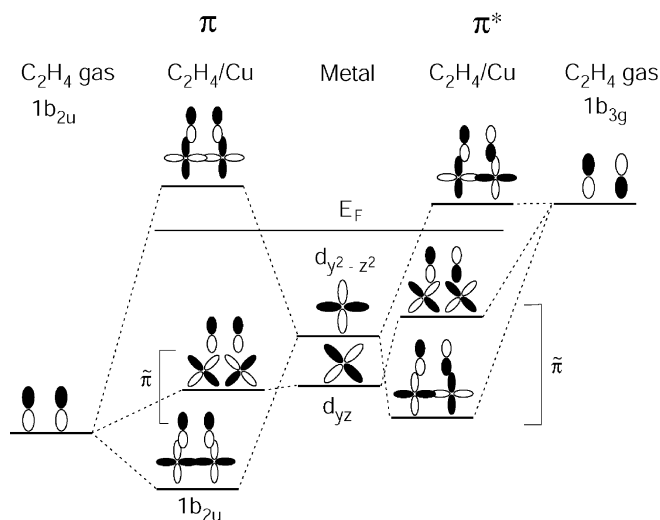


Fig. 56. Molecular orbital diagram showing  $\pi$  and  $\pi^*$  interactions with metal d orbitals.

$\pi(1b_{3u})$  character. These results are in agreement with the DCD model (see Fig. 52), where a donation of  $\pi$  electrons into empty states and back-donation into  $\pi^*$  states yields a symmetry mixing in the occupied and unoccupied orbitals.

A simplified schematic molecular orbital diagram is shown in Fig. 56. The figure shows the interaction between the metal 3d band and the occupied  $\pi$  orbital (left part) and the unoccupied  $\pi^*$  orbital (right part). The interaction with the  $\pi$  and  $\pi^*$  orbitals results in a large number of bonding, non-bonding and anti-bonding combinations in the figure; only three energy levels of each  $\pi$  and  $\pi^*$  symmetry are drawn in the figure. The anti-bonding orbitals remain unoccupied, the bonding occupied and the non-bonding, which are close to the Fermi level, may be more or less occupied depending on the metal d band. The strength of the bond to the surface is determined by the amount of  $\pi$  and  $\pi^*$  states being occupied. It is important here to realize that the  $\pi$  and  $\pi^*$  states cannot mix directly due to symmetry; any charge-transfer between these orbitals must be mediated by the surface, as in the established DCD model.

An alternative description of the bonding is through the “spin-uncoupling” mechanism [169], where the bonding is described as a bond preparation through excitation of a  $\pi$  electron into the molecular  $\pi^*$  orbital, producing the molecular state that can bind to the surface. The initial excitation will rehybridize the molecule to  $sp^3$ , and populate the  $\pi^*$  orbital with 0.5 electrons/atom. In this step, the molecule is prepared for bonding and the structure is distorted to a structure very similar to the adsorbed molecule; in the particular case of ethylene this structure corresponds to the excited eclipsed triplet state [169]. In this picture, the first step would correspond to a singlet–triplet transition. The bonding to the surface is then formed through the loss of  $\pi^*$  electron charge and gain in the  $\pi$  states, yielding the same final charge distribution as predicted by the DCD model. The mechanism can be viewed as an equilibration of  $\pi$  and  $\pi^*$  occupation with respect to the metal states.

The advantage with the spin-uncoupling or bond-preparation picture [169] is that it provides an estimate of the energy cost of the rehybridization required to form the bond to the substrate as well as the prediction of barriers between physisorbed and chemisorbed states in certain cases. Since the chemisorption energy is the balance between the cost to prepare for bonding and the gain from bond formation this allows to obtain the strength of the bond to the surface. In [169], a surprisingly stable carbon–metal  $\sigma$

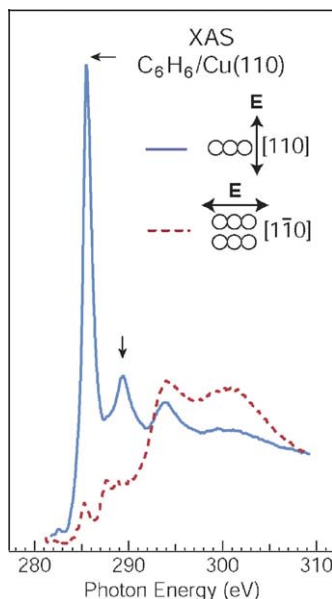


Fig. 57. Angular-resolved XA spectra for benzene on Cu(1 1 0). The excitation energies used to generate XE spectra are indicated through the arrows.

bond energy of  $51 \pm 2$  kcal/mol was obtained from considering acetylene, ethylene and benzene on various copper surfaces.

Let us now turn to benzene adsorbed on Cu(1 1 0). Fig. 57 shows the XA spectra which demonstrate that benzene is adsorbed with the molecular plane parallel to the surface with no azimuthal orientation (only one in-plane direction is shown). In this case, we can only resolve in and out-of-plane orbitals in the XE spectra. Fig. 58 shows XE spectra for benzene adsorbed on Cu(1 1 0) for two different excitation energies, 285 and 289 eV, corresponding to the  $C\ 1s \rightarrow \pi^*(e_{2u})$  excitation and into the continuum, respectively [34–36]. From angular-resolved measurements we derive the pure  $\pi$  and  $\sigma$  spectra, which are shown in the lower and upper parts of Fig. 58. Compared to ethylene there are more dramatic changes in the XE spectra of benzene between the two excitation energies, which provides an immediate demonstration that the gas-phase separation between occupied  $\pi$  and unoccupied  $\pi^*$  is maintained to a much higher degree than what was found for ethylene.

Benzene in the gas-phase transforms according to the  $D_{6h}$  symmetry group and the XE spectra have in this case been shown to be governed by the parity selection rules. For the adsorbate, the presence of the surface breaks the inversion symmetry of the gas-phase molecule. The interaction with the surface furthermore results in a geometry distortion and different positions of the carbon atoms with respect to the substrate atoms resulting in a lowering of the symmetry to  $C_{2v}$  [34]. Due to the lowered symmetry we should expect substantially smaller changes with excitation energy for resonant XES processes than observed in gas phase. However, due to the fact that the chemical shifts of the different  $C\ 1s \rightarrow \pi^*$  intermediate states are small in comparison with the lifetime width of the  $C\ 1s$  core hole, interference is still present causing the intensity of certain transitions to be quenched in the spectra [61]. The smaller the shift, i.e. the weaker the interaction with the substrate, the more gas-phase-like the XE spectra become. The  $C\ 1s \rightarrow \pi^*$  excitation shows a relatively narrow line for adsorbed benzene, indicating that the chemical shifts are relatively small.

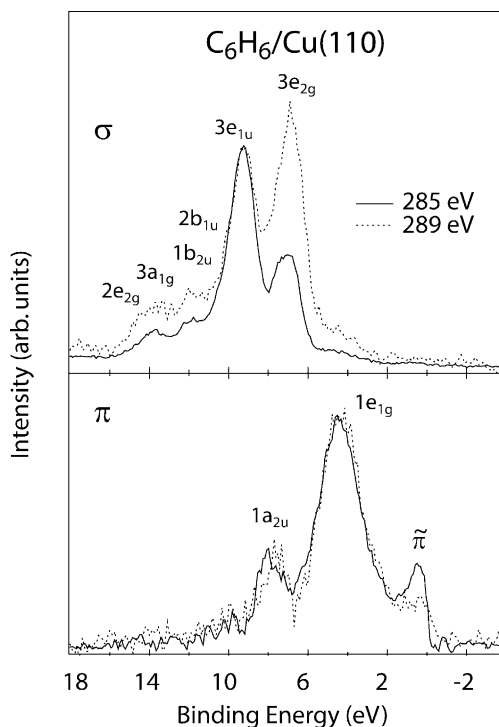


Fig. 58. Resonantly and non-resonantly excited  $\sigma$  (top) and  $\pi$  (bottom) emission spectra for benzene on Cu(1 1 0).

Most of the peaks in the  $\sigma$  symmetry spectra are similar to the gas phase spectrum indicating very small changes of the  $\sigma$  states upon adsorption, which is similar to the case found for ethylene. The spectrum for pure  $\pi$  symmetry (dashed line) reveals three distinct peaks: the  $1a_{2u}$  and  $1e_{1g}$  out-of-plane  $\pi$  orbitals and a third state, labeled  $\tilde{\pi}$ , not seen for the free molecule. The enhancement of the  $\tilde{\pi}$  state after a  $C\ 1s \rightarrow \pi^*(e_{2u})$  excitation shows that this state has a symmetry similar to the unoccupied  $e_{2u}$  state. The new  $\tilde{\pi}$  state is located just below the Fermi level with a sharp cut-off. We anticipate that the unoccupied  $e_{2u}$  orbital interacts with a broad continuum of metal states and becomes broadened with a tail extending below the Fermi level [36]. Obviously, the mixing of HOMO- and LUMO-like states of the adsorbate-substrate complex is less pronounced for benzene than for ethylene.

The occupied electronic structure as measured using XES can thus provide a firm, experimental basis for a critical evaluation of models of the surface chemical bond. In particular, we find the reduced occupancy in the  $\pi$  levels and population of  $\pi^*$  as predicted in the DCD model. Since the dependence on the excitation energy is much weaker in ethylene than for benzene we can immediately conclude that the interaction is much stronger for ethylene although the resulting chemisorption energies are quite similar. For ethylene, the  $\pi$  level becomes partially unoccupied such that it can be involved in the excitation process and  $\pi^*$  becomes sufficiently occupied to give a clear signal in the XES. Thus, as the excitation energy is varied, both  $\pi$  and  $\pi^*$  will contribute to the absorption cross-section and both  $\pi$  and  $\pi^*$  contribute to the decay as well; dramatic effects on the resulting spectra with different excitation energies are thus not expected. For benzene, the interaction is weaker due to the additional stabilization from the aromatic ring system, which can be readily concluded from the strong dependence on the excitation energy.

In the present section, we have thus shown how the atom-specific probe of X-ray emission spectroscopy in combination with the symmetry selection rules imposed by resonant excitation can be employed to determine the symmetry of the electronic states that are responsible for the substrate–adsorbate coupling of chemisorbates with symmetry-equivalent atoms. The validity of the conclusions drawn from the experimental data has been verified by state-of-the-art DFT calculations. We would like in particular to strongly emphasize the interplay between experiment and theory for strengthening and extending the analysis as shown in the atomic decomposition above.

#### 4.3.2. Chemical bonding of benzene on Cu(1 1 0) and Ni(1 0 0) surfaces

Let us return to benzene which adsorbs weakly on Cu and strongly on Ni. It is interesting to study how the adsorption strength is reflected in the electronic structure of the adsorbate–substrate complex.

XE and XA spectra for benzene on Cu(1 1 0) and Ni(1 0 0) are shown in Figs. 59 and 60 [35,36]. XE spectra were taken at an excitation energy corresponding to the C 1s to  $\pi^*(e_{2u})$  transition as discussed in Section 4.3.1. The spectra are plotted on a photon energy scale and a valence hole binding energy scale by subtracting the C 1s binding energies of 284.1 and 284.9 eV for benzene adsorbed on Ni and Cu, respectively [36]. If we start with states of  $\pi$  symmetry (dashed lines), we find three distinct peaks. The  $1a_{2u}$  and  $1e_{1g}$   $\pi$ -like orbitals are essentially intact from the gas phase, while the third state, labeled  $e_{2u}$ , is not seen for the free molecule. In Section 4.3.1, it was shown, based on symmetry selection rules, that this state is derived from the LUMO  $e_{2u}$  orbital that becomes occupied upon adsorption. We anticipate a similar bonding mechanism as discussed in the previous section for adsorbed ethylene with the exception of a weaker rehybridization due to the extra stability in the  $\pi$  system from the aromatic character.

The new occupied  $e_{2u}$  state appears differently in the spectra from benzene on Cu and Ni. In the case of adsorption on Ni (Fig. 60), the new  $\pi$  state is located 1.7 eV below the Fermi level and hence overlapping

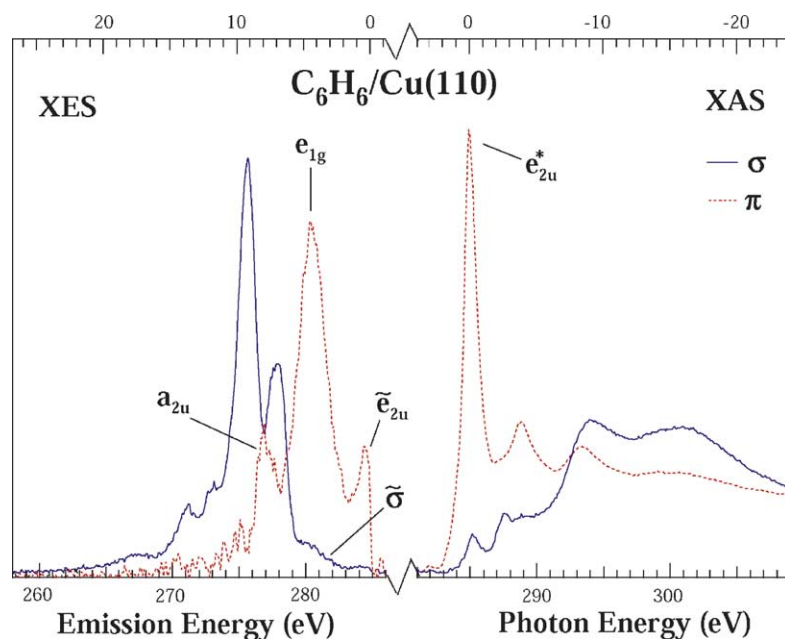


Fig. 59. Symmetry-resolved XE and XA spectra of benzene adsorbed on Cu(1 1 0).

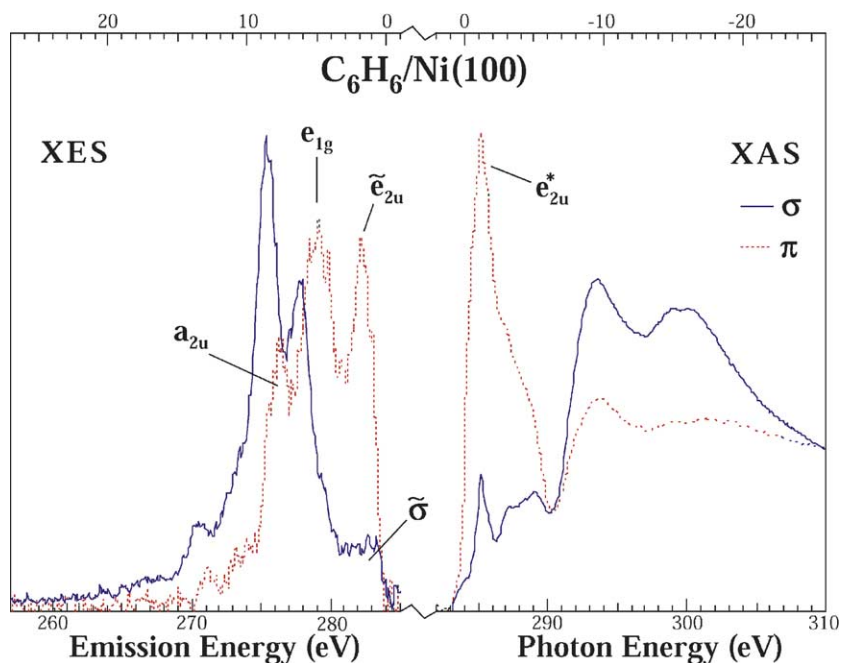


Fig. 60. Symmetry-resolved XE and XA spectra of benzene adsorbed on Ni(1 0 0).

the Ni d band region. The fraction of adsorbate character of this state has to be of similar magnitude as that of the higher binding energy  $\pi$  orbitals since the observed emission intensity is of comparable strength. The formation of a single bonding state rather than a band suggests that the  $e_{2u}$  orbital interacts mainly with a narrow distribution of states, i.e. the Ni d band. For benzene adsorbed on Cu (Fig. 59), the new occupied  $e_{2u}$  orbital is located just below the Fermi level with an indication of a cut-off at the Fermi level. The adsorbate character in this orbital is rather low. This is also reflected in the relatively strong peak from the anti-bonding orbital in the XA spectrum in Fig. 59. Our observations suggest that the unoccupied  $e_{2u}^*$  orbital interacts with a broad continuum of metal states and becomes broadened with a tail extending below the Fermi level. There is no distinct separation between the bonding and anti-bonding part.

In the  $\sigma$  symmetry XE spectra in Figs. 59 and 60 (solid lines) we find, at binding energies larger than 5 eV, an orbital structure identical to that of the free molecule [36]. In addition we find for benzene on Cu two new weak structures at binding energies below 5 eV. These structures appear at the same binding energies as the  $1e_{1g}$  and  $e_{2u}$  orbitals seen in the  $\pi$  symmetry spectrum. We can anticipate some symmetry mixing due to rehybridization as discussed for ethylene in the previous section. For benzene adsorbed on Ni the  $\sigma$  symmetry spectrum is different. Here, we find significant  $\sigma$  intensity all the way to the Fermi level, marked  $\tilde{\sigma}$  in Fig. 60. A simple admixture of  $\sigma$  and  $\pi$  states is not sufficient to explain the appearance of new  $\sigma$  states in the spectrum, since then we would expect a  $\sigma$  electron distribution which resembles the  $\pi$  states with a peak at 1.7 eV (the back-bonding  $e_{2u}$  orbital). The 2p valence states parallel to the surface must therefore interact with the metal somewhat differently than the perpendicular 2p states. The band-like character of the  $\sigma$  states indicates a hybridization of benzene  $\sigma$  states with the broad Ni sp band in addition to the d band. We expect this to be attributed to a major distortion in the carbon skeleton going

towards tetrahedral coordination. Such a distortion has in fact been proposed for the inverted boat chemisorption structure of benzene that would result from bonding of benzene in the triplet excited quinoid state; this excited state corresponds to the molecule prepared for forming two covalent bonds to the substrate [169].

#### 4.4. Lone pair interactions

In the following section, we will discuss adsorbate metal interactions in molecular systems where there are no free radicals or unsaturated  $\pi$  system that can be involved in the surface bonding. The molecules in this section all have some extent of lone pair character. We will discuss water adsorption on Pt(1 1 1) where there are two different bonding configurations to the surface: oxygen lone pair metal interaction and hydrogen bonding with the substrate. Large molecules can often be viewed as built from different functional groups joined together by molecular bonds of strength comparable to the intramolecular bonds within the respective building units. By using the bond-prepared functional groups as a starting point, new electronic states appearing for the more complex molecules can be accounted for. Thus, in order to be able to address questions regarding reactivities of biologically interesting molecules on metal surfaces, a detailed knowledge about the chemically important functional groups of the system can be very helpful. The adsorption of formate on Cu(1 1 0) [56] is of particular interest, since it provides an example of an adsorbate–substrate interaction via a carboxylic group. Another example is the adsorption of ammonia on Cu(1 1 0) [76], which similarly represents the interaction of an amino group with a metal surface. Furthermore, we will combine these functional groups into the amino acid glycine ( $\text{NH}_2\text{--CH}_2\text{--COOH}$ ) and investigate its binding to the Cu(1 1 0) metal surface. This example leads us to also consider the effects of hydrogen bonding on the electronic structure since this determines the adsorbate overlayer structure. We will, however, begin by discussing water adsorption on Pt(1 1 1) where there are two different bonding configurations to the surface oxygen lone pair metal interaction and hydrogen bonding with the substrate.

##### 4.4.1. Water on Pt(1 1 1)

The structure of water on metal surfaces in general has traditionally been considered a buckled “bilayer ice” where only every second water binds to the metal [170,171] (see Fig. 61A). The bilayer model is well accepted but has never been proven through any structural determination. Recently, this model has been shown to be incorrect based on XAS, XES and XPS studies along with DFT calculations of the overlayer structure of water on Pt(1 1 1) [172]. Using a direct relationship between core and valence electronic structure and adsorbate geometry, it was shown that water is adsorbed in a rather flat layer, not the predicted bilayer, forming bonds with both O and H atoms to the Pt substrate at distances of 2.35 and 2.6 Å, respectively (Fig. 61B).

Fig. 62A shows XA and XE spectra of the  $p_z$  component (perpendicular to the surface) of water on Pt(1 1 1) [172]. The in-plane spectra are very similar to that of bulk ice. Two different theoretical model calculations of the XA spectra corresponding to two different orientations of the OH groups that are not involved in hydrogen bonding between water molecules are shown in the figure. The uncoordinated OH groups can either point towards vacuum (H-up) or towards the surface (H-down). The computed H-up structure gives rise to a strong feature at 536.5 eV assignable to orbitals localized at the uncoordinated OH bond pointing toward vacuum [173]. In the H-down configuration, the peaks are broadened and loose intensity due to interactions with the Pt surface. Comparison with the experimental X-ray absorption

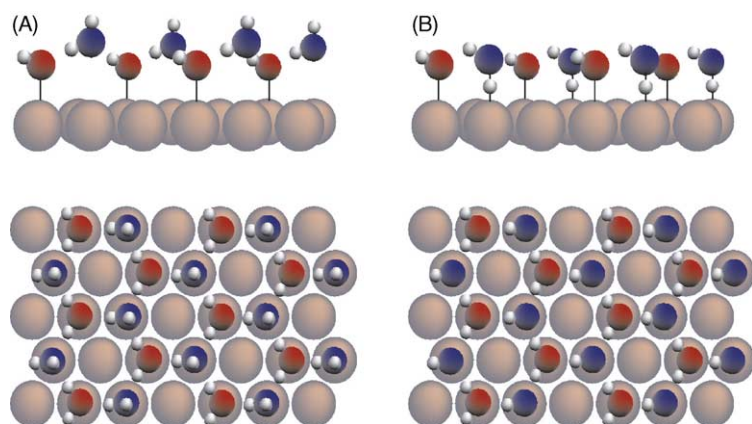


Fig. 61. (A) The bilayer ice structure on metal surfaces. Red and blue spheres represent O atoms. Half of the water molecules bind directly to the surface metal atoms. The other half are displaced toward the vacuum in the H-up configuration. (B) The “flat ice” structure on metal surfaces. Red and blue spheres represent O atoms in Pt–O and Pt–HO bonding water molecules, respectively. All water molecules bind to the surface metal atoms. The thickness of the layers is 0.96 Å (a) and 0.25 Å (b), respectively.

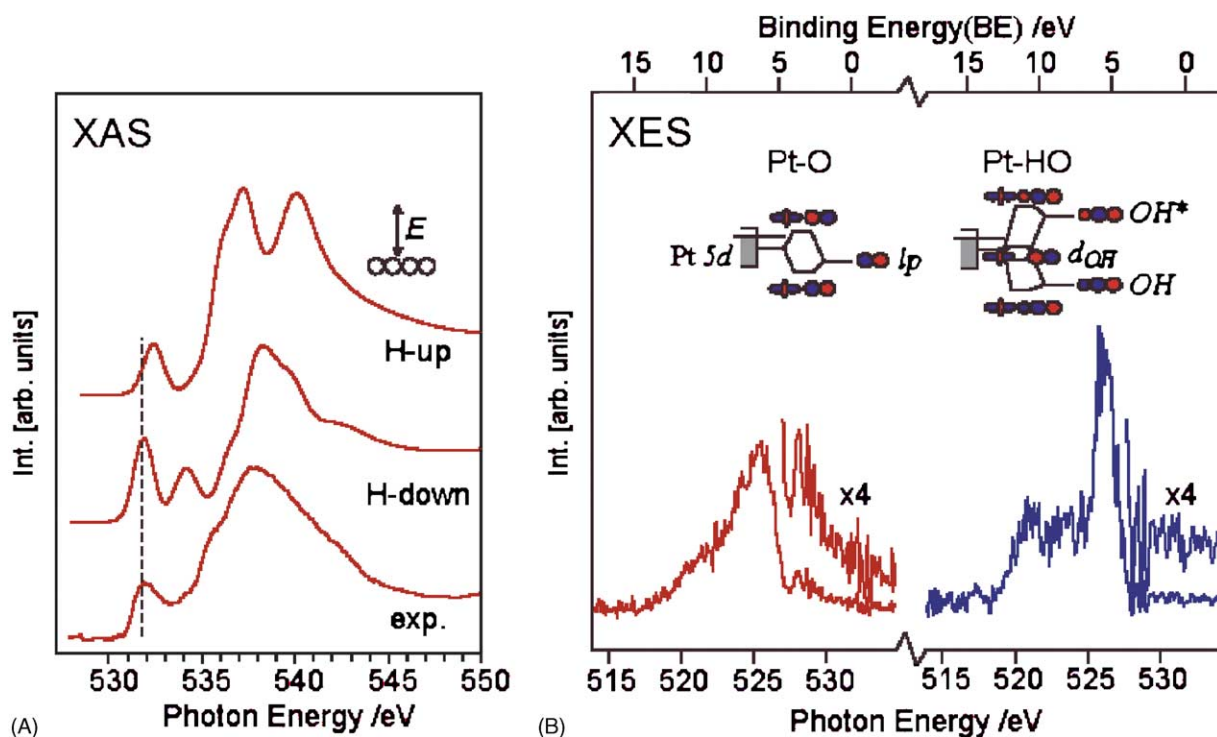


Fig. 62. (A) Computed  $p_z$  component XA spectra of the flat ice on Pt(1 1 1) with uncoordinated OH toward the vacuum (H-up) and toward the substrate (H-down). The H-down spectrum is in agreement with the experimental XA spectrum (bottom). (B) XE spectra ( $p_z$  components) from Pt–O (left) and Pt–HO (right) bonding species showing the occupied orbital structure. The spectra were obtained by exciting at 532 and 538 eV and applying a subtraction procedure. The insets represent schematic diagrams of the Pt–O and Pt–HO bonding interactions.

spectrum immediately shows that this feature is missing except for a weakly discernible shoulder; this provides evidence that the H-down configuration is preferred.

By carefully tuning the excitation photon energy, we selectively observe the occupied electronic states projected on the oxygen atom of, respectively, the Pt–O and Pt–HO bonding species (Fig. 62B). We compare the XE spectra for the water molecules binding through oxygen and hydrogen and focus on the  $p$  components projected along the (vertical)  $z$ -direction, which corresponds to the direction of the surface bond. The interaction of the O lone pair (lp) orbital of the Pt–O bonding species with the substrate d band will result in bonding and anti-bonding combinations. We can find the bonding combination as the strong asymmetric peak between 6 and 15 eV. We can recognize a weak feature between 4 eV and the Fermi level that has an anti-bonding character in the molecular orbital analysis of the computed XE spectrum. This band is not fully occupied and we can observe the unoccupied part of this band in the XA spectrum as the peak at 532 eV (Fig. 62A). We can see the repulsive character of the Pt–O bonding in the charge density difference plot (Fig. 63). The charge density is decreased along the bond indicating charge polarization to the surroundings in order to minimize the Pauli repulsion between the lone pair orbital and the Pt d orbital. The Pt–O species will be oriented on the surface with the molecular plane parallel to the surface. This means that the molecular dipole will maximize its interaction with the substrate through a metal image dipole. Since the water molecule dipole is very large, 1.8 D, this interaction will be substantial. Although the orbital interaction for the Pt–O species is repulsive we anticipate that there will be an overall attractive bonding due to the strong electrostatic dipole–image dipole interaction.

For the Pt–HO bonding species, the two OH groups in the water molecule have different surroundings; either coordination to the surface or involved in a donating H-bond to another water in the overlayer. This asymmetry results in a substantial rehybridization of the molecular orbital structure into localized OH orbitals. If we only consider the OH orbital directed to the surface and one Pt atom a simple molecular orbital picture for the Pt–HO interaction can be derived. The bonding involves three atoms in the interaction and results in three molecular orbitals that are different in the number of nodes (Fig. 62B, right). The lowest orbital is bonding and the highest antibonding between hydrogen and Pt. The middle orbital will have a node between the O and the Pt indicating a non-bonding interaction and essentially pure oxygen  $p$  character, seen in the XE spectrum at 5 eV. The other two orbitals will reside above and below this state and will not have a prominent intensity in the XE spectrum since they involve mainly hydrogen character. The antibonding orbital is composed of mainly Pt character and forms a broad band with contributions above the Fermi level, seen in the XA spectrum around 535 eV. The rearrangement of charge due to net bonding contributions can be seen in the charge density difference plot in Fig. 63. We observe an increase of density between the H and Pt atoms (electron pairing) from the bonding

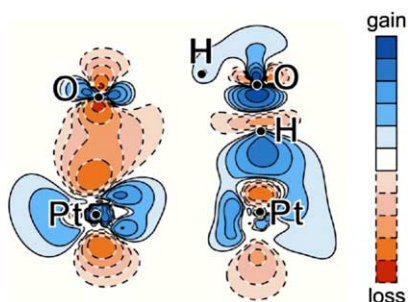


Fig. 63. Charge density difference plots for Pt–O (left) and Pt–HO (right) bonding species.

combination and a decrease on the H atom along the OH bond from the non-bonding combination. We can thus say that the Pt–HO bonding results in the formation of a Pt–H bond together with the weakening of the water internal O–H bond.

#### 4.4.2. Adsorption of formate and acetate on Cu(1 1 0)

The formate ion binds in an upright conformation via the oxygen atoms to the Cu(1 1 0) surface with the O–O bond azimuthally oriented along the  $[1 \bar{1} 0]$  direction [174]. As described previously, we can thus project the valence electronic structure on the corresponding atomic  $2p_x$ ,  $2p_y$ , and  $2p_z$  orbitals. In addition to electrostatic interaction (ionic bonding), we expect the covalent interaction with the metal to be dominated by the O  $2p_z$ , i.e. the  $a_1$  orbitals pointing towards the surface. Covalent contributions would give rise to new states and the formation of bonding and antibonding components, while a strictly ionic interaction would generate only minor perturbations of the occupied orbitals. In order to facilitate the following discussion we show the valence orbitals of the gas-phase formate anion in Fig. 64, where the size of the lobes illustrate the computed amplitude of the orbital on that atom.

The symmetry group of formate is  $C_{2v}$  and we have taken the  $x$ -axis orthogonal to the molecular plane. With respect to this plane, we can speak of local  $\pi$  symmetry orbitals, perpendicular to the molecular plane, and in-plane  $\sigma$  orbitals. The O  $2p_x$  and C  $2p_x$  atomic orbitals form three molecular orbitals: the  $1b_1$   $\pi$  O–C bonding orbital, the non-bonding  $1a_2$  oxygen lone pair, which is also the HOMO, and the unoccupied antibonding  $2b_1$  (LUMO + 1), which constitutes the  $\pi^*$  O–C antibonding resonance in the X-ray absorption spectrum. The  $2b_1$  is polarized towards the carbon as a consequence of the higher electron affinity of oxygen; this is similar to what is observed for, e.g. the  $\pi^*$  orbital of the CO molecule.

The other MOs have local  $\sigma$  character with varying amounts of O  $p_z$  contribution. The  $6a_1$  orbital is nearly degenerate with the HOMO. It is made up by  $p_z$  orbitals from the carbon and oxygen atoms, dominated by its oxygen contribution. The  $5a_1$  and the  $4a_1$  orbitals contain a large C  $2s$  contribution, in addition to the  $p$  contributions. The  $4b_2$  orbital, again with dominant oxygen contribution, is also close in energy to the HOMO. It is the first orbital with significant  $p_y$  contributions. The  $3b_2$  orbital is nearly degenerate with the  $4a_1$  orbital. We will now investigate how the molecular orbitals are affected by bond formation to the surface.

The XE spectra are presented in Fig. 65 together with the orbital assignment and computed XE and RIXS spectra, to which we will return later. We denote the process RIXS when we have to consider core hole states with different symmetries (see Sections 2.1 and 2.5.3 for more detailed discussions). For now we note that the computed XES gives a good representation of the spectrum such that we can use the computational results to give detailed orbital assignments. In the experimental  $p_z$  spectrum, we immediately see significant intensity, indicated by  $\tilde{a}_1$ , on the low binding energy side;  $p_z$  corresponds to the  $\sigma$  symmetry and is where we expect to find indications of covalent bonding to the substrate. The formate  $6a_1$  orbital forms bonding and antibonding combinations with the metal  $d$  band. In the spectra, the bonding combination has been denoted  $6\tilde{a}_1$  while the antibonding combination is represented by the  $\tilde{a}_1$  states. The bonding electronic states have essentially adsorbate character while the antibonding states instead are strongly polarized towards the substrate, as evidenced by the relative intensities. Part of the  $\tilde{a}_1$  electronic states are unoccupied giving rise to a net bonding to the surface. In this spectral region, we also expect bonding combinations due to the interaction of the metal valence bands with previously unoccupied formate MOs, e.g. the formate  $7a_1$  orbital. This further strengthens the surface chemical bond.

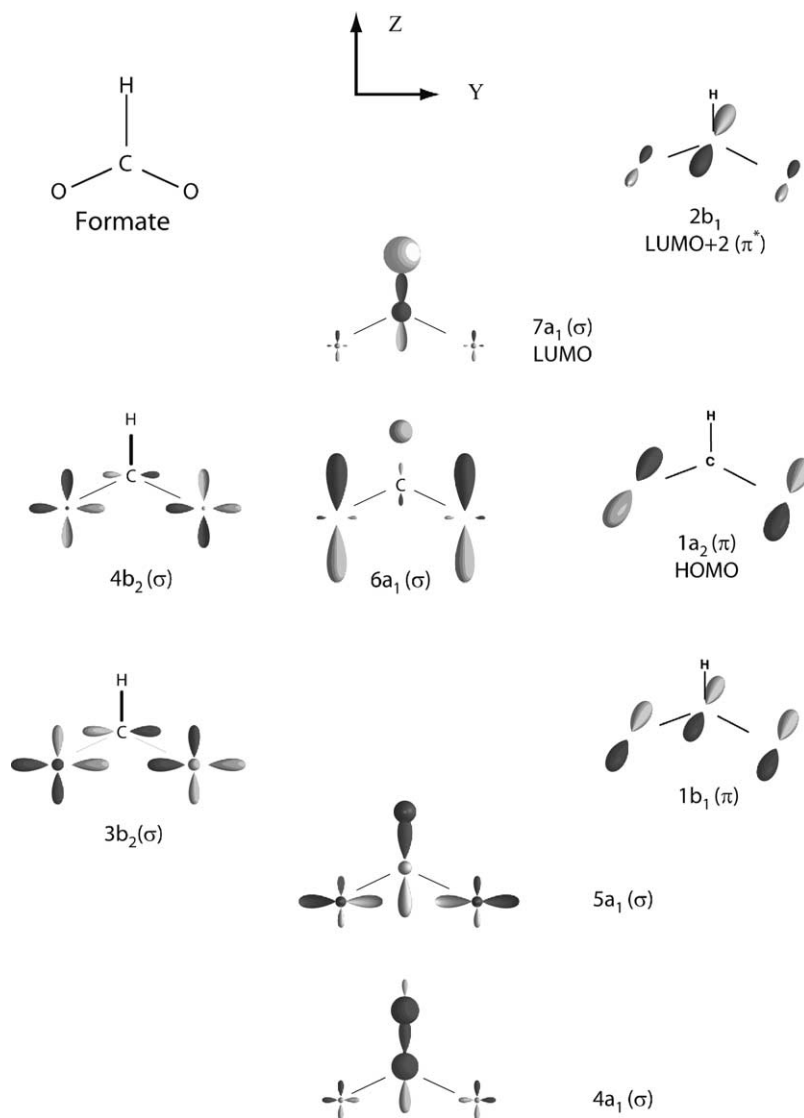


Fig. 64. Valence orbitals of the formate ion. O–C  $\pi$  character is contained within the  $b_1$  and  $a_2$  orbitals and local O–C  $\sigma$  character in the  $a_1$  and  $b_2$  orbitals.

The  $4b_2$  orbital also contains oxygen  $p_z$  contributions that can interact directly with the substrate. Since this orbital also has  $p_y$  contributions the resulting intensity between 0–3 eV can be identified in the experimental  $p_y$  spectrum while in the  $p_z$  spectrum this contribution is masked by the larger  $\tilde{a}_1$  contribution. Both orbitals contribute to the net bonding, however, as seen from CSOV calculations where specific orbital mixings are sequentially allowed and the effect on the energy monitored. We find from these studies that also energetically the  $\tilde{a}_1$  contribution dominates the bonding to the substrate. In the  $\pi$  symmetry ( $p_x$ ), we again find some intensity near the Fermi level, which must be due to the formation of antibonding states between the  $1a_2$  HOMO and the metal. The splitting is small and also the

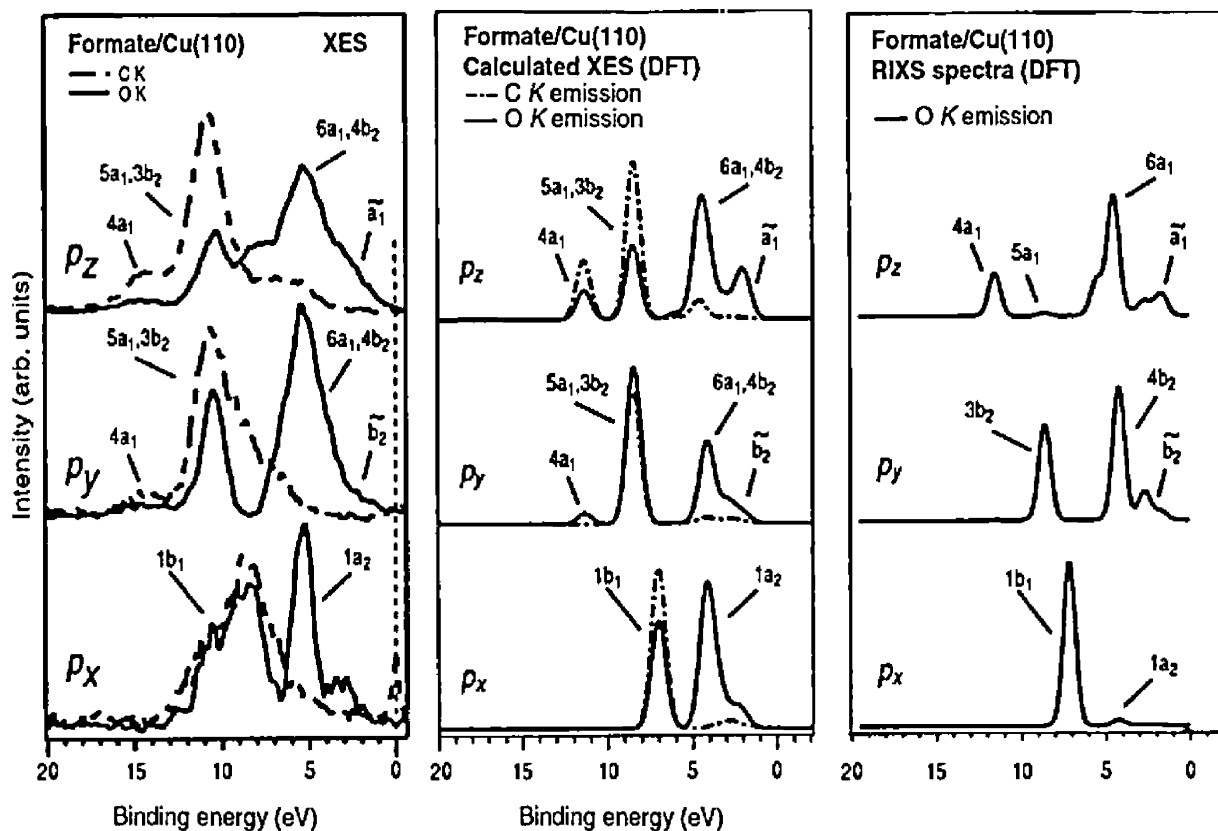


Fig. 65. Experimental (left panel) and theoretical C 1s and O 1s XE spectra of formate. The experimental spectra were recorded at the  $1s \rightarrow \pi^*$  threshold at 288.5 eV for carbon and 533.6 eV for oxygen. The middle panel shows the computed spectra assuming non-resonant excitation while the right panel shows the computed O 1s RIXS spectrum.

energetic contribution, which is due to the adsorbate–substrate distance, which is too long to allow any significant  $\pi$  bonding.

Although we have identified clear effects of covalent contributions to the bonding it is still ionic contributions that dominate the binding energy. The Mulliken population analysis with the large basis sets used in the present study results erroneously in a near-neutral adsorbate. A more reliable measure of the ionicity is provided by the computed dipole moment as function of distance above the surface; for an ionic system, or an anion interacting with an induced image charge, this should be linear with the slope corresponding to the ionic charge. This is indeed the case both for formate and acetate on Cu(1 1 0) as seen in Fig. 66 where the slope indicates charges near 0.9.

Returning now to the computed XE spectra in Fig. 65, we have a quite reasonable agreement including also the weaker states resulting from the bonding to the surface. However, in the oxygen  $p_y$  spectrum the intensity relationship between the  $5a_1/3b_2$  and  $6a_1/4b_2$  peaks shows a problem with much too little intensity in the second peak. The spectrum shown in the middle panel was computed non-resonantly and in an effort to resolve the discrepancy we have included a calculation (denoted RIXS) where we consider symmetry selection rules for the oxygen emission (right panel) to better mimic the experimental conditions and account for the equivalence of the two oxygens. This resolves the problem which indicates

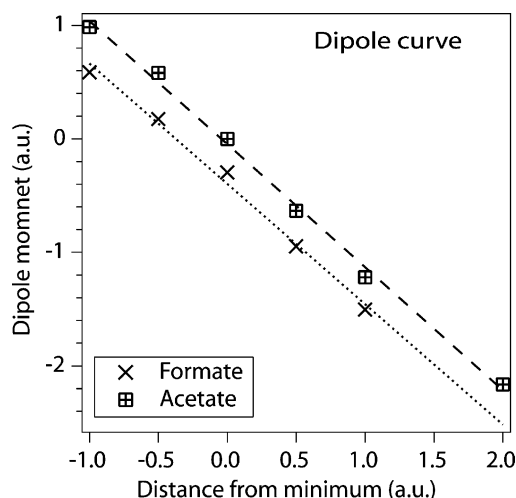


Fig. 66. Computed dipole moments for formate and acetate on a  $\text{Cu}_{10}$  cluster model of the  $\text{Cu}(1\ 1\ 0)$  surface. The linear variation of the computed dipole moment as function of distance from the surface indicates a predominantly ionic bonding.

that the relative intensities in this case do depend on the excitation mode, while the character and energy position of the transitions do not.

Introducing symmetry selection rules has consequences on the  $1a_2$  peak in the  $p_x$  spectrum, which goes from very intense to very low intensity. This is due to the strict selection rules that are introduced when core excitations occur from levels of specific symmetry. The core levels of formate are of  $a_1$  and  $b_2$  symmetry and the  $\pi^*$  level is the  $2b_1$  orbital. The dipole selection rule in  $C_{2v}$  symmetry excludes transitions  $a_1 \rightarrow a_2$  and  $b_2 \rightarrow b_1$ . Using the  $\pi^*$  as the resonant orbital results in excitations only from the  $a_1$  core level into which the  $a_2$  level cannot decay. Thus, this intensity all but vanishes in the calculation, but not in the experiment. This is most likely due to vibronic coupling in the intermediate state similar to what has been found for  $\text{CO}_2$  [175,176], but this is difficult to include in the calculations for chemisorbed formate. The calculations still provide a good understanding of the spectral features and of the spectroscopic process. With this we now turn to the case of acetate to investigate how the features are affected by exchanging the proton in formate for a methyl group to generate acetate.

The adsorption geometry for acetate corresponds to that of formate, i.e. the molecule binds, in an upright position on the copper rows, with both oxygens. The XE spectrum of acetate on  $\text{Cu}(1\ 1\ 0)$  is shown in direct comparison with formate in Fig. 67. We will build our analysis of the spectrum on that of formate in combination with the methyl group orbitals shown in Fig. 68. The methyl unit transforms according to the  $C_{3v}$  point group and the occupied orbitals will be of  $a_1(\sigma)$  and  $e(\pi)$  symmetry which will form bonding and antibonding combinations with the formate orbitals (the hydrogen removed). The experimental C 1s excited spectrum has been decomposed in contributions from the carboxylic and methyl carbons by exciting into the  $\pi^*$  and  $\sigma_{\text{CH}^*}$  resonances, respectively.

Most of the hydrogen contribution in the formate orbitals is located in the  $5a_1$  orbital, which also has an energy favorable for interacting with the methyl fragment. The features indicated in the acetate  $p_z$  spectrum are the  $5a_1$  and  $6a_1$  (and  $7a_1$ ) bonding combinations with the  $\sigma_{\text{methyl}}$ . Since the non-bonding  $\sigma_{\text{methyl}}$  orbital is intermediate between the  $5a_1$  and  $6a_1$  levels the resulting  $5a_1$  combination is dominated by the carboxylic carbon while the  $6a_1$  derived level becomes dominated by the methyl carbon. We see

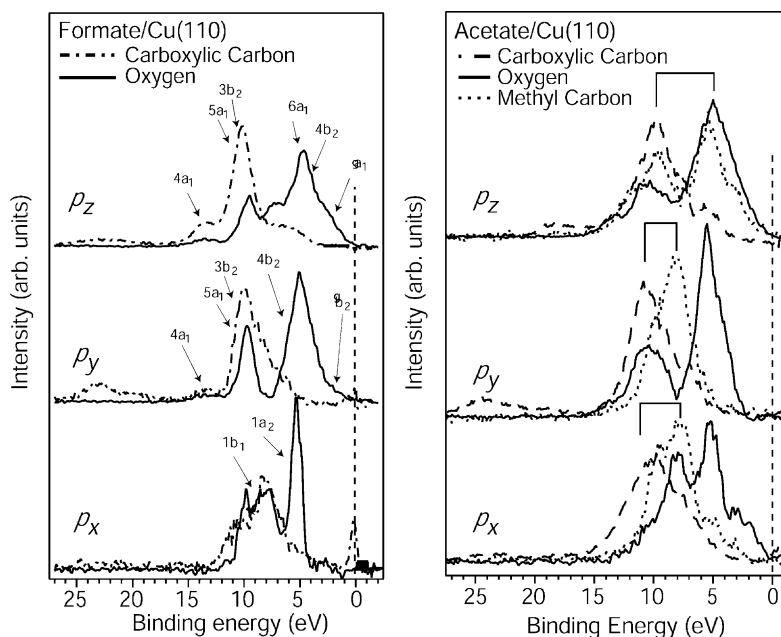


Fig. 67. Symmetry-resolved XE spectra of formate and acetate on Cu(1 1 0). The Fermi level is indicated by the vertical dashed line. The interaction between the methyl and carboxy groups in the case of acetate gives rise to bonding and anti-bonding states with a split indicated by the solid lines. Excitation energies for the carboxy group are given in Fig. 65, while that for the methyl carbon was 287.0 eV with the  $E$ -vector perpendicular to the surface.

that the  $\sigma$  states of the methyl carbon contribute all the way up to the Fermi level such that the substrate hybridization propagates through the entire molecule.

The interaction with the methyl  $\pi$  orbitals provides an interesting example of hyperconjugation. This concept deals with the interaction between a  $sp^3$  hybridized substituent and the  $\pi$  system of a conjugated  $sp^2$  hybridized skeleton. The two methyl  $\pi$  components will interact with the formate to form bonding and antibonding combinations: the  $\pi_{x,CH_3}$  with the  $1b_1$   $\pi$  orbital of formate and the  $\pi_{y,CH_3}$  with the  $3b_2$  orbital. The resulting bonding and antibonding combinations are indicated in the  $x$ - and  $y$ -component spectra in the figure.

It is interesting to note that it is only in the  $\sigma$  symmetry ( $p_z$ ) that the methyl group participates in the substrate hybridization. It should thus not be expected that the rotation of the methyl group around the C–C  $\sigma$  bond should be affected by the interaction with the substrate. This is indeed verified by direct calculation.

We will end this section by comparing the chemisorption energies of the formate and acetate, where the formate is substantially more strongly bound to the substrate. The binding energies turned out to be rather method-dependent with DFT giving 3.7 and 3.3 eV for formate and acetate, respectively, while Hartree–Fock resulted in 4.8 and 4.0 eV. For strongly ionic interactions the contribution of dynamical correlation to the bonding is expected to be small (using the ionic dissociation limit) and this is indeed the case; for formate the contribution was found to be only 0.2 eV. The reason for the varying results is that the ionization potential of the  $Cu_{10}$  cluster used is substantially overestimated at the DFT level while it is underestimated compared to the experimental workfunction using Hartree–Fock. In spite of this, both

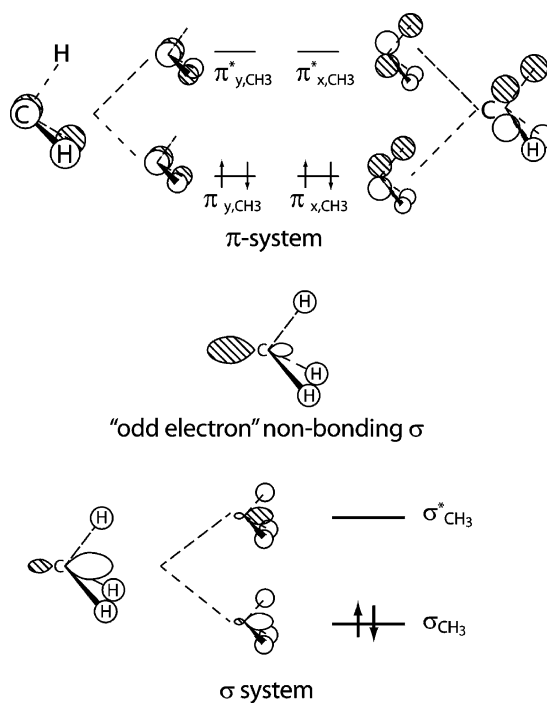


Fig. 68. Group orbitals of the pyramidal methyl radical used in the analysis of the bonding to the carboxylic group. The  $\sigma$  bond involves the singly-occupied non-bonding fragment  $\sigma$  orbital.

methods result in a larger binding energy for formate than acetate. The origin of this can be traced to the electron donating methyl group, which destabilizes somewhat the anionic state for acetate. In fact, the computed electron affinities of the two molecules are 3.3 eV (formate) and 2.9 eV (acetate). As seen from the parallel dipole moment curves in Fig. 66, both adsorbates have the same ionicity and the difference in binding energy can thus be related to the difference in electron affinity, i.e. the energy gained from the electron transfer. Once the ionic state has been reached the interaction with the substrate is very similar.

#### 4.4.3. Adsorption of ammonia on Cu(1 1 0)

The occupied orbitals of  $\text{NH}_3$  are, using  $C_{3v}$  notation,  $1a_1 2a_1 1e 3a_1$ . For free  $\text{NH}_3$ , the two lowest unoccupied orbitals are the  $4a_1$  and the doubly degenerate  $2e$  orbital. Choosing the  $z$ -axis along the  $C_3$  axis, the  $2p_x$  and  $2p_y$  orbitals correspond to the  $E$  representation and the  $2p_z$  and all nitrogen  $s$  orbitals to the  $A_1$  representation. The XE spectra for ammonia/Cu(1 1 0) are depicted in Fig. 69 together with the corresponding calculated spectra. Assuming an adsorption structure where the ammonia  $C_3$  axis is positioned near the surface normal, states of mainly  $e$  symmetry are expected in normal emission and the  $a_1$ -derived electronic states in the  $2p_z$  spectrum. However, the saturated  $\text{NH}_3$  monolayer is found to induce strong adsorbate–adsorbate interaction, causing the molecules to tilt, possibly in a bilayer-like structure with two  $\text{NH}_3$  per unit cell. In the XE spectra, this is revealed by the fact that both the  $3a_1$  and the  $1e$  transitions are visible in both spectra. Based on the angular distribution of the XE spectra, we have been able to estimate a mean tilt angle from the surface normal of 40–45° for the saturated monolayer. It

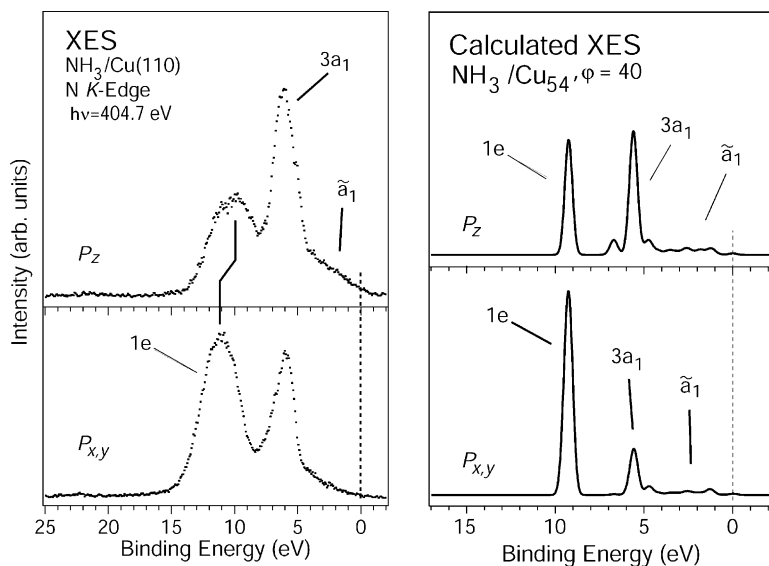


Fig. 69. Experimental (left) and computed (right) decomposed XE spectra of NH<sub>3</sub>/Cu(1 1 0). The upper panels contain states of mainly a<sub>1</sub> symmetry and the lower ones mainly e symmetry. In order to find agreement with experiment the molecules must be tilted ( $\approx 40^\circ$ ) in the calculations.

is clear that hydrogen bonding between the molecules is a significant factor in causing the observed tilt and building up the overlayer structure.

The chemical bonding to the surface is achieved via orbitals of a<sub>1</sub> symmetry. The adsorbate–substrate hybrid levels exhibiting mainly metal character are represented by the  $\tilde{a}_1$  states. It has been shown that back-donation into the previously unoccupied ammonia 4a<sub>1</sub> orbital, and a simultaneous 3a<sub>1</sub> donation into the substrate plays an important role in the surface chemical bond [76].

The adsorption of NH<sub>3</sub> on transition metals has traditionally been explained as the formation of a 3a<sub>1</sub> metal bonding combination together with a strong dipole interaction with the substrate. However, while this simple line of reasoning regarding the covalent bond might hold for some metals it is certainly not true for all. For instance, both the position and population of the metal valence bands are crucial in the bond formation. In the case of copper, the d band position implies that both the bonding and antibonding 3a<sub>1</sub> hybrids will be occupied. In previous studies, this has led to the conclusion that the covalent contribution to the adsorption energy instead goes via the metal 4sp band [177–179].

Previous theoretical work on small Cu clusters has attempted to make a subdivision between covalent and electrostatic contributions to the total adsorption energy. The conclusion was that the major part of the adsorption energy can be associated to the electrostatic contribution [177,180]. A standard CSOV analysis does not resolve this issue since there is no straightforward way to make a subdivision between the contributions; polarization steps are also important for the formation of covalent bonds. Instead we chose to investigate how much of the adsorption energy that can be accounted for by utilizing a purely electrostatic model; this provides an upper limit to the electrostatic contribution.

There are two different types of electrostatic interaction to be considered: the ammonia dipole interaction with the surface and the ionic interaction due to charge transfer between the molecule and the substrate. The first interaction can be estimated to be 0.02 eV using the calculated dipole moment of the

free  $\text{NH}_3$  molecule of 1.8 Debye and an image plane centered within the first Cu layer. From this low value we can conclude that the direct dipole contribution can be neglected. To obtain the ionic contribution, we estimated the charge transfer by calculating the Mulliken charge on the adsorbate. The result was a charge of about +0.15, giving a total electrostatic contribution of  $\sim 0.1$  eV, assuming the same image plane as above. Although we have to be careful with the absolute values, the obtained electrostatic contributions are significantly lower than, e.g. the calculated DFT adsorption energy of  $\sim 0.78$  eV. This means that the bonding only can be viewed within a covalent description, with more or less polar character.

Analyzing the covalent contribution in more detail reveals that the charge transfer goes via the  $A'$  symmetry states, i.e. through the adsorbate  $a_1$  levels. Our results indicate that the important covalent contribution to the bonding comes from the donation of the  $3a_1$  molecular orbital into the substrate and a subsequent back-donation into the  $4a_1$  orbital. Since the electronic charge on the adsorbate decreases upon adsorption (+0.15) the donation of the  $3a_1$  into the substrate dominates. However, back-donation into the  $4a_1$  orbital also contributes to the bonding. In addition, based on overlap population analysis, we find the overall interaction between the ammonia  $3a_1$  and the Cu 4sp valence band to be slightly bonding; this is in agreement with previous work on copper surfaces. In terms of the overall contribution to the adsorption energy, this is however not found to be the dominating interaction of the Cu 4sp band. In the initial interaction with the surface, the doubly occupied  $3a_1$  orbital will experience repulsion by the metal states of  $\sigma$  symmetry. This repulsion must be reduced in order for the molecule to approach close enough to form a bond to the surface. As indicated by substrate population analysis, this is accomplished by polarizing the central 4sp density out towards the surrounding metal centers. The result is a dative type stabilizing [122] interaction between the  $3a_1$  orbital and the substrate, allowing for the surface chemical bond to be formed.

#### 4.4.4. *More complex molecules and interactions: glycine and hydrogen bonding*

Having documented the bonding properties of the carboxylic and amino groups it is possible to extend the discussion to more complicated molecules. The interaction of a methyl group with adsorbed formate is represented by acetate/Cu(1 1 0) [56]. Another interesting system is the simplest amino acid glycine adsorbed on Cu(1 1 0); the most stable adsorption structure, deduced from a combination of core-level spectroscopy and theory [174], is shown in Fig. 70B. In this system, the oxygen atoms are aligned along the  $[1 \bar{1} 0]$  direction of the substrate and a second chemisorption bond is formed at the nitrogen end of the molecule involving Cu atoms in the neighboring  $[1 \bar{1} 0]$  row. As in the case of formate and acetate, this enables a complete partition into atomic  $2p_x$ ,  $2p_y$ , and  $2p_z$  contributions providing a truly detailed picture of the electronic structure of the adsorbed glycine [57,79]. This indeed opens fascinating perspectives as to the applications of XES to the study of larger, biologically interesting molecules in interaction with substrates.

One of the purposes with the previously discussed applications was to build up knowledge of the interactions of specific chemical groups with the metal substrate. The formate adsorption system represents the bonding of the carboxylic group, which was found to be mainly ionic with some covalent contributions in the  $a_1$  and  $b_2$  symmetries. The effect on the molecular orbital structure from adding a methyl group to the formate to give acetate could be described in terms of bonding and anti-bonding combinations of the original formate orbitals with those of the added methyl group. For ammonia, we have obtained similar results with orbital modifications in the  $a_1$  symmetry leading to some depletion of occupied states and that the previously unoccupied  $4a_1$  orbital contributes to the spectrum near the Fermi

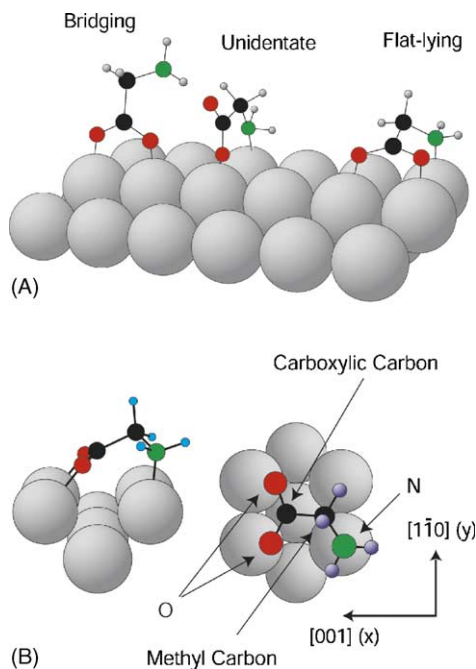


Fig. 70. (A) Optimized adsorption structures for deprotonated glycine on Cu(1 1 0) with, from left to right, bridging, unidentate and the most stable flat-lying species. (B) Details of the most stable flat-lying structure.

level. We will now investigate to what extent we can transfer this knowledge to a combined system, i.e. glycine adsorbed on Cu(1 1 0). Glycine is the simplest amino acid and can chemically be described as amino-acetic acid. Thus, it consists precisely of the chemical groups that have been investigated.

The chemistry of glycine adsorbing from gas phase onto Cu(1 1 0) has been studied by Barlow et al. [181] using reflection absorption infrared spectroscopy (RAIRS). The chemistry is interesting with several different adsorption structures, depending on the experimental conditions, until the most stable, ordered ( $3 \times 2$ ) structure is reached. At the lowest temperatures (below 85 K), some of the glycine molecules were found to be still protonated, while at higher temperatures all adsorbates existed in the deprotonated form. The initial adsorption was determined to be bridging through the carboxylic group (see Fig. 70A) with a computed chemisorption energy of 1.2 eV [79], but at higher coverages becoming unidentate with respect to the carboxylic group and bonding also with the amino end; the energy gain is 0.11 eV. The driving force behind this restructuring can be assumed to be the lateral repulsion between the standing up, polar molecules at the surface, which can be alleviated by rearranging the dipoles. Finally, annealing of this high-coverage phase to 430 K resulted in bridging bonding at the carboxylic group and bonding at both the amino and carboxylic ends gaining another 1.02 eV assuming also the release of  $H_2$  (Fig. 70B). That this most stable structure for adsorption on the clean substrate does not occur at the lower temperatures is due to the presence of the hydrogens at the surface (or subsurface) that presumably force the carboxylic group to bind unidentate. We note in passing the similarity in behavior of the carboxylic group in aqueous solution and at the metal surface: the protons can be viewed in the chemisorption case as very effectively “solvated” by the conduction band electrons in the metal. The structural model for the final molecular geometry is in agreement with the results of the photoelectron

diffraction [182] study by Woodruff and coworkers and with our own analyses of the geometry on the basis of experimental XA and XE spectra and density functional calculations [57,79,174].

In the glycine molecule there are three different elements (C, N, O), which can easily be distinguished in threshold-excited XES. The two chemically different carbon atoms in the carboxylic and methyl groups need some special consideration, however, and this requires consideration of the X-ray absorption spectrum. The fact that the two carbons give rise to energy-separated XAS resonances can be used to selectively excite the core-levels, thus achieving a separation between the two carbon groups. The carboxylic carbon spectra were thus recorded at the  $1s \rightarrow \pi^*$  threshold at 288.3 eV with the  $E$ -vector of the incident light held along the surface normal, which gives a maximum X-ray absorption cross-section for these emission spectra. The spectra of the methyl group were measured at an excitation energy of 291.2 eV, which corresponds to threshold-excitation to a C–H  $\sigma^*$  resonance [174]. In this way, the spectra for all four heavier atoms in the adsorbate could be obtained. By furthermore using the azimuthal orientation of the adsorbate on the substrate, the spectra could be additionally decomposed into contributions from the  $2p_x$ ,  $2p_y$ , and  $2p_z$  components of each molecular orbital as shown in Fig. 71.

The bonding of glycine to the surface can be understood in terms of the bonding of the end group building blocks ammonia and formic acid. In similarity with [61], the carboxylic group of glycine deprotonates to form a bond with two (almost) equivalent oxygens. The nitrogen binds with a lone pair sticking into the surface similar to the case of ammonia [76]. The X-ray emission data of nitrogen show the same hybridization of  $p_z$  levels with the surface, which in the case of ammonia was interpreted as a  $3a_1-4a_1$  hybridization with the metal. The carboxylic end of the molecule also forms bonds through hybridization of  $p_z$  levels with the surface, as was also the case of formate. One important difference here

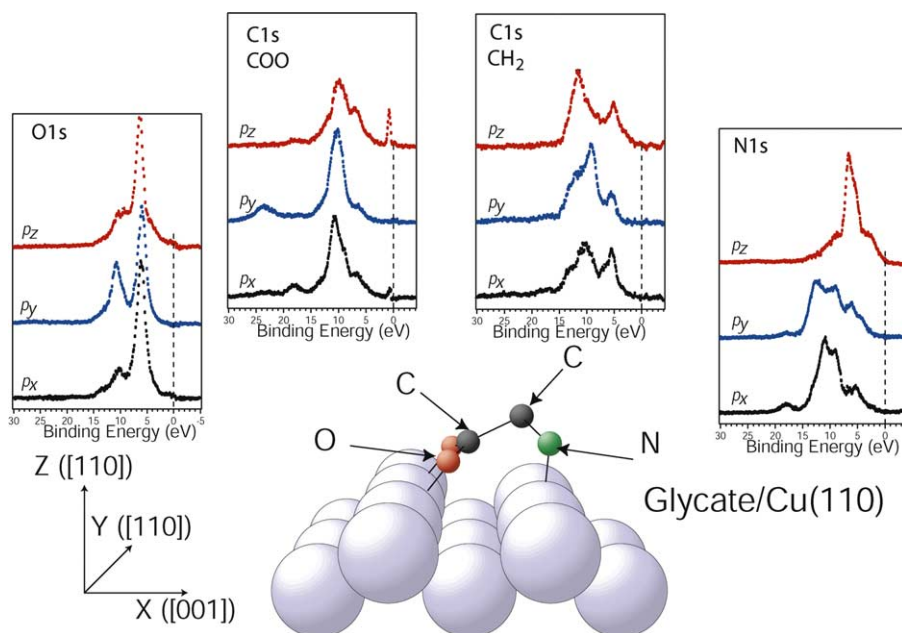


Fig. 71. Symmetry- and atom-resolved XE spectra of deprotonated glycine on Cu(1 1 0) displaying clockwise from the left: oxygen, carboxylic carbon, methyl carbon and nitrogen K shell XE spectra with from top to bottom the  $p_z$ ,  $p_y$  and  $p_x$  spectrum contributions.

is that the plane of the carboxylic group of glycine is no longer normal to the surface, but is more parallel to it. For glycine, the carboxyl  $\pi$  orbitals point directly into the surface, and are responsible for the bonding, in contrast to the case of formate where the carboxylic  $\pi$ -type orbitals are not involved in the interaction with the surface. Still, a large part of the chemical bond between the carboxylic group of glycine with the surface should come from a formation of an image charge in the surface, like in the case of the carboxylic acids.

In order to analyze the spectra, theoretical calculations were performed on a model of the adsorbate system which included 1 glycine on a cluster model of the Cu(1 1 0) surface consisting of 15 all-electron copper atoms. For this system, all degrees of freedom of the adsorbate were optimized and both XA and XE spectra were computed and compared with experiment as well as with the previously discussed experimental and computed spectra for formate; the results for XES are shown in Fig. 72.

There are several comments to be made here. If we first focus on the glycine oxygen spectra we find a very good agreement for both the  $p_x$  and  $p_z$  spectra, but for the  $p_y$  spectrum the intensity ratio between the two main components is inverted compared with experiment. This was also found for the calculations of the oxygen spectra for formate and in that case it was necessary to perform the full symmetry-selective calculation. As discussed in Section 4.4.2, this is due to the near-degeneracy of the two core levels in the equivalent oxygens. It might be expected that the same effect should apply also in the case of glycine, but inclusion of the interference effects turns out to have smaller effects here and the origin of the discrepancy must be sought elsewhere. A clue to the solution is found from the XA spectra where in particular the spectrum for nitrogen is poorly represented in the calculations.

In the model with a single adsorbate on the cluster, we have neglected the presence of the neighboring adsorbates. This resulted in an adsorbate structure that is in fairly close agreement with the molecular structure determined experimentally. The coverage of glycine molecules on the surface is high, however, which makes it possible that the adsorbed glycine molecules can interact through intermolecular hydrogen bonds. In order to examine this possibility, we have optimized the structure of two glycine molecules on a  $\text{Cu}_{36}$  cluster where also the copper atoms directly involved in the bonding were relaxed; here a hydrogen atom on the amino group of one of the molecules is found to exhibit a typical hydrogen bond length (1.88 Å) to one of the oxygens. The internal glycine structure obtained is, however, not very different from the one obtained from the earlier optimization of a single glycine.

Computing both the XAS and XES from this model of two hydrogen-bonded glycine molecules on the cluster, our calculations show that, particularly for the nitrogen, the XA spectra are very much affected by the inclusion of the hydrogen bond in the model (Fig. 73). This might be considered surprising since the hydrogen bond is energetically weak. However, as discussed in the case of spin-uncoupling in unsaturated hydrocarbon adsorption [169], the binding energy is always the balance between the bonding gained and the cost to rehybridize in order to form the bond. Thus, a weak bond does not imply a weak interaction, but a small resulting net energy gain. We will return to this topic again when we discuss the adsorption of alkanes and for now we content ourselves with noting the significant effects on the nitrogen XA spectrum from the introduction of one H-bond. In the previous investigations, where only one glycine molecule was included in the model, we tentatively assigned the discrepancy between the calculated and the experimental XAS data for nitrogen as due to difficulties to describe typical Rydberg state interactions with the surface. However, these discrepancies should rather be attributed as due to the lack of hydrogen bonding interactions in the smaller model.

For the oxygen, it is mainly the XE spectra that are modified in the direction of the experiment. This is the expected effect in a hydrogen bonded system: the absorption measures the *unoccupied* 2p density of

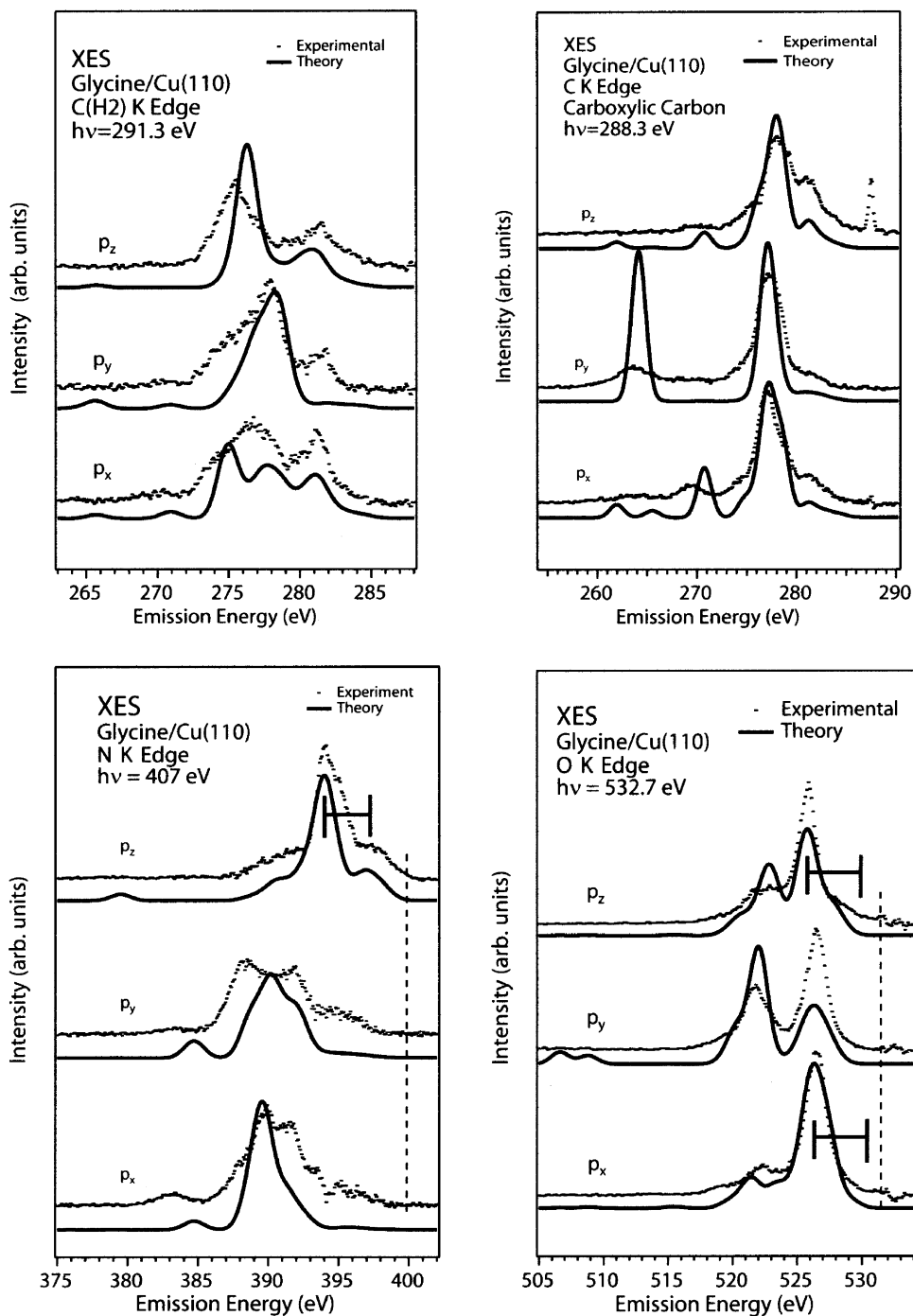


Fig. 72. Comparison of experimental (dotted) and computed (solid)  $2p_x$ ,  $2p_y$  and  $2p_z$  resolved XE spectra of glycine on Cu(1 1 0). The Fermi level is indicated by the vertical dashed lines. The chemical bond to the surface involves the N  $2p_z$  and O  $2p_{xz}$  orbital components; the bonding and antibonding components in the interaction with the metal valence bands are indicated by the solid lines.

### Hydrogen bonding in glycine

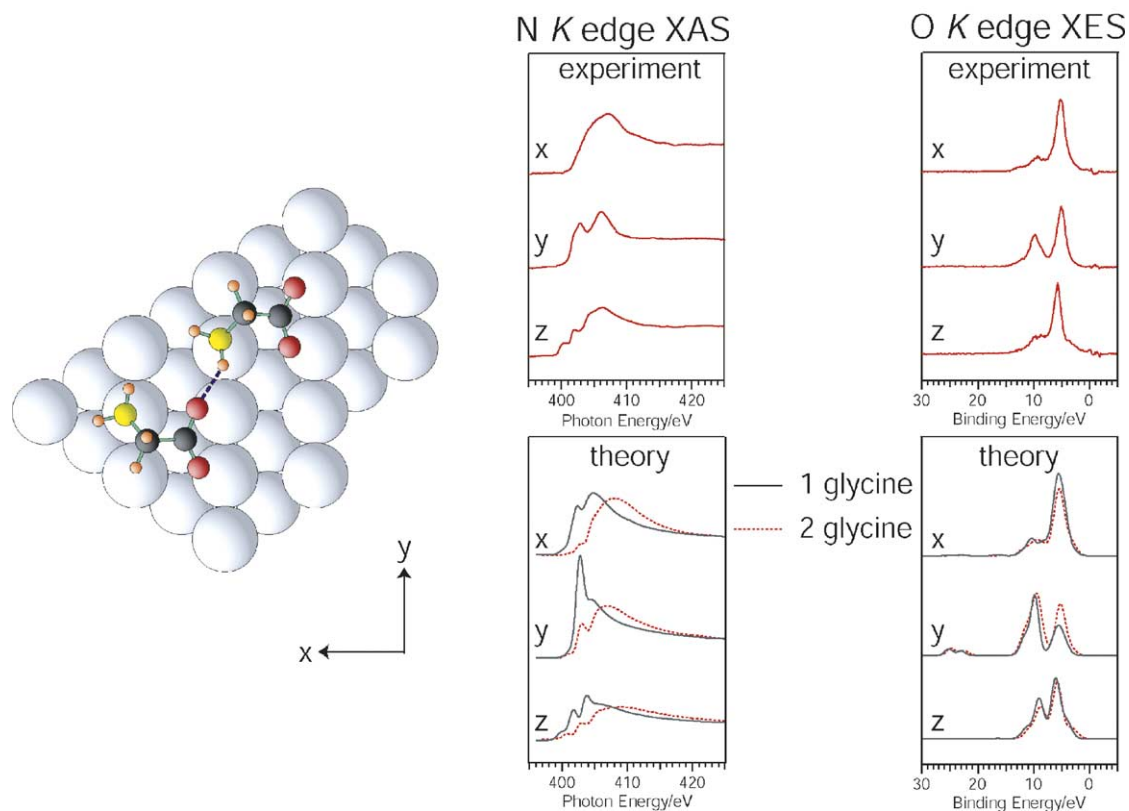


Fig. 73. Comparison of computed (bottom) and experimental (top) XA (left) and XE (right) spectra at the nitrogen and oxygen K-edges, respectively. The theoretical spectra compare two models: a single molecule (black) and two (red) molecules connected through an N–H···O hydrogen bond.

states with higher sensitivity on the electron deficient proton donor while emission measures the *occupied* 2p density which is greater on the electron-rich acceptor, i.e. on the oxygen. Within the (3 × 2) overlayer, however, both oxygens can interact with protons: one with a proton from the amino group and the other with one of the protons in the aliphatic –CH<sub>2</sub>– of the aliphatic carbon as well as with a neighboring amino group. To investigate whether this could have additional effects we have optimized the full overlayer structure using a plane wave-based DFT calculation with periodic boundary conditions [183]; the resulting structure is shown in Fig. 74.

Based on this geometry we took as our final computational cluster model three glycine molecules on an all-electron Cu<sub>37</sub> cluster and both XA and XE spectra were computed. For the nitrogen no significant changes are obtained in the absorption spectra from adding the third glycine; the amino group was already fully coordinated in the dimer model. In the oxygen p<sub>z</sub> XA spectrum there is an interesting development as the modeling is extended from one to three glycines (Fig. 75). Introducing the first H-bond (Fig. 75, middle column) we find that a feature at around 535 eV appears, also present in the experiment, which is interpreted as another sign of the hydrogen bond formation, but weaker than seen in

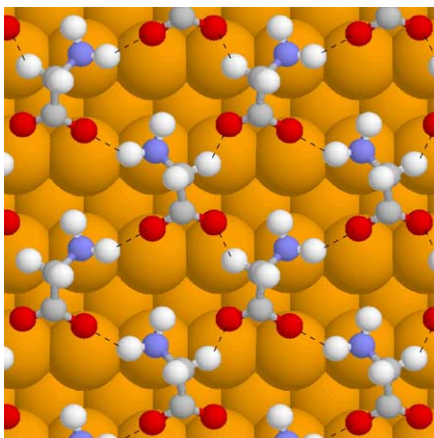


Fig. 74. Optimized structure of  $(3 \times 2)$  overlayer of deprotonated glycine on Cu(1 1 0). The intermolecular hydrogen bonds are indicated by the dashed lines.

the nitrogen spectrum. It could be questioned whether this feature is the result of molecular orbital changes due to the hydrogen-bond formation or due to the slight change in geometry compared to the cluster optimization. This was tested by computing the spectra with the second glycine removed from the cluster. With only one glycine, in the same optimized structure, the additional peak disappears and it is

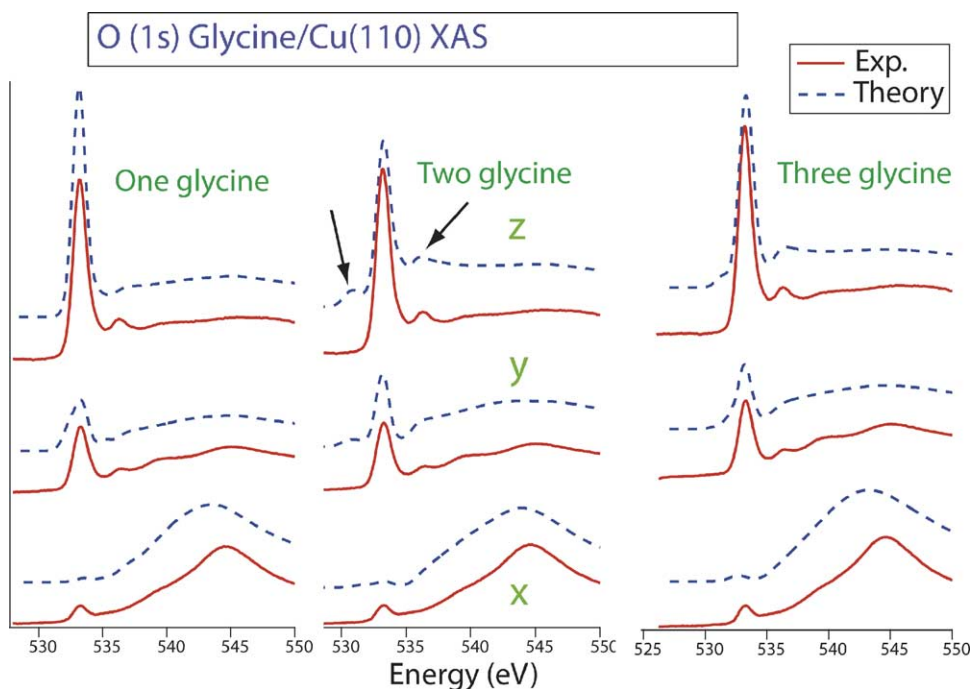


Fig. 75. Comparison of computed (upper curves, blue) and experimental (lower curves, red) (X, Y, Z)-resolved XA O 1s spectra of glycine on Cu(1 1 0) for three different cluster models. From left to right: a single molecule, two molecules interacting through a  $\text{N-H} \cdots \text{O}$  H-bond and three molecules with a fully coordinated carboxylic group.

thus clear that this feature is due mainly to direct orbital changes due to the hydrogen bond. Analysis shows that this feature is dominated by contributions from the oxygen atom directly involved in the hydrogen bond. In the computed H-bonded  $O p_z$  spectrum, we find an extra peak at about 530 eV which is not present in the experiment. An analysis of the computed XA data shows that this feature is dominated by contributions from the oxygen atom, which is not involved in the hydrogen bond to the amino end of the neighboring molecule. Finally, extending the model to include the third H-bonded glycine removes this feature leaving the final spectra in excellent agreement with experiment.

The formation of intermolecular hydrogen bonds could explain the  $(3 \times 2)$  structure as obtained from LEED. The arrangement depicted in Fig. 74 (which is consistent with the LEED data) is one of two possibilities to form hydrogen bonds involving both oxygens on all of the adsorbates. The structure shown in Fig. 74 is the so-called heterochiral for which the two molecules in the unit cell have C–C–N angles in different directions. Recently, also a homo-chiral model was proposed from STM investigations of glycine on Cu(1 1 0) [184], but this has been questioned in later work [185,186]. We will discuss our own investigation of the two overlayer structures in terms of X-ray spectroscopies and our extension to compute XE spectra within a plane waves framework [80].

Optimizing the two overlayer structures using the Dacapo program [80] we find a very small, 0.035 eV per molecule, energy difference between them favoring the heterochiral structure. In both structures, there are H-bonds to each oxygen in the carboxylic group, which makes the XA and XE spectra for the two structures look very similar and we cannot distinguish between the two possibilities. Computing also the STM images from the two models using the Tersoff–Hamann approximation [187] the agreement is quite poor for the homochiral model, but not completely convincing for the heterochiral. Nonetheless, it seems clear that the observed structure should be the heterochiral one, since the homochiral would lead to four inequivalent oxygens in disagreement with the photoelectron diffraction data of Woodruff and coworkers [185,186].

We will end this section by discussing in some more detail the anomalous oxygen  $p_y$  spectrum. For formate, we found that symmetry selection rules were important for establishing the intensity ratio between the two main peaks, but for glycine in the model with two H-bonded molecules the effects were much smaller but in the expected direction. We can now investigate this for the more complete model with three glycines; the results are shown in Fig. 76. We find very large effects from introducing the intermediate state in the analysis both between the non-resonantly excited and the symmetry-selective calculations and also among the various excited intermediate states. However, there is no clear-cut selection that brings all projections into agreement simultaneously; for the  $p_y$  symmetry we find a very good intensity ratio by going up to the LUMO + 8 for the intermediate state, but this destroys the agreement for the out-of-plane  $p_z$  component. The latter is instead very well represented by the LUMO intermediate state. Using states in-between these resulted in spectra very similar to the ones shown in the figure. So what can be wrong?

There are four main effects that we may consider: errors in the geometry, problems with the representation of the intermediate state, vibronic coupling and dynamics in the core-excited intermediate state during the lifetime of the core hole ( $\approx 3.6$  fs). There are some discrepancies in the comparison with experiment for the oxygen geometry for which the CPMD optimized structure (used for the three-molecule model) has copper-oxygen distances of 2.13/2.10 Å compared with the experimental 2.02/2.00 Å [185]. This could affect the spectra somewhat, but not introduce a large discrepancy. The XA part of the symmetry-selective calculation on the other hand is performed without the presence of the core hole. This is due to the necessity to maintain the equivalence between the two oxygens in the calculations

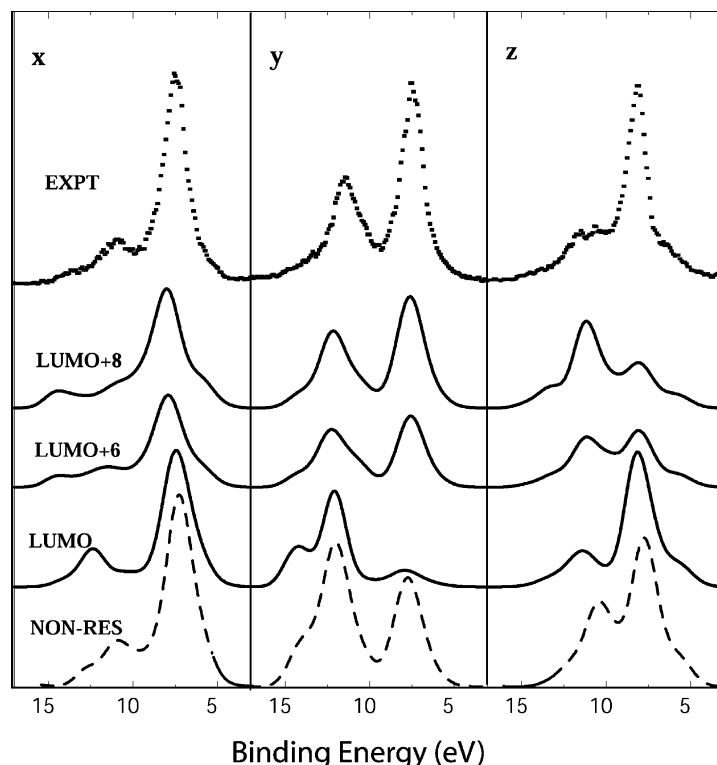


Fig. 76. Computed non-resonant and resonantly excited XE spectra using three H-bonded deprotonated glycines on a  $\text{Cu}_{37}$  cluster model of the  $\text{Cu}(1\ 1\ 0)$  surface. In sequence from bottom to top we show the computed non-resonantly excited and resonantly excited using the LUMO, LUMO + 6 and LUMO + 8 intermediate states in comparison with experiment (top). The panels from left to right show the  $p_x$ ,  $p_y$  and  $p_z$  components.

in order to obtain the symmetry-selective effects; a localized core hole would break the symmetry. However, although the excited states without the presence of the core hole tend to be very poorly represented, we do not find significant differences between the spectra generated with and without the core hole in this particular case.

Using our implementation of XES in the CPMD code [188] we can reinvestigate the oxygen XE spectrum with respect to full coverage as well as core hole dynamics. The results are shown in Fig. 77. This is an interesting alternative improvement of the theoretical X-ray emission spectrum: after the X-ray absorption, the core hole excited-state has a finite lifetime of approximately 3.6 fs, during which the system can evolve. Hence, the ground state geometry is strictly speaking not representative for a XES simulation. To account for this lifetime effect, the core hole excited-state dynamics was followed for 3.6 fs starting from the (geometry optimized) hetero structure with nuclear velocities set to zero. Dynamics in a non-resonant core hole excited-state was modeled by performing Car-Parrinello MD on the system with one oxygen pseudo-potential replaced by a pseudo-potential generated from an electron configuration  $1s^1 2s^2 2p^3$  with single occupation in the 1s orbital.

The geometry of the carboxylic group changes somewhat during the 3.6 fs long simulation. The C–O bond to the core hole excited oxygen atom increases by 0.04 Å and the other C–O bond decreases by a similar amount. The changes in the geometry, due to the core hole excited-state dynamics, only resulted

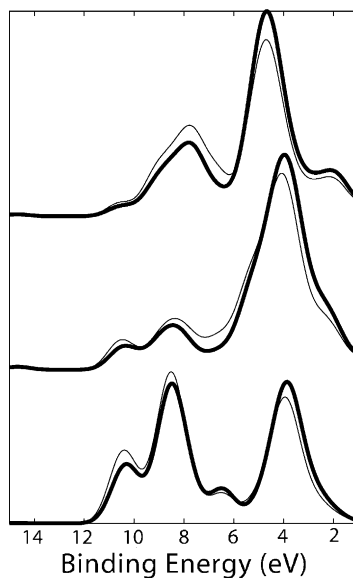


Fig. 77. Computed non-resonantly excited O 1s XE spectra using cluster model of three H-bonded deprotonated glycines with (thick lines) and without (thin lines) accounting for the core hole lifetime. From top to bottom we show symmetry-resolved spectra corresponding to  $p_z$ ,  $p_x$  and  $p_z$ .

in minor changes in the XE spectrum, however. Although the spectral changes were in the right direction the effect was too small to account for the discrepancy between theory and experiment in the oxygen X-ray emission spectra. A complete resolution of this discrepancy must await future work.

In conclusion, we find that the intramolecular structure of glycine on Cu(1 1 0) is mainly determined by the adsorbate–surface chemical bond, but that the arrangement of the molecules on the surface seems to be governed by the intermolecular hydrogen bonds.

#### 4.5. Saturated hydrocarbons

We have in the previous sections described different chemisorption bonding interactions. In contrast, the adsorption of saturated hydrocarbons on metallic substrates is typically considered as an example of a weak physical interaction, which is dominated by van der Waals forces. The classification of this type of interaction, denoted physisorption where no direct bonds are formed between the adsorbate and substrate, has been based on the heat of adsorption. A physically adsorbed state is considered to be one in which the heat of adsorption is comparable to the heat of vaporization or sublimation. For the interaction of alkanes with metal surfaces, the heat of adsorption is similar to the sublimation temperature and the interaction has consequently been characterized as a weak physical adsorption. In this section, we will demonstrate based on XES, XAS and DFT studies of *n*-octane on Cu(1 1 0) that there are still surprisingly large and important chemical bonding interactions with the surface that are beyond a physical adsorption picture. There are relatively large internal geometry distortions in the molecule and a relatively short H–Cu bond distance due to this interaction. The C–C bond is shortened and the C–H bond pointing towards the surface elongated due to the Cu–H interaction. This means that the molecule has taken a small step towards dehydrogenation. There is thus an important interaction of the molecular orbitals involving the

CH group that points to the surface with the sp and d bands in the metal. It leads to a weak electron pairing between the CH and Cu atoms.

#### 4.5.1. *n*-Octane adsorbed on Cu(1 1 0)

Adsorption of saturated hydrocarbons on a Cu substrate is a good model system for the purpose to investigate the electronic structure since the d band interaction appears entirely in the occupied states, making the effects more clearly visible and the analysis of the electronic structure easier. There is an advantage to use the (1 1 0) surface with a two-fold symmetry if the molecule adsorbs with preferential alignment allowing projection of the electronic structure in three directions as discussed in the previous sections.

The XE and XA spectra, symmetry-resolved in three directions, are shown in Fig. 78 [189,190]. Note that both the XE and XA spectra are shown on a binding energy scale relative to the Fermi level. Shown in the right part of Fig. 78 are the XA spectra. The top spectrum, showing the  $p_x$  contribution is characterized by a main feature at  $-8.8$  eV binding energy, with a shoulder on the high binding energy side, and in the  $p_y$  spectrum, there is a main feature at  $-6.8$  eV. Both these features can be assigned to different  $CC\sigma^*$  shape resonances. There are spectral features around  $-3.5$  eV binding energy both in the

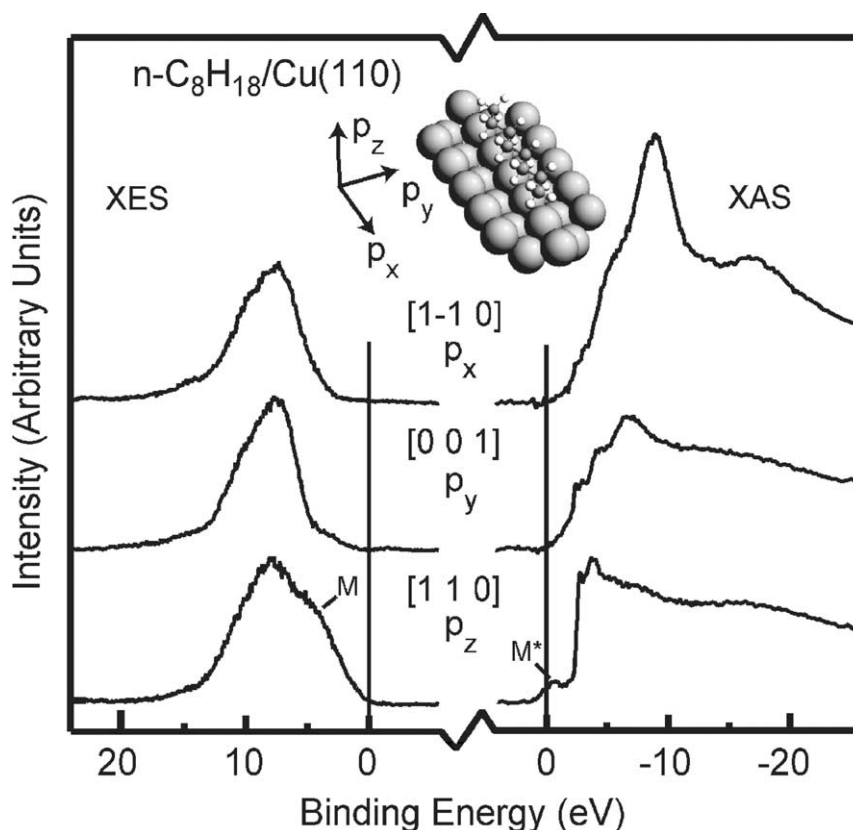


Fig. 78. Experimental symmetry-resolved XE and XA spectra of *n*-octane adsorbed on Cu(1 1 0). The spectra are projected along the three high symmetry directions of the surface. The alignment of the *n*-octane molecule on the surface is shown in the inset.

$p_y$  and  $p_z$  spectra, assigned to transitions into  $CH^*$  orbitals. The  $p_z$  spectrum also shows significant intensity right at the Fermi level, previously denoted  $M^*$  [191]. Since the strong  $CC\sigma^*$  shape resonance has its maximum intensity in the  $p_x$  spectrum we can conclude that the molecular axis is oriented parallel with the Cu rows as shown in the insert of Fig. 78. This observation is consistent with other results using complementary techniques such as reflection absorption infrared spectroscopy (RAIRS) [192,193]. The XE spectra in the left panel of Fig. 78 show the occupied C 2p projected density of states. All these spectra are characterized by a broad feature around 8 eV binding energy. This large width is typical for alkanes, and arises due to band formation [194] and vibronic coupling of the C 2p derived molecular orbitals. The  $p_z$  spectrum, however, shows an additional feature at 5 eV appearing as a consequence of the interaction with the metal surface; we denote this feature  $M$ . We will now turn our attention to a theoretical determination of the adsorbate geometry and electronic structure. This is at present a non-trivial task since, apart from uncertainties due to the choice of functional in the DFT treatment, all interactions are not accounted for in present DFT approaches.

We know that dispersion forces are not accounted for within DFT, so it will not be possible to describe the geometries of systems that are characterized by these weak interactions. Typically, the potential energy curves for weakly bound surface adsorbates are very shallow, leading to a large uncertainty in the adsorbate–substrate distance. The total energy in such cases may thus not be a reliable measure for the theoretical determination of the geometric structure, but the electronic structure should be. This follows from the fact that the dispersion interaction in itself does not in a direct way alter the orbital structure except for the indirect changes caused by distortions of the geometry due to the enhanced interaction with the surface. The molecular orbitals provide a more sensitive measure in this case since orbital interactions depend on the overlaps which depend near-exponentially on the distance. Having available a reliable and accurate way to compute molecular orbital overlap-dependent properties we can thus instead perform a more sensitive systematic investigation of how the XA and XE spectra are influenced by changes of different structural parameters. Comparison with the experimental results allows us then to draw conclusions on the structure of the adsorbed molecule [189].

The positions and intensities of the  $CC\sigma^*$  shape resonances are sensitive to the C–C bond length. The geometry of the adsorbed molecule was determined by systematically computing theoretical XA spectra for different geometries as shown in Fig. 79. The structure of the carbon skeleton was determined by fitting the  $CC\sigma^*$  shape resonances in the XA spectra to the experiment. The best agreement was obtained for a C–C bond length of 1.49 Å [189], which is shorter than for the optimized isolated molecule (1.53 Å). The occupied metal-induced states are not sensitive to changes in the C–C skeleton of the molecules, but to the molecule–surface distance as well as both bond length and direction of the C–H bonds. In order to reproduce the  $M$  feature in the spectral calculations as shown in Fig. 80, the molecule had to be pushed in to a C–Cu distance of 2.7 Å and the C–H bonds pointing towards the surface had to be elongated from 1.10 to 1.18 Å, and rotated towards the surface [189]. In some sense, the molecule has made a small step towards dehydrogenation by weakening the C–H bond and strengthening the C–C bond.

The energy cost for pushing the molecule closer to surface compared to the optimized carbon–metal distance of 2.7–3.0 Å, without changing the internal structure, is 0.75 eV according to the calculations [189]. The energy increase upon rehybridization from  $sp^3$  to the obtained  $sp^{2.8}$  is 0.21 eV at 2.7 Å. The cost of the rotation of the C–H bond is 0.39 eV and the stretch of the bond costs 0.57 eV. This means that the total energy cost for the change in geometry is 1.92 eV. This should be compared with the energy we can expect to gain from the dispersion interaction. If we assume that this is the same as the total

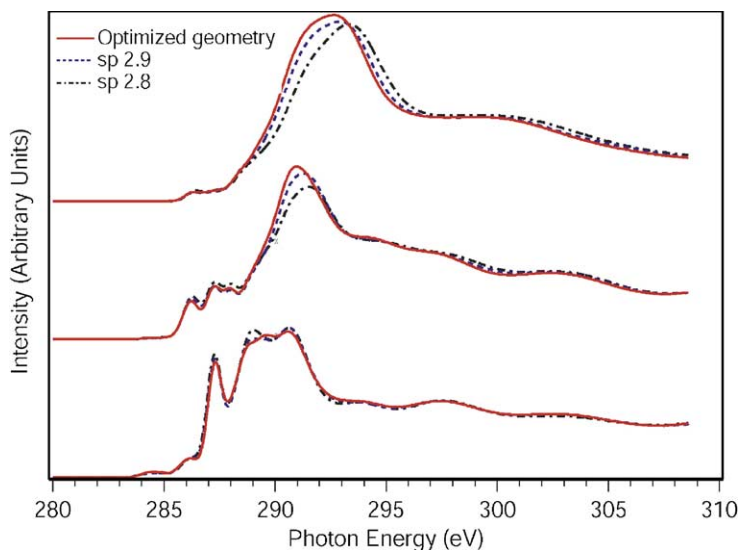


Fig. 79. Calculated XA spectra of adsorbed *n*-octane for different C–C bond lengths and C–C–C angles corresponding to the indicated hybridization schemes.

adsorption energy for alkanes, the energy is approximately 2–4 kcal/mol per carbon atom [195]. This means that the dispersion energy will be between 0.7 and 1.4 eV for octane. It seems not to be energetically favorable, but considering that the structural changes were performed arbitrarily without any geometry optimizations on the surface, the energy cost for the proposed distortion is still reasonable and within the theoretical error bars considering the size of the system.

With this agreement between the experimental and theoretical XE and XA spectra, we can go further and analyze the molecular orbitals involved in the interaction between the adsorbate and surface. Looking at the occupied molecular orbitals and comparing these with the corresponding gas phase orbitals, we find that the CH bonding orbitals pointing in the out-of-plane direction mix with the copper d band to form new three-center orbitals. The out-of-plane CH bonding orbitals span the energy range from 13 to 7 eV. All these orbitals are similar to the corresponding gas phase orbitals, but they also show bonding interaction with the copper d orbitals. Some of these orbitals and the corresponding gas phase orbitals are plotted in Fig. 81. In the region of the copper d band, there is a large number of orbitals mainly with copper d character, but also some CH bonding character, showing mainly antibonding character with the metal atoms, as shown in the orbital on the right in Fig. 81. The intensity in the XE spectra around 5 eV is assigned to these states.

We can summarize the orbital interactions with the Cu substrate in a schematic diagram shown in Fig. 82. The new M band has mainly metal character, but also some carbon character. The octane orbitals contributing to this band are mainly the bonding CH orbitals, since these are closer in energy to the Cu d band, but also to a smaller extent antibonding CH\* orbitals. The band, which is completely occupied, is both bonding and antibonding with the surface, leading to a net repulsion. Also the much broader Cu sp band interacts with the octane orbitals, leading to an extended weak band. The unoccupied part of this band can be seen in the XA spectra as the M\* spectral feature. This indicates that all bonding and antibonding states are not fully occupied. Can we anticipate a potential covalent bonding?

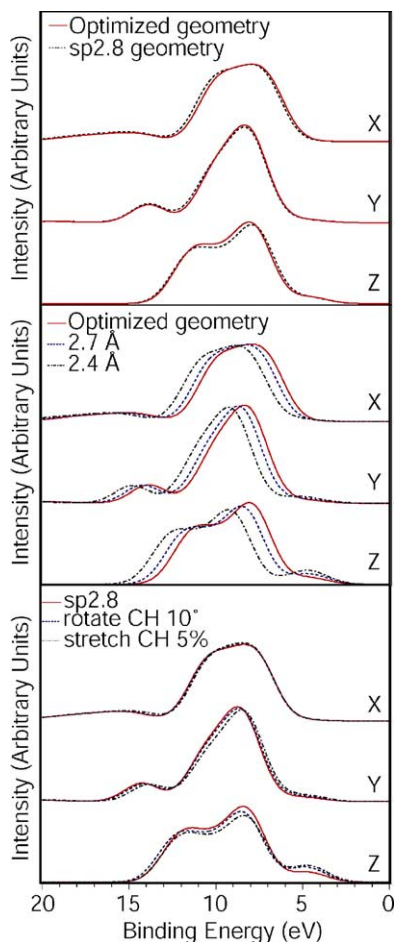


Fig. 80. The top panel shows the calculated XE spectra for two different carbon skeleton geometries in the *n*-octane molecule on a copper cluster. The middle panel shows the carbon–metal distance dependence of the XE spectra. The bottom panel shows the dependence of the XE spectra on changes in the CH bonds.

Fig. 83 shows the difference in charge density compared with the free, but distorted molecule, as it is allowed to interact with the surface. We observe small but significant changes in the charge density. Along the CH-plane, there is a polarization of the C–H bonds towards the C atoms and charge depletion close to the hydrogen atoms. This is part of breaking up the C–H bonds due to mixing of C–H bonding and antibonding orbitals. This mixing leads to a weakening of the C–H bonds and results in the observed elongation of the C–H bonds pointing towards the surface. Along the CuH-plane, there is a loss of charge on the H atoms, and a build up of charge between the H and Cu atoms, which means that there is electron sharing between the adsorbate and substrate. From a closer inspection we can derive that it is mainly the Cu  $p_z$  states that are involved in the bonding. Furthermore, there are some changes in the substrate, which can be related to an spd-rehybridization in the Cu. The net charge does not increase on the molecule, indicating that the bonding model suggested by Wöll et al. [196] is not appropriate for a non-strained molecule. Their model does not allow for much interaction, and the adsorbate–surface distance is too

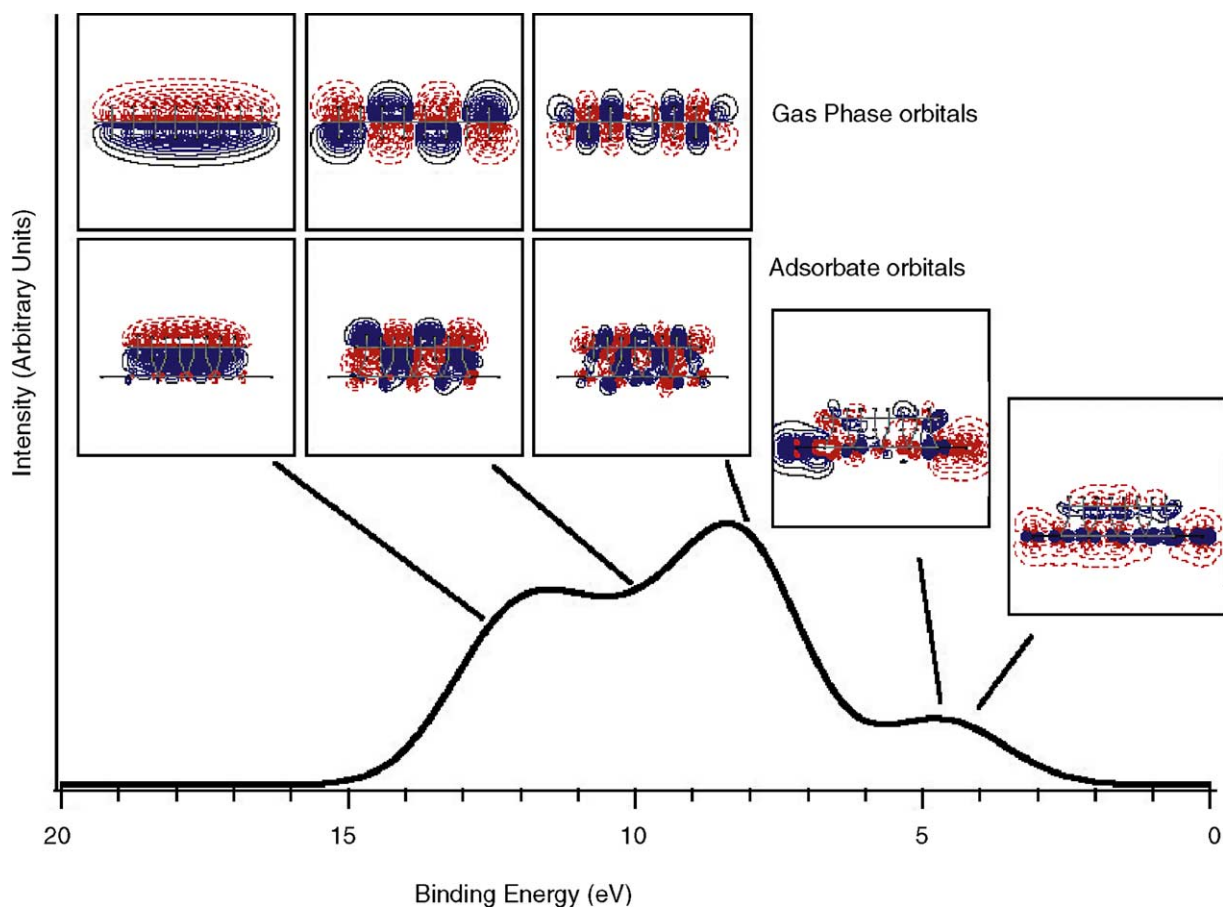


Fig. 81. Computed XE spectrum along the  $[110]$  direction, together with plots of the  $xz$ -projection of some of the corresponding molecular orbitals. The corresponding gas-phase orbitals are also shown.

long to allow for any interaction with the relatively small bonding CH orbitals. Based on our charge density difference plots, we conclude that the interaction is a combination of both donation and back-donation, involving the Cu 4sp band. Even though the bond is weak, it is likely that this is the driving force behind the changes observed in the structure of the molecule.

#### 4.5.2. Difference between octane on Ni and Cu surfaces

As shown in previous work by Hammer and Norskov [105], the nobility of metals is directly related to the position of the metal d band with respect to the Fermi level. Can we predict the differences in interaction of octane with different transition metals, based on that picture?

In Fig. 84, computed carbon local p densities of states, projected along the out-of plane ( $p_z$ ) direction, are shown for octane adsorbed on both Cu and Ni. The main spectral difference between the two substrates is the position of the 3d metal-induced states (M), which follows the position of the metal d band. In Cu, all these states are entirely below the Fermi level, leading to a net repulsion in the interaction with the 3d contribution. However, in the case of Ni the antibonding states continue above the Fermi level, and this interaction can start to contribute to the adsorption energy. In this case, we can anticipate

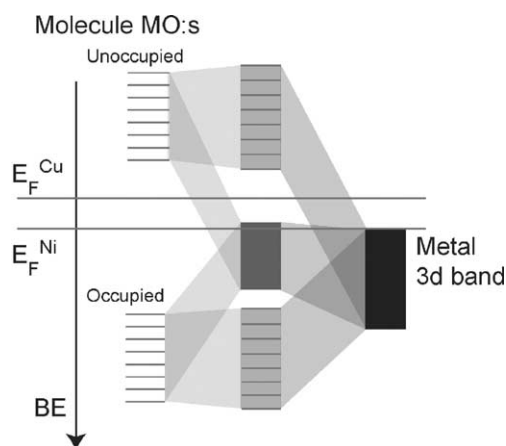


Fig. 82. A schematic figure showing the interaction between the C–H orbitals and the metal d band, which leads to a strong mixing of molecular orbitals.

that the molecule will move closer to the surface, due to the increased bonding, leading to further rehybridization and weakening of the C–H bonds. As the d band moves towards and over the Fermi level, this increases the possibility for charge donation to the surface, and formation of a more dative bond similar to the agostic bonding in organometallic compounds. From these results we can predict, in accordance with [105], that when we move further to the left in the periodic table the bonding will

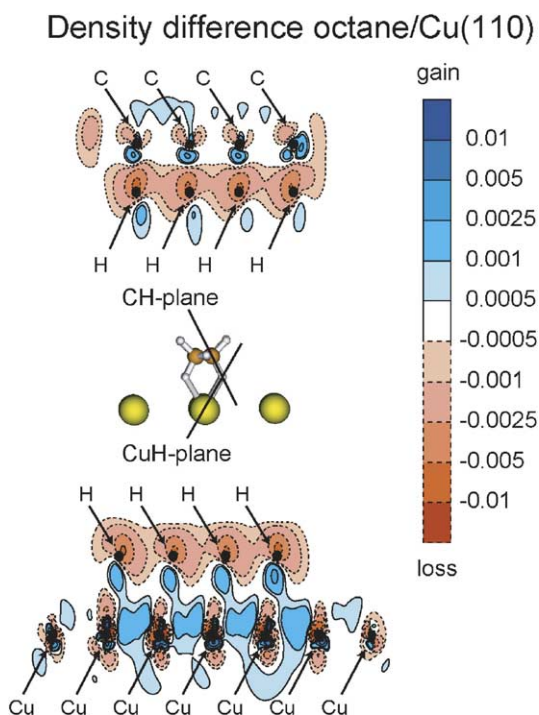


Fig. 83. Charge density difference plotted along the C–H plane (top) and the Cu–H plane (bottom).

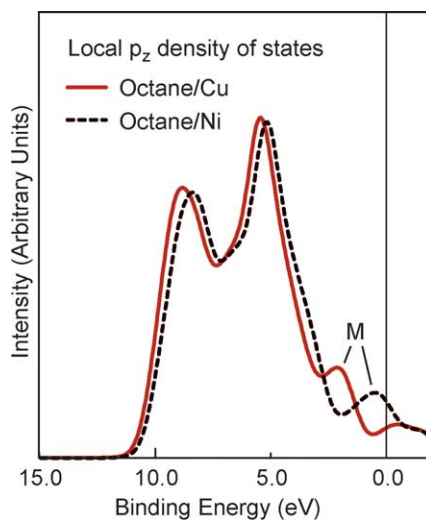


Fig. 84. The calculated local  $p_z$  density of states projected onto the out-of-plane ( $p_z$ ) direction for *n*-octane on Cu and Ni.

become even stronger, and all C–H bonds will be broken, depositing strongly bound carbon on the surface, thus yielding a less efficient catalyst.

#### 4.6. Summary of adsorbate–metal bonding

Let us now summarize what we have learned from all the detailed studies of the different chemisorption systems. In the presented systems in this review, the adsorbate bond strength ranges from 5 to 0.3 eV per functional group in the molecular system. Is it possible to get an overview and relate the electronic structure of the adsorbates to a simple picture of the surface chemical bond?

First of all, we can characterize the interaction in terms of ionic and covalent bonding. The adsorbate species where electrostatic interaction makes a significant contribution to the overall bonding are represented by the carboxylic acids. Since the acidic hydrogen atoms are dissociated from the molecule we can regard these adsorbates as ionic carboxylates. As discussed in Section 4.4.2, there is some charge transfer to the substrate which partly reduces the electrostatic interaction. The ionic contribution to the adsorption strength is of the order of a few eV [56]. In the case of water and ammonia that are molecules with a substantial dipole moment there could be electrostatic contributions of a magnitude smaller than 1 eV. In the water monolayer on Pt(1 1 1), the Pt–O species is oriented with the molecular plane parallel to the surface [172] which optimizes the dipole–image dipole interaction whereas for ammonia the dipole is oriented at an angle of 40–45° to the surface providing only a smaller electrostatic contribution [76]. This is most likely compensated by the formation of H-bonds in the overlayer, which would not be possible for the upright geometry.

Most adsorbates presented in this review interact via covalent bonding, i.e. electron pair sharing. There is either an unpaired orbital, a  $\pi$  electron system or a lone pair orbital on the interacting functional group that facilitates the bonding. The strongest bond is formed for the unpaired radical atom that can interact directly with the metal and form bonding and antibonding states upon interaction with metal d states. It is usually necessary to form such unpaired states through a dissociation process on the surface as

represented by the atomic C, N and O adsorbates. In that sense the reaction is more complex but from a bond perspective we can regard this in a simple way. If only the bonding states are occupied a strong bond is created, as in adsorption on transition metals, whereas if both bonding and antibonding states are occupied Pauli repulsion will make the bond rather weak, as on noble metals. In the latter case, there could still be some bonding involving sp electrons. However, it is not likely that this interaction is strong enough to compensate for the dissociation energy for N<sub>2</sub> and O<sub>2</sub> on noble metal surfaces.

In molecular adsorbate systems where the interaction is mainly taking place through  $\pi$  electron systems we can identify two different bonding mechanisms for N<sub>2</sub>, CO and unsaturated hydrocarbons. Diatomic molecules typically adsorb with the molecular axis perpendicular to the surface whereas the unsaturated hydrocarbons adsorb parallel to the surface. We showed in Section 4.2 the importance of the balance between  $\sigma$  repulsion and  $\pi$  bonding for CO and N<sub>2</sub> on metal surfaces. This balance is affected by the metal coordination which leads to that N<sub>2</sub> only adsorbs in on-top sites whereas CO can populate a large range of different sites with nearly equal adsorption energy. We could ask the question why CO and N<sub>2</sub> do not adsorb with the molecular axis parallel to the surface similar to adsorbed ethylene?

If we look in a simple way on the  $\pi$  electron system of N<sub>2</sub> interacting with a metal surface in a perpendicular geometry and lying flat on the surface there are rather different molecular orbital diagrams that emerge as shown in Fig. 85. As discussed in Section 4.2.1, the  $\pi$  electron system assumes the allylic configuration for the perpendicular geometry. It means that the  $1\pi$  and  $2\pi^*$  orbitals mix with each other to form a new set of orbitals, generating for instance the occupied lone pair orbital. Typically for N<sub>2</sub> adsorption the mixing is of the order of 10–20% into both the  $1\pi$  and  $2\pi^*$  orbitals. Usually, a larger population of the  $2\pi^*$  orbital is observed compared with the depopulation of the  $1\pi$  orbital providing the simple energetic relationship with the position of the d band. However, for a lying-down species the symmetry due to the interaction with the surface is different. As discussed in Section 4.3.1 for adsorbed ethylene, the  $1\pi$  and  $2\pi^*$  levels cannot mix and will instead interact independently with different d orbitals of appropriate symmetry in the metal (see Fig. 85). This bonding mechanism can be described in the discussed spin-uncoupling model. We prepare the interaction by exciting an electron from the  $1\pi$  to the  $2\pi^*$  level generating two unpaired bonding orbitals that can interact with the metal. From the knowledge of the excitation energy of the molecule and the interaction energy of the bond-prepared orbitals, the adsorption energetics and geometries have successfully been predicted for a large number of unsaturated hydrocarbons adsorbed on surfaces. In the case of CO and N<sub>2</sub> the excitation energy is of the order of 10 eV, which is extremely high. It means that the bond-prepared orbital interaction will not be strong enough on most surfaces to compensate this large excitation energy. It is therefore more efficient to slightly mix the  $\pi$  system in the allylic configuration to open for bonding to the surface. In a simple perturbative treatment, this involves only 10–20% of the excitation energy. This geometry is more stable in spite of the  $\sigma$  repulsion that can be avoided in the lying-down geometry. The latter also compensates the internal bond length, where  $\sigma$  interaction shortens and  $\pi$  interaction elongates the bond resulting in essentially no change from the free molecule. In the case of a lying-down species, there is no compensation from the  $\sigma$  system resulting in a strong elongation of the internal bond leading to a precursor state to dissociation.

On specific surfaces such as Fe(1 1 1) and stepped surfaces, where both atoms can more efficiently bond to active sites with energetics overcoming the excitation energy, the lying-down species becomes more favorable [197–199]. A similar balance should be expected for O<sub>2</sub> where the  $1\pi$  to  $2\pi^*$  excitation energy is much smaller, 4.1 eV [139], and where already unpaired electrons are available in the  $\pi$  system for bonding. O<sub>2</sub> usually adsorbs with the molecular axis parallel to most metal surfaces prior to

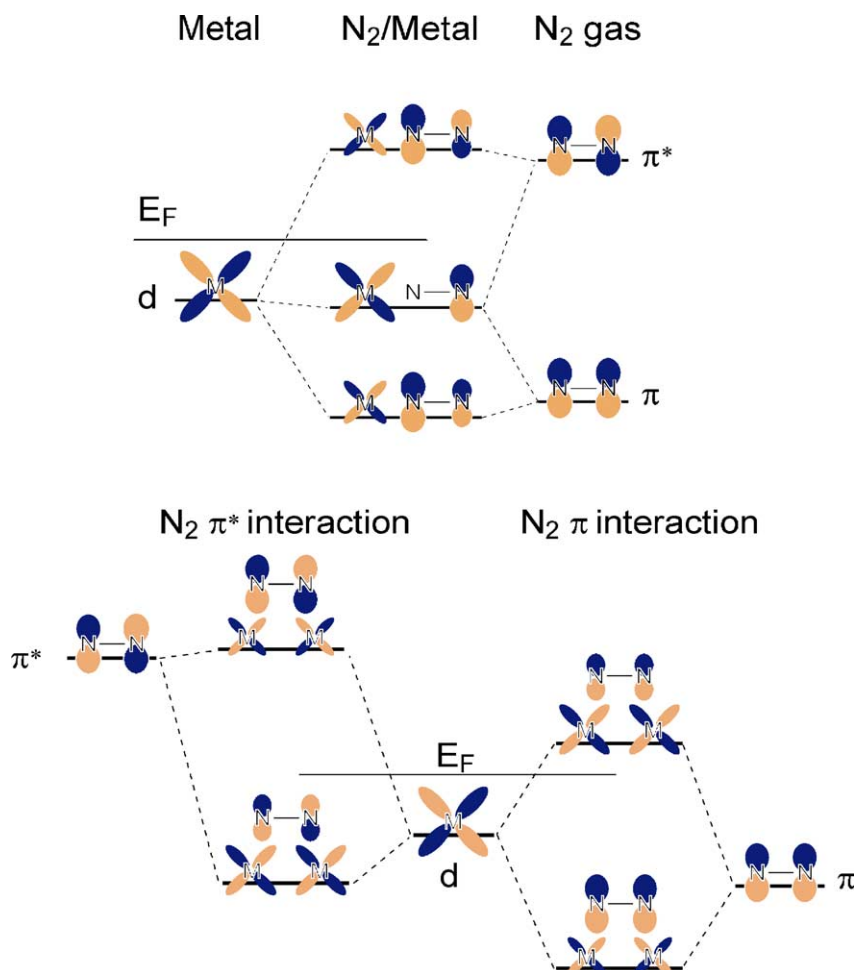


Fig. 85. The molecular orbital diagram for N<sub>2</sub> interaction in a linear fashion with one Ni atom in an allylic configuration and for N<sub>2</sub> interaction side-on with two Ni atoms.

dissociation [19,200,201]. It becomes energetically favorable for the molecule to avoid the perpendicular geometry and adsorb with the molecular axis parallel to the surface. It has been estimated that such a difference in molecular orientation results in a difference in bond energy of 2 eV for O<sub>2</sub> on Ni [202].

The  $\pi \rightarrow \pi^*$  excitation energies of the unsaturated hydrocarbons, ethylene and benzene, discussed in the present review are of a similar magnitude, 3.5–4 eV, as for O<sub>2</sub>. They thus have easy access to the unoccupied  $\pi^*$  in the bond formation with the substrate and can be expected, as is also found, to bind with the molecular axis or plane parallel to the surface. We may view the bonding in terms of the DCD model with  $\pi$  donation into the substrate coupled with back-donation from the substrate into the unoccupied  $\pi^*$ . This description of the chemisorption bond is correct as seen from the XES measurements providing both occupied  $\pi^*$  and unoccupied  $\pi$  character [35]. The same bonding scheme can be obtained from the alternative spin-uncoupling mechanism, where the  $\pi \rightarrow \pi^*$  excitation necessary to form covalent bonds to the substrate is explicitly taken into account [169]. The resulting bond strength per  $\sigma$  bond formed is surprisingly constant,  $51 \pm 2$  kcal/mol, and very similar to the  $\sigma$  bond energy for the Pt–C interaction in

ethylene decomposition [203,204]. The computed resulting chemisorption energies span a rather narrow interval from 5 to 20 kcal/mol, which means that the binding energy *per carbon atom* for benzene becomes substantially smaller than for acetylene and ethylene. This is due to the aromatic stabilization in the benzene ring: in order to have the same *per carbon* binding energy six  $\sigma$  bonds would have to be formed. This would require a prohibitive excitation energy since the complete aromatic structure of the ring system would need to be broken.

In molecules that have lone pairs that interact with the metal surface the locality of the orbital is essential. We can see this in the comparison between the lone pair interactions in water and ammonia. In water the lone pair is a doubly occupied pure atomic 2p orbital perpendicular to the molecular plane. It forms bonding and antibonding states with respect to the metal d and sp bands. For simplicity, we only discuss the d band. The bonding state will mainly have molecular character and the antibonding state metal d character. Since, for the late transition metals, the d band is nearly fully occupied the antibonding state will mostly be filled resulting in Pauli repulsion. In comparison with the previously discussed radical adsorption the much stronger interaction involving unpaired electrons leads to larger splitting of the bonding and antibonding states where the latter will be above the d band in its energetic position and therefore not populated for transition metals. That water still binds with the molecular axis parallel to the surface where the lone pair points directly to the metal atoms is caused by the strongly attractive dipole–image dipole interaction. In the case of ammonia the lone pair is of rather different character. It corresponds to the  $3a_1$  molecular orbital that also contains hydrogen contributions. The major difference with water is that this orbital can mix with the empty  $4a_1$  orbital. Since the energetic splitting is not too large between the  $3a_1$  and  $4a_1$  orbitals this mixing is not too costly energetically. This mixing moves bond order from the N–H bond to lone pair bonding with the metal. In principle, the same interaction could also take place in adsorbed water with a perpendicular geometry where the  $3a_1$  orbital could interact in a similar fashion. However, in this adsorbate geometry the electrostatic contribution through dipole interaction will be much smaller and therefore it is not favorable. The  $\sigma$  system in  $N_2$  and CO could also give rise to similar lone pair interactions. Since the splitting between the occupied  $5\sigma$  and unoccupied  $6\sigma$  orbitals is of the order of 30 eV due to the extremely short internal bond distance it is very costly to mix these orbitals. This makes the  $\sigma$  system very stiff and the interaction with the metal is similar to that of the water lone pair orbital. However, the relatively short substrate–adsorbate distance for CO and  $N_2$  required for  $\pi$  interaction makes the  $\sigma$  system repulsive to a large extent.

Finally, let us consider the bonding of X–H groups to metal surfaces. This constitutes the weakest bonding covered in the present review. We have discussed two types of X–H interactions on surfaces, the Pt–HO species in adsorbed water on Pt(1 1 1) and *n*-octane adsorbed on Cu(1 1 0). In the case of octane on Cu there is a weak electron pairing between the hydrogen atom in the C–H group and the metal surface. This arises through interaction of both C–H bonding and antibonding orbitals with the d and sp bands. In order to create the bond the internal C–H bond is weakened to reduce the bond order and simultaneously the C–C bond is strengthened. We anticipate that the O–H group in water on Pt will behave in a similar manner where the internal O–H bond is weakened due to bonding to the metal surface.

To conclude, we have demonstrated the importance of XES experiments and DFT calculations to provide the necessary ingredients in the derivation of the electronic structure of adsorbates. The atom-specific probing of molecular orbitals makes the interpretation of XES experiments relatively simple and provides a strong basis for an experimental population analysis that can be directly compared to theoretical calculations. We have shown in the present review that we can obtain an overall understanding of chemical bonding on metal surfaces using a chemically intuitive molecular orbital picture.

## 5. Future outlook

With the successful development of XES for adsorbate systems as presented in this review we can see unique opportunities for new applications of this method to study a large variation of adsorbates on different surfaces. In the present review we have only described adsorbates on metal surfaces. It is essential to bring this technique to investigate other non-metallic substrates. There have been some recent studies of molecules on the, for the electronic industries, important semiconductor surfaces [205]. Oxide surfaces represent other substrates where many reactions vital for the environment occur. The electrostatic interaction is expected to be the dominating mechanism for molecular adsorption on oxide surfaces. However, there are systems where also covalent bonding could be important. The recent structure determination for CO, NO and NH<sub>3</sub> on NiO(1 0 0) [206] has demonstrated that theoretical calculations lead to much too large adsorption distances for all these systems. Clearly some fundamental aspects in the understanding of the bonding to the surface are not understood and the common picture of a mainly electrostatic interaction must be questioned. The balance between exchange and dynamical correlation and, in particular, the necessity for an accurate inclusion of exchange in the description of the NiO substrate has been indicated from theoretical studies of CO and NO on NiO(0 0 1) [207,208]. The experimental challenge for studies on oxide surfaces will be a higher probability for beam damage and it will therefore be essential for new instrumentation providing higher sensitivity.

In heterogeneous catalysis, the system is often rather complex with nanosized particles on a supporting material. There is clear evidence that many catalytic surfaces are not uniformly active, but the activity occurs only at specific sites where a special arrangement of surface atoms or special chemical composition exists. Variation of particle size gives rise to changes in the surface structure where the relative concentrations of atoms in steps, kinks and terrace sites are altered. It has recently been demonstrated that nearly all catalytic reactions that involve breaking of molecular bonds as a rate limiting step take place at steps and kink sites [209]. In a similar manner, many important reactions on naturally occurring mineral surfaces can be related to defect sites. It will be important to investigate in the future the bonding interaction of adsorbates at these active sites using XES and DFT. A stepped single-crystal surface represents a system with lowered symmetry. The *E*-vector of the incoming light can be aligned in three directions, along the step, perpendicular to the step and perpendicular to the surface allowing for a precise determination of the orientation and detailed geometry of an adsorbate in conjunction with DFT calculations. Both stepped and in particular kinked surfaces have unidirectional asymmetry perpendicular to the step or along the kink direction. It has recently been shown that unidirectional asymmetry in the charge distribution gives rise to variation of the spectral intensity in XA spectra of polymers [210]. We would expect to see intensity variations depending on whether the direction of the incident light is from the upper or lower part of the step or kink atoms. It will also be possible to probe intermediates during a catalytic reaction at intermediate pressures using XES.

Water is the most abundant compound in the biosphere and covers most real solid surfaces. The understanding of the water–solid interface is essential for many different processes in electrochemistry, corrosion, molecular environmental science, biomaterials, catalysis and for the development of the future hydrogen technology. X-ray spectroscopy using synchrotron radiation is a photon-in photon-out technique, including XAS with fluorescence detection. It is now possible to make SiN windows strong enough to withstand high pressures and thin enough to allow sufficient transmission of soft X-ray photons. XAS and XES experiments have recently successfully been performed on bulk liquid water

using thin SiN windows [64,211–213]. This furthermore offers new challenges to drive the theory development to include a strong coupling between the electronic structure and thermal motion in the system as well as, in specific cases, the nuclear dynamics that can be induced through the core excitation.

The development of ultrafast X-ray sources will offer new capabilities in the near future. We can envisage that an ultrafast laser can be used to stimulate a chemical reaction which can subsequently be probed with an extremely short X-ray pulse to generate core holes for XES measurements. By changing the delay between the pump and probe pulses a new dynamic range will become feasible. This is a standard procedure for femtosecond laser spectroscopy [214] where the excitation and probe steps involve valence electrons that are delocalized over many atomic centers making it difficult to analyze complex systems in detail. It would be an important development if we can probe how molecular orbitals are transformed during a chemical reaction in an atom-specific way around the center where the interesting chemistry takes place. This will open new prospects to locally study changes in molecular orbitals on surfaces during surface reactions. The ultimate chemist dream experiment would finally become possible.

## Acknowledgments

The work presented in the present review covers an exciting time when third-generation synchrotron radiation facilities became operational during the 1990s. This project was initially started on the experimental side together with Nial Wassdahl and without his devoted enthusiasm much would not have happened in the early days with X-ray emission spectroscopy on surfaces. We were very fortunate to have early access to the Advanced Light Source in Berkeley, where a large fraction of the beamtime at the high flux undulator beamline 8.0 was made available to this project through our collaboration with IBM, Almaden. Through this collaboration we benefited to a large extent from the strong interest and deep knowledge of soft X-ray science of Jo Stöhr. The support at the beamline from Mahesh Samant and Clemens Heske has been extremely valuable to us. We also like to acknowledge the enthusiasm, support and sources obtained from Joseph Nordgren and Nils Mårtensson. Simultaneously Pettersson was working together with Hans Ågren, Vincenzo Carravetta and Olav Vahtras to build into the DISCO direct SCF program by Faegri and Almlöf also a treatment of effective core potentials (ECP) for metal cluster studies. This, in combination with the work of Ågren, Carravetta and Vahtras to include treatment of inner-shell spectroscopies would enable the application of these to surface adsorbates. This collaboration formed the early introduction to the theoretical treatment of X-ray spectroscopies for which we are deeply grateful. The results discussed in our review have naturally been obtained in collaboration with a large number of extraordinary students who have worked very dedicatedly on these, many times very difficult, problems. We recognize the significant and valuable efforts of Thomas Wiell, Peter Bennich, Luciano Triguero, Alexander Föhlisch, Jörgen Hasselström, Mats Nyberg, Olof Karis, Barbara Brena, Dennis Nordlund and Henrik Öström in this respect. We have also benefited from collaborating with several excellent postdoctoral fellows Martin Weinelt, Hirohito Ogasawara, Peter Väterlein, Christine Kolczewski and Klaus Weiss as well as the assistant professor Yi Luo. Michael Odelius has extended the simulations to include CPMD and thus core-excited dynamics. We are grateful to Boris Minaev for introducing us to spin-uncoupling. We also like to acknowledge valuable discussions with Jens Norskov, Dietrich Menzel and Wilfred Wurth. Funding for this work has been provided by the Swedish Research Council, the Göran Gustafsson Foundation, the Swedish Foundation for Strategic Research, National

Science Foundation grant CHE-0089215 and the US Department of Energy, Office of Basic Energy Sciences through the Stanford Synchrotron Radiation Laboratory and the Advanced Light Source. We are grateful for generous allotments of CPU time at the National Swedish Computer Centers at NSC and PDC.

## References

- [1] G.A. Somorjai, *Introduction to Surface Chemistry and Catalysis*, Wiley, New York, 1994.
- [2] A. Meisel, G. Leonhardt, R. Szargan, *X-Ray Spectra and Chemical Binding*, Springer-Verlag, Berlin, 1989.
- [3] J. Nordgren, G. Bray, S. Cramm, R. Nyholm, J.-E. Rubensson, N. Wassdahl, *Rev. Sci. Instrum.* (1989) 60.
- [4] J. Nordgren, E.Z. Kurmaev, *J. Electron. Spectrosc. Relat. Phenom.* 110–111 (2000).
- [5] N. Wassdahl, A. Nilsson, T. Wiell, H. Tillborg, L.C. Duda, J. Guo, N. Mårtensson, J. Nordgren, J.N. Andersen, R. Nyholm, *Phys. Rev. Lett.* 69 (1992) 812.
- [6] D.P. Woodruff, T.A. Delchar, *Modern Techniques of Surface Science*, Cambridge University Press, New York, 1986.
- [7] A. Nilsson, H. Tillborg, N. Mårtensson, *Phys. Rev. Lett.* 67 (1991) 1015.
- [8] A. Nilsson, M. Weinelt, T. Wiell, P. Bennich, O. Karis, N. Wassdahl, J. Stöhr, M. Samant, *Phys. Rev. Lett.* 87 (1997) 2847.
- [9] S.D. Kevan, *Angle-Resolved Photoemission*, Elsevier, Amsterdam, 1992.
- [10] K. Horn, J. Dinardo, W. Eberhardt, H.J. Freund, *Surf. Sci.* 118 (1982) 465.
- [11] P. Bennich, T. Wiell, O. Karis, M. Weinelt, N. Wassdahl, A. Nilsson, M. Nyberg, L.G.M. Pettersson, J. Stöhr, M. Samant, *Phys. Rev. B* 57 (1998) 9274.
- [12] H. Kuhlenbeck, H.B. Saalfeld, U. Buskotte, M. Neumann, H.J. Freund, E.W. Plummer, *Phys. Rev. B* 39 (1989) 3475.
- [13] H.J. Freund, H. Kuhlenbeck, in: W. Eberhardt (Ed.), *Applications of Synchrotron Radiation: High Resolution Studies of Molecules and Molecular Adsorbates*, vol. 35, Springer-Verlag, Berlin, 1995.
- [14] K. Siegbahn, C. Nordling, G. Johansson, J. Hedman, P.F. Heden, K. Hamrin, U. Gelius, T. Bergmark, L.O. Werme, R. Manne, Y. Baer, *ESCA Applied to Free Molecules*, North-Holland, Amsterdam, 1969.
- [15] C.S. Fadley, in: C.R. Brundle, A.D. Baker (Eds.), *Electron Spectroscopy: Theory, Techniques and Applications*, vol. 2, Academic Press, New York, 1978.
- [16] S. Hufner, *Photoelectron Spectroscopy*, Springer-Verlag, Berlin, 1995.
- [17] W.F. Egelhoff, *Surf. Sci. Rep.* 6 (1986) 253.
- [18] N. Mårtensson, A. Nilsson, in: W. Eberhardt (Ed.), *Applications of Synchrotron Radiation: High Resolution Studies of Molecules and Molecular Adsorbates*, vol. 35, Springer-Verlag, Berlin, 1995.
- [19] J. Stöhr, *NEXAFS Spectroscopy*, Springer-Verlag, Berlin, 1992.
- [20] A. Nilsson, E. Zdansky, H. Tillborg, O. Björneholm, N. Mårtensson, J.N. Andersen, R. Nyholm, *Chem. Phys. Lett.* 197 (1992) 12.
- [21] J.C. Fuggle, in: C.R. Brundle, A.D. Baker (Eds.), *Electron Spectroscopy: Theory, Techniques and Applications*, vol. 4, Academic Press, London, 1981.
- [22] N. Mårtensson, A. Nilsson, *J. Electron. Spectrosc. Relat. Phenom.* 72 (1995) 1.
- [23] W. Eberhardt, in: W. Eberhardt (Ed.), *Applications of Synchrotron Radiation: High Resolution Studies of Molecules and Molecular Adsorbates*, vol. 35, Springer-Verlag, Berlin, 1995.
- [24] F. Gelmukhanov, H. Ågren, *Phys. Rep.* 312 (1999) 87.
- [25] O. Karis, A. Nilsson, M. Weinelt, T. Wiell, C. Puglia, N. Wassdahl, N. Mårtensson, M. Samant, J. Stöhr, *Phys. Rev. Lett.* 76 (1996) 1380.
- [26] J.-E. Rubensson, *J. Electron. Spectrosc. Relat. Phenom.* 110–111 (2000) 135.
- [27] A. Nilsson, N. Mårtensson, *Physica B* 208–209 (1995) 19.
- [28] J. Sakurai, *Advanced Quantum Mechanics*, Addison-Wesley, Menlo Park, CA, 1967.
- [29] C. Keller, M. Stichler, G. Comelli, F. Esch, S. Lizzit, W. Wurth, D. Menzel, *Phys. Rev. Lett.* 80 (1998) 1774.
- [30] A. Föhlisch, J. Hasselström, O. Karis, D. Menzel, N. Mårtensson, A. Nilsson, *J. Electron. Spectrosc. Relat. Phenom.* 101–103 (1999) 303.
- [31] A. Nilsson, *J. Electron. Spectrosc. Relat. Phenom.* 126 (2002) 3.

- [32] A. Föhlisch, P. Bennich, J. Hasselström, O. Karis, A. Nilsson, L. Triguero, M. Nyberg, L.G.M. Pettersson, *Phys. Rev. B* 16 (2000) 16229.
- [33] C. Keller, M. Stichler, G. Comelli, F. Esch, S. Lizzit, D. Menzel, W. Wurth, *Phys. Rev. B* 57 (1998) 11951.
- [34] L. Triguero, Y. Luo, L.G.M. Pettersson, H. Ågren, P. Väterlein, M. Weinelt, A. Föhlisch, J. Hasselström, O. Karis, A. Nilsson, *Phys. Rev. B* 59 (1999) 5189.
- [35] L. Triguero, A. Föhlisch, P. Väterlein, J. Hasselström, M. Weinelt, L.G.M. Pettersson, Y. Luo, H. Ågren, A. Nilsson, *J. Am. Chem. Soc.* 122 (2000) 12310.
- [36] M. Weinelt, N. Wassdahl, T. Wiell, O. Karis, J. Hasselström, P. Bennich, A. Nilsson, J. Stöhr, M. Samant, *Phys. Rev. B* 58 (1998) 7351.
- [37] P. Skytt, P. Glans, K. Gunnelin, J.H. Guo, J. Nordgren, Y. Luo, H. Ågren, *Phys. Rev. A* 55 (1997) 812.
- [38] N. Mårtensson, A. Nilsson, *J. Electron. Spectrosc. Relat. Phenom.* 75 (1995) 209.
- [39] T. Wiell, H. Tillborg, A. Nilsson, N. Wassdahl, N. Mårtensson, J. Nordgren, *Surf. Sci.* 304 (1994) 451.
- [40] U. von Barth, G. Grossmann, *Phys. Rev. B* 25 (1982) 5150.
- [41] J.J. Yeh, I. Lindau, *At. Data Nucl. Data Tables* 32 (1985) 1.
- [42] N. Correia, A. Flores-Riveros, H. Ågren, K. Helenelund, L. Asplund, U. Gelius, *J. Chem. Phys.* 83 (1985) 2035.
- [43] A. Föhlisch, M. Nyberg, P. Bennich, L. Triguero, J. Hasselström, O. Karis, L.G.M. Pettersson, A. Nilsson, *J. Chem. Phys.* 112 (2000) 1946.
- [44] A. Föhlisch, N. Wassdahl, J. Hasselström, O. Karis, D. Menzel, N. Mårtensson, A. Nilsson, *Phys. Rev. Lett.* 81 (1998) 1730.
- [45] A. Nilsson, P. Bennich, T. Wiell, N. Wassdahl, N. Mårtensson, J. Nordgren, O. Björneholm, J. Stöhr, *Phys. Rev. B* 51 (1995) 10244.
- [46] H. Tillborg, A. Nilsson, T. Wiell, N. Wassdahl, N. Mårtensson, J. Nordgren, *Phys. Rev. B* 47 (1993) 16464.
- [47] L. Pettersson, N. Wassdahl, M. Bäckström, J.-E. Rubensson, J. Nordgren, *J. Phys. B* 18 (1985) 125.
- [48] P. Bennich, Thesis, Department of Physics, Uppsala University, Uppsala, 1996.
- [49] A. Nilsson, N. Mårtensson, *Phys. Rev. B* 40 (1989) 10249.
- [50] B. Hernnäs, O. Björneholm, A. Nilsson, H. Tillborg, A. Sandell, N. Mårtensson, M. Karolewski, J.N. Andersen, *Phys. Rev. B* 23 (1993) 16052.
- [51] P.D. Johnson, S.L. Hulbert, *Phys. Rev. B* 35 (1987) 9427.
- [52] J. Rogozik, V. Dose, K.C. Prince, A.M. Bradshaw, P.S. Bagus, K. Hermann, P. Avouris, *Phys. Rev. B* 32 (1985) 4296.
- [53] A. Sandell, O. Björneholm, A. Nilsson, E. Zdansky, H. Tillborg, J.N. Andersen, N. Mårtensson, *Phys. Rev. Lett.* 70 (1993) 2000.
- [54] H. Tillborg, A. Nilsson, N. Mårtensson, J.N. Andersen, *Phys. Rev. B* 47 (1993) 1699.
- [55] A. Föhlisch, M. Nyberg, J. Hasselström, O. Karis, L.G.M. Pettersson, A. Nilsson, *Phys. Rev. Lett.* 85 (2000) 3309.
- [56] O. Karis, J. Hasselström, N. Wassdahl, M. Weinelt, A. Nilsson, M. Nyberg, L.G.M. Pettersson, J. Stöhr, M. Samant, *J. Chem. Phys.* 112 (2000) 8146.
- [57] J. Hasselström, O. Karis, M. Nyberg, L.G.M. Pettersson, M. Weinelt, N. Wassdahl, A. Nilsson, *J. Phys. Chem. B* 104 (2000) 11480.
- [58] F. Gelmukhanov, H. Ågren, *Phys. Rev. A* 49 (1994) 4378.
- [59] P. Skytt, J.-H. Guo, N. Wassdahl, J. Nordgren, Y. Luo, H. Ågren, *Phys. Rev. A* 52 (1995) 2572.
- [60] P. Glans, K. Gunnelin, P. Skytt, J.-H. Guo, N. Wassdahl, J. Nordgren, H. Ågren, F. Gelmukhanov, T. Warwick, E. Rotenberg, *Phys. Rev. Lett.* 76 (1996) 2448.
- [61] L. Triguero, Y. Luo, L.G.M. Pettersson, H. Ågren, P. Väterlein, M. Weinelt, A. Föhlisch, J. Hasselström, O. Karis, A. Nilsson, *Phys. Rev. B* 59 (1999) 5189.
- [62] N. Mårtensson, P. Balzer, P. Bruhwiler, J.O. Forsell, A. Nilsson, A. Stenborg, B. Wannberg, *J. Electron. Spectrosc. Relat. Phenom.* 70 (1994) 117.
- [63] J. Nordgren, J. Guo, *J. Electron. Spectrosc. Relat. Phenom.* 110–111 (2000) 1.
- [64] J.H. Guo, Y. Luo, A. Augustsson, J.E. Rubensson, C. Sätze, H. Ågren, H. Siegbahn, J. Nordgren, *Phys. Rev. Lett.* 89 (2002) 137402.
- [65] T. Tokushima, Y. Harada, M. Watanabe, Y. Takata, E. Ishiguro, A. Hiraya, S. Shin, *Surf. Rev. Lett.* 9 (2002) 503.
- [66] D. Nordlund, J.O. Forsell, A. Nilsson, unpublished data.
- [67] V. Carravetta, L.G.M. Pettersson, O. Vahtras, H. Ågren, *Surf. Sci.* 369 (1996) 146.

- [68] H. Ågren, V. Carravetta, O. Vahtras, L.G.M. Pettersson, *Chem. Phys. Lett.* 222 (1994) 75.
- [69] H. Ågren, V. Carravetta, O. Vahtras, L.G.M. Pettersson, *Theor. Chem. Acc.* 97 (1997) 14.
- [70] L. Triguero, L.G.M. Pettersson, *Surf. Sci.* 398 (1998) 70.
- [71] P. Hohenberg, W. Kohn, *Phys. Rev.* 136 (1964) 864.
- [72] C. Kolczewski, R. Puttner, O. Plashkevych, H. Ågren, V. Staemmler, M. Martins, G. Snell, M. Sant'anna, G. Kaindl, L.G.M. Pettersson, *J. Chem. Phys.* 115 (2001) 6426.
- [73] J.C. Slater, *Adv. Quant. Chem.* 6 (1972) 1.
- [74] J.C. Slater, K.H. Johnson, *Phys. Rev. B* 5 (1972) 844.
- [75] M.E. Casida, C. Daul, A. Goursot, K. Hermann, A. Koester, L.G.M. Pettersson, E. Proynov, A. St-Amant, D.R. Salahub (Principal authors), V. Carravetta, H. Duarte, N. Godbout, J. Guan, C. Jamorski, M. Leboeuf, V. Malkin, O. Malkina, M. Nyberg, L. Pedocchi, F. Sim, L. Triguero, A. Vela (Contributing authors), deMon-KS StoBe version 1.0, deMon Software, Program can be obtained from <http://w3.rz-berlin.mpg.de/~hermann/StoBe/index.html>, 2001.
- [76] J. Hasselström, A. Föhlisch, O. Karis, M. Weinelt, A. Nilsson, M. Nyberg, L.G.M. Pettersson, J. Stöhr, *J. Chem. Phys.* 110 (1999) 4880.
- [77] M. Staufer, U. Birkenheuer, T. Belling, F. Nörtemann, N. Rösch, M. Stichler, C. Keller, W. Wurth, D. Menzel, L.G.M. Pettersson, A. Föhlisch, A. Nilsson, *J. Chem. Phys.* 111 (1999) 4704.
- [78] L. Triguero, L.G.M. Pettersson, *Surf. Sci.* 398 (1998) 70.
- [79] M. Nyberg, J. Hasselström, O. Karis, N. Wassdahl, M. Weinelt, A. Nilsson, L.G.M. Pettersson, *J. Chem. Phys.* 112 (2000) 5420.
- [80] M. Nyberg, M. Odelius, A. Nilsson, L.G.M. Pettersson, *J. Chem. Phys.* 119 (2003) 12577.
- [81] L. Triguero, L.G.M. Pettersson, H. Ågren, *J. Phys. Chem.* 102 (1998) 10599.
- [82] B. Roulet, J. Gavoret, P. Nozieres, *Phys. Rev.* 178 (1969) 1072.
- [83] P. Nozieres, C. de Dominicis, *Phys. Rev.* 178 (1969) 1097.
- [84] U. von Barth, G. Grossmann, *Solid State Commun.* 32 (1979) 645.
- [85] U. von Barth, G. Grossmann, *Phys. Scr.* 21 (1980) 580.
- [86] G. Mahan, *Solid State Phys.* 29 (1974) 75.
- [87] D. Pines, P. Nozieres, *The Theory of Quantum Liquids*, Benjamin, New York, 1966.
- [88] V.I. Grebennikov, Y.A. Babanov, O.B. Sokolov, *Phys. Status Solidi* 79 (1977) 423.
- [89] L. Yang, H. Ågren, L.G.M. Pettersson, J.-H. Guo, C. Sätze, A. Föhlisch, A. Nilsson, J. Nordgren, *Phys. Scr.* 59 (1999) 138.
- [90] A. Mattsson, I. Panas, P. Siegbahn, U. Wahlgren, H. Åkeby, *Phys. Rev. B* 36 (1987) 7389.
- [91] M. Wuttig, R. Franchy, H. Ibach, *Surf. Sci.* 213 (1989) 103.
- [92] M.C. Ascensio, M.J. Aswing, A.L.D. Kilcoyne, D.P. Woodruff, A.W. Robinson, T. Lindner, J.S. Somers, D.E. Ricken, A.M. Bradshaw, *Surf. Sci.* 126 (1990) 1.
- [93] I.K. Robison, E. Vlieg, S. Ferrer, *Phys. Rev. B* 41 (1990) 6954.
- [94] H.C. Zeng, R.A. McFarlane, K.A.R. Mitchell, *Surf. Sci.* 208 (1998) 571.
- [95] H.C. Zeng, R.N.S. Sodhi, K.A.R. Mitchell, *Surf. Sci.* 188 (1987) 599.
- [96] T. Lederer, D. Arvanitis, M. Tischer, G. Comelli, L. Troeger, K. Baberschke, *Phys. Rev. B* 40 (1993) 11277.
- [97] S.M. Driver, D.P. Woodruff, *Surf. Sci.* 492 (2001) 11.
- [98] J.T. Hoelt, M. Polcik, M. Kittel, R. Terborg, R.L. Toomes, J.H. Kang, D.P. Woodruff, *Surf. Sci.* 492 (2001) 1.
- [99] T. Wiell, J.E. Klepail, P. Bennich, O. Björneholm, N. Wassdahl, A. Nilsson, *Phys. Rev. B* 58 (1998) 1655.
- [100] R. Hoffmann, *Solids and Surfaces: A Chemists View of Bonding in Extended Structures*, VCH Publishers Inc., New York, 1988.
- [101] A. Nilsson, J. Hasselström, A. Föhlisch, O. Karis, L.G.M. Pettersson, M. Nyberg, L. Triguero, *J. Electron. Spectrosc. Relat. Phenom.* 110–111 (2000) 15.
- [102] J.H. Onuferko, D.P. Woodruff, B.W. Holland, *Surf. Sci.* 178 (1986) 528.
- [103] E. Dudzik, A.G. Norris, R. McGrath, G. Charlton, G. Thornton, B. Murphy, T.S. Turner, D. Norman, *Surf. Sci.* 433–535 (1999) 317.
- [104] E.O.F. Zdansky, A. Nilsson, H. Tillborg, O. Björneholm, N. Mårtensson, J.N. Andersen, R. Nyholm, *Phys. Rev. B* 48 (1993) 2632.
- [105] B. Hammer, J.K. Norskov, *Nature* 376 (1995) 238.
- [106] J.H. Onuferko, D.P. Woodruff, B.W. Holland, *Surf. Sci.* 87 (1979) 3573.

- [107] Y. Gauthier, R. Baudoing-Savois, K. Heinz, H. Landskron, *Surf. Sci.* 251–252 (1991) 493.
- [108] T. Lederer, D. Arvanitis, M. Tischer, G. Comelli, L. Tröger, K. Baberschke, *Phys. Rev. B* 48 (1993) 11277.
- [109] W. Oed, H. Lindner, U. Starke, K. Heinz, K. Müller, J.B. Pendry, *Surf. Sci.* 224 (1989) 179.
- [110] C.L. Allyn, T. Gustafsson, E.W. Plummer, *Solid State Commun.* 24 (1977) 531.
- [111] D.E. Eastman, K. Cashion, *Phys. Rev. Lett.* 27 (1971) 1520.
- [112] F. Delbecq, P. Sautet, *Phys. Rev. B* 59 (1999) 5142.
- [113] B. Gumhalter, K. Wandelt, P. Avouris, *Phys. Rev. B* 37 (1988) 8048.
- [114] T. Gustafsson, E.W. Plummer, in: B. Feuerbacher, B. Fitton, R. Willis (Eds.), *Photoemission from surfaces*, Wiley, London, 1977.
- [115] S.S. Sung, R. Hoffman, *J. Am. Chem. Soc.* 107 (1985) 578.
- [116] B. Hammer, Y. Morikawa, J.K. Nørskov, *Phys. Rev. Lett.* 76 (1996) 2141.
- [117] E. Wimmer, C. Fu, A. Freeman, *Phys. Rev. Lett.* 55 (1985) 2618.
- [118] F. Greuter, D. Heskett, E.W. Plummer, H.J. Freund, *Phys. Rev. B* 27 (1983) 7117.
- [119] W. Wurth, *Vacuum* 40 (1990) 3.
- [120] P. Hu, D.A. King, M.H. Lee, M.C. Payne, *Chem. Phys. Lett.* 246 (1995) 73.
- [121] P.S. Bagus, C.J. Nelin, C.W. Bauschlicher, *Phys. Rev. B* 28 (1983) 5423.
- [122] P.S. Bagus, K. Hermann, *Phys. Rev. B* 33 (1986) 2987.
- [123] G. te Velde, E. Baerends, *Chem. Phys. Lett.* 177 (1993) 399.
- [124] M. Grunze, P.A. Dowben, R.G. Jones, *Surf. Sci.* 141 (1984) 455.
- [125] J. Stohr, R. Jaeger, *Phys. Rev. B* 26 (1982) 4111.
- [126] D.P. Woodruff, *J. Electron. Spectrosc. Relat. Phenom.* 126 (2002) 55.
- [127] D.I. Sayago, J.T. Hoefft, M. Polcik, M. Kittel, R.L. Toomes, J. Robinson, D.P. Woodruff, M. Pascal, C.L.A. Lamont, G. Nisbet, *Phys. Rev. Lett.* 90 (2003) 116104.
- [128] C.R. Brundle, P.S. Bagus, D. Menzel, K. Hermann, *Phys. Rev. B* 24 (1981) 7041.
- [129] D. Dubois, R. Hoffman, *Nouv. J. Chim.* 1 (1977) 479.
- [130] R. Hoffmann, M.M.L. Chen, D. Thorn, *Inorg. Chem.* 16 (1977) 503.
- [131] M. Dewar, *The Molecular Orbital Theory of Organic Chemistry*, McGraw-Hill, New York, 1969.
- [132] T.A. Albright, J.K. Burdett, M.H. Whengbo, *Orbital Interactions in Chemistry*, Wiley, New York, 1985.
- [133] O. Björneholm, A. Nilsson, E. Zdansky, A. Sandell, H. Tillborg, J.N. Andersen, N. Mårtensson, *Phys. Rev. B* 47 (1993) 2308.
- [134] H. Öström, Thesis, Department of Physics, Stockholm University, Stockholm, 2004.
- [135] S. Andersson, J.B. Pendry, *Phys. Rev. Lett.* 43 (1979) 363.
- [136] J.T. Hoefft, M. Polcik, D.I. Sayago, M. Kittel, R. Terborg, R.L. Toomes, J. Robinson, D.P. Woodruff, M. Pascal, G. Nisbet, C.L.A. Lamont, *Surf. Sci.* 540 (2003) 441.
- [137] J.T. Stuckless, N. Al-Sarraf, C. Wartnaby, D.A. King, *J. Chem Phys.* 99 (1993) 2202.
- [138] H. Tillborg, A. Nilsson, N. Mårtensson, *Surf. Sci.* 273 (1992) 47.
- [139] K.P. Huber, G. Herzberg, *Molecular Spectra and Molecular Structure*, Van Nostrand Reinhold, New York, 1979.
- [140] A. Eichler, J. Hafner, *Phys. Rev. B* 57 (1998) 10110.
- [141] G. Blyholder, *J. Phys. Chem.* 68 (1964) 2772.
- [142] M. Mavrikakis, B. Hammer, J.K. Nørskov, *Phys. Rev. Lett.* 81 (1998) 2819.
- [143] P. Uvdal, P.A. Karlsson, C. Nyberg, S. Andersson, N.V. Richardsson, *Surf. Sci.* 251–252 (1988) 167.
- [144] J.C. Tracy, *J. Chem. Phys.* 56 (1972) 2748.
- [145] S.Y. Tong, A. Maldonado, C.H. Li, M.A. van Hove, *Surf. Sci.* 94 (1980) 73.
- [146] H. Öström, L.G.M. Pettersson, A. Nilsson, unpublished data.
- [147] L. Westerlund, L. Jönsson, S. Andersson, *Surf. Sci.* 199 (1988) 109.
- [148] A. Sandell, O. Björneholm, A. Nilsson, B. Hernnäs, J.N. Andersen, N. Mårtensson, *Phys. Rev. B* 49 (1994) 10136.
- [149] H.P. Bonzel, *Surf. Sci. Rep.* 8 (1987) 43.
- [150] H.P. Bonzel, G. Pirug, in: D.A. King, D.P. Woodruff (Eds.), *The Chemical Physics of Solid Surfaces and Heterogeneous Catalysis*, vol. 6, Elsevier, Amsterdam, 1992.
- [151] N. Al-Sarraf, J.T. Stuckless, D.A. King, *Nature* 360 (1992) 243.
- [152] J. Hasselström, A. Föhlisch, R. Denecke, A. Nilsson, F. de Groot, *Phys. Rev. B* 62 (2000) 11192.

- [153] F. Sette, J. Stöhr, E.B. Kollin, D.J. Dwyer, J.L. Gland, J.L. Robbins, A.L. Johnson, *Phys. Rev. Lett.* 54 (1985) 935.
- [154] W. Wurth, C. Schneider, E. Umbach, D. Menzel, *Phys. Rev. B* 34 (1986) 1336.
- [155] H. Over, H. Bludau, R. Kose, G. Ertl, *Phys. Rev. B* 51 (1995) 4661.
- [156] J.J. Weimer, E. Umbach, D. Menzel, *Surf. Sci.* 159 (1985) 83.
- [157] M. Tushaus, P. Gardner, A.M. Bradshaw, *Surf. Sci.* 286 (1993) 212.
- [158] M. Kiskinova, G. Pirug, H.P. Bonzel, *Surf. Sci.* 133 (1983) 321.
- [159] R. Davis, D.P. Woodruff, O. Schaff, V. Fernandez, K.M. Schindler, P. Hofmann, K.U. Weiss, R. Dippel, V. Fritzsche, A.M. Bradshaw, *Phys. Rev. Lett.* 74 (1995) 1621.
- [160] A. Strisland, A. Beutler, A.J. Jaworowski, R. Nyholm, B. Setlik, D. Heskett, J.N. Andersen, *Surf. Sci.* 410 (1998) 330.
- [161] S. Jenkins, D.A. King, *J. Am. Chem. Soc.* 122 (2000) 10610.
- [162] J. Hasselström, A. Föhlisch, P. Väterlein, C. Nyberg, L.G.M. Pettersson, C. Heske, A. Nilsson, unpublished data.
- [163] S.J. Murray, P. Finetti, F.M. Leibsle, R.D. Diehl, R. McGrath, *Phys. Lett.* 237 (1995) 474.
- [164] G. Chiarello, A. Cupolillo, A. Amoddeo, L.S. Caputi, O. Comite, S. Scalse, L. Pagano, E. Colavita, *Surf. Sci.* 371 (1997) 45.
- [165] M. Nyberg, A. Föhlisch, L. Triguero, A. Bassan, A. Nilsson, L.G.M. Pettersson, unpublished data.
- [166] H. Öström, A. Föhlisch, M. Nyberg, M. Weinelt, C. Heske, L.G.M. Pettersson, A. Nilsson, *Surf. Sci.* 559 (2004) 85.
- [167] M.J.S. Dewar, *Bull. Soc. Chim. Fr.* 18 (1951) 79.
- [168] J. Chatt, L.A. Duncanson, *J. Chem. Soc.* (1953) 2939.
- [169] L. Triguero, L.G.M. Pettersson, B. Minaev, H. Ågren, *J. Chem. Phys.* 108 (1998) 1193.
- [170] P.A. Thiel, T.E. Madey, *Surf. Sci. Rep.* 7 (1987) 211.
- [171] M.A. Henderson, *Surf. Sci. Rep.* 46 (2002) 1.
- [172] H. Ogasawara, B. Brena, D. Nordlund, M. Nyberg, A. Pelmenchikov, L.G.M. Pettersson, A. Nilsson, *Phys. Rev. Lett.* 89 (2002) 276102.
- [173] M. Cavalleri, H. Ogasawara, L.G.M. Pettersson, A. Nilsson, *Chem. Phys. Lett.* 364 (2002) 363.
- [174] J. Hasselström, O. Karis, M. Weinelt, N. Wassdahl, A. Nilsson, M. Nyberg, L.G.M. Pettersson, M. Samant, J. Stöhr, *Surf. Sci.* 407 (1998) 221.
- [175] P. Skytt, P. Glans, J.-H. Guo, K. Gunnelin, C. Sätthe, J. Nordgren, F.K. GelMukhanov, A. Cesar, H. Ågren, *Phys. Rev. Lett.* 77 (1996) 5035.
- [176] A. Cesar, F. GelMukhanov, Y. Luo, H. Ågren, P. Skytt, P. Glans, J.-H. Guo, K. Gunnelin, J. Nordgren, *J. Chem. Phys.* 106 (1997) 1827.
- [177] G.J.C.S. van de Kerkhof, W. Biemolt, A.P.J. Jansen, R.A. van Santen, *Surf. Sci.* 284 (1993) 361.
- [178] W. Biemolt, G.J.C.S. van de Kerkhof, P.R. Davies, A.P.J. Jansen, R.A. van Santen, *Chem. Phys. Lett.* 188 (1992) 477.
- [179] W. Biemolt, A.P.J. Jansen, M. Neurock, G.J.C.S. van de Kerkhof, R.A. van Santen, *Surf. Sci.* 287–288 (1992) 183.
- [180] P.S. Bagus, K. Hermann, C.W. Bauschlicher, *J. Chem. Phys.* 81 (1984) 1966.
- [181] S. Barlow, K. Kitching, S. Haq, N.V. Richardson, *Surf. Sci.* 401 (1998) 322.
- [182] N.A. Booth, D.P. Woodruff, O. Schaff, T. Giessel, R. Lindsay, P. Baumgärtel, A. Bradshaw, *Surf. Sci.* 397 (1998) 258.
- [183] L.G.M. Pettersson, A. Nilsson, S. Myneni, Y. Luo, M. Nyberg, M. Cavalleri, L. Ojamäe, L.-Å. Näslund, H. Ogasawara, M. Odelius, A. Pelmenchikov, *J. Synchrotron Radiat.* 8 (2001) 136.
- [184] Q. Chen, D.J. Hankel, N.V. Richardson, *Surf. Sci.* 497 (2002) 37.
- [185] J.-H. Kang, R.L. Toomes, M. Polcik, J.-T. Hoelt, V. Efsthathiou, D.P. Woodruff, A. Bradshaw, *J. Chem. Phys.* 118 (2003) 6059.
- [186] R.L. Toomes, J.-H. Kang, D.P. Woodruff, M. Polcik, M. Kittel, J.-T. Hoelt, *Surf. Sci.* 522 (2003) 9.
- [187] J. Tersoff, D.R. Hamann, *Phys. Rev. B* 31 (1985) 805.
- [188] M. Odelius, unpublished data.
- [189] H. Öström, L. Triguero, K. Weiss, H. Ogasawara, M.G. Garnier, D. Nordlund, L.G.M. Pettersson, A. Nilsson, *J. Chem. Phys.* 118 (2003) 3782.
- [190] H. Öström, L. Triguero, M. Nyberg, H. Ogasawara, L.G.M. Pettersson, A. Nilsson, *Phys. Rev. Lett.* 91 (2003) 046102.
- [191] G. Witte, K. Weiss, P. Jakob, J. Braun, K.L. Kostov, C. Wöll, *Phys. Rev. Lett.* 80 (1998) 121.
- [192] W.L. Manner, G.S. Girolami, R.G. Nuzzo, *Langmuir* 14 (1998) 1716.
- [193] M.A. Chesters, P. Gardner, E.M. MacCash, *Surf. Sci.* 209 (1989) 89.
- [194] J.T. Pireaux, S. Svensson, E. Basilier, P.Å. Malmqvist, U. Gelius, R. Gaudario, K. Siegbahn, *Phys. Rev. A* 14 (1976) 2133.

- [195] T.E. Madey, J.T. Yates, *Surf. Sci.* 76 (1978) 397.
- [196] C. Wöll, K. Weiss, P.S. Bagus, *Chem. Phys. Lett.* 332 (2000) 553.
- [197] M. Grunze, M. Golze, W. Hirschwald, H.J. Freund, H. Plum, U. Selp, M. Tsai, G. Ertl, J. Kuppers, *Phys. Rev. Lett.* 53 (1984) 850.
- [198] S. Dahl, A. Logadottir, C. Egeberg, J.H. Larsen, I. Chorkendorff, E. Tornqvist, J.K. Norskov, *Phys. Rev. Lett.* 83 (1999) 1814.
- [199] S. Dahl, A. Logadottir, C.H. Jacobsen, J.K. Norskov, *Appl. Catal. A* 222 (2001).
- [200] C. Puglia, A. Nilsson, B. Hernnäs, O. Karis, P. Bennich, N. Mårtensson, *Surf. Sci.* 342 (1995) 119.
- [201] R.J. Guest, B. Hernnäs, P. Bennich, O. Björneholm, A. Nilsson, R.E. Palmer, N. Mårtensson, *Surf. Sci.* 1992 (1992) 239.
- [202] A. Sandell, A. Nilsson, N. Mårtensson, *Surf. Sci.* 241 (1991) 1.
- [203] E.A. Carter, *Chem. Phys. Lett.* 169 (1990) 218.
- [204] E.A. Carter, B.E. Koel, *Surf. Sci.* 226 (1990) 339.
- [205] A. Föhlisch, F. Hennies, W. Wurth, N. Witkowski, M. Nagasono, M.N. Piancastelli, L.V. Moskaleva, K.M. Neyman, N. Rösch, *Phys. Rev. B* 69 (2004) 153408.
- [206] J.T. Hoelt, M. Kittel, M. Polcik, S. Bao, R.L. Toomes, J.H. Kang, D.P. Woodruff, M. Pascal, C.L.A. Lamont, *Phys. Rev. Lett.* 87 (2001) 86101.
- [207] T. Bredow, *J. Phys. Chem. B* 106 (2002) 7053.
- [208] C. Di Valentin, G. Pacchioni, T. Bredow, D. Dominguez-Arisa, F. Illas, *J. Chem. Phys.* 117 (2002) 2299.
- [209] J.K. Norskov, T. Bligaard, A. Logadottir, S. Bahn, L.B. Hansen, M. Bollinger, H. Bengaard, B. Hammer, Z. Sljivancanin, M. Mavrikakis, Y. Xu, S. Dahl, C.H. Jacobsen, *J. Catal.* 209 (2002) 275.
- [210] J. Stöhr, M. Samant, *J. Electron. Spectrosc. Relat. Phenom.* 98–99 (1999) 189.
- [211] S. Myneni, Y. Luo, L.-Å. Näslund, M. Cavalleri, L. Ojamäe, H. Ogasawara, A. Pelmenchikov, P. Wernet, P. Väterlein, C. Heske, Z. Hussain, L.G.M. Pettersson, A. Nilsson, *J. Phys. Condens. Matter* 14 (2002) 213.
- [212] P. Wernet, D. Nordlund, U. Bergmann, H. Ogasawara, M. Cavalleri, L.-Å. Näslund, T.K. Hirsch, L. Ojamäe, P. Glatzel, M. Odelius, L.G.M. Pettersson, A. Nilsson, *Science* 304 (2004) 995 (First published on the web 1 April 2004; 10.1126/science.1096205).
- [213] L.-Å. Näslund, M. Cavalleri, H. Ogasawara, P. Wernet, D.C. Edwards, M. Sandström, S. Myneni, A. Nilsson, L.G.M. Pettersson, *J. Phys. Chem. A* 107 (2003) 6869.
- [214] C. Hess, S. Funk, M. Bonn, G. Ertl, M. Wolf, *Appl. Phys. A* 71 (2000) 477.
- [215] A. Nilsson, *J. Electron. Spectrosc. Relat. Phenom.* 93 (1998) 143.
- [216] A. Föhlisch, M. Stichler, C. Keller, W. Wurth, A. Nilsson, unpublished data.
- [217] H. Öström, H. Ogasawara, L.G.M. Pettersson, A. Nilsson, *Surf. Sci.*, in press.
- [218] L. Weinhardt, O. Fuchs, C. Danz, C. Heske, E. Umbach, unpublished data.